

Final Report for AFOSR STTR Contract F49620-02-C-0098
Development and Application of the High Bandwidth
Powered Resonance Tube

A. B. Cain and C. C. Nelson
Innovative Technology Applications Company

G. Raman
Illinois Institute of Technology

E. J. Kerschen
University of Arizona

9th November 2005

20060117 040

REPORT DOCUMENTATION PAGE

AFRL-SR-AR-TR-06-0001

The public reporting burden for this collection of information is estimated to average 1 hour per response, including gathering and maintaining the data needed, and completing and reviewing the collection of information. Send comments and information, including suggestions for reducing the burden, to Department of Defense, Washington Headquarters Service, 1215 Jefferson Davis Highway, Suite 1204, Arlington, VA 22202-4302. Respondents should be aware that notwithstanding any form that may appear on this collection of information, it does not display a currently valid OMB control number.

PLEASE DO NOT RETURN YOUR FORM TO THE ABOVE ADDRESS.

1. REPORT DATE (DD-MM-YYYY) 09-11-2005		2. REPORT TYPE Final Report		3. DATES COVERED (From - To) From September 2002 to May 2005	
4. TITLE AND SUBTITLE Development and Application of the High Bandwidth Powered Resonance Tube				5a. CONTRACT NUMBER F49620-02-C-0098	
				5b. GRANT NUMBER	
				5c. PROGRAM ELEMENT NUMBER	
6. AUTHOR(S) A. Cain, G. Raman, E. Kerschen, and C. Nelson				5d. PROJECT NUMBER	
				5e. TASK NUMBER	
				5f. WORK UNIT NUMBER	
7. PERFORMING ORGANIZATION NAME(S) AND ADDRESS(ES) Innovative Technology Applications Company, LLC Illinois Institute of Technology 13448 Foerstlacs Drive 10 W 32nd Street Creve Coeur, MO 63141 Chicago, IL 60616				8. PERFORMING ORGANIZATION REPORT NUMBER ITA-TR-2005-03	
9. SPONSORING/MONITORING AGENCY NAME(S) AND ADDRESS(ES) Air Force Office of Sci. Res. SciScientific 875 North Randolph Street Suite 325, Room 3112 Arlington, Virginia 22203 MA				10. SPONSOR/MONITOR'S ACRONYM(S) AFRL/AFOSR	
				11. SPONSOR/MONITOR'S REPORT NUMBER(S)	
12. DISTRIBUTION/AVAILABILITY STATEMENT Unlimited					
13. SUPPLEMENTARY NOTES					
14. ABSTRACT The Powered Resonance Tube (PRT) actuator, which is an adaptation of the Hartmann whistle, was selected for bandwidth enhancement. The operation and nearfield features of this actuator were characterized both experimentally and computationally. An improved analytical theory was developed for the prediction of the frequency of actuation. The analytical frequency prediction formula overcame difficulties with the conventional quarter wavelength theory by accounting for the compliance and mass of the fluid in the integration slot in the prediction of resonance frequencies of the system, leading to improved predictions for the resonant frequency. Advances in the program included development of a control system, directivity behavior, the role of harmonics, a miniaturized version of the PRT, Helmholtz based PRTs to reduce geometric constraints, a design GUI for Helmholtz systems. A demonstration of a PRT based flow control system applied to an impinging jet flow reduced both overall sound pressure level and tonal sound and identified the reduced mass flow benefits of applying actuation at an optimized frequency.					
15. SUBJECT TERMS Actuators, Flow Control, Acoustics, Impinging Jets, Impingement Tones, Resonance, Powered Resonance Tubes, Helmholtz Resonators					
16. SECURITY CLASSIFICATION OF:			17. LIMITATION OF ABSTRACT UU	18. NUMBER OF PAGES 169	19a. NAME OF RESPONSIBLE PERSON Alan B. Cain
a. REPORT U	b. ABSTRACT U	c. THIS PAGE U			19b. TELEPHONE NUMBER (include area code) (314) 576-1639

Contents

1	Summary	1
1.1	Overview	1
1.2	Introduction	2
1.3	Background on Actuators	2
1.4	Basic Behavior	2
1.5	Simulation Studies	5
1.6	Impinging Jet Acoustic Suppression Success	6
1.7	The Helmholtz Theory	6
1.8	Helmholtz PRT Simulations and Experiments	7
1.9	Miniaturized High Bandwidth PRT System	8
1.10	Graphical User Interface	10
1.11	Commercialization Efforts	10
2	Development and Study of an Initial Prototype	11
2.1	Overview	11
2.2	Background on Actuators	12
2.3	Benefits of High Frequency Excitation	13
2.4	Objective for Prototype Broadband Actuator Development	13
2.5	Powered Resonance Tube Development	14
2.6	Initiation of Experiments	15
2.6.1	Setup	15
2.6.2	Error analysis	16
2.7	Experimental Results	16
2.7.1	Frequency and Amplitude Characteristics	16
2.7.2	Pressure Measurements within the PRT	23
2.7.3	Detailed Characterization of the Nearfield	24
2.8	Initial Simulation Studies	28
2.9	Approaches for Controlling the PRT	31
2.10	Prototype Summary	42

3	Impinging Tone Suppression Using the Powered Resonance Tube	45
3.1	Overview	45
3.2	Introduction to Jet Impingement Tones	45
3.3	Jet Impingement Tone Experimental Apparatus	49
3.4	Jet Impingement Tone Results and Discussion	50
3.4.1	Impingement Tone Characterization	50
3.4.2	Impingement Tone Suppression	53
3.4.3	Role of Resonant Acoustic Frequency in Impingement Tone Suppression . . .	62
3.4.4	Augmentation of the Secondary Tone	63
3.5	Conclusions Regarding Suppression of Jet Impingement Tones Using PRTs	63
4	Resonance Characteristics and Actuation Signal Directivity	66
4.1	Overview	66
4.2	Introduction to the Resonance Tube Characteristics and Directivity Study	66
4.3	Experimental Methodology	67
4.4	Results and Discussion	69
4.4.1	Resonance Characteristics of the PRT	69
4.4.2	Actuation signal Directivity	73
4.5	Conclusions from the Experimental Study of Resonance Tube Characteristics and Directivity	81
5	Simulation of the PRT	83
5.1	Overview	83
5.2	Simulation Methodology	83
5.2.1	Axisymmetric Geometry Idealization	83
5.2.2	Pressure (Reynolds Number) Scaling	83
5.2.3	Flow Solver	84
5.3	Simulations of Straight Tube PRT Actuators	84
5.3.1	Effect of Primary Flow	93
5.3.2	Effect of Nozzle Pressure Ratio	95
5.3.3	The Effect of Including a Turbulence Model	96
5.4	Simulation of Helmholtz Based PRT Actuators	96
5.4.1	Geometry of the Helmholtz PRTs	96
5.4.2	Operating Conditions Studied	98
5.4.3	Results	98
5.4.4	Nonlinear Effects	108
5.5	Conclusions regarding PRT Simulations	111

6	Helmholtz PRT Theory	114
6.1	Introduction	114
6.2	Axial-wave theory for a Helmholtz resonator	115
6.2.1	End corrections	116
6.2.2	Axial-wave theory: free response of a Helmholtz resonator	117
6.2.3	Axial-wave theory: forced response of a Helmholtz resonator	118
6.3	Low-frequency theory for a Helmholtz resonator	119
6.3.1	Low-frequency theory: free response of a Helmholtz resonator	120
6.3.2	Low-frequency theory: forced response of a Helmholtz resonator	121
6.4	Numerical results and discussion	122
6.4.1	Resonance frequencies	122
6.4.2	Mode shapes	125
6.4.3	Capacities	127
6.4.4	Comparison to numerical simulation	129
6.5	Conclusions Regarding a Helmholtz Based PRT	131
7	Miniaturized PRT	133
7.1	Overview	133
7.2	Setup	133
8	Helmholtz PRT Design Tool	140
8.1	Overview	140
8.2	Screen Layout	140
8.3	Frequency Calculation	140
8.4	Geometry Calculation	144
	Acknowledgements	146
	Bibliography	147
A	Helmholtz PRT Actuator Design Code Source	151

List of Figures

1.1	Schematic diagram of Powered Resonance Tube (PRT) experimental set-up	3
1.2	Experimental data base of actuator frequency versus actuator depth is shown with a reference simulation data point and the curve for the basic theory. New theoretical results of Kerschen were obtained in this STTR effort and show improved agreement.	4
1.3	An example of simulation results at different supply pressures compared with the new theory developed in this effort.	5
1.4	Non-dimensional resonance frequency Ω of a Helmholtz resonator, as a function of the non-dimensional neck length l_n/l . The four curves correspond to $d_c/d_n = 2, 3, 4$ and 5 (top curve to bottom curve).	7
1.5	Comparison of the low frequency theory, low frequency theory with end corrections, axial wave theory with end corrections and a numerical simulation result for a Helmholtz based, powered resonance tube.	8
1.6	The miniaturized quarter wavelength and Helmholtz PRT actuators and a close-up detail of the Helmholtz resonator.	9
2.1	Schematic diagram showing an axisymmetric Powered Resonance Tube (PRT). The supply jet is on the left hand side and the resonance tube is on the right. The gap between the two is referred to as the "integration slot."	14
2.2	Frequency and amplitude characteristics of Powered Resonance Tubes (PRTs) at an NPR of 3.72 (NPR_Standard = 1.15 NPR).	18
2.3	Three dimensional map of actuation sound pressure levels for various values of the spacing parameter (jet-to-resonance tube), supply pressure and tube depth. (NPR_Standard = 1.15 NPR).	19
2.4	Iso-surface extracted from three dimensional map of Figure 2.3. The 140 dB iso-surface represents the acceptable target amplitude for effective actuation. (NPR_Standard = 1.15 NPR).	20
2.5	Hysteresis errors in frequency and sound pressure level with increasing and decreasing depth	21
2.6	Spectra at various resonance tube depths. (a) Decreasing depth. (b) Increasing depth.	22
2.7	Pressure time series from externally located microphone and from pressure transducer at the closed end of the tube at various frequencies. (a) 2.5 kHz. (b) 5 kHz. (c) 9 kHz.	23
2.8	Time-averaged features in the near field on the $x-y$ plane (I & II). (a) RMS pressure levels. (b) Sound pressure levels at actuation frequency. (c) Relative phase (degrees). NPR = 3.38 (NPR_Standard = 1.15 NPR), $s/D = 1$ and $l/D = 1$	25

2.9	Time-averaged features in the near field on the $y - z$ plane (I & II). (a) RMS pressure levels. (b) Sound pressure levels at actuation frequency. (c) Relative phase (degrees). Compressed air flow in actuator is from right to left. NPR = 3.38 (NPR_Standard = 1.15 NPR), $s/D = 1$ and $l/D = 1$	26
2.10	Sound pressure directivity of the PRT in the $y - z$ plane. Angles are with respect to the y -axis.	27
2.11	Phase-averaged near field pressure depicted on the $x - y$ plane (I & II). Phase difference from frame-to-frame (a-e) is 72 degrees. Measurement grid is shown in (f).	29
2.12	Phase-averaged near field pressure depicted on the $y - z$ plane (I & II). Phase difference from frame-to-frame (a -e) is 72 degrees. Measurement grid is shown in (f). Compressed air flow in actuator is from right to left.	30
2.13	Pressure contours from a simulation of a powered resonance tube using the WIND code with buffer zones to minimize reflected pressure waves from the outer boundaries. The nozzle pressure ratio for these simulations was 3.72. Time steps: (a) 32,400 and (b) 32,600. Compressed air flow in actuator is from left to right.	32
2.14	Iso-Mach contours from a simulation of a powered resonance tube using the Wind code. The nozzle pressure ratio for these simulations was 3.72. Time steps: (a) 31,400 (b) 32,200 and (c) 33,200. Compressed air flow in actuator is from left to right.	33
2.15	A time trace of the pressure in the far field. Solution calculated for 30,000 time steps.	34
2.16	Two approaches to creating a computer controlled high bandwidth actuator.	34
2.17	Spectra showing results of the Look Up Table (LUT) approach. The vertical line depicts the prescribed frequency and the spectrum represents the resulting actuation signal. (see Table 2.1 for the errors in using this method). NPR = 3.72 (NPR_Standard = 1.15 NPR).	36
2.18	Effectiveness of various control strategies in obtaining a prescribed frequency.	37
2.19	Effectiveness of Single Input Single Output (SISO) Feed Back controller (FB) showing its response to various input frequencies using the Look Up Table (LUT) as an initial estimator.	38
2.20	Features of the PRT that make the LUT approach ineffective (see marked regions). Pressure spectra with changing depth are shown for the following cases. (a) Optimal case, (b) jump to higher harmonics, (c) high frequency noise, (d) frequency gaps, (e) only low frequency, (f) higher harmonic jumps with frequency gaps.	39
2.21	Flow chart of the algorithm for the Multi Input Multi Output (MIMO) Feed Back controller (FB) used to control both the spacing and the depth of the PRT.	41
2.22	Response of the MIMO feedback controller for an input frequency of 9 kHz. The figure also illustrates the scanning of the spacing parameter (s/D) 0.8-1.08 to produce the prescribed frequency at the highest amplitude. Represents the saved points. (a) Frequency and (b) sound pressure level.	43
3.1	STOVL engine in hovering mode and impingement tone	46
3.2	Schematics of the impingement tone feedback mechanism.	47
3.3	Schematic diagram of the Powered Resonance Tube (PRT).	48
3.4	PRT integrated jet impingement tone set-up.	49

3.5	Impingement tone frequency staging: comparison of phase lock theory and experimental data a) without lift plate, b) with lift plate ($M_j = 0.86$, $C_1 = 1.66$, $D_M = 1.25$). Presence of the lift plate improves the fit of the data with the theoretical prediction.	51
3.6	Impingement tone amplitude and overall SPL variation a) without lift plate, b) with lift plate ($M_j = 0.86$, $D_M = 1.25$). Presence of the lift plate increases the mean overall SPL the mean tonal SPL of the impingement tone.	52
3.7	Variation in the frequency due to the change in Mach number (a) $h/D_M = 2.4$, (b) $h/D_M = 3.2$. The plots show the location of baseline impingement tone cases which were tested for the suppression and proximity of these tones with the corresponding resonant acoustic frequency (full wavelength acoustic frequency based on the stand-off distance between the lift plate and the ground plate).	54
3.8	Impingement tone amplitude and overall SPL variation due to the change in Mach number. (a) $h/D_M = 2.4$, (b) $h/D_M = 3.2$. For $h/D_M = 3.2$ the impingement tone is weaker as compared to $h/D_M = 2.4$	55
3.9	Salient features of the PRT for different nominal frequency settings. a) frequency, and b) tonal amplitude. Except for the 17,500 Hz the variation in the nominal frequency of the PRT due to the change in PRT stagnation pressure is marginal. However, variation in the SPL in all the cases is significant of the order of 10 dB.	56
3.10	Primary impingement tone suppression. (a) 3,296 Hz ($M_j = 0.88$, $h/D_M = 2.4$), and (b) 4,272 Hz ($M_j = 0.86$, h/D_M). For same level of maximum suppression, selecting the acoustic tone of the appropriate frequency reduces the NPR and hence the mass flow rate by 50%. This proves the fact that high frequency forcing is an effective and far superior strategy, as compared to the oscillatory mass injection.	57
3.11	Primary impingement tone suppression against the parameter PRT tone frequency/impingement tone frequency ($M_j = 0.88$, $h/D_M = 2.4$). The deterioration in the collapse of the data suggests that frequency might not be the most important variable affecting suppression.	58
3.12	Primary impingement tone suppression against the parameter PRT tonal SPL ($M_j = 0.88$, $h/D_M = 2.4$). Tonal SPL proves to be a successful parameter for all the cases except for the no tone case. The zero depth PRT achieves its suppression through the splashing of the oscillatory mass flow. Isolation of the "no tone" PRT hints us mass flow to be one of the crucial variables behind the suppression.	59
3.13	Primary impingement tone suppression against the parameter "PRT mass flow rate \times PRT tonal SPL". (a) 3296 Hz ($M_j = 0.88$, $h/D_M = 2.4$), and (b) 4272 Hz ($M_j = 0.86$, $h/D_M = 2.4$). The parameter "PRT mass flow rate \times PRT tonal SPL" proves to be successful for both the impingement tones. Good collapse suggests that, PRT mass flow rate and PRT tonal SPL are the most crucial variables which affect the suppression. The figure (especially (a)) also points out the optimum frequency for the suppression (i.e. 12,000 Hz).	60
3.14	overall SPL suppression (a) 3,296 Hz ($M_j = 0.88$, $h/D_M = 2.4$), and (b) 4,272 Hz ($M_j = 0.86$, $h/D_M = 2.4$). As in the case of Figure 3.10, the present figure represents the suppression data in a raw form. As apparent from the figure, PRTs can achieve suppression up to and above 10 dB.	61
3.15	Primary impingement tone suppression ($M_j = 0.86$, $h/D_M = 3.2$). Comparison with Figure 3.13(a) and 3.13(b) shows that for 3,662 Hz and 4,272 Hz tones, suppression starts picking up late as compared to 3,296 Hz tone. Hence, 3,662 Hz and 4,272 Hz tones are difficult to suppress. Our conjecture is that the close proximity of these tones with the "resonant acoustic frequency" (Figure 3.7) is responsible their suppression. .	62

3.16	Primary impingement tone spectrum. (a) 4,272 Hz ($M_j = 0.86$, $h/D_M = 2.4$), and (b) 3,296 Hz ($M_j = 0.88$, $h/D_M = 2.4$). The nature of the suppressed as well as unsuppressed spectra of 4,272 and 3,296 Hz impingement tone is different. When unsuppressed, the 4,272 Hz spectra shows strong harmonic content. The 3,296 Hz spectrum does not contain any strong harmonic, but it shows weak harmonic and sub-harmonic spike. When suppressed, the 3,296 Hz tone shows an additional spike (referred to as a "secondary tone") at 4,272 Hz.	64
3.17	Secondary impingement tone augmentation ($M_j = 0.88$, $h/D_M = 2.4$)	65
4.1	Schematic diagram of Powered Resonance Tube (PRT) experimental set-up	68
4.2	SPL map of the PRT at different Nozzle Pressure Ratios (NPRs). The white islands denote the combinations of depth and spacing at which PRT resonates—also referred to as active spacing. The thick lines show shock cell termination distance as per Tam's model [Tam, 1995], thus facilitates a comparison between active spacing and theoretical shock cell length.	70
4.3	Comparison of the PRT Active spacing (s/D)—the spacing at which the PRT resonates—and the shock cell termination distance (x_{shock}/D) (PRT resonator tube depth (l/D) = 0.2). (a) first shock cell (b) second shock cell (c) third shock cell	72
4.4	Influence of the Nozzle Pressure Ratio (NPR) on the active spacing (s/D)—the spacing at which the PRT resonates—at depth (l/D) = 0.2. (a) NPR = 3.33, i.e., NPR below 4, when the jet shows diamond shock cell structure (b) NPR = 4.29, i.e., NPR above 4, when the jet shows barrel shock cell structure.	73
4.5	Influence of the PRT spacing (s/D) on the its resonance frequency. a. NPR = 2.62 b. NPR = 3.57 c. NPR = 4.29. For a particular depth (l/D), resonant frequency remains unaltered due to the change in spacing (s/D).	74
4.6	Phase averaged snapshots of 4 kHz ($f + 2f + 3f$) PRT signal (NPR = 3.33, PRT jet is flowing form left to right). Each sub-figure is a phase averaged snapshot of the acoustic field at 300 phase interval. The black or white regions, enclosed by dotted rectangles, represent lobes with concentrated acoustic energy.	76
4.7	Propagation directivity of 4 kHz PRT signal with different harmonic content: (a) fundamental frequency, f (b) first harmonic, $2f$ (c) second harmonic $3f$ (d) $f + 2f$ (e) $f + 2f + 3f$. (NPR = 3.33, the PRT jet is flowing form left to right, dotted rectangles denote the prominent lobes for which directivity vectors are plotted). . . .	77
4.8	Change in the PRT signal directivity due to the change in the frequency. a. 3 kHz (f) b. 4 kHz (f) c. 6 kHz (f) d. 8 kHz (f) e. 9 kHz (f) f. 12 kHz (f) (dotted rectangles denote the prominent lobes for which directivity vectors are plotted).	78
4.9	p_{rms} map of 4 kHz PRT signal with different harmonic content: (a) fundamental (f) (b) first harmonic ($2f$) (c) second harmonic ($3f$) (d) ($f + 2f$) (e) ($f + 2f + 3f$). (NPR = 3.33, PRT jet is flowing form left to right).	79
4.10	Experimental repeatability for pressure variation along the line $z/D = 2.8$ for the PRT signal of 3 kHz (f). (PRT jet is flowing form left to right) The large error bars just down stream of the resonator tube exit ($x/D = 5.6$) are the result of the hydrodynamic fluctuations caused by the jet flow spilling over the nozzle block. . .	80
4.11	Comparison of 6 kHz fundamental and 3 kHz first harmonic PRT signal. (a) 6 kHz (f): phase averaged snapshot (b) 3 kHz ($2f$): phase averaged snapshot (c) 6 kHz (f): p_{rms} plot (d) 3 kHz ($2f$): p_{rms} plot (PRT jet is flowing form left to right, dotted rectangles denote the prominent lobes for which directivity vectors are plotted). . .	81

4.12	Comparison of 12 kHz fundamental and 4 kHz second harmonic PRT signal. (a) 12 kHz (f): phase averaged snapshot (b) 4 kHz ($3f$): phase averaged snapshot (c) 12 kHz (f): p_{rms} plot (d) 4 kHz ($3f$): p_{rms} plot (PRT jet is flowing from left to right, dotted rectangles denote the prominent lobes for which directivity vectors are plotted).	82
5.1	A comparison of the results of nonlinear computation and a refined linear theory (including inertia of the fluid in the integration slot) for predicting the effects of resonance tube depth on the resonance frequency.	85
5.2	Experimental data base of actuator frequency versus actuator depth. Also shown are curves for the basic theory and the refined theory with $s/d = 2.8$, and one simulation data point.	86
5.3	Low Reynolds number pressure history of the resonance tube over the first 60,000 time steps.	87
5.4	High Reynolds number pressure history of the resonance tube over the first 60,000 time steps.	88
5.5	Experimental pressure history.	88
5.6	Pressure contours for the low Reynolds number case after 60,000 time steps.	89
5.7	Pressure contours for the high Reynolds number case after 60,000 time steps.	90
5.8	Mach contours for the low Reynolds number case after 60,000 time steps.	91
5.9	Mach contours for the high Reynolds number case after 60,000 time steps.	92
5.10	Vorticity contours for the low Reynolds number case after 60,000 time steps.	93
5.11	Vorticity contours for the low Reynolds number case after 60,000 time steps.	94
5.12	Pressure oscillations on the wall in a Mach 0.5 freestream and boundary layer driven from below by a powered resonance tube.	95
5.13	Resonance frequency as a function of nozzle pressure ratio (NPR) for a "shallow" resonance tube.	96
5.14	Two resonators and detail drawing of a Helmholtz resonator (dimensions in inches)	97
5.15	Comparison of the simulation results to the Kerschen theory predictions	99
5.16	Pressure trace and narrowband SPL near the integration slot exit for Case 1	100
5.17	Pressure trace and narrowband SPL near the integration slot exit for Case 2	101
5.18	Pressure trace and narrowband SPL near the integration slot exit for Case 3	102
5.19	Pressure trace and narrowband SPL near the integration slot exit for Case 4	103
5.20	Spectral power distribution comparison of four PRT geometries.	104
5.21	Snapshots from one cycle of the PRT exterior pressure wave radiation	105
5.22	Snapshots of slot pressure from one operational cycle of the PRT	106
5.23	Snapshots of pressure in the nozzle and resonator from one operational cycle of the PRT	107
5.24	Snapshots of vorticity in the nozzle, slot, and resonator from one operational cycle of the PRT	109
5.25	Pressure time history for simulation case 9 measured about 1/4" downstream of the integration slot, 60,000 timesteps.	110

5.26	Pressure time history for simulation case 10 measured about 1/4" downstream of the integration slot, 120,000 timesteps.	111
5.27	Pressure time history for simulation case 11, 90,000 timesteps.	112
5.28	The Fourier transform of the pressure time history for simulation case 11.	112
5.29	Instantaneous pressure contours for case 11 after 120,000 time steps.	113
6.1	Non-dimensional resonant frequency Ω_1 of a Helmholtz resonator, as a function of the nondimensional neck length α_n . $A_c/A_n = 4, 9, 16$, and 25 (top curve to bottom curve).	123
6.2	Resonant frequency Ω_1 of a Helmholtz resonator as a function of the area ratio A_n/A_c , for the case of optimum geometry ($\alpha_n = 0.5$).	123
6.3	Resonant frequency Ω_1 of an axisymmetric Helmholtz resonator as a function of the diameter ratio d_n/d_c , for the case of optimum geometry ($l_n = l_c$).	124
6.4	Comparison of the low-frequency theory and axial-wave theory predictions for the resonant frequency Ω_1 as a function of α_n . $A_c/A_n = 4$ (top curves) and 16 (bottom curves).	125
6.5	Pressure mode shapes for free resonance of a Helmholtz resonator, plotted as a function of x/l . $A_c/A_n = 1, 4, 9, 16$ and 25 (bottom curve to top curve for $x/l > \alpha_n$).	126
6.6	The capacity C for forced response of a Helmholtz resonator at frequency Ω , plotted as a function of the frequency ratio Ω/Ω_1 . $A_c/A_n = 1, 4$ and 16 (bottom curve to top curve).	128
6.7	Comparison of the low-frequency theory and axial-wave theory predictions for the capacity C of a Helmholtz resonator, plotted as a function of the frequency ratio Ω/Ω_1 . $A_c/A_n = 4$ (bottom curves) and 16 (top curves).	130
6.8	Comparison of the frequency obtained in the simulation to that predicted by the various analytical models.	131
7.1	The miniaturized quarter wavelength and Helmholtz PRT actuators and a close-up detail of the Helmholtz resonator. (repeat of Figure 1.6).	134
7.2	Spectra for the 1/16" straight tube and Helmholtz resonator with the apparatus set at 4kHz.	135
7.3	Time series for the 1/16" straight tube and Helmholtz resonator with the apparatus set at 4kHz.	135
7.4	Spectra for the 1/16" straight tube and Helmholtz resonator with the apparatus set at 7kHz.	136
7.5	Time series for the 1/16" straight tube and Helmholtz resonator with the apparatus set at 7kHz.	136
7.6	Frequency versus depth with theoretical and measured values.	137
7.7	Frequency versus depth with theoretical data and all resonating measured values.	137
8.1	Design tool appearance when computing Helmholtz PRT actuator geometry based on a desired frequency	141
8.2	Summary window of the Helmholtz PRT actuator design code	143
8.3	Design tool appearance when computing Helmholtz PRT actuator geometry based on a desired frequency	144

List of Tables

1.1	Comparison of simulation versus theory for two geometries	8
1.2	Comparison of Simulation, Theory, and Experiment	9
2.1	Frequency error analysis measurements for the PRT	16
2.3	Amplitude error analysis measurements for PRT	17
2.4	The Calculated Velocities of the Compression and Expansion Waves.	24
2.5	Summary of effectiveness of Look Up Table (LUT) approach and Feed Back controller (FB) in producing high frequency excitation signals based on prescribed inputs in ascending order. The error when using the feedback controller depends on the frequency bandwidth (20 Hz for our experiments) that depends on sampling frequency (80 kHz) and number of points in the spectrum (4096).	35
2.6	Effect of resonance tube depth ratio (d/D) on the resulting frequency, sound pressure level, acoustic power and acoustic energy (spacing parameter, $s/D = 1.2$, $NPR = 3.72$).	37
3.1	PNLT analysis for 4272 Hz impingement tone and 17,500 Hz PRT frequency setting	59
4.1	Measurement parameters used in the PRT signal directivity study.	71
5.1	Frequency as a function of the nozzle pressure ratio. "NR" denotes no resonance.	95
5.2	PRT Geometries	97
5.3	Summary of Results	98
5.4	Comparison of simulation versus theory for two geometries	108
5.5	Comparison of Simulation, Theory, and Experiment	110
7.1	A table of Frequency vs. spacing and pressure for a depth of 1/2" in the Helmholtz resonator.	138
7.2	A table of Frequency vs. spacing and pressure for a depth of 1/2" in the 1/16" straight tube resonator.	139

Nomenclature

Acronyms

AFC	Active flow control
DAQ	Data acquisition
FB	Feed-back
FFT	Fast Fourier Transform
CD	Convergent-Divergent (as in nozzles)
LUT	Look up table
MIMO	Multiple input multiple output
NPR	Nozzle pressure ratio
OASPL	Overall sound pressure level
PNLT	Perceived noise level corrected for the tone
PRT	Powered resonance tube
QWL	Quarter Wavelength
SISO	Single input single output
STOVL	Short Takeoff Vertical Landing
SPL	Sound pressure level (reference pressure is $20 \mu\text{Pa}$)

Roman Symbols

A	Area
c	Speed of sound
C_1	Constant accounting for convective velocity of coherent structures
C_2	Constant accounting for changes in feedback acoustic velocity
D	Jet nozzle diameter
d	Diameter
f	Frequency of the acoustic wave
H	Helmholtz number
h	Stand-off distance between the nozzle exit and ground plate
L_{shock}	Shock cell length
l	Resonator length
l_c	Resonator cavity length
l_n	Effective resonator neck length, including end corrections
M	Fully expanded Mach number based on plenum pressure
m	Mass flow rate
n	Stage number
p	Pressure
s	Integration slot width (spacing between the PRT nozzle and resonator tube)
u	Velocity
x, y, z	Cartesian coordinate directions
x_{shock}	Shock cell termination distance

Greek Symbols

Δ_n	Phase shift associated with acoustic wave reflection
λ	Wavelength of the actuator signal
Ω	Nondimensional Helmholtz PRT resonance frequency
ω	Resonance frequency

Subscripts

0	Stagnation properties
e	Properties at the nozzle exit plane
b	Ambient properties
c	Helmholtz resonator cavity properties
j	Jet properties at fully expanded condition
M	Properties of the main jet nozzle
n	Helmholtz resonator neck properties
rms	Root mean square value
∞	Free stream properties

Chapter 1

Summary

1.1 Overview

This section of the final report summarizes activities conducted as part of the Air Force Office of Scientific Research STTR program on the development of high-bandwidth actuators. High bandwidth allows use of the same actuator at various locations on an aircraft and over a range of flight speeds. The actuator selected for bandwidth enhancement was the Powered Resonance Tube (PRT) actuator, which is an adaptation of the Hartmann whistle. The device is capable of producing high frequency and high amplitude pressure and velocity perturbations for active flow control applications. The program began with the development of a first-generation high-bandwidth actuator. The operation and nearfield features of this actuator were characterized both experimentally and computationally and an improved analytical theory was developed for the prediction of the frequency of actuation. The detailed nearfield data provided information of the actuation signal directivity and its variation with actuation frequency. One of the prototype actuators produces frequencies ranging from 1,600 to 15,000 Hz at amplitudes as high as 160 dB near the source. The computational work was conducted at Reynolds numbers lower than that in the experiments, and established the Reynolds numbers required to simulate details observed in the experiments. The analytical frequency prediction formula overcame difficulties with the conventional quarter wavelength theory by accounting for the compliance and mass of the fluid in the integration slot in the prediction of resonance frequencies of the system, leading to improved predictions for the resonant frequency.

One of the goals of this project was to create a computer controlled high-bandwidth actuator. This effort began with the creation of a computer look up table that was based on very detailed experimental data (for various resonance tube depths, integration slot spacings and supply pressures). The look up table approach was only partly successful in producing a reliable actuator, due to the presence of jumps to higher modes, high frequency noise, and gaps in the resonance response curves. To overcome these difficulties, a closed-loop feedback control system with multiple inputs and multiple outputs was developed. This approach produced a system that was able to provide actuation signals at the prescribed frequency.

Towards the end of the program miniature PRT actuators were developed and applied to the technologically important problem of high-speed jet impingement noise suppression. The final efforts of this program focused on creating a high-bandwidth actuator whose frequency range allows some geometric flexibility of the design. This flexibility is accomplished by integrating the Helmholtz resonator concept into an axial PRT resonator system. With such an approach one can get a wider frequency variation within a given geometry constraint.

1.2 Introduction

High bandwidth actuation is essential for the effective application of Active Flow Control (AFC) to improve the efficiency of both internal and external fluid flow systems. Successful application to aircraft systems can produce lighter, more agile aircraft, with increased range and payload. The design of an active flow control system requires knowledge of unsteady flow phenomena and selection of appropriate actuators, sensors, and a control algorithm. The present effort focused on the development of high-bandwidth actuators for active flow and noise control applications. It should be noted that the powered resonance tube derives its name from the Hartmann resonance tube. The term "powered" indicates that both "non-powered" (deriving energy from the free stream) and "powered" (requiring secondary air) versions are possible. The term "bandwidth" refers to the range of frequencies of effective operation. The goal of the current work was to demonstrate a powered resonance tube that can generate strong tones over a frequency "bandwidth" of approximately one order of magnitude, and is done as a part of the USAF's program on "high bandwidth actuators." Thus, it should be noted that the term "bandwidth" is not intended to convey an instantaneous output state but rather the range of conditions over which the device is applicable.

1.3 Background on Actuators

The basic actuator for this work is an extension of the Hartman resonance tube (also referred to as the Hartman whistle). The resonance tube phenomenon was first described by Hartmann in 1918 (see [Hartmann and Troll, 1922], [Hartmann, 1931]). The Hartmann whistle apparatus consists of a jet aimed at the open end of a tube that is closed at the other end. There are two phases during the operation of this device. In the first phase, the jet penetrates the tube and compresses the air within the tube. In the second phase, the compressed air in the tube empties itself. Under favorable conditions the cycle perpetuates itself. However, fixed geometry actuators can produce effective actuation only over a small range of frequencies. This poses a problem because one requires a new actuator every time there is a change in geometric or fluid dynamic parameters. Extending earlier fixed frequency efforts ([Raman et al., 2000], [Raman et al., 2001], [Raman and Kibens, 2001], [Kastner and Samimy, 2002]), the goal was to use the oscillatory pressures and velocities produced by this device to design a high bandwidth actuator. Examples of possible applications include the high frequency excitation for suppression of flow-induced resonance in weapons bay cavities ([Stanek et al., 2000]) and jet-ground impingement tones in STOVL aircraft.

1.4 Basic Behavior

In Figure 1.1 a prototype high bandwidth PRT is presented. Figure 1.2 shows a comparison of experimental data with the original quarter-wavelength (QWL) theory and the new theory developed in this program for the variation of actuator resonance frequency versus depth. In this report NPR is defined as the ratio of the stagnation pressure to ambient pressure. The data of Figure 1.2 were acquired at an NPR of 3.72 for various values of the spacing parameter (integration slot width or jet to resonance tube spacing). The experimental data is generally grouped along a smooth curve, except for a few data points showing a higher mode response.

The experimental data with a fundamental mode response is in good agreement with the refined theory of [Kerschen, 2001] that considers the acoustic coupling of the resonance tube and the integration slot. The Kerschen theory accounts for the interaction of the resonance tube with the integration slot; the compliance and mass of the fluid in the integration slot are incorporated into the prediction. The prediction of this refined theory for an integration slot width equal to the supply jet diameter is shown in Figure 1.2. The refined theory is in much better agreement with the

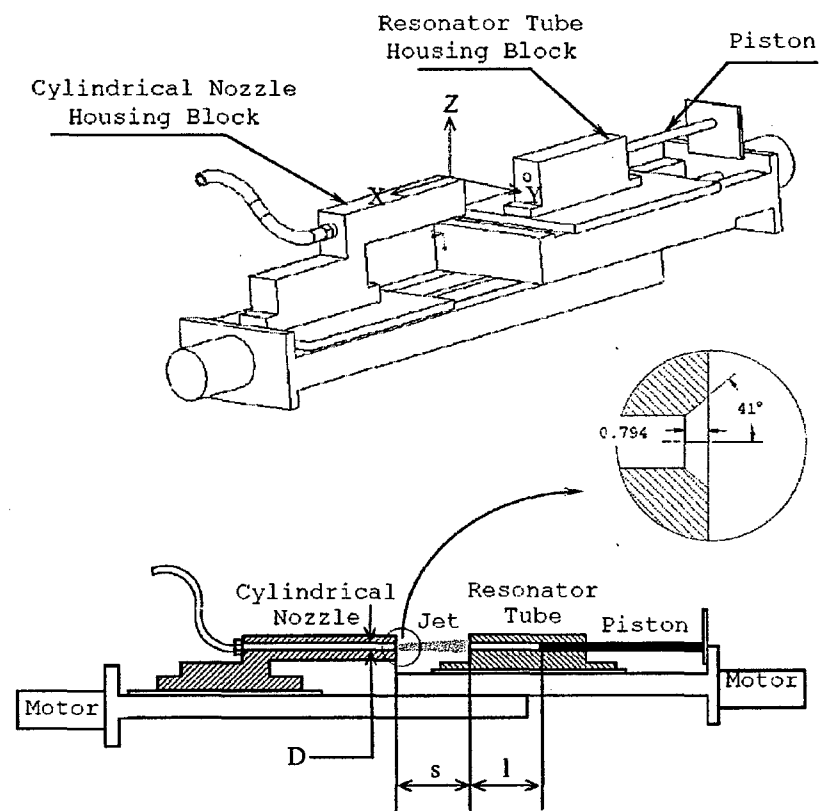


Figure 1.1: Schematic diagram of Powered Resonance Tube (PRT) experimental set-up

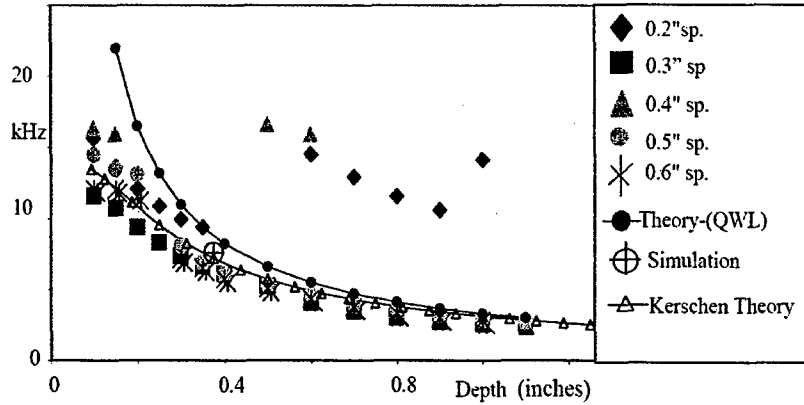


Figure 1.2: Experimental data base of actuator frequency versus actuator depth is shown with a reference simulation data point and the curve for the basic theory. New theoretical results of Kerschen were obtained in this STTR effort and show improved agreement.

experimental data, remaining quite accurate even at small values of the tube depth. Essentially, for small tube depths, the inertia of the fluid in the integration slot becomes important, significantly reducing the resonance frequency relative to the prediction of the basic theory. The frequency versus depth curve was also simulated numerically. Figure 1.5 shows a comparison of the numerical results with those predicted by the new theory.

A detailed experimental data base was created by measuring the frequency and sound pressure level at various tube depths and spacing parameters for a range of NPR values. The results are reported in [Sarpotdar et al., 2005a]; some of the results will also be presented later in Chapter 2 of this report.

From the data base reported in [Sarpotdar et al., 2005a], it is clear that there are only limited regions of parameter space that produce high amplitude. Thus an effective computer-controlled actuator would have to search for the correct integration slot spacing at each depth. In addition, the data base shows a relationship between the theoretical shock spacing of a jet at the corresponding NPR and integration slot spacing that produces the peak amplitude. The PRT device sometimes exhibits jumps to higher modes or does not produce a stable resonance at all under some conditions. These features and others shown by the data base would make a look up table ineffective.

Significant improvement was obtained by going to a feedback controlled Single Input Single Output (SISO) system, and the performance of the system was enhanced further by going to a Multiple Input Multiple Output (MIMO) system. [Sarpotdar et al., 2005a] shows the directivity of a PRT actuator at different actuation frequencies. The directivity was observed to change as one progresses from the fundamental frequency to the harmonics. In addition, it was noted that the directivity changed from downstream to upstream (relative to the actuator supply jet direction) when the fundamental actuation frequency was increased from 3 to 12 kHz. p_{rms} plots indicate that the lobes fluctuate in the strength as they shift upstream. Hence, if the target area is placed where the signal loses its strength, the efficiency of the actuator may decrease. Thus, along with the orientation, the distance between the actuator and the region where the signal is focused is also important.

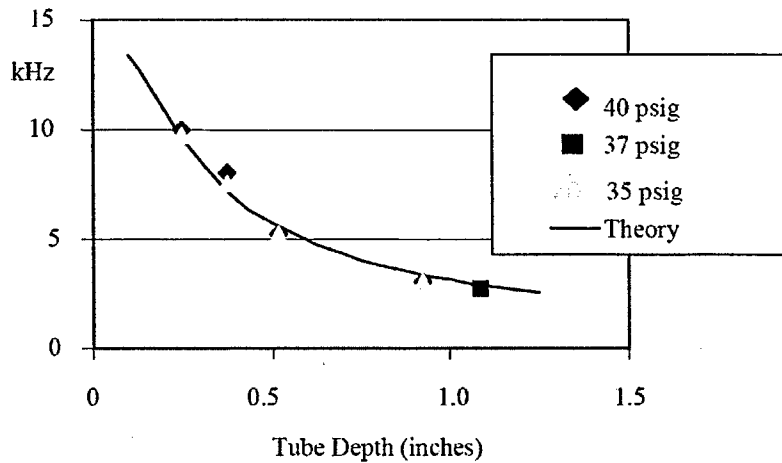


Figure 1.3: An example of simulation results at different supply pressures compared with the new theory developed in this effort.

1.5 Simulation Studies

To explore the flow physics and better understand the mechanisms involved, direct numerical simulations of the PRT flowfield were performed using the Wind flow solver, and its successor, Wind-US. Wind (and Wind-US) is a general purpose Euler and Navier-Stokes Solver (see [Bush et al., 1998], [Power and Underwood, 1999], [Nelson and Power, 2001], [Lankford and Nelson, 2002], and for Wind-US, [Nelson et al., 2004]). The simulations provide details of the unsteady flow inside the actuator, as well as features of the external acoustic radiation. Figures 1.2 and 1.3 demonstrate good comparisons between the simulation, experimental and theoretical results. Detailed results are presented in Chapter 5 and have been published in [Cain et al., 2002a], [Cain et al., 2002b], [Cain et al., 2003a], [Cain and Kerschen, 2003], [Cain et al., 2004] and [Nelson et al., 2006].

An alternative problem formulation using slip-wall boundary conditions inside the PRT walls was executed to gain further insight into the physics of this problem. The alternate formulation results shows that under some conditions the initial oscillations decay to steady flow when the PRT walls have a slip-wall boundary condition (the fluid itself retains the same level of viscosity as the no-slip wall calculations). For other conditions, the slip wall simulation results are essentially identical to viscous wall simulations. Chapter 5 will discuss this point further.

The question of the behavior being affected by turbulence was examined by first conducting calculations that were laminar, and then re-calculating with the Mentor SST two-equation turbulence model included. The results showed no effect of the turbulence model on tone frequency or amplitude for the case examined. On the other hand, changing the Reynolds number was observed to have significant effects. Calculations were first performed at a Reynolds number lowered by a factor of 490 (achieved by setting the freestream pressure to 0.03 psia) relative to the experiments performed at Illinois Institute of Technology. These computations match the primary tonal frequency and are within about 3 dB in amplitude; however, they are very periodic at the fundamental tonal frequency and show a nearly sinusoidal pressure signal. In contrast, simulations performed at a Reynolds number reduced by a factor of 49 (achieved by setting the freestream pressure to 0.3 psia) relative to the experiments show a somewhat more erratic pressure time trace, with more harmonic content,

and a “noisy” signal very similar to what is observed in the experiments.

1.6 Impinging Jet Acoustic Suppression Success

The suppression of jet impingement tones by high-frequency excitation of the jet shear layer using Powered Resonance Tube (PRT) actuators was investigated. Subsonic jet Mach numbers were considered. The work began by characterizing impingement tone staging behavior for a fixed Mach number and various stand-off distances. Since the experiments involved variations in both the PRT and impingement tone settings, they involved manipulation of a number of variables. Some of the variables were acoustic in nature, whereas the others were flow related. Through careful experimental and analytical studies the most significant variables responsible for the suppression were identified. The work also underlines the importance of high-frequency excitation by revealing the fact that, for the same suppression level, selecting the optimal excitation frequency can reduce the required actuator mass flow rate by almost 50%; as compared to non-tonal mass injection. The overall SPL reduction observed in the subsonic impinging jet using the PRTs was as much as 12 dB. The study reveals that impingement tones of certain frequencies were easier to suppress than other tones; the conjecture is that this is related to the relationship between the stand-off distance and the natural acoustic wavelength. Impingement tones for which the stand-off height matched the full acoustic wavelength ($h = \lambda$) were found to be more difficult to suppress than the miss-matched frequencies. The results on this study of acoustic suppression in subsonic jets using PRTs are presented in greater detail in Chapter 3 and in [Sarpotdar et al., 2005b].

1.7 The Helmholtz Theory

The Powered Resonance Tube (PRT) actuator is an effective device for producing high-amplitude pressure oscillations; however, for low frequency applications the PRT actuator can be quite long due to the quarter-wavelength (QWL) requirement. In order to reduce the actuator length, an alternative design in which the QWL tube is replaced by a Helmholtz resonator is proposed. The Helmholtz resonator has a narrow neck coupled to a backing cavity of larger diameter. The resonant frequency is determined by the ratio of fluid stiffness in the backing cavity to fluid mass in the neck; proper choice of geometry leads to an actuator length small compared to the length of a QWL tube. A number of issues that are important in assessing the Helmholtz PRT actuator concept have been addressed. These include the reductions in actuator length (or frequency), the capacity of the resonator to absorb an unsteady volume flux, and the influences of dissipation and nonlinearity.

Two theories for Helmholtz resonator behavior were developed, the low-frequency theory and the axial-wave theory. In both theories, the cross-sectional dimensions of the resonator neck and cavity are assumed small compared to the acoustic wavelength. This allows transverse wave motion to be ignored in the analysis, leading to significant simplifications. For the low-frequency theory, the lengths of the neck and cavity are also assumed to be small compared to the acoustic wavelength, while for the axial-wave theory these lengths may be on the order of the acoustic wavelength. The low-frequency theory leads to simpler results than the axial wave theory, but has the disadvantage that the transition from Helmholtz behavior to quarter-wavelength behavior is not accurately represented, since the axial lengths are also assumed small compared to the acoustic wavelength.

Predictions for the non-dimensional resonance frequency $\Omega = \omega l/c$ as a function of the normalized neck length l_n/l are presented in Figure 1.4. Here, ω is the resonance frequency, l_n is the “effective” length of the neck including end corrections, l_c is the length of the cavity, and $l = l_n + l_c$ is the total “effective” length of the resonator. The predictions shown in Figure 1.4 are based on the axial-wave theory. Results for four values of the diameter ratio, $d_c/d_n = 2, 3, 4$ and 5, are presented. For $l_n/l = 0$ or 1, the geometry reduces to a quarter-wavelength tube and the normalized frequency takes

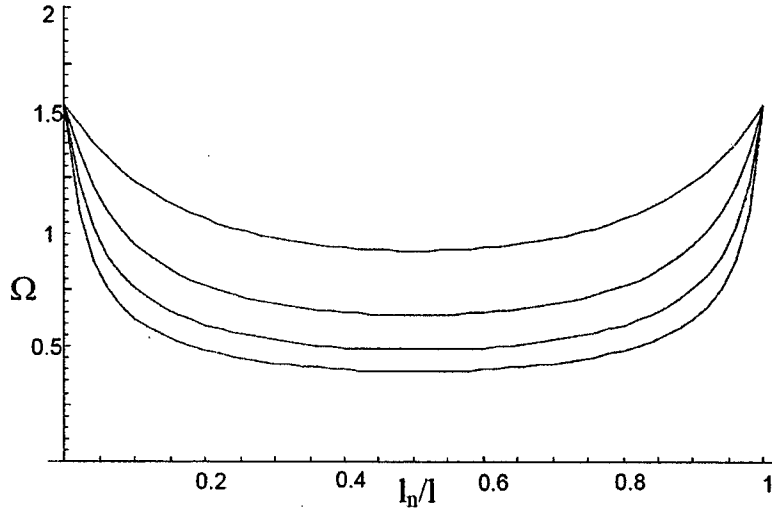


Figure 1.4: Non-dimensional resonance frequency Ω of a Helmholtz resonator, as a function of the non-dimensional neck length l_n/l . The four curves correspond to $d_c/d_n = 2, 3, 4$ and 5 (top curve to bottom curve).

on the quarter-wavelength value $\Omega = \pi/2$. One can see that substantial reductions in the resonance frequency are obtained for Helmholtz geometries in the range $0.2 < l_n/l < 0.8$. Additional features of Helmholtz resonator behavior, including acoustic mode shapes and the capacity of the resonator to absorb an unsteady volume flux in the presence of an external pressure field, are discussed in Chapter 6 and reported in [Kerschen et al., 2004].

1.8 Helmholtz PRT Simulations and Experiments

Numerical simulations and experiments for Helmholtz PRT actuators were also carried out. In Figure 1.3, the resonance frequency obtained in a simulation is compared to analytical predictions of varying degrees of sophistication. The low-frequency theory in the absence of neck end corrections leads to the highest prediction for the resonance frequency. This prediction lies substantially above the simulation point. The geometry considered in the simulations has a very short neck, so that the end corrections substantially increase the effective mass in the neck, lowering the resonance frequency. The low-frequency theory with neck end corrections lies just slightly above the simulation point. Finally, for the parameter values in this case, the more refined axial-wave theory provides a prediction that is slightly lower than the corresponding result from the low-frequency theory. The prediction of the axial wave theory with neck end corrections is in very good agreement with the result obtained from the numerical simulation.

A big picture comparison between the simulations and the theory for two different geometries is presented in Table 1.1. The simulation data corresponds to a geometry with $s/D = 1$ (integration slot width to supply jet diameter) and a Nozzle Pressure Ratio (NPR) of 3.52. The computational grid contained 8 zones and somewhat over 100,000 cells. The simulation Reynolds numbers were “low” for these cases (freestream pressure was 0.03 psia). The supply jet and Helmholtz neck diameter were both $1/4$ ” with a Helmholtz backing cavity diameter of $1/2$ ”. The main points to be made from the data in Table 1.1 are that in case 1, the Helmholtz response for the simulation corresponds very

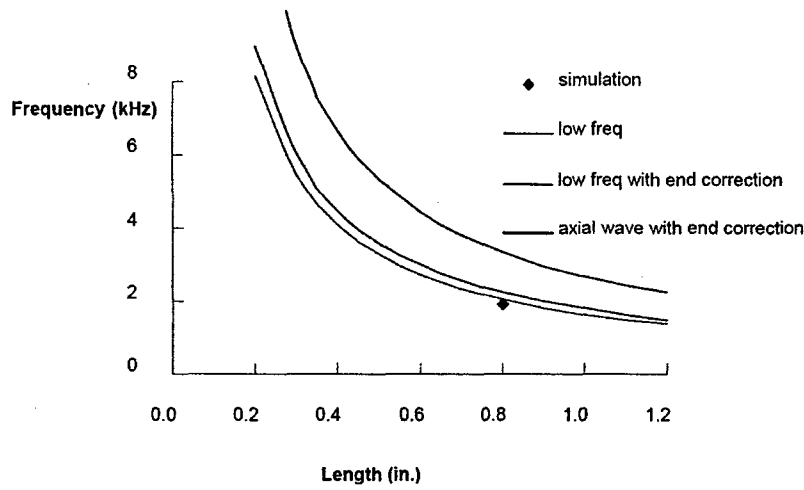


Figure 1.5: Comparison of the low frequency theory, low frequency theory with end corrections, axial wave theory with end corrections and a numerical simulation result for a Helmholtz based, powered resonance tube.

Table 1.1: Comparison of simulation versus theory for two geometries

Case # / Type of Data	Helmholtz Frequency	Screech Frequency
1 / Simulation	2,264 Hz-decaying	Not observed
1 / Theory	2,210 Hz	N/A
2 / Simulation	2,500Hz-decayed	15,454Hz dominant
2 / Theory	1,753 Hz	15,720 Hz

closely with the theory (no screech present), while in case 2 screech is present and the agreement between theory and simulation is not nearly as close.

Additional information on the behavior of a Helmholtz PRT actuator is obtained from the simulation, experimental, and theoretical results presented in Table 1.2. The data corresponds to an $s/D = 2$. The simulation Reynolds numbers were “medium” for these cases (0.12 psia freestream pressure). The supply jet and Helmholtz neck diameter were both 1/8” for these cases with a Helmholtz backing cavity diameter of 1/4”. The most important conclusion from the data in Table 1.2 is that the Helmholtz response predicted by theory is in reasonable agreement with experiment and computation when screech is not present. However, increasing NPR above 3 decreases the likelihood of a Helmholtz response and increases the likelihood of screech. Finally, the presence of screech seems to shift the frequency of the Helmholtz response if it is present.

1.9 Miniaturized High Bandwidth PRT System

In addition to the development of a high-bandwidth PRT actuator, and a Helmholtz PRT actuator for low frequencies, a prototype miniaturized high-bandwidth PRT actuator was also constructed. It consists of three cylindrical actuators of identical outside dimensions. Each had a variable depth by way of a movable piston and a constant area nozzle jet of the same diameter as the resonator

Table 1.2: Comparison of Simulation, Theory, and Experiment

Case # /type	NPR	Helmholtz freq	Screech freq	Peak SPL
3 / Experiment	3	2,500 Hz	Not observed	137 dB
3 / Simulation	3	1,964 Hz	Not observed	142 dB
3 / Theory	N/A	2,290 Hz	Not calculated	Not predicted
4 / Experiment	4.67	~ 4,000 Hz	~18,000 Hz	137 dB
4 / Simulation	4.67	~2,700	~17,500 Hz	Not measured
4 / Theory	N/A	2,290 Hz	Not calculated	Not predicted
5 / Experiment	6	None observed	~14,000 Hz	139 dB
5 / Simulation	6	None observed	~18,000 Hz	Not measured
5 / Theory	N/A	2,290 Hz	Not calculated	Not predicted

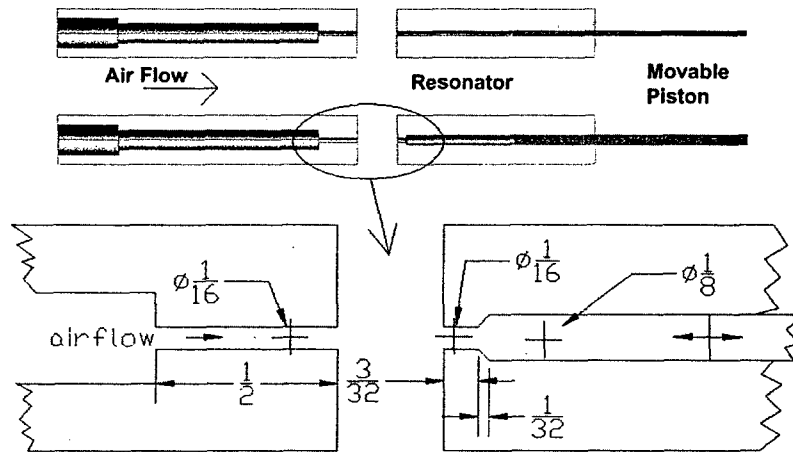


Figure 1.6: The miniaturized quarter wavelength and Helmholtz PRT actuators and a close-up detail of the Helmholtz resonator.

openings. The resonators were a 1/8" straight tube, a 1/16" straight tube, and a 1/16" × 1/8" Helmholtz resonator. The 1/16" straight tube and Helmholtz resonators are detailed Figure 1.6.

A control program was written which used the data from an initial experimentally constructed database to find a starting position of the actuator based on a target frequency and either the supply pressure or minimum required SPL. The program would output the minimum supply pressure if a minimum SPL was given. Then the spacing and depth were set to the position giving the maximum SPL at that pressure and frequency from the data table. The spacing was varied iteratively to maximize the SPL, then the depth was varied iteratively to tune the frequency to within 5Hz, which was the frequency resolution of the FFT program. Both the low frequency and axial wave theories with end corrections (reported in Chapter 6) fell within the range of the measured data. Chapter 7 describes the miniaturized powered resonance tube system in greater detail.

1.10 Graphical User Interface

A Microsoft Visual Basic based design tool has also been developed. The purpose of the tool is to guide in the design of Helmholtz based PRT actuators. The software uses the axial wave approximation described in Chapter 6 and provides both a forward mode (input the geometry and calculate a resonance frequency) and an inverse mode (input the desired frequency and calculate a proposed geometry). Chapter 8 describes the graphical user interface in greater detail.

1.11 Commercialization Efforts

From the beginning of the Phase II Program, many conversations as well as some face-to-face meetings were conducted to explore possible commercialization of the PRT systems. Applications considered included control of combustion instability, suppression of jet impingement noise, and elimination of jet screech. There were positive responses on several occasions, but unfortunately concrete steps forward have yet to occur. Companies with whom potential commercialization was discussed include Honeywell, Pratt, UTRC, and Rolls Royce.

Chapter 2

Development and Study of an Initial Prototype

2.1 Overview

High bandwidth actuation is essential for the effective application of Active Flow Control (AFC) to improve the efficiency of systems that involve both internal and external fluid flow. Successful application to aircraft systems can produce lighter, agile aircraft with increased range, payload and reduced noise. The design of an active flow control system requires knowledge of flow phenomena and selection of appropriate actuators, sensors, and a control algorithm. The present paper focuses on the development of high bandwidth actuators for active flow and noise control applications. It should be noted that the powered resonance tube derives its name from the Hartmann resonance tube. The term “powered” indicates that both “unpowered” (deriving energy from the free stream) and “powered” (requiring secondary air) versions are possible. The term “bandwidth” refers to the range of frequencies of effective operation. The goal was to demonstrate a powered resonance tube that can generate strong tones over a frequency “bandwidth” of approximately one order of magnitude, and is done as a part of the USAF’s program on “high bandwidth actuators.” Thus, it should be noted that the term “bandwidth” is not intended to convey an instantaneous output state but rather the range of conditions over which the device is applicable.

AFC techniques can be separated into two classes based on flow physics [Cain et al., 2001]. The first class (AFC-I) involves the use of unsteady forcing to excite instability waves of laminar flows, or the large scale structures of turbulent flows. AFC-I techniques have been explored extensively in the past decade (see [Kral, 1999] and [Gad-el Hak, 2000]). The second class (AFC-II), has been developed more recently and involves the use of actuators to force turbulent boundary and free-shear layers at frequencies higher than the amplified instabilities of the base flow (see [Wiltse and Glezer, 1993] and [Cain et al., 2001]). The quest for a high bandwidth actuator is preceded by the recognition that the two classes of AFC have different bandwidth requirements, as discussed below.

To apply AFC across the full operating envelope of an air vehicle, actuators with high bandwidth and large dynamic range are required. To illustrate this consider the actuator bandwidth requirements for a military transonic air vehicle. For this illustration it is assumed that the minimum and maximum speeds of interest for tactical military aircraft differ by a factor of eight. It is also assumed that the streamwise locations of interest for actuators vary by a factor of eight. Further reasoning is based on an estimate of the boundary layer thickness, which for laminar boundary layers scales with the square root of the downstream distance, x and the inverse square root of the flow speed u . The thickness of the turbulent boundary layer scales roughly with the $6/7$ power of the downstream distance, x

and the $1/7$ power of the flow speed, u . AFC-I techniques have more stringent requirements and the actuator must produce an unsteady flow disturbance at a frequency that is near the frequency of the naturally occurring instability waves or large-scale structures. The required frequency scales as $f \propto u^{3/2}$. Thus, for a laminar boundary layer one obtains $f \propto u^{3/2}x$, while for a turbulent boundary layer one obtains $f \propto u^{8/7}x^{-6/7}$. Now consider an actuator on a fixed location on a vehicle. In order for the actuator to be effective for AFC-I over a speed range of 8, a bandwidth range of $8^{3/2} \approx 23$ would be required for a laminar boundary layer, while a bandwidth range of $8^{8/7} \approx 11$ would be required for a turbulent boundary layer. In reality the laminar scaling overestimates the requirement in many situations, since one would anticipate a significant shift in transition location over a speed range of 8. Thus, for AFC-I techniques, a reasonable estimate for the desired bandwidth range for an actuator at a fixed location is, say 16. One can also consider the possibility of AFC-I applications using the same actuator at all locations on a vehicle. In this case, the desired bandwidth range increases to 64, for both laminar and turbulent cases.

AFC-II techniques involve excitation of disturbances at frequencies somewhat higher than that of the amplified modes of the turbulent boundary layer or free-shear layer. Here the bandwidth requirements are more modest. The instability modes or large-scale structures that respond to excitation from AFC-I have a limited frequency band (at a given point in the boundary or free shear layer). It is only necessary to force the turbulent flow at some frequency somewhat above this range. Therefore for AFC-II techniques, the possibility of effecting flow control using the same actuator at a variety of locations on a vehicle appears realistic.

2.2 Background on Actuators

Several innovative flow control techniques have emerged in recent years. Among these are piezoelectric actuators, zero mass flux actuators [Wiltse and Glezer, 1993, Wiltse and Glezer, 1998] and fluidic actuators. However, the above types of actuators are suited more for laboratory experiments. In full scale flight applications they can prove to be fragile and have significant power and maintenance requirements, and may not be able to provide the necessary bandwidth.

The actuator developed for the current work is based on the Hartmann resonance tube (also referred to as the Hartmann whistle). The resonance tube phenomenon was first described by Hartmann in 1918 (see [Hartmann and Troll, 1922] and [Hartmann, 1931]). The Hartmann whistle apparatus consists of a jet aimed at the open end of a tube which is closed at the other end. There are two phases during the operation of this device. In the first phase, the jet penetrates the tube and compresses the air within the tube. In the second phase the compressed air in the tube empties itself. Under favorable conditions the cycle perpetuates itself. However, fixed geometry actuators can only produce effective actuation over a small range of frequencies. This poses a problem because a new actuator is required every time there is a change in geometric or fluid dynamic parameters. Extending earlier fixed frequency efforts ([Raman et al., 2000], [Raman et al., 2001], [Raman and Kibens, 2001]), the goal was to use the oscillatory pressures and velocities produced by this device to design a high bandwidth actuator. Examples of possible applications include the high frequency excitation for suppression of flow induced resonance in weapons bay cavities ([Cain, 1997], [Raman et al., 2001], [Raman et al., 2000], [Stanek et al., 2000], and [Stanek, 2005]) and jet-ground impingement tones in STOVL aircraft.

The phenomena associated with such resonance tubes has been studied by several researchers including [Thompson et al., 1992] and [Brocher et al., 1970]. The resonance frequency was proposed by [Brocher et al., 1970] to be equal to approximately the acoustic frequency $f = c/(4l + ecf)$, where f is the resonance frequency, c is the ambient speed of sound, l is the length of the tube, and ecf is the end correction factor. Note that the frequency of excitation produced by this device depends primarily on its depth. Secondary factors that can alter frequency include the nozzle

pressure ratio of the supply nozzle and the spacing between the jet exit and the open end of the resonance tube. A variation of the Hartmann tube known as the Hartmann-Sprenger tube was studied by [Iwamoto, 1990] and [Iwamoto and Deckker, 1985]. [Wilson, 1958] and [Wilson and Resler, 1959] studied a glass resonance tube using pulsed Schlieren photography. Wilson's work documents the movement of waves within the tube during the compression and evacuation phases within the tube and also documents the temperature variations at the closed end of the tube.

2.3 Benefits of High Frequency Excitation

An additional motivation to develop a high bandwidth PRT is due to the benefits of using high frequency excitation (AFC-II) for control applications. High frequency excitation (AFC-II) departs from the conventional philosophy (AFC-I) of exciting the shear layer only within the range of frequencies where the large scale structures (see [Kibens, 1980]) are amplified. The rationale in the conventional excitation approach (AFC-I) was to energize the large structures that in turn enhance mixing. In contrast, when frequencies higher than the amplified large scale range are excited, changes in the development of the large scales and the mean flow can occur (see [Wiltse and Glezer, 1993]). An important consequence of the high frequency excitation is that the direct addition of shorter scales apparently accelerates the dynamics of energy cascade across a broad range of wave numbers. In situations involving resonant acoustics, low frequency excitation reduces the amplitude of resonant tones by detuning the feedback loop. On the other hand, high frequency excitation may destroy the organization in the initial shear layer that is necessary to sustain flow induced resonance. Typically, the use of low frequency excitation (in the range of naturally amplified flow instabilities) results in the suppression of some modes and is generally accompanied by the augmentation of some other modes. In contrast, high frequency excitation (AFC-II) has the capability of eliminating all tones present, as well as reducing the broadband sound, in a cavity in subsonic or supersonic flight. The ability to suppress all tones is especially important in situations where the resonant frequencies are difficult to anticipate. For example, in the work of [Raman et al., 1999] on jet-cavity interactions two types of tones were observed. The first type was described by $H = 0.3nM_j^{1/2}$ for $n = 1, 2, 3$, where H is the Helmholtz number given by fl/c , where f is the frequency, l the cavity length, and c the speed of the sound. The second type of tone can be approximated by the relationship $H = (n + 1)/4$ for $n = 1, 2, 3$. The former type resembles the Rossiter modes whereas the latter type is independent of cavity length (note that the classical Rossiter modes may occur only in idealized laboratory experiments). The point here is that with conventional low frequency excitation one needs to know the frequencies of the tones that are expected under various conditions. High frequency excitation has the potential to suppress all flow induced resonances and does not require detailed knowledge of the frequencies of tones present under various conditions.

2.4 Objective for Prototype Broadband Actuator Development

For the current work, the approach for developing a prototype high bandwidth actuator consisted of first selecting a candidate actuator and then devising a method to extend its bandwidth. This search for an actuator revealed that excitation devices that produced high amplitude signals generally leveraged a resonance mechanism. Examples are piezoelectric elements mounted on structural members, and devices that exhibit aeroacoustic resonance. The former type of actuator (piezoelectric) was considered briefly but was dropped in favor of the latter type (aeroacoustic). The actuator selected for bandwidth enhancement was the Powered Resonance Tube (PRT) actuator, which is capable of producing high frequency and high amplitude oscillations.

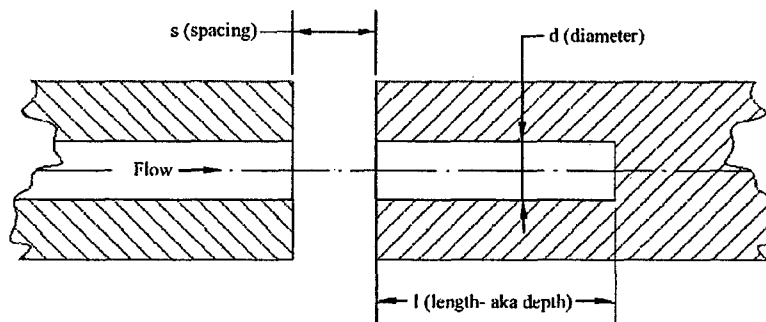


Figure 2.1: Schematic diagram showing an axisymmetric Powered Resonance Tube (PRT). The supply jet is on the left hand side and the resonance tube is on the right. The gap between the two is referred to as the "integration slot."

The frequency produced can be approximately represented by the quarter wavelength frequency of a tube that is closed at one end. First, it was demonstrated that high bandwidth could be produced by manually varying the depth of the PRT. This was followed by a more refined effort using a computer controlled mechanism that varied the depth of the tube in response to user selected frequencies. These efforts were successful in obtaining an order of magnitude variation in frequency with a significant dynamic range. Specific objectives are listed below:

- Characterize the unsteady actuation signals produced by the PRT device in the nearfield.
- Develop and demonstrate high bandwidth capability.
- Begin with a Look Up Table (LUT) approach and proceed to demonstrate Single Input Single Output (SISO) and Multi Input Multi Output (MIMO) feedback control of the actuator.

2.5 Powered Resonance Tube Development

Figure 2.1 shows a schematic of a single powered resonance tube. The supply jet is seen on the left hand side and the resonance tube on the right hand side. Previous work has focused on two versions of the resonance tube. The original version used an under-expanded sonic jet containing a shock train. In the second version [Brocher et al., 1970] demonstrated that a "wake producing" cylinder laid along the jet axis allows the full oscillation amplitude to be achieved for ideally expanded supersonic jets. [Hartmann, 1931], [Wilson, 1958] and [Brocher et al., 1970] have pointed out that the former version is very sensitive to spacing between the jet and mouth of the resonance tube. This is because the expanding region of the jet is a stable region for a shock present in the flow, whereas the converging region is unstable, so that the shock will not remain there.

For a resonance tube to operate, the spacing between the nozzle exit and the tube mouth should be such that it positions the shock in the unstable region. When the shock is in the unstable region it is strongly affected by downstream conditions and will readily oscillate. The desired spacing between the nozzle exit and the resonance tube depends on the shock cell dimensions that are determined by the supply pressure. This explains the sensitivity to both spacing and supply pressure. In contrast, in the latter version, the jet is ideally expanded and has no shock cells. However, the sting does generate oscillations with a lower sensitivity to the pressure and spacing. This work demonstrates

that using a properly designed control system even the former version of the resonance tube can produce oscillations consistently. A similar control system is expected to function quite easily for the latter version of the device. Note that although the latter version is less sensitive to supply pressure and spacing it still needs fine tuning to produce the maximum amplitude. The frequency of the resonance depends only on the depth of the tube for subsonic or ideally expanded supersonic jets. The distance between the supply jet and the resonance tube determines the efficiency of this process. The mass flow requirements depend on the diameter of the supply jet and typically range from 0.01 kg/sec to 0.15 kg/sec for tubes with diameters ranging from 1/16" to 1/4".

Although the Hartmann tube has been known for many years it has never been used before as an active flow control actuator. [Raman et al., 2000] demonstrated its potential for use as an AFC actuator. However, the demonstrator was not suitable for use as an actuator since the flow spilled out circumferentially in all directions. For effective actuation a device that can inject perturbations into a flow efficiently is desired. At the beginning of integration efforts a semi-circular shroud was used. The shroud or shield (when applied properly) did not alter the effectiveness of the resonance tube phenomenon. Two generations (Gen-I and Gen-II) of a more complex version of this device were developed. The Gen I type actuator, which was designed to integrate with the weapons bay cavity at DERA (UK), was described by [Raman et al., 2001] and [Raman and Kibens, 2001] and will only be briefly mentioned herein. The actuator consisted of a flow conditioned plenum fed by a high pressure air line. The flow exited the plenum through seven supersonic (CD) nozzles with an exit diameter of 0.635 cm and a design Mach number of 2. The seven jet nozzles were aimed at a block containing seven resonance tubes with a diameter of 0.635 cm and a depth of 1.27 cm. An axial needle was present at the center of each of the jet nozzles. The needle enhances the operation of these nozzles at supersonic Mach numbers as originally proposed by [Brocher et al., 1970] to prevent cessation of oscillations for certain conditions. Also present in the actuator is a scalloped plate spacer between the supply jet and the resonance tube. [Stanek et al., 2000] describe the results from the cavity noise suppression experiments in the UK. The device suppressed cavity tones by 29 dB at $M = 1.19$.

A second generation device (Gen-II) was built to integrate with the jet impingement apparatus at Boeing Saint Louis. The Gen-II actuator could switch between 7 and 15 powered resonance tubes and had a bleed facility at the rear that allowed the mass flow to be varied. This actuator was successful in suppressing impingement tones (see [Raman and Kibens, 2001]).

2.6 Initiation of Experiments

2.6.1 Setup

The experimental set-up was shown in Figure 1.1. It consists of a 0.635 cm diameter jet with a chamfered exit facing the open end of the resonance tube that is closed at the other end. Note that the chamfer was necessary for the production of high amplitude oscillations. A piston fitted inside the tube changes the tube depth. The piston has an O-ring built in to prevent leakage of air. This setup was used as a prototype to test the parameters of the powered resonance tube. The piston remained fixed while the resonance tube slid over it to change tube depth. The distance between the jet and the tube (gap), referred to as the "spacing parameter" or "spacing" was changed by computer control to examine its effect on both the frequency and the amplitude of the sound. Microphones and pressure sensors at various locations in the vicinity of the actuator were used to measure the frequency and amplitude of the fluctuations produced by this device. The power spectrum of the acoustic signal was computed for various resonance tube depths and jet-to-resonance-tube spacings. A computer controlled traversing mechanism moved both the piston (for changing depth) and the supply jet for changing the spacing (tuning). Next, a detailed experimental database was generated that was used as a lookup table in early computer controlled experiments.

Table 2.1: Frequency error analysis measurements for the PRT

d/D	Frequency (kHz)													
	Asc. ^a	Des. ^b	Asc.	Des.	Asc.	Des.	Asc.	Des.	Asc.	Des.	Asc.	Des.	Asc.	Des.
	run 1	run 1	run 2	run 2	run 3	run 3	run 4	run 4	run 5	run 5	Mean	Mean	σ	σ
0.8	9.844	9.756	9.820	9.756	9.828	9.784	9.860	9.780	9.860	9.780	9.842	9.771	0.02	0.01
1.2	7.764	7.692	7.760	7.704	7.768	7.700	7.772	7.704	7.780	7.708	7.769	7.702	0.01	0.01
1.6	6.472	6.440	6.472	6.444	6.476	6.452	6.492	6.452	6.492	6.452	6.481	6.448	0.01	0.01
2.0	5.188	5.176	5.180	5.176	5.180	5.216	5.220	5.208	5.212	5.200	5.196	5.195	0.02	0.02
2.4	4.260	4.236	4.256	4.240	4.260	4.240	4.260	4.240	4.264	4.240	4.260	4.239	0.00	0.00
2.8	3.680	3.672	3.684	3.676	3.684	3.672	3.692	3.672	3.696	3.680	3.687	3.674	0.01	0.00
3.2	3.308	3.304	3.308	3.304	3.312	3.300	3.308	3.304	3.324	3.304	3.312	3.303	0.01	0.00
3.6	3.008	2.992	3.008	2.996	3.008	2.996	3.008	2.996	3.012	3.000	3.009	2.996	0.00	0.00
4.0	2.756	2.744	2.756	2.744	2.760	2.752	2.756	2.756	2.760	2.756	2.758	2.750	0.00	0.01
4.4	2.540	2.540	2.540	2.540	2.540	2.540	2.540	2.540	2.540	2.540	2.540	2.540	0.00	0.00

^aAsc.: ascending order^bDes.: descending order

2.6.2 Error analysis

There are two types of errors: external and internal. The former is based on knowledge of the accuracy of the instrumentation, while the latter is based on the data and repeatability of the experiment. For the microphone measurement, the only available information is the precision of the microphone. The precision of the microphone provided by the manufacturer is 0.5 dB which results in a microphone measurement error of ± 1 dB based on a zero order estimate, for the frequency range from 0-10 kHz. For the Kulite pressure transducer, the calibration sheet provided states that the error is less than $\pm 3\%$. To state the external errors a statistical analysis of the data was needed. Hence numerous measurements were conducted on the powered resonance tube to establish the uncertainty, validate the data, and study the repeatability of the experiment. A major objective was to show that the phenomenon is stationary with the variation of the resonance amplitude and frequency within an acceptable range. This evaluation was represented by a statistically estimated standard deviation σ then using a 95% confidence interval of 2σ . These measurements are tabulated in Tables 2.1 and 2.3. From Table 2.1 it can be seen that the frequency error is less than 40 Hz for each case of ascending and descending order with a 70 Hz hysteresis error. While from Table 2.3 it can be seen that the sound pressure level error is 2.24 dB with a hysteresis error of 3.8 dB.

2.7 Experimental Results

2.7.1 Frequency and Amplitude Characteristics

Figure 2.2(a) shows the variation of actuator resonance frequency versus depth. In this report NPR is defined as the ratio of the stagnation pressure to ambient pressure. The data of Figure 2.2(a) were acquired at an NPR of 3.72 for various values of the spacing parameter (integration slot width or jet to resonance tube spacing). Two theoretical predictions of the resonance frequency are also shown in Figure 2.2(a). The basic theory is the standard quarter wavelength resonance frequency (QWL), for an open-closed resonance tube. The experimental data is in good agreement with the basic theory for long tube depths, but gradually diverges from the basic theory as the depth of the resonance tube decreases. In order to develop a better understanding of this behavior, a refined

Table 2.3: Amplitude error analysis measurements for PRT
SPL (dB)

d/D	Asc. ^a run 1	Des. ^b run 1	Asc. run 2	Des. run 2	Asc. run 3	Des. run 3	Asc. run 4	Des. run 4	Asc. run 5	Des. run 5	Asc. Mean	Des. Mean	Asc. σ	Des. σ
0.8	148	147	148	147	148	146	148	147	148	148	148.0	146.6	0.00	0.55
1.2	147	151	148	151	148	151	148	151	148	151	147.8	151.0	0.45	0.00
1.6	155	153	155	153	155	152	156	154	155	153	155.2	153.0	0.45	0.71
2.0	148	144	149	145	148	145	149	144	149	146	148.6	144.8	0.55	0.84
2.4	153	149	153	150	154	150	153	150	153	150	153.2	149.8	0.45	0.45
2.8	152	148	150	149	149	149	151	150	151	149	150.6	149.0	1.14	0.71
3.2	141	139	140	138	142	140	143	139	141	139	141.4	139.0	1.14	0.71
3.6	144	146	145	147	146	147	145	148	144	147	144.8	147.0	0.84	0.55
4.0	147	143	148	145	145	144	146	145	147	143	146.6	144.2	1.14	1.00
4.4	143	144	143	143	144	143	143	144	143	144	143.2	143.6	0.45	0.55

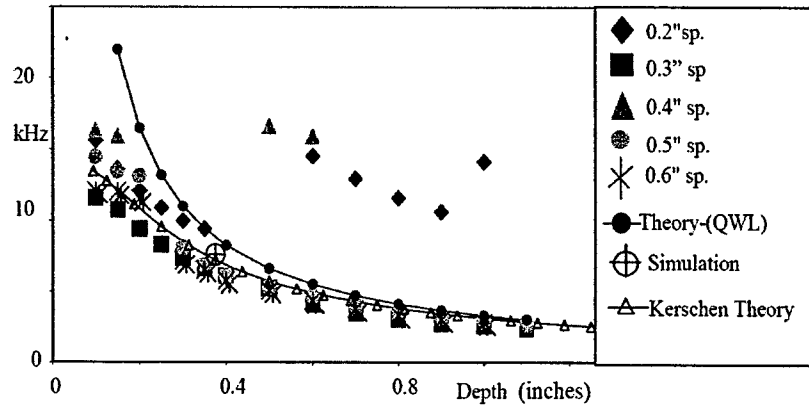
^aAsc.: ascending order

^bDes.: descending order

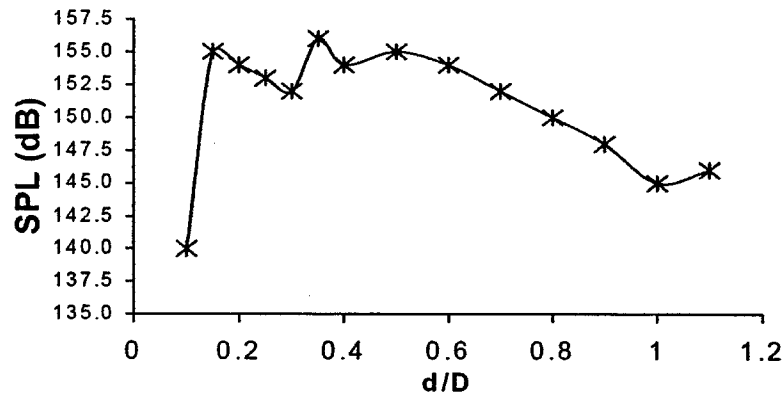
theory was developed [Kerschen, 2001] that considers the acoustic coupling of the resonance tube and the integration slot. The Kerschen theory accounts for the interaction of the resonance tube with the integration slot, and the compliance and mass of the fluid in the integration slot are incorporated into the prediction. The prediction of this refined theory for an integration slot width of s/D is shown in Figure 2.2(a). The refined theory is in much better agreement with the experimental data, remaining quite accurate even at small values of the tube depth. Essentially, for small tube depths, the inertia of the fluid in the integration slot becomes important, significantly reducing the resonance frequency relative to the prediction of the basic theory.

Many numerical simulations of the PRT actuator have been carried out. One reference case was shown in Figure 2.2(a) for a tube depth of $l/D = 1.5$, an integration slot width of $s/D = 1$, and a supply NPR of 3.5. Details of the simulation are discussed in a later section. A single result from the numerical simulations is used for comparison with the experimental results in Figure 2.2(a). The resonance frequency obtained in the simulation ($f = 7.6$ kHz) is also shown in Figure 2.2(a). The result is seen to be in good agreement with the experimental data and refined theory. The simulation also predicts the amplitude of the resonance. Accounting for the pressure scaling (to be discussed), the simulation result corresponds to an amplitude of 160 dB, in fairly good agreement with the laboratory value of 157 dB. Other simulation results are shown later in the report and also correspond well with the experiments.

Note that in these experiments the frequency could be changed from 14 kHz to about 1.6 kHz and amplitude varied from 137 dB to 160 dB. A documentation of the amplitude of sound at a nearfield microphone location (0.635 cm away from the PRT) with varying resonance tube depth (various frequencies) is provided in Figure 2.2(b). A detailed experimental data base was created by measuring the frequency and sound pressure level at various tube depths and spacing parameters for a range of NPR values (see Figures 2.3 and 2.4). The resonance tube database consisted of measured frequencies at various depths. The frequency was measured for depths ranging from l/D of 0.4 to 1.6 in steps of 0.2 l/D . From l/D of 1.6 to 4.4 a depth increment of 0.4 l/D was used. The spacing between the supply jet and the resonance tube was varied from s/D of 0.4 to 2.8 in steps of 0.254 cm. The database covered a supply pressure range from NPR = 2.89 to 3.93 in 6 equal increments. Thus, there were 686 data points describing the behavior of the resonance tube at various depths, spacings and pressures. From Figure 2.3 it is clear that on each plane there are limited regions of high amplitude. Thus an effective computer controlled actuator would have to search for the correct integration slot spacing at each depth.



(a) Actuation frequency versus depth for various values of the spacing parameter (jet-to-resonance-tube spacing).



(b) Actuation amplitude versus depth for various values of the spacing parameter (jet-to-resonance-tube spacing).

Figure 2.2: Frequency and amplitude characteristics of Powered Resonance Tubes (PRTs) at an NPR of 3.72 (NPR_{Standard} = 1.15 NPR).

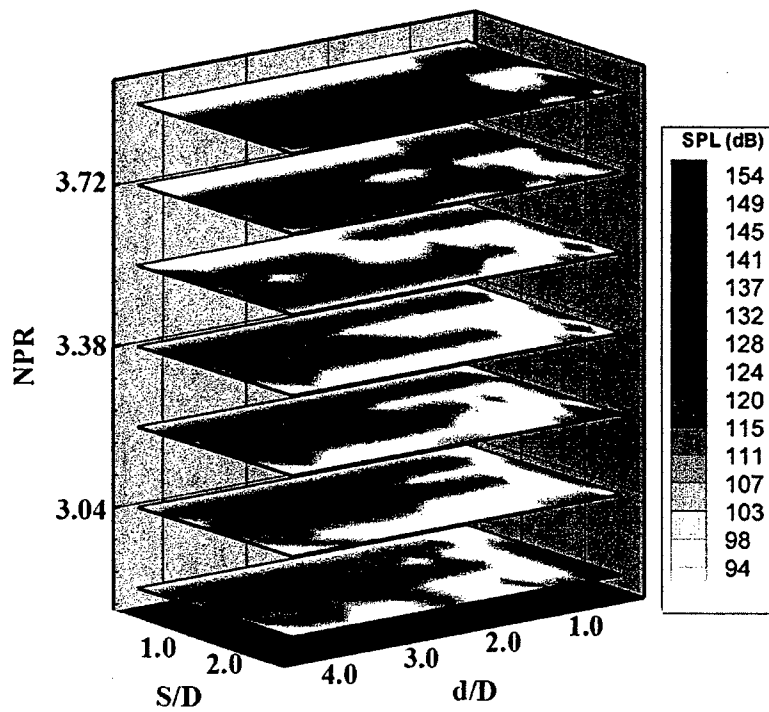


Figure 2.3: Three dimensional map of actuation sound pressure levels for various values of the spacing parameter (jet-to-resonance tube), supply pressure and tube depth. (NPR_Standard = 1.15 NPR).

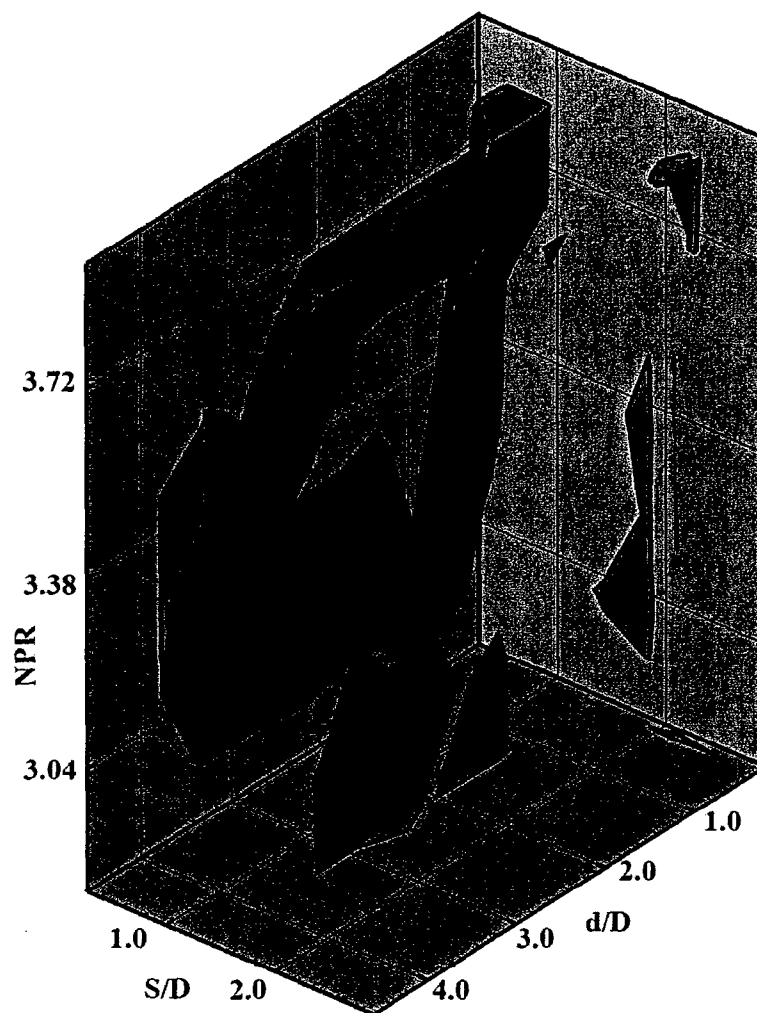


Figure 2.4: Iso-surface extracted from three dimensional map of Figure 2.3. The 140 dB iso-surface represents the acceptable target amplitude for effective actuation. (NPR_{Standard} = 1.15 NPR).

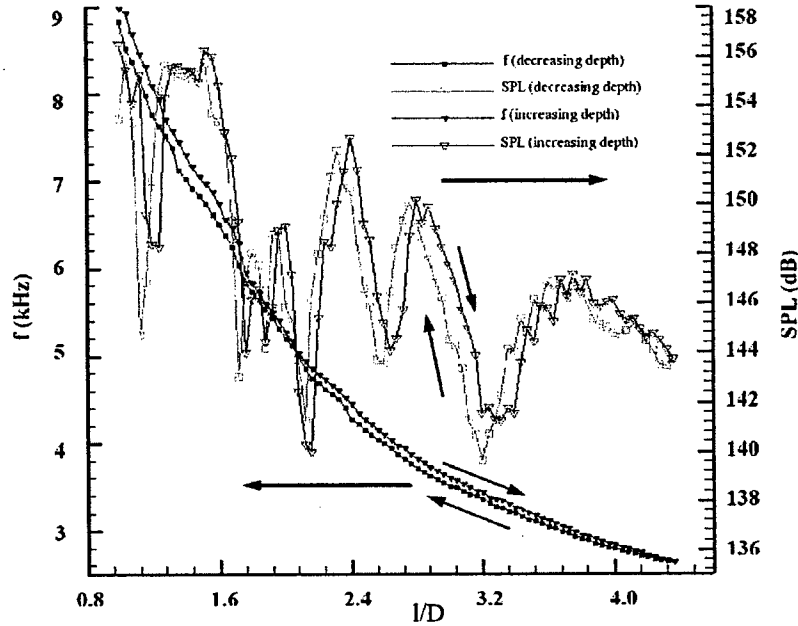


Figure 2.5: Hysteresis errors in frequency and sound pressure level with increasing and decreasing depth

The amplitude of actuation is characterized using metrics from linear acoustic theory such as acoustic power, W . This is derived from the Sound Pressure Level (SPL) as follows: $SPL = 20 \log_{10}(p_{rms}/p_{ref})$ where $p_{ref} = 20 \mu\text{Pa}$. The acoustic power $W = (p_{rms}^2/c\rho_0) 4\pi R^2$, where R is the distance from the microphone to the resonance tube, ρ_0 is the density of air (1.21 kg/m^3), and c is the ambient speed of sound (343 m/s). The metric described above is subject to several assumptions (including spherical radiation of sound into open space). The usefulness of the sound power metric is that it eliminates the microphone location as a parameter (sound pressure level depends on the microphone location but the sound power is a characteristic of the source that is independent of microphone location). The acoustic efficiency of this device was calculated by taking the ratio of output power to input power. Input power is given by the product of supply pressure and volume flow rate. Output power was measured using a Kulite probe that was moved to the opening of the integration slot. At this location the Kulite sensor recorded a level of 169 dB. The acoustic efficiency was found to be 9% if one considers the RMS level integrated over the entire spectrum and 6.85% if one only considers energy concentrated at the resonance frequency.

This database is then used to generate a look up table program for controlling the resonance tube such that the desired frequency is obtained at the highest amplitude. A Visual BASIC program was written in order to implement the look-up table database. The traversing mechanism was calibrated before generating the look up table program. When a desired frequency is input to the program it calculated the depth and moved the piston to the appropriate depth. Figures 2.5 and 2.6 depict the frequency variations when the tube depth is changed including the effect of hysteresis. The fundamental frequency (lowest curve) is tabulated and analyzed for errors in Tables 2.1 and 2.3.

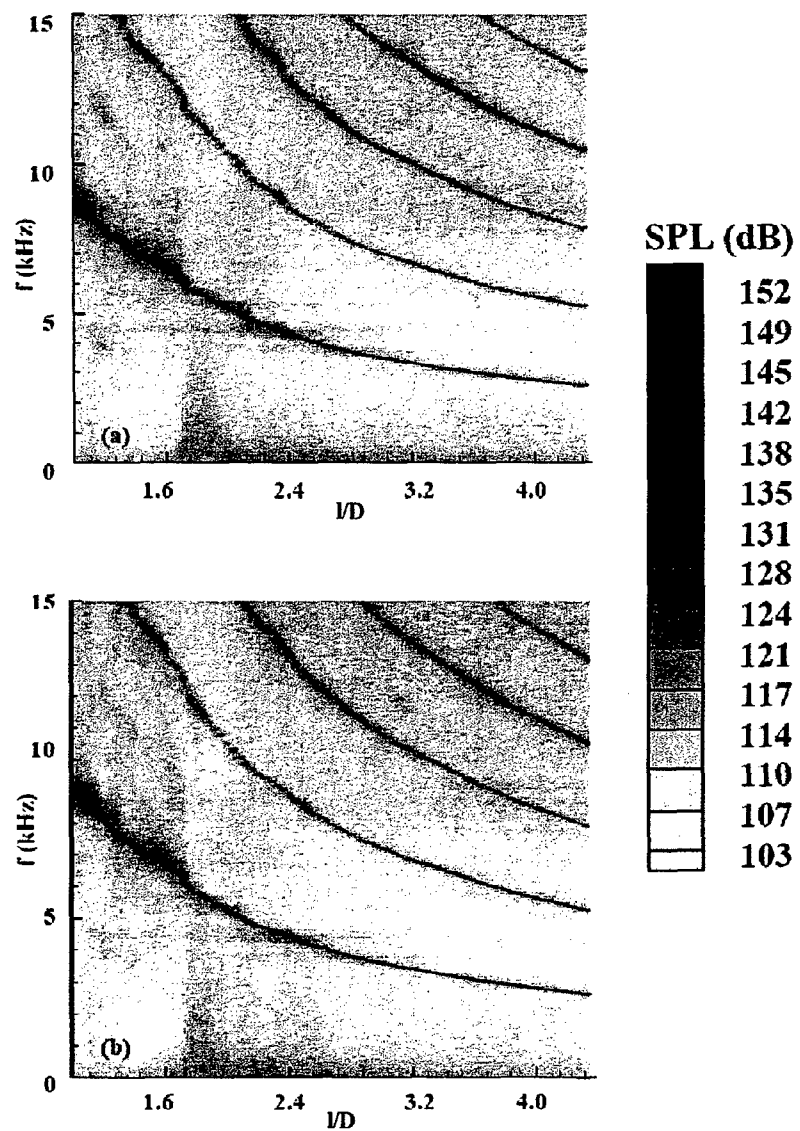


Figure 2.6: Spectra at various resonance tube depths. (a) Decreasing depth. (b) Increasing depth.

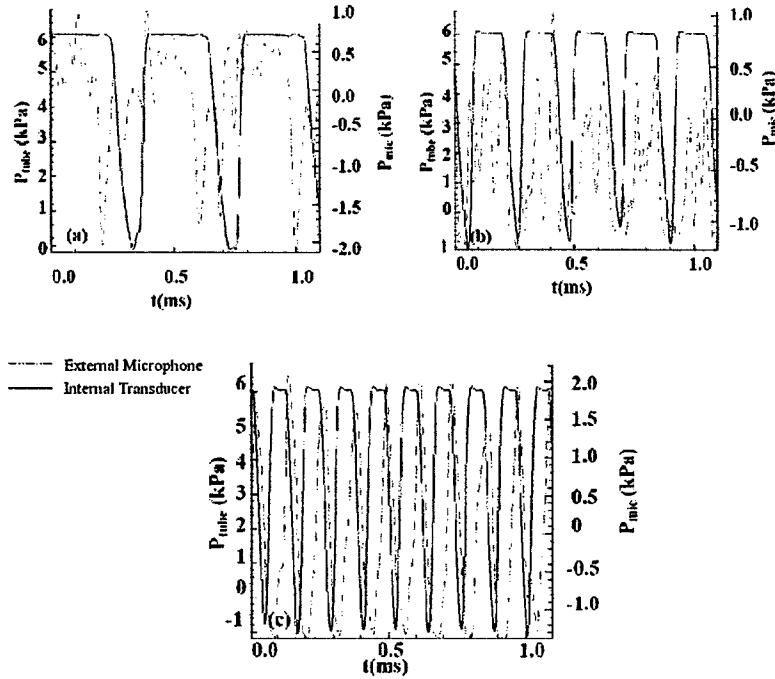


Figure 2.7: Pressure time series from externally located microphone and from pressure transducer at the closed end of the tube at various frequencies. (a) 2.5 kHz. (b) 5 kHz. (c) 9 kHz.

2.7.2 Pressure Measurements within the PRT

Flow visualization experiments conducted by [Kastner and Samimy, 2002] have revealed some very interesting visual features of PRT actuators. However, a detailed characterization of unsteady pressures in the nearfield is desired and this is one of the objectives of the present work. Figure 2.7 shows pressure time traces from sensors located internal and external to the tube. Measurements within and outside the tube were made at PRT operating frequencies of 2.5, 5 and 9 kHz. It should be mentioned that the time segment for the three parts is the same; 0.0011s, which explains the increase in number of cycles as the frequency increases. From Figure 2.7 it can be seen that for all the frequencies, the shape of the pressure inside the tube was the same. For the 2.5 kHz case shown in Figure 2.7(a) the pressure increases from -1,000 Pa to 61,000 Pa in $56 \mu\text{s}$ (14% of cycle time), stays at 61,000 Pa for $216 \mu\text{s}$ (55% of cycle time) and decays back to -1,000 Pa in $122 \mu\text{s}$ (31% of cycle time). The total time is $394 \mu\text{s}$ after which the whole cycle repeats itself again. In the case of the 5 kHz tone shown in Figure 2.7(b) the pressure rises from -13,000 Pa to 61,000 Pa in $40 \mu\text{s}$ (19% of cycle time), stays at 61,000 Pa for $102 \mu\text{s}$ (49% of cycle time) and then goes down to -13,000 Pa in $122 \mu\text{s}$ (32% of cycle time) with a total cycle time of $264 \mu\text{s}$. Finally, for the 9 kHz case shown in Figure 2.7(c) the pressure rises from -12,000 Pa to 61,000 Pa in $34 \mu\text{s}$ (28% of cycle time), stays at 61,000 Pa for $42 \mu\text{s}$ (35% of cycle time) and then drops to -12,000 Pa in $45 \mu\text{s}$ (37% of cycle time) with a total cycle time of $121 \mu\text{s}$. From the shape of the time series in all cases, it can be seen that the pressure time series inside the tube has a very regular shape. In contrast, the microphone signal is not very regular, possibly because of the reflections of sound in the near field by the traverse mechanism and supporting table.

Table 2.4: The Calculated Velocities of the Compression and Expansion Waves.

Case	t rise (μs)	Velocity (ft/s)	Mach no.	t slew (μs)	Velocity (ft/s)	Mach no.
2.5 kHz	56	1785.71	1.64835	122	819.672	0.75662
5 kHz	40	1041.67	0.96154	68	612.745	0.56561
9 kHz	34	612.745	0.56561	45	462.963	0.42735

The nonlinear effects within the resonance tube are clearly illustrated by the results of Figure 2.7. By examining the pressures within the tube it is found that in general, the dwell time is around 50% of the total cycle time and the rise time is less than the slew time. The rise time represents the time needed for the compression wave to travel in the tube and the slew time is the time needed for the expansion wave to travel out of the tube. By knowing these two facts, it is clear that the compression wave travels faster than the expansion wave.

The Quarter Wavelength Theory assumes that all the waves (compression, reflected compression, expansion and reflected expansion) are Mach waves and travel with the local speed of sound and the flow velocity in the tube is negligible. To examine this further, the velocity of the compression and expansion waves for each case were calculated and are given in Table 2.4. It can be seen that the velocity of the compression wave is higher than that of the expansion wave and as the frequency increases (depth decreases) the velocity decreases for both compression and expansion waves. In addition, the compression wave velocity is higher than the speed of sound. At 9 kHz the calculated velocities for both compression and expansion waves are less than the speed of sound. The time trace measured within the tube displays a longer dwell time at high pressures alternating with shorter dwell times at low pressures. In contrast, for the time trace measured outside the tube the dwell times are indistinguishable.

2.7.3 Detailed Characterization of the Nearfield

The nearfield data shown in Figures 2.8 and 2.9 represent the $y - z$ and $x - y$ planes I and II (see Figure 1.1). The data for planes I and II were obtained by traversing a Kulite sensor over the entire nearfield. Part (a) of Figures 2.8 and 2.9 shows the total RMS pressure signal integrated over the entire spectrum. Part (b) represents the pressure levels at the actuation frequency and (c) represents the phase relative to a second fixed sensor. Note that the propagation of the wave is normal to the phase front.

The data shown in Figures 2.8 and 2.9 reveal some very interesting features. In the transverse plane ($x - y$, Figure 2.8) the actuation signal exhibits two distinct lobes caused perhaps by a transverse flapping mode instability (this flapping instability appears to prefer the transverse direction over the vertical direction where the jet is constrained at the bottom). The phase data exhibit isotropy. Figure 2.9 represents data in the axial plane ($y - z$) and shows that the actuation is biased in the upstream direction (relative to the direction of the supply jet). This finding is significant and may determine the deployment configuration of the actuator. For example, with the free stream going from left to right, one may want to have the actuation opposing the free stream in a counterflow like fashion for jet mixing enhancement applications or alternatively choose a co-flowing arrangement as in directed synthetic jets. The directivity of the PRT on the $y - z$ plane is shown in Figure 2.10. Detailed phase averaged data are shown in Figures 2.11 and 2.12 for the $x - y$ and $y - z$ planes (I, II).

The measurements were made by moving a sensor over the entire nearfield (see measurement grid in each figure) and using a second reference sensor as a trigger for phase-averaging. Phase averaged

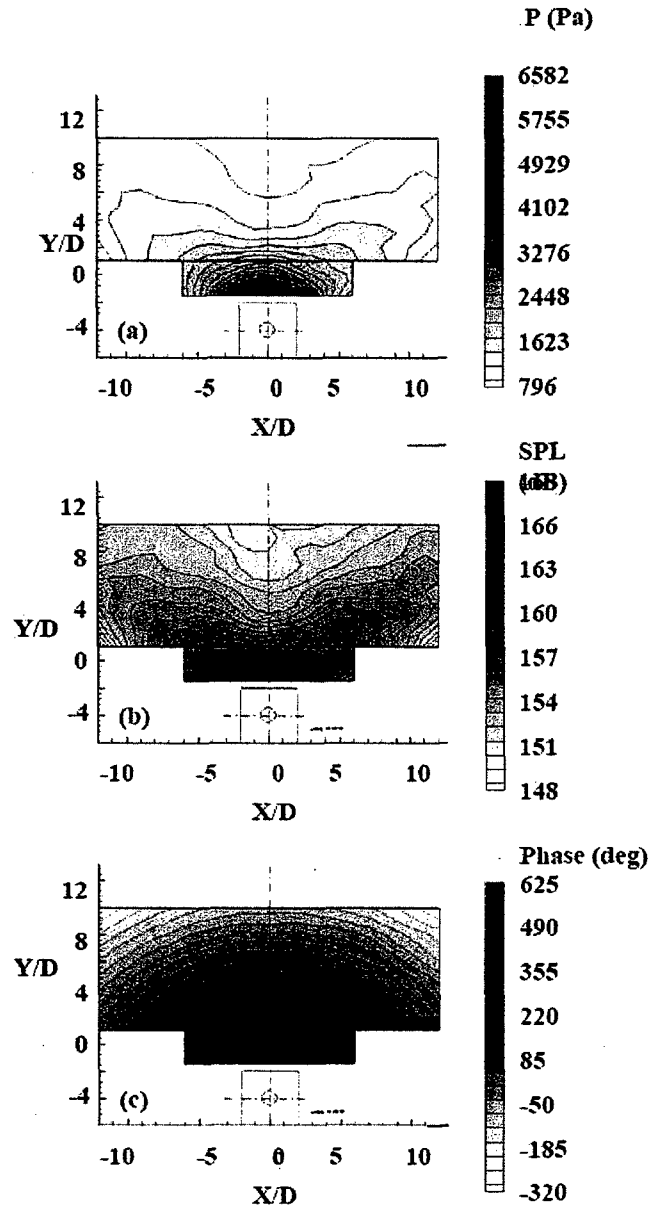


Figure 2.8: Time-averaged features in the near field on the $x-y$ plane (I & II). (a) RMS pressure levels. (b) Sound pressure levels at actuation frequency. (c) Relative phase (degrees). $NPR = 3.38$ ($NPR_{\text{Standard}} = 1.15 NPR$), $s/D = 1$ and $l/D = 1$.

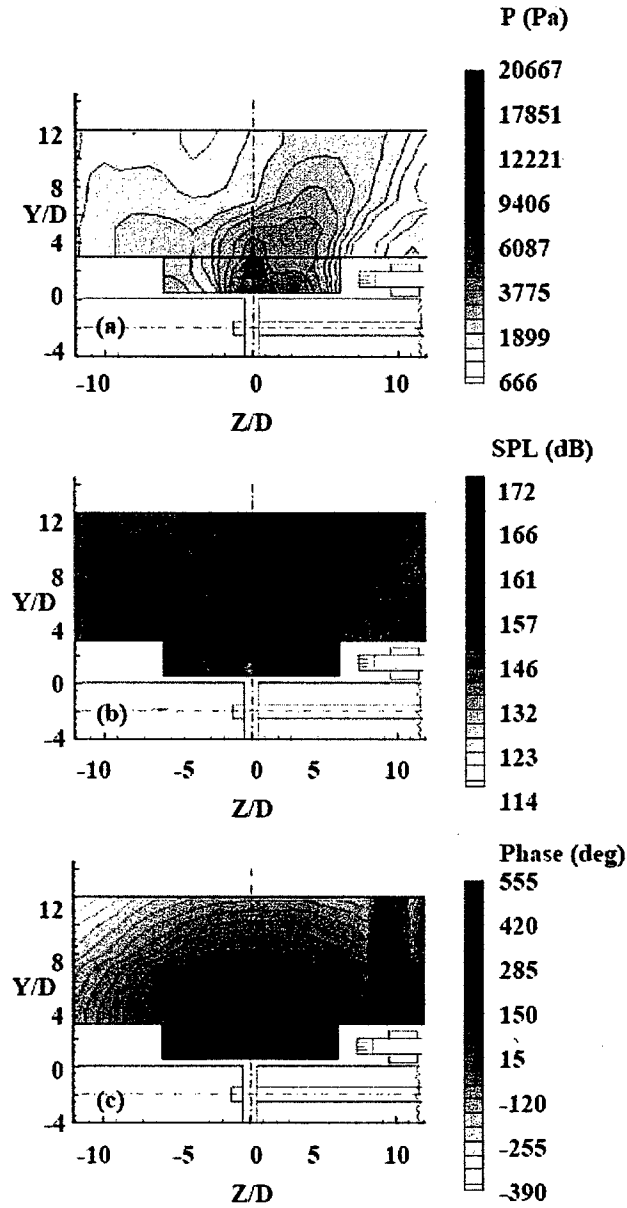


Figure 2.9: Time-averaged features in the near field on the $y-z$ plane (I & II). (a) RMS pressure levels. (b) Sound pressure levels at actuation frequency. (c) Relative phase (degrees). Compressed air flow in actuator is from right to left. $\text{NPR} = 3.38$ ($\text{NPR}_{\text{Standard}} = 1.15 \text{ NPR}$), $s/D = 1$ and $l/D = 1$.

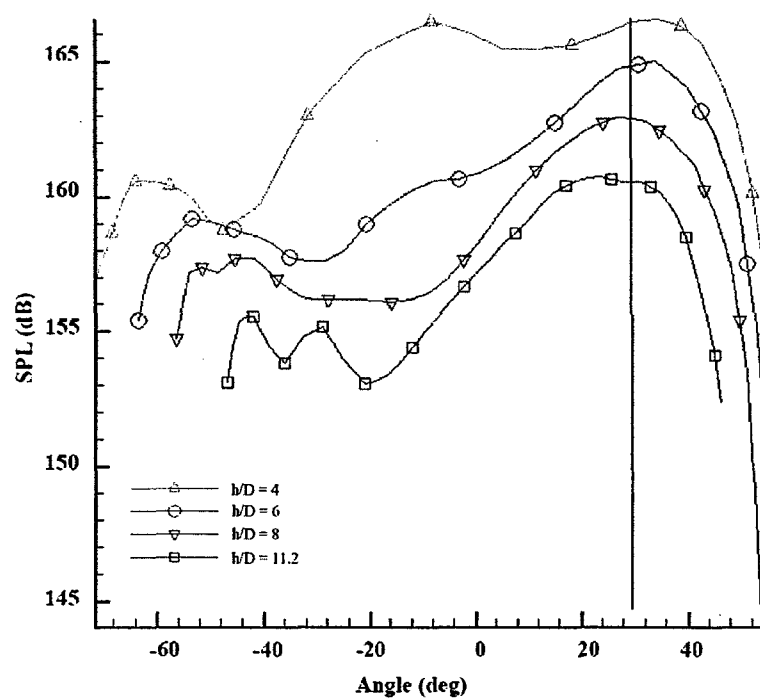


Figure 2.10: Sound pressure directivity of the PRT in the $y - z$ plane. Angles are with respect to the y -axis.

data were acquired at an operating NPR of 3.5, $s/D = 1$ spacing and an operational frequency of 9 kHz ($l/D \approx 0.92$) with a sampling frequency of 200 kHz. The reference microphone was band pass filtered (between 8kHz and 10kHz) and the probe signal was analog low pass filtered at 16 kHz prior to sampling; its purpose is to remove high-frequency components that would otherwise be aliased, or folded down to lower frequencies. Data were ensemble averaged over 100 oscillation cycles. The phase difference from frame-to-frame is 36 degrees. By comparing the phase averaged information of Figure 2.11 to the time averaged picture of Figure 2.8 one can see how the dual lobes emerge on averaging over time.

2.8 Initial Simulation Studies

In this section a few examples of simulations of the PRT actuator are discussed. Later, in Chapter 5, much more information and more examples on the simulations will be given. Here the formulation of the computational problem and numerical method are summarized followed by a discussion of a few key results and physical insights

To explore the flow physics and better understand mechanisms, direct numerical simulations of the resonance tube's flowfield were performed using the Wind flow solver (and Wind-US, its successor code). Wind(-US) is a general purpose Euler and Navier-Stokes Solver (see [Bush et al., 1998], [Power and Underwood, 1999], [Nelson and Power, 2001], [Lankford and Nelson, 2002], and, for Wind-US, [Nelson et al., 2004]). The simulations provide details of the unsteady flow inside the actuator, as well as features of external acoustic radiation. Final solutions were obtained using the Wind code with a third order spatial scheme and third order Runge-Kutta time integration. Although the work of [Cain and Bower, 1995] suggests the use of a fifth order scheme may be the best option available in the Wind code, the presence of a strong oscillating shock and internal zone boundaries makes the third order scheme advantageous in this application. To minimize the issue of outer boundary reflections "buffer zones" were used with added numerical damping in these buffer regions only. Grid refinement and algorithm studies suggest that the present results are invariant to grid and algorithm for modest changes.

The geometry tested in the laboratory had a number of complexities that would require an unreasonably large grid and enormous computational resources to simulate. In order to do meaningful simulations with modest computational resource requirements, simplifying approximations are required. The first such approximation was to assume an axisymmetric geometry and flowfield. The second approximation was a reduced Reynolds number. These two simulations permit direct numerical simulations with a modest grid.

The basic geometry for the computation consists of a supply tube feeding the integration slot and resonance tube, and an axisymmetric far field. The supply tube has a 1.27 cm diameter at the reservoir, tapers conically to a 0.635 cm diameter constant section, and then has a brief flare into the integration slot. The conical section and the constant diameter section are both 1.27 cm long. The grid in the supply tube, integration slot, and resonance tube has nominally square cells roughly 0.01575 cm on a side. In the farfield the cell size gradually expands from 0.01575 cm to roughly 0.254 cm on a side. Thus, there are roughly 280 cells per acoustic wavelength in the supply tube, integration slot and resonance tube, and at least 16 cells per wavelength at the far edges of the outer grid.

A typical sound radiation field, characterized by the far field, is shown in Figure 2.13. The simulation shown in Figure 2.13 is based on viscous no-slip boundary conditions, which will be shown to be very important. The fields in Figure 2.13(a-c) are snapshots spanning approximately one period of oscillation, after the calculation has advanced 31,400 timesteps. At this point in the calculation the field has advanced approximately 16 periods of the basic 7.6 kHz resonance. In the first wavelength (approximately 4.445 cm) from the integration slot, some asymmetries are present. As the pressure

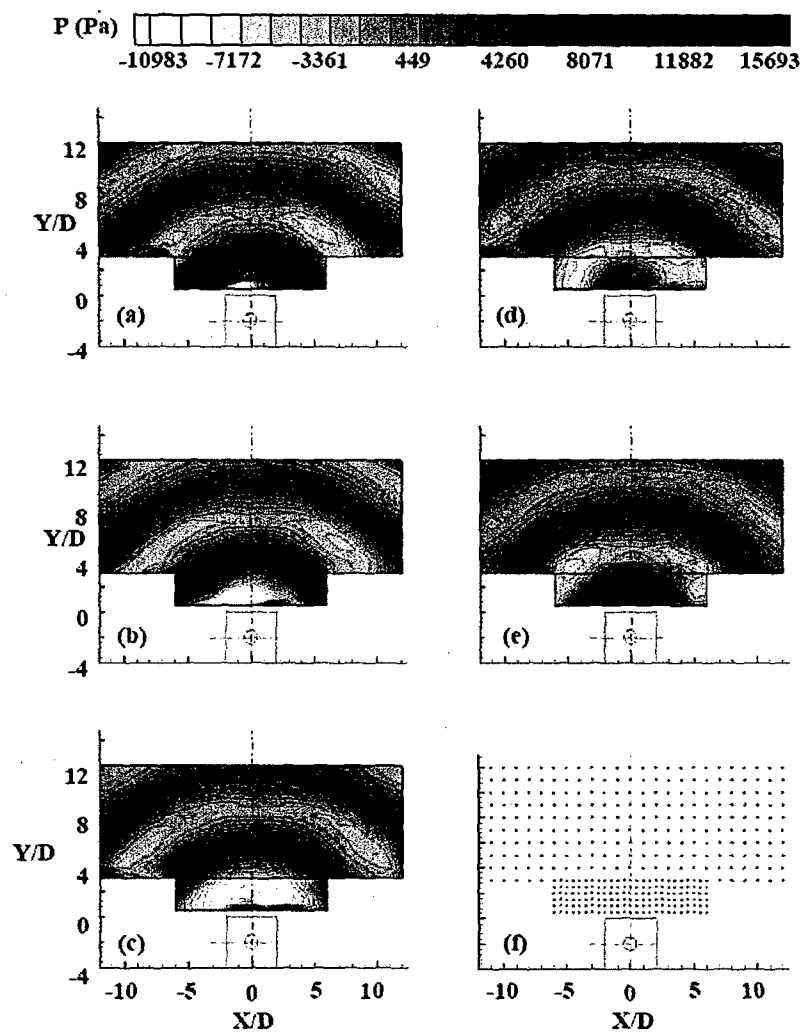


Figure 2.11: Phase-averaged near field pressure depicted on the $x-y$ plane (I & II). Phase difference from frame-to-frame (a-e) is 72 degrees. Measurement grid is shown in (f).

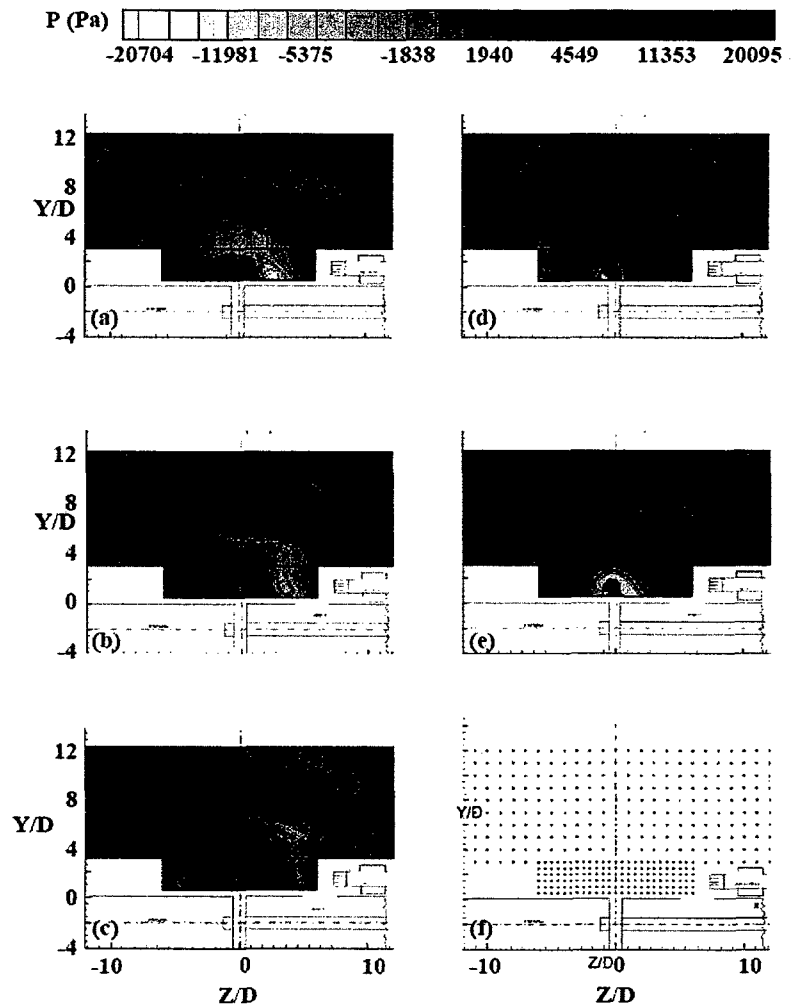


Figure 2.12: Phase-averaged near field pressure depicted on the $y-z$ plane (I & II). Phase difference from frame-to-frame (a -e) is 72 degrees. Measurement grid is shown in (f). Compressed air flow in actuator is from right to left.

wave moves into the farfield, the evolution shows stronger radiation to the left than to the right. One possible explanation is that the asymmetric flow in the integration slot turns the acoustic waves to the left.

A more detailed perspective of the source field is given by the corresponding Mach contours in the supply tube, integration slot, and resonance tube, shown in Figure 2.14(a-c). There are two major points from Figure 2.14(a-c). First note that the flow in the integration slot is almost entirely confined to a narrow channel up the wall on the resonance tube side. This feature is present in all snapshots examined. The second important point is that the shock structure oscillates back and forth across the integration slot, varying in extent from as far as 7/8 of the distance across the integration slot to as little as 3/8 of the distance across the integration slot.

The periodic nature of the flow and acoustic field is illustrated by a pressure measurement, taken at the bottom of zone 4 (the outer field) about 0.635 cm from the edge of the integration slot. Figure 2.15 shows the time history of the pressure and its basic nature over the first 30,000 timesteps of evolution of both a viscous wall and a slip wall calculation. The alternative problem formulation using slip wall boundary conditions was executed to gain further insight into the physics of this problem. From these alternate formulation results, it is found that viscous effects are required for the resonance to setup. Results presented later in the report will address these findings in more detail.

One additional difference between the computations and experiments concerns details of the geometry. The computational supply jet issues from a smooth contraction as previously described. In contrast, the experimental geometry contains a sudden contraction. Losses for a sudden contraction in incompressible flow are approximately 35% based on the information in Blevins [25]. By interpolation of the computational frequency response at various values of NPR values discussed in [Cain et al., 2002b] the experiments were estimated to have a 24% system loss. The direct experimentally measured loss was 28.4%.

2.9 Approaches for Controlling the PRT

The two approaches to devising a high bandwidth PRT are depicted in Figure 2.16. The first approach was a Look Up Table (LUT) approach that relied on an extensive database. The second approach used either the Quarter Wave Length (QWL) or the LUT as an initial estimate and varied either the resonance tube depth, d (SISO- Single Input Single Output) or both the spacing parameter, s , and the depth, d (MIMO- Multi Input Multi Output) within a feedback loop until satisfactory results were obtained.

Based on the extensive data base, it was found that the resonance tube depth is the primary parameter in controlling the PRT's resonance frequency. In addition it was found that if the correct values of pressure and spacing were used, changing only the depth can produce frequencies ranging from 2700 Hz to 9000 Hz. For the computer controlled PRT tests an NPR of 3.5 and a spacing of $s/D = 1$ were chosen based on the results of Figure 2.3. Then, after averaging both increasing and decreasing depth curves, a 6th order polynomial curve fit to the data was obtained. The equation representing the curve fit is:

$$\begin{aligned} d/D = & 11.6168 \times 10^{-24} f^6 - 7.0172 \times 10^{-19} f^5 + 20.2436 \times 10^{-15} f^4 - \\ & 29.782 \times 10^{-11} f^3 + 22.9436 \times 10^{-7} f^2 - 9.1516 \times 10^{-3} f + 16.9996 \end{aligned}$$

Where f is the desired frequency in Hertz, and d/D is the depth ratio.

Some of the results of this type of controller are shown in Figure 2.17 in the form of spectra of the sound produced. In addition Table 2.5 provides information on the input frequency, output frequency and the output frequency error. From these results it can be seen that this method produced the

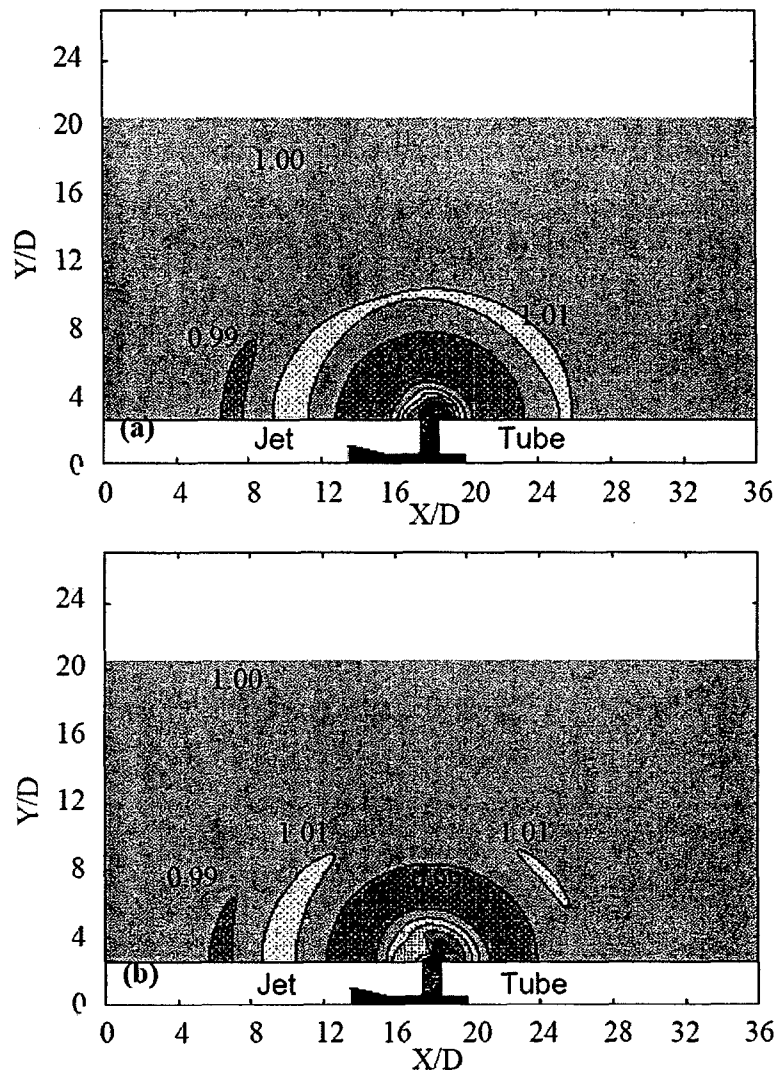


Figure 2.13: Pressure contours from a simulation of a powered resonance tube using the WIND code with buffer zones to minimize reflected pressure waves from the outer boundaries. The nozzle pressure ratio for these simulations was 3.72. Time steps: (a) 32,400 and (b) 32,600. Compressed air flow in actuator is from left to right.

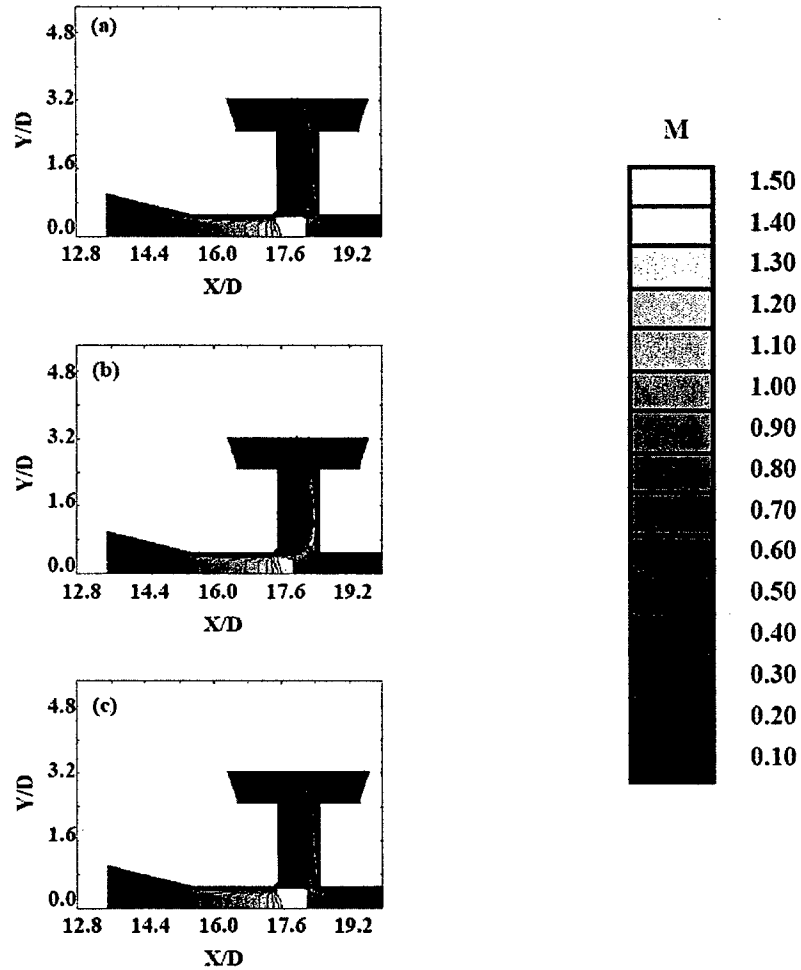


Figure 2.14: Iso-Mach contours from a simulation of a powered resonance tube using the Wind code. The nozzle pressure ratio for these simulations was 3.72. Time steps: (a) 31,400 (b) 32,200 and (c) 33,200. Compressed air flow in actuator is from left to right.

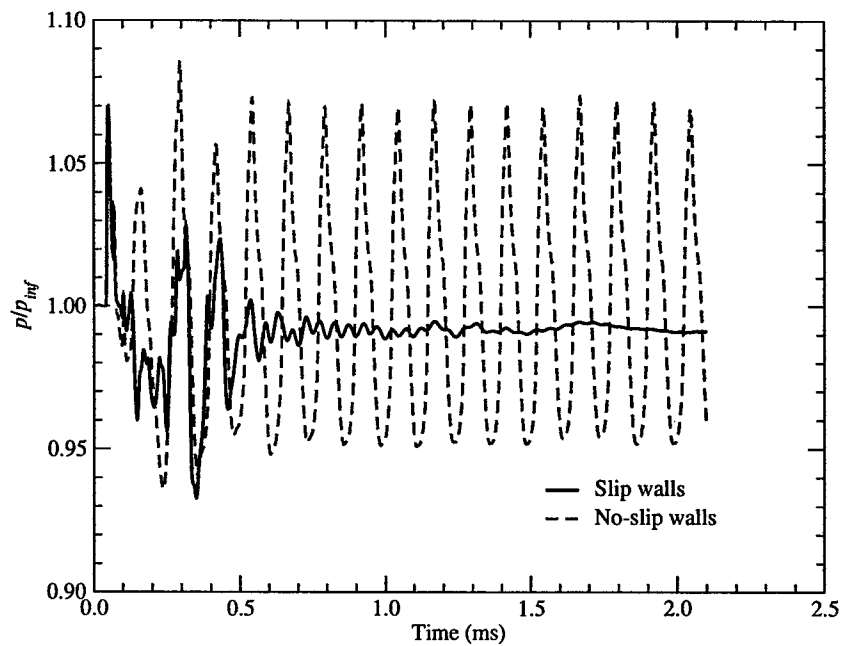


Figure 2.15: A time trace of the pressure in the far field. Solution calculated for 30,000 time steps.

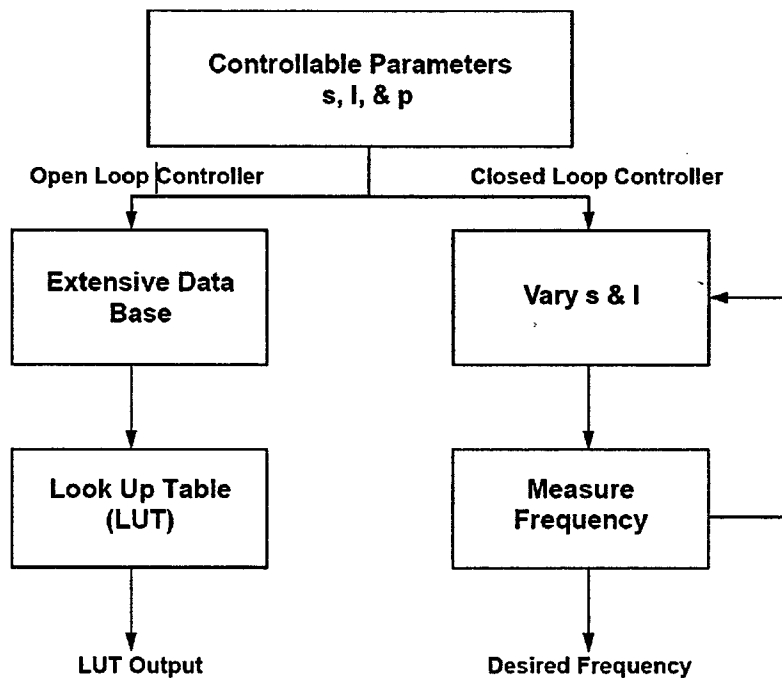


Figure 2.16: Two approaches to creating a computer controlled high bandwidth actuator.

Table 2.5: Summary of effectiveness of Look Up Table (LUT) approach and Feed Back controller (FB) in producing high frequency excitation signals based on prescribed inputs in ascending order. The error when using the feedback controller depends on the frequency bandwidth (20 Hz for our experiments) that depends on sampling frequency (80 kHz) and number of points in the spectrum (4096).

Input Frequency (kHz)	LUT Output Frequency (kHz)	LUT Error (Percent)	FB Output Frequency (kHz)	FB Error (Percent)
2.5	2.58	2.40	2.52	0.80
3	3.008	0.27	2.99	0.67
4	4.023	0.57	4.02	0.50
5	4.992	0.16	5.02	0.40
6	6.144	2.40	6.01	0.20
7	6.976	0.34	7.02	0.29
8	8.046	0.57	8.02	0.25
9	9.216	2.40	8.98	0.22
10	10.3	3.00	9.99	0.01
11	11.65	5.91	10.98	0.18

prescribed frequency with a maximum error of 6%. But in addition to the errors shown in the table, changes in supply pressure could create situations where the device produced no tones at a given integration slot spacing. In addition if errors occurred in the plant (or the system) or if noise was present, the controller could not respond since it did not receive any feedback. It is therefore necessary to search for a more robust method that incorporates feedback to handle noise within the system and reduce the output error.

The effectiveness of the LUT and FB approaches is summarized in Tables 2.5 and 2.6. The look up table method was made possible by very detailed data taken under various conditions. Significant improvement in obtaining the desired frequency is obtained by using feedback. Details of the resonance tube depth on the resulting frequency, sound pressure level, and acoustic power are given in Table 2.6. Figure 2.18 compares various control strategies in obtaining the prescribed frequency. The departure from the QWL prediction increases at higher frequencies (lower tube depths). If the QWL is used as an initial estimator reasonable convergence is obtained within 8 iterations. Using the LUT as an initial estimator the SISO controller provides better results (Figure 2.19). Due to the complexity of the functioning of the PRT, SISO control is not very effective. Five possible problems are illustrated in Figure 2.20.

The first step towards building a closed loop controller was to make it a single input (frequency) single output (depth) (SISO) controller. At the start of this step, Quarter Wave Length (QWL) theory was used as an estimator and a routine needed to be chosen for iterating depth (l). A fixed point iteration method was used to iterate for the depth and this produced the prescribed frequency. A depth increment of $l/D = 0.2$ was used for the results presented in this report. The iteration was limited by the error between the measured frequency and the input frequency. And this error was calculated based on the input parameters for the spectral calculations such as, sampling frequency and number of points per record, which defined the resolution of the spectrum calculated.

The controller used in these experiments was built using a LABVIEW program that acquired the data from the microphone, calculated the spectrum, and iteratively changed depth. Figure 2.18 shows the differences in errors resulting from the use of the quarter wavelength (QWL) as an open loop controller, using the look up table (LUT) as an open loop controller and the feedback controller (FB), which uses the QWL as an initial estimator. It can be seen that the feedback controller

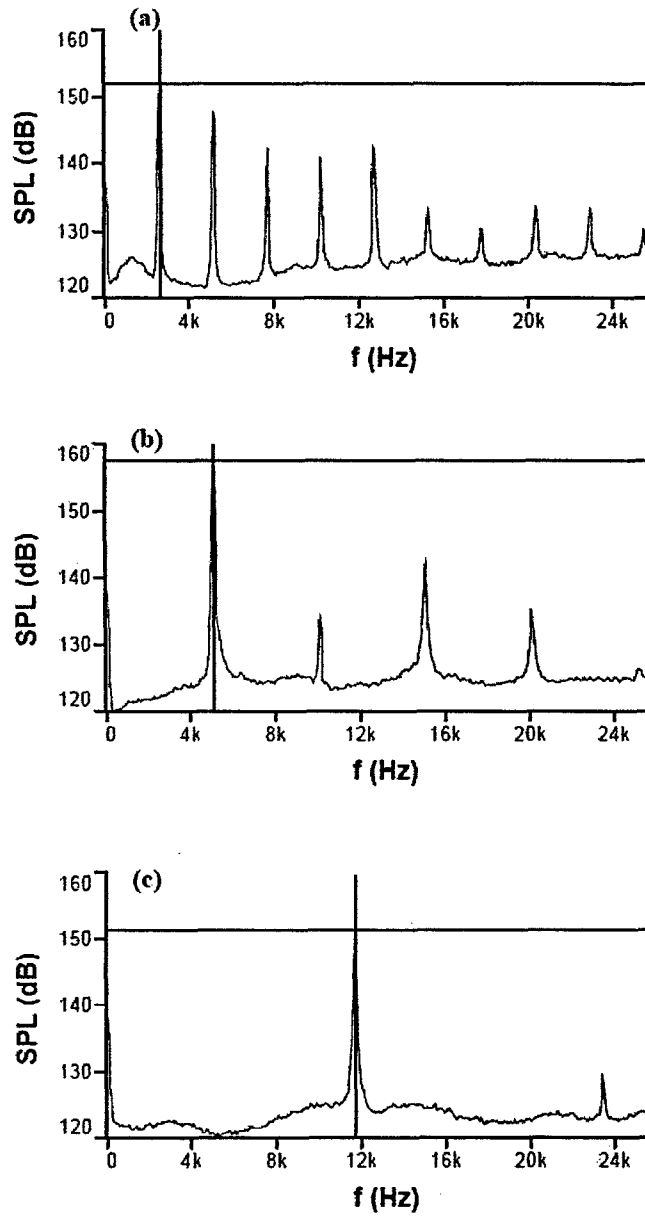


Figure 2.17: Spectra showing results of the Look Up Table (LUT) approach. The vertical line depicts the prescribed frequency and the spectrum represents the resulting actuation signal. (see Table 2.1 for the errors in using this method). NPR = 3.72 (NPR_{Standard} = 1.15 NPR).

- (a) $d/D = 4$, input and output frequencies are 2.50 and 2.56 kHz, respectively
- (b) $d/D = 2$, input and output frequencies are 5.00 and 4.99 kHz, respectively
- (c) $d/D = 0.4$, input and output frequencies are 11.00 and 11.65 kHz, respectively.

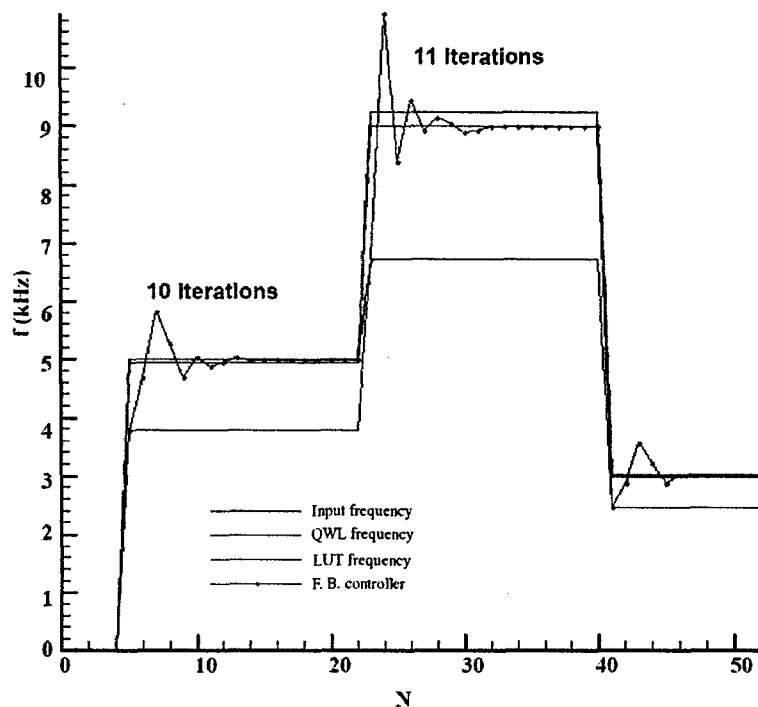


Figure 2.18: Effectiveness of various control strategies in obtaining a prescribed frequency.

Table 2.6: Effect of resonance tube depth ratio (d/D) on the resulting frequency, sound pressure level, acoustic power and acoustic energy (spacing parameter, $s/D = 1.2$, $NPR = 3.72$).

d/D	f (kHz)	SPL (dB)	p_{rms} (Pa)	W (Watts)	E (Joules)	Eff. (%)
0.4	11.58	137	141.59	0.18	0.15	0.003
0.6	10.75	154	1002.37	8.89	7.37	0.175
0.8	9.41	156	1261.91	14.10	11.83	0.278
1.0	8.32	155	1124.68	11.20	9.54	0.221
1.2	7.36	151	709.63	4.46	3.87	0.088
1.4	6.66	157	1415.89	17.74	15.70	0.350
1.6	6.14	156	1261.91	14.10	12.70	0.278
2.0	5.25	154	1002.37	8.89	8.36	0.175
2.4	4.10	154	1002.37	8.89	9.20	0.175
2.8	3.46	154	1002.37	8.89	10.07	0.175
3.2	3.07	152	796.21	5.61	6.86	0.111
3.6	2.75	152	796.21	5.61	7.45	0.111
4.0	2.56	149	563.68	2.81	3.97	0.055
4.4	2.37	150	632.46	3.54	5.36	0.070

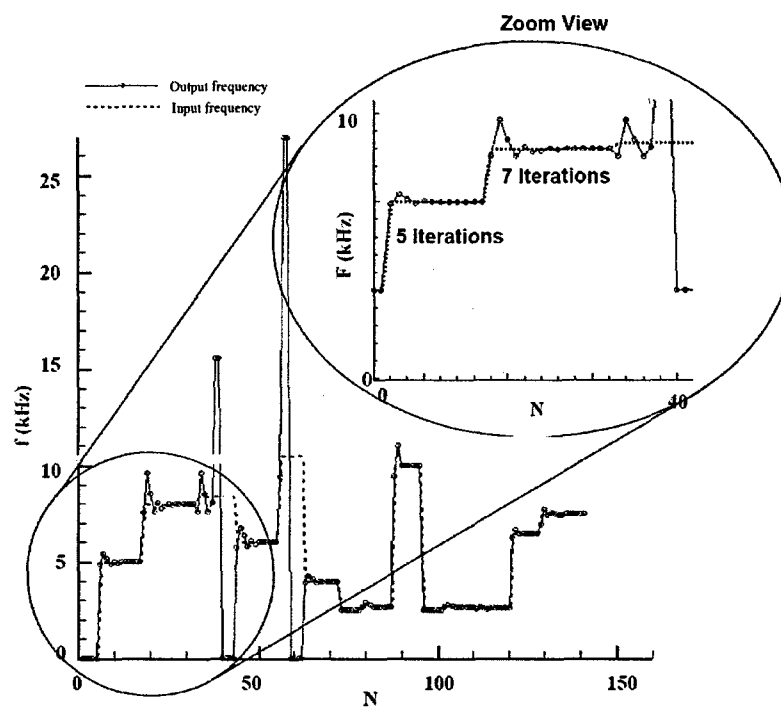


Figure 2.19: Effectiveness of Single Input Single Output (SISO) Feed Back controller (FB) showing its response to various input frequencies using the Look Up Table (LUT) as an initial estimator.

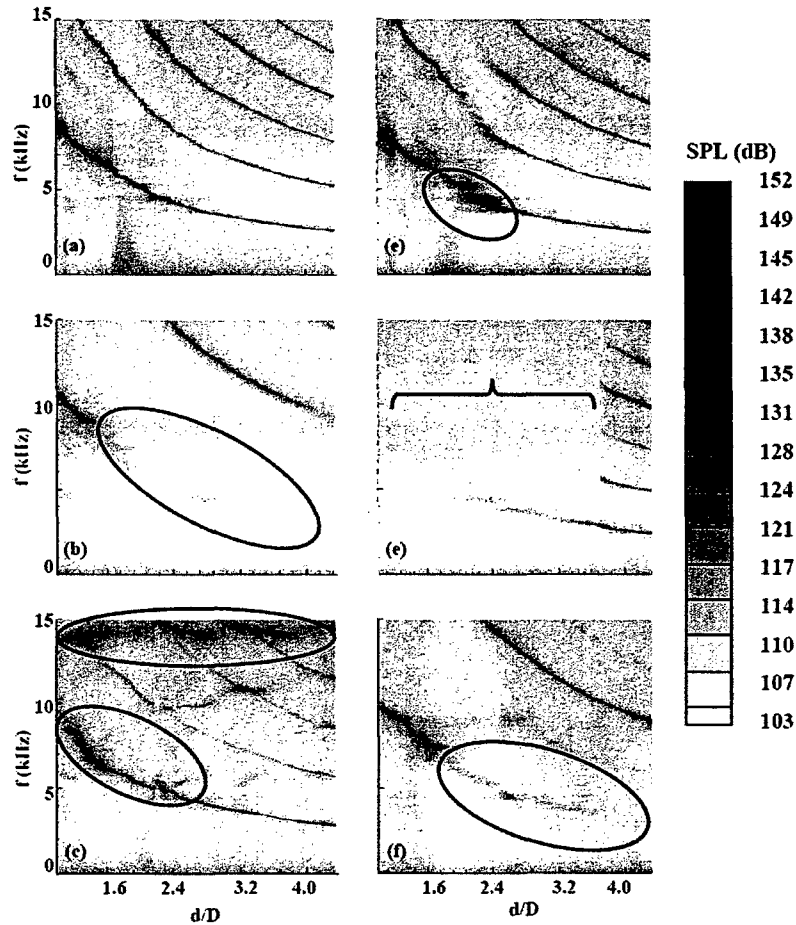


Figure 2.20: Features of the PRT that make the LUT approach ineffective (see marked regions). Pressure spectra with changing depth are shown for the following cases. (a) Optimal case, (b) jump to higher harmonics, (c) high frequency noise, (d) frequency gaps, (e) only low frequency, (f) higher harmonic jumps with frequency gaps.

reduced the error to around 20 Hz (based on 4096 point per record and 80 kHz sampling rate), which in comparison to both QWL and LUT is a huge step in improving the control. It should be mentioned that the iteration time depends on the time required to acquire the data, the time required to calculate the spectrum and the time required to move the motor to the new depth. In order to reduce the time required to lock on to a frequency one can either reduce the iteration time or the number of iterations. To reduce the iteration time, the time needed to acquire the data to calculate the spectrum can be reduced by increasing the sampling rate, reducing the number of points per record, or reducing the number of records, or increasing the speed of the motor. To reduce the number of iterations, the LUT was proposed as an estimator based on the results shown in Figure 2.18. Figure 2.19 shows the results and response of such a controller. This controller could successfully reduce the number of iterations by 70% of that required when the QWL was used as an estimator, for the same value of error tolerance (as seen on the zoomed view). In general, it can be seen that the controller works well and finds the prescribed frequency within 3-8 iterations. However, there are some situations where the controller failed to work. For example, when the prescribed frequency was 8.2 kHz, the controller failed since a strong harmonic appeared at 16 kHz. This result and others created some challenges for the user. These challenges are summarized in Figure 2.20.

Figure 2.20(a) shows the spectrum vs. depth contours under favorable conditions of spacing and pressure, which are not easy to obtain at all times. For example, (Figure 2.20(b) and 2.20(f)) show how the higher harmonics can dominate the spectrum, and makes it impossible to obtain a frequency lower than 8.5 kHz. Figure 2.20(c) shows the presence of high frequency noise at different depths, which makes it difficult for the controller to find the required frequency. In some cases the frequency variation was not continuous i.e. some gaps appeared at specific frequencies, which make it difficult for the controller to find certain frequencies as shown in Figure 2.20(c) and 2.20(d). In other cases only low frequencies can be found in the spectrum and no tones appeared at depths where high frequencies were expected, as shown in Figure 2.20(e). In order to solve these problems, a second input to the controller was required. Since the integration slot spacing acts like a tuning parameter, it could be varied to change the shape of the contours (shown in Figure 2.20) and at the same time change the SPL, i.e. to obtain maximum SPL at a given frequency.

In the improved approach the spacing parameter was scanned to find the best value (one that produced the maximum SPL). The spacing is limited to a specific range, which is the instability region of the diamond shape shock cell structure of the jet. So, the minimum, maximum and step size of the spacing were fed in to the controller. Following this, each spacing step was applied, the frequency was locked on to using the program used previously (frequency lock loop), the SPL was saved and a new step was initiated (the spacing loop) as shown in the flow chart of Figure 2.21. When the spacing loop yielded the maximum possible value of SPL, the spacing corresponding to the maximum value of SPL, was chosen and the frequency-lock program was run again. The response of this controller for an input frequency of 9 kHz and spacing range of $s/D = 0.8$ to 1.08 with a 0.254 cm step size is represented in Figure 2.22. The plot shows 8 fields, starting from $s/D = 0.8$ to 1.08, which represents the spacing used each time in the spacing loop. The prescribed and measured frequencies vs. number of iterations are plotted in the upper part and SPL vs. number of iteration are plotted in the lower part. So, for example at a spacing of $s/D = 0.8$ the frequency was locked at 9 kHz after 13 iterations and the corresponding SPL (155 dB) was saved. Then, the next spacing was set ($s/D = 0.84$) and the same procedure repeated.

The stored data points of the spacing and SPL are marked in circles. Based on these results, the optimal spacing of $s/D = 1.08$, which produced the maximum SPL, was chosen and the frequency lock routine was run again, to obtain 9 kHz at 157 dB. It should be mentioned here that logic was incorporated into the program to terminate the frequency-lock loop if any unusual result occurs (like higher harmonics, frequency gaps, etc.).

Since the PRT phenomenon is nonlinear and it is hard to predict the occurrence of the tone, a fixed point iteration method was used as a controller. By examining this type of method, it can be easily

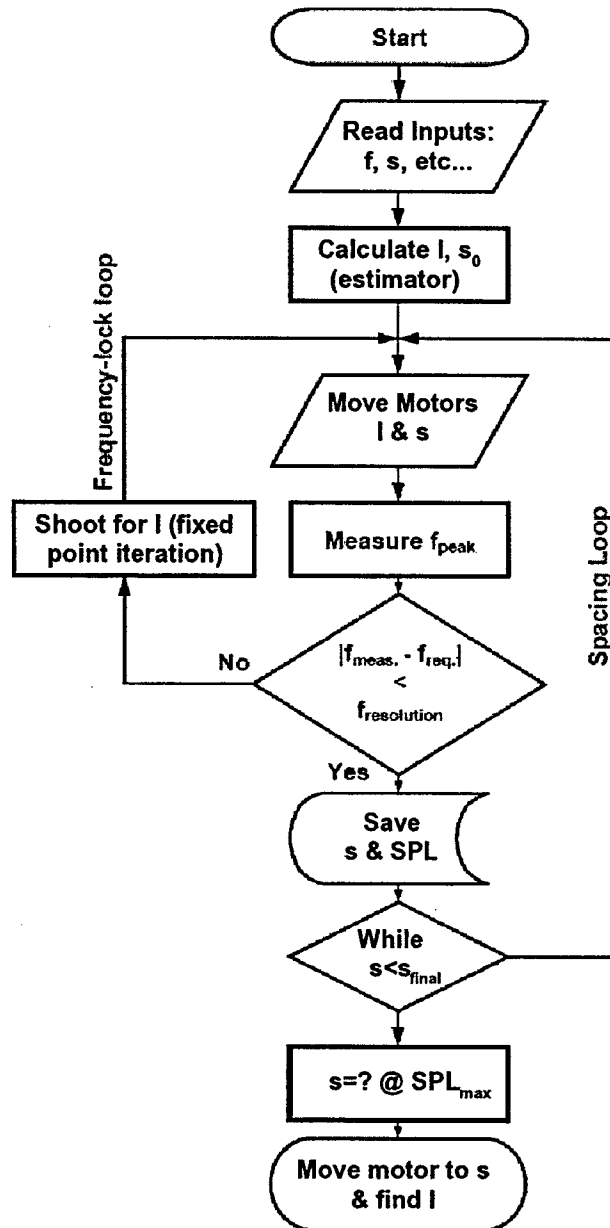


Figure 2.21: Flow chart of the algorithm for the Multi Input Multi Output (MIMO) Feed Back controller (FB) used to control both the spacing and the depth of the PRT.

noticed that it is a pure gain change method. The time needed by this controller to lock to the required frequency was presented in the current study as number of iterations. The time needed for a single iteration mainly depends on the time needed to collect the data and on the time of moving the motors to the required distance.

When using the SISO FB controller, it was found that it can compensate for internal noise, and sometimes for external noise as well. But, for some cases, it could not compensate for large external perturbations such as a big change in pressure. As a result the MIMO FB controller was constructed. From the mapping results, it was found that the pressure and spacing are correlated. So, if the pressure changes and results in the absence of resonance, a change in spacing can compensate for that and can produce the resonance again. Based on this observation, the MIMO FB controller was built. Where it scans a range of spacing specified by the user locks on to the required frequency, and saves the corresponding SPL value at each spacing value. Therefore, using this controller not only solved the problem in producing the tone if the pressure condition changed, but it also could be made to find the highest SPL level at that frequency. To demonstrate the improvements obtained using this closed loop controller over the open loop type, various frequencies were chosen to be run on both controllers and the resultant frequency is tabulated in Table 2.5. The table shows a significant reduction in error when going from the LUT method to the FB method. Where in LUT method the maximum error was 5.9% compared to 0.8% in FB method. The last point to be discussed about the controller is the role of the estimator; it was clearly shown how the estimator affects the number of iterations needed by the controller to lock on to the required frequency. It was shown that the LUT estimator reduced the number of iterations by 30% compared to the QWL estimator. Since the LUT estimator was based on a 6th degree polynomial curve fit, an increase in the degree or in the significant figures in the fitting equation can result in a more accurate estimator, and consequently less iteration and faster control.

2.10 Prototype Summary

A prototype high bandwidth actuator based on the Powered Resonance Tube (PRT) concept was developed and demonstrated. The PRT concept involves a high speed jet that impinges on the open end of an open-closed resonance tube. This device is capable of producing flow oscillations of high amplitude and high frequency. The actuator could produce frequencies ranging from 500 Hz to 15,000 Hz at amplitudes up to 160 dB. The experimental developments were complemented by analytical modeling and direct numerical simulations.

Analytical modeling of the acoustic resonances in the PRT geometry [Kerschen, 2001] was carried out in order to understand how the geometrical parameters influence the resonance frequency. For the smaller tube depths, associated with higher resonance frequencies, the integration slot geometry was found to play an important role in determining the resonant frequency.

Direct numerical simulations of the unsteady flow in the PRT actuator were carried out in order to explore the flow physics and better understand the fundamental mechanisms responsible for the resonance. Scaled simulations of the powered resonance have been achieved with good correspondence to laboratory experiments in terms of the frequency (simulated at 7.6 kHz) and amplitude (a simulation value of 160 dB) of their resonant response. The simulations suggest new insights into the complexity and details of the flowfield.

The initial simulations at very low Reynolds number show that the flow in the integration slot is primarily on the resonance tube side with almost no flow on the supply tube side of the integration slot. Results to be presented later will show that this is not the case at higher Reynolds numbers.

Extensive experimental data were acquired and then used to create a look up table program for computer controlled operation. Detailed measurements useful for understanding physics and validating

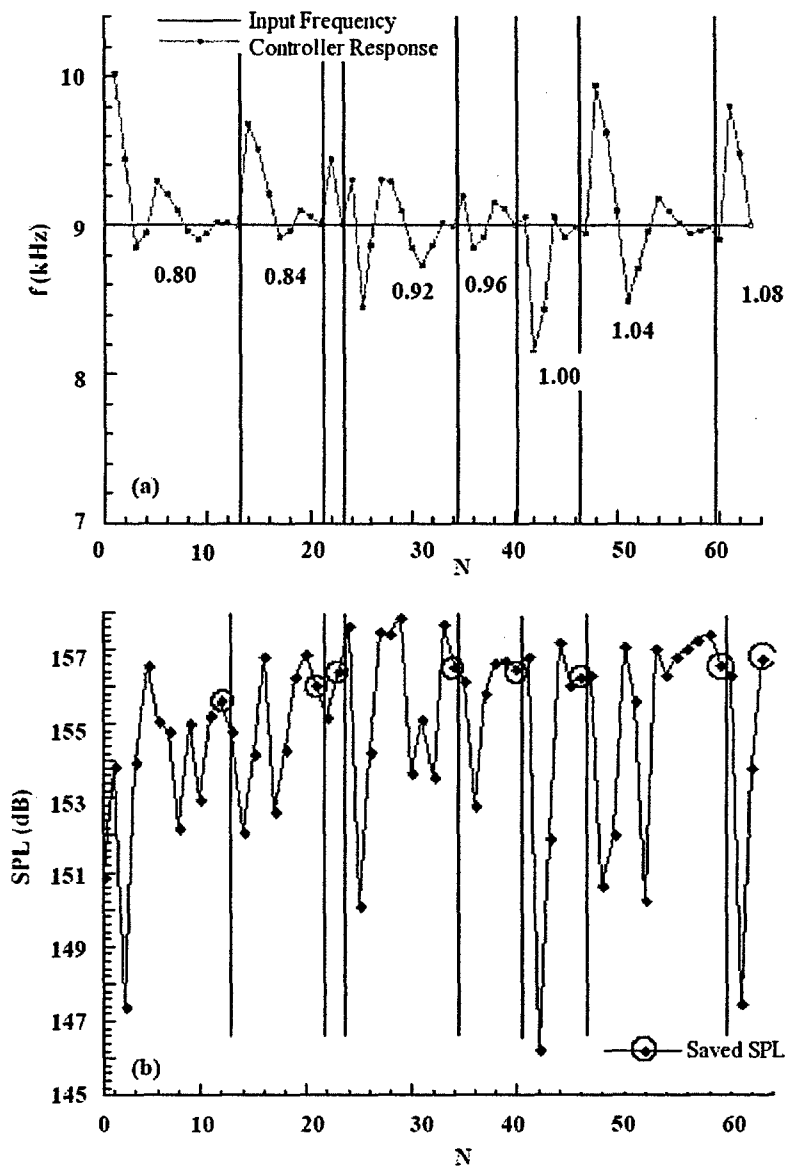


Figure 2.22: Response of the MIMO feedback controller for an input frequency of 9 kHz. The figure also illustrates the scanning of the spacing parameter (s/D) 0.8-1.08 to produce the prescribed frequency at the highest amplitude. Represents the saved points. (a) Frequency and (b) sound pressure level.

simulations were made. The detailed characterization also provides guidance for actuator deployment. Finally, it is believed that numerous applications exist for such high bandwidth actuators including jet mixing, impingement noise suppression, and weapons bay applications.

Chapter 3

Impinging Tone Suppression Using the Powered Resonance Tube

3.1 Overview

In this chapter the jet impingement tone phenomenon and the capability of the powered resonance tube for acoustic suppression in the subsonic Mach number range is examined. The suppression utilizes high frequency excitation of the main jet shear layer by Powered Resonance Tube (PRT) actuators, for the impingement tone suppression. Since the experimentation included variation in both the PRT and impingement tone settings new insights have been gained. Some of the variables examined were acoustic in nature, whereas the others were fluidic. Through careful experimental and analytical studies the most significant variables responsible for the suppression are identified. The work also underlines the importance of high frequency excitation by revealing the fact that, for the same suppression level, selecting the optimal acoustic tone can reduce the mass flow rate by almost 50%; as compared to suppression due to oscillatory mass injection. The study reveals that impingement tones of certain frequencies were easier to suppress than others and offers a conjecture for it. Some of the other issues addressed include staging behavior of the impingement tone, Perceived Noise Level Corrected for the Tone (PNLT) as a measure of effective suppression, and the presence of additional spikes in the suppressed impingement tone spectra.

3.2 Introduction to Jet Impingement Tones

When a free jet of air with high velocity (i.e. $M > 0.6$) and high Reynolds number ($Re > 2 \times 10^5$) is directed normally on a flat plate it gives rise to discrete tones of very large amplitude noise at discrete frequencies—referred to as jet impingement tones[Tam and Ahuja, 1990]. This phenomenon poses many problems when it arises in practical situations. In laser cutting, it is a common practice to remove the molten mass of metal with the help of high speed jet of air. Here the quality of the cut depends on the oscillatory behavior of the jet. A stable jet, free from any impingement tones, is a prerequisite for deeper, cleaner and straighter laser cuts[Masuda and Nakamura, 1992]. Thin glass sheets are prone to cracks when tempered by a cold air jet with impingement tones[Aratani et al., 1995]. One of the methods of surface coating, known as cold gas dynamic spray coating, is carried out by blasting the fine grain metal powder directly on to the surface to be coated with the help of a high velocity jet of air. Here, the properties of the surface finish largely depends on the stability of the jet. An unstable jet is found to deteriorate the surface finish. Another example of great importance is Short Take-Off Vertical Landing (STOVL)

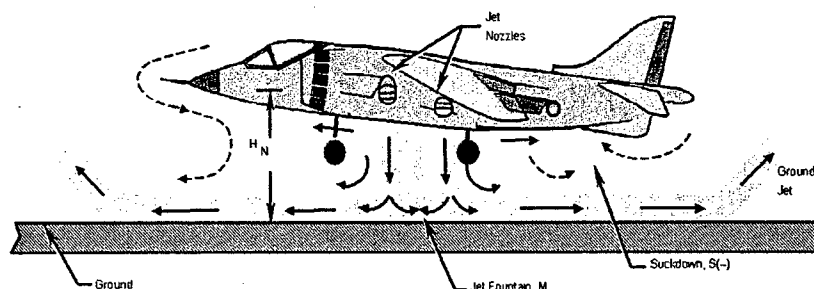


Figure 3.1: STOVL engine in hovering mode and impingement tone

aircraft engines [Krothapalli et al., 1999]. As shown in Figure 3.1, when the aircraft is close to the ground, the plumes from the engines hit the ground and produce impingement tones. Lift loss, sonic fatigue, and ground erosion caused by the hot plumes of STOVL engines in the hovering mode are among the concerns that motivated this work.

Figure 3.2 shows a schematic of the feedback loop of the jet impingement tone. The interaction of the unsteady flow with the ground surface gives rise to pressure disturbances. These disturbances travel upstream, reach the lip of the nozzle, there they are scattered off the edge of the nozzle and create a wavelength matching allowing excitation of the shear layer through the receptivity process. This periodic excitation strengthens the shear layer instabilities producing large scale coherent structures. When these large scale structures hit the ground plane, the sound generation mechanism is further intensified, thus completing the feedback loop and producing high intensity discrete frequency tones known as impingement tones. In the experiments, the amplitude level of the tone was as high as 145 dB (measured at $3.2 D_M$ from the main nozzle), whereas the frequency depended on a number of parameters viz. Mach number of the jet, the standoff distance between the nozzle exit and the ground plate and finally the exit diameter of the nozzle.

An example of flow control, specifically pertaining to the impingement tone includes the work of [Sheplak and Spina, 1994] who used a high speed co-flow to shield the main jet shear layer from the disturbance waves. This method achieved suppression in the broadband noise levels greater than 10 dB and also completely suppressed the impingement tone, but at the cost of large mass flow rate (up to 20-25% of the main jet). Recently, [Alvi et al., 2003] made an effort to control the impingement tone. They employed a circular array of micro jets around the periphery of the main jet to demonstrate reduction in the overall SPL (8 dB).

Depending on the relation of the forcing frequency of the perturbations with that of the original instability frequency, active flow control can be further divided into two groups—AFC-I and AFC-II. AFC-I involves the use of low frequency unsteady forcing to excite instability waves of a laminar flow, or the large scale structure of a turbulent flow. This technique has been used extensively in the past decade [Cain et al., 2003b]. The second class (AFC-II), that has been developed more recently, involves high frequency forcing of the turbulent boundary or shear layer; i.e. higher than the neutral frequency predicted by the linear stability theory. It was [Wiltse and Glezer, 1998] who first discovered the effect of high frequency excitation of the turbulent shear layer. They found a dramatic alteration in the development of a turbulent shear layer. Analysis of their measurements showed that high frequency excitation in the transitional region of the shear layer inhibits the growth rate of large scale structures. The numerical work of [Cain et al., 2001] showed that beyond a threshold level, the magnitude of suppression of the turbulent kinetic energy increased monotonically with increasing amplitude of the high frequency forcing. For a given forcing energy, the largest reduction in the turbulent kinetic energy was achieved at frequencies two or three times the neutral frequency

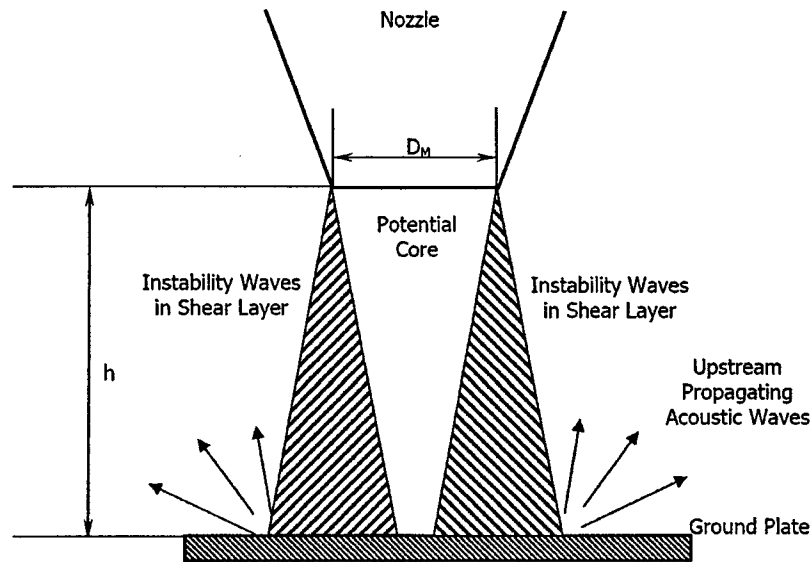


Figure 3.2: Schematics of the impingement tone feedback mechanism.

determined from the linear stability theory.

For the impingement tone, the formation of coherent structures is important. Since high frequency forcing of the shear layer in the transition region inhibits the formation of large scale structure, one can expect that high frequency acoustic signal from the PRTs would suppress the impingement tone.

The Powered Resonance Tube (PRT) or Hartmann Whistle [Hartmann and Troll, 1922] as it is often referred to, is an actuator based on aeroacoustic principles [Brocher et al., 1970, Raman et al., 2004a]. It consists of a supersonic under-expanded jet aimed at a cylindrical tube open at one end and closed at the other. Figure 3.3 shows a version of the PRT that was used in the experiments. Apart from the cylindrical nozzle and the cylindrical resonance tube one can also see a piston and shield. In the present application the piston is used to control the depth of the cylindrical tube which in turn governs the frequency of the signal produced by the device. The shield helps to direct the signal towards the region where flow control is desired. Due to its potential for operating at large bandwidths (3 to 18 kHz), and producing high amplitude levels (above 150 dB) [Raman et al., 2004a], the PRT is a potential device for use in Active Flow Control applications [Kastner et al., 2004, Murugappan and Gutmark, 2003].

The present chapter focuses on two sets of experiments. The first set characterizes the salient features of the impingement tone. It also shows the influence of lift plate (prototype of the airframe structure) on the frequency staging behavior of the tones. The second set of experiments, addresses the payoff of this work, namely an evaluation of the effectiveness of the PRTs in suppressing the impingement tone. These experiments are accompanied by analyses and numerous observations to highlight some of the important parameters in the suppression mechanism.

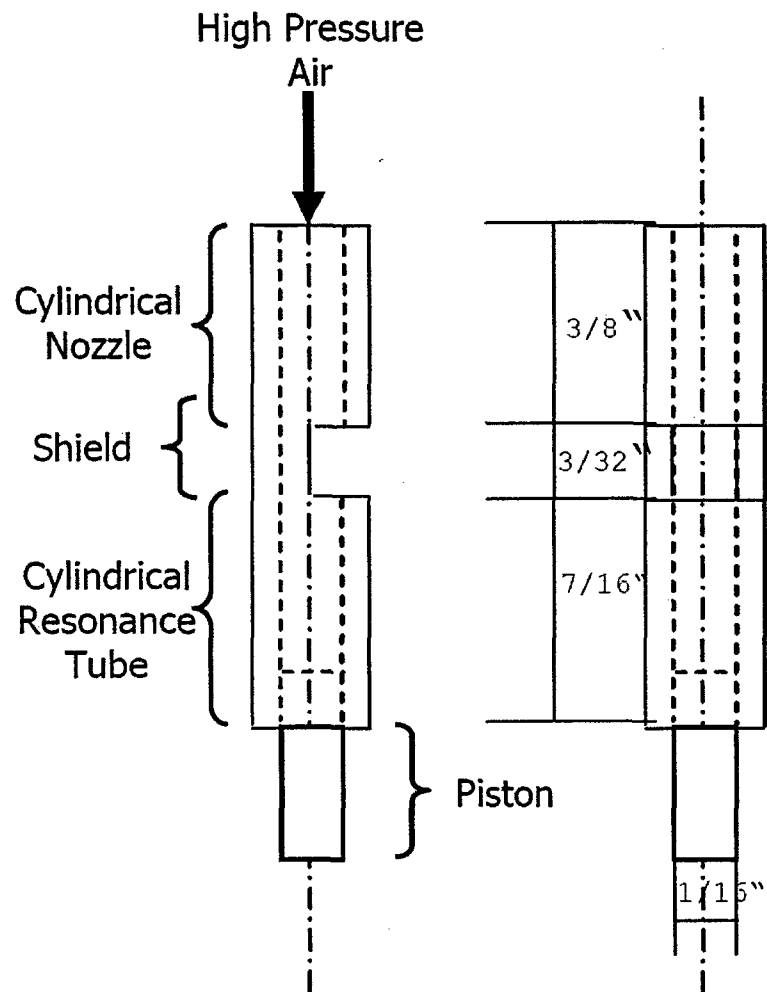


Figure 3.3: Schematic diagram of the Powered Resonance Tube (PRT).

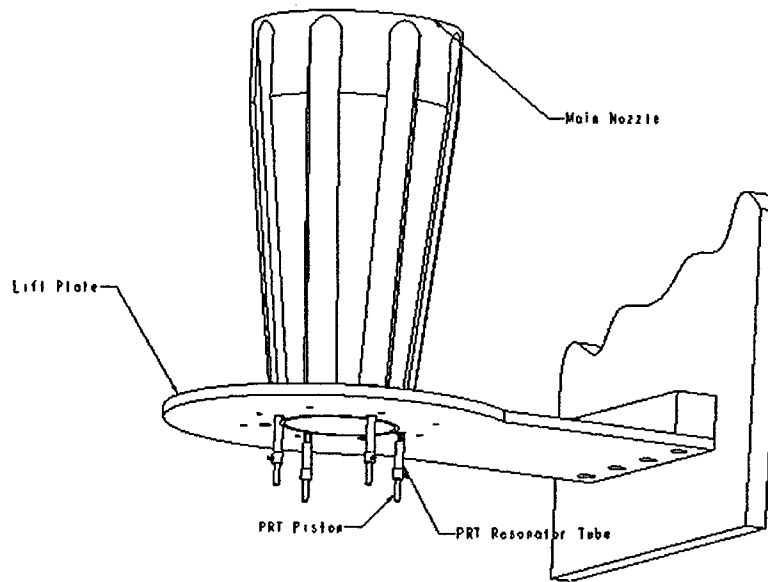


Figure 3.4: PRT integrated jet impingement tone set-up.

3.3 Jet Impingement Tone Experimental Apparatus

Figure 3.4 shows a schematic of the impingement tone set-up with PRTs integrated into it. It consists of a convergent conical nozzle (referred to as main nozzle) with an exit diameter of 3.175 cm (1.25") and contraction ratio of 1.6 and a taper angle of 70. The main nozzle receives air through a cylindrical plenum with 15.24 cm diameter and 91.44 cm length (6"×36"). A circular plate, referred to as lift plate, of 10.16 cm (4") diameter is mounted flush with the main nozzle exit to simulate the effect of the airplane body. The jet emanating from the main nozzle impinges on a square steel ground plate of the size 68.58cm×68.58cm×0.635cm (27"×27"×1/4") which can be adjusted to any desired stand off distance from the main nozzle.

Around the circumference of the main nozzle, four PRTs with their cavity openings facing the main jet are fitted. The PRTs receive air through a plenum chamber having 7.62 cm diameter and 91.44 cm length (3"×36") via individual flexible hoses. Care was taken to keep these hoses straight, since, otherwise it was found to affect the performance of the PRTs.

Both the main jet and PRT plenums are instrumented with Setra 204 pressure transducers to measure the stagnation pressure. The large size (1.25") of the main nozzle resulted in a rapid blow down operation. This necessitated monitoring of the main jet plenum pressure through the data acquisition system. The electrical output of the Setra transducer, connected to the main jet plenum chamber, was input to the data acquisition system for this purpose. Once the air supply to the main nozzle was turned on and as the main nozzle stagnation pressure (i.e. plenum pressure) approached the desired pressure, data was acquired for 1.6 seconds at a sampling rate of 500 kHz through two channels of the DAQ system. One of the channels measured the stagnation pressure of the main jet, whereas, the other was connected to a B&K 4393 microphone situated at $3.2 D_M$ (4") from the main nozzle. To avoid aliasing, the microphone signal was passed through a 4th order analog Bessel filter (manufactured by Ithaco). Here the high-pass set to 10 Hz, whereas low-pass limit was set to

100 kHz.

Once the signal was obtained, the time series was broken into five segments. The mean main jet stagnation pressure of each segment varied marginally from the desired value. This variation was of the order of 4.20×10^{-3} NPR (0.1 psi). The segment which had the mean pressure closest to the desired pressure was identified. It is this segment which was processed for further analysis. Here one must note that, total processed data consisted of 200 records, where each record contained 4096 data points. For choosing the data-strip which had the mean pressure closest to the desired pressure, a moving window spanning 100 records was used. The window moved in the step of 20 records to scan the complete data.

3.4 Jet Impingement Tone Results and Discussion

3.4.1 Impingement Tone Characterization

Before demonstrating the use of high frequency acoustic excitation in suppressing the impingement tone, it was imperative to examine the characteristics of the impingement tone by itself. In order to characterize the salient features such as tonal frequency, tonal SPL, and overall SPL of the impingement tone, the main jet was run at a fully expanded Mach number $M_j = 0.86$, for stand-off distances (h/D_M) ranging from 1.6 to 3.3 in steps of 0.1. Measurements were made with and without the lift plate at each step.

Figure 3.5 shows a comparison between experimentally obtained impingement tone frequencies and theoretically predicted frequency variation curves—also known as staging curves. In the figure each continuous line represents a particular stage, based on following phase locking relation proposed by Powell [Powell, 1953].

$$\frac{1}{f} = \frac{1}{n + \Delta_n} \left[C_1 \frac{h}{u_j} + C_2 \frac{h}{c_\infty} \right] \quad (3.1)$$

Each stage corresponds to a different value of n . In the above expression, so as to get good fit between the experimental data and theoretical prediction, the convective velocity of the coherent structures is assumed to be 0.6 times the free jet velocity i.e. $C_1 = 1.66$. Acoustic waves are assumed to travel in the region exterior to the jet. Hence, C_2 was assumed to be 1. The phase shift (Δ_n) associated with the acoustic wave reflection from the ground plate was assumed to be zero. As shown in the Figure 3.5(a), in the absence of the lift plate, phase locking shows very little influence on the impingement tone frequency.

Except for the initial range of the stand-off distances, the impingement tone frequency remains more or less constant. The conjecture is that installing the lift plate strengthens the coupling between the shear layer and acoustic instabilities by increasing the amount of acoustic energy scattered from the nozzle region. Hence, as shown in the Figure 3.5(b), in the presence of the lift plate the experimentally obtained frequencies show a better match with theory.

Figure 3.6 shows the variation in the overall SPL and tonal SPL. Figures 3.6(a) and 3.6(b) correspond to the cases run without the lift plate and with the lift plate, respectively. In the absence of the lift plate, the mean overall SPL was found to be 143 dB. Whereas, the mean tonal SPL was found to be 138 dB. The lift plate was found to increase these values by 3 dB and 2 dB, respectively. The difference between the overall SPL and the tonal SPL indicates the strength of the tone in a sense that a small difference in these values indicates a strong tone. By this account, in both the cases, for small stand-off distances one can see that the tone is very weak. Due to the better agreement of the measured frequencies with the theoretical prediction and due to production of tones with higher acoustic level, which are better amenable to suppression, all the experiments from this point on were conducted with lift plate in place.

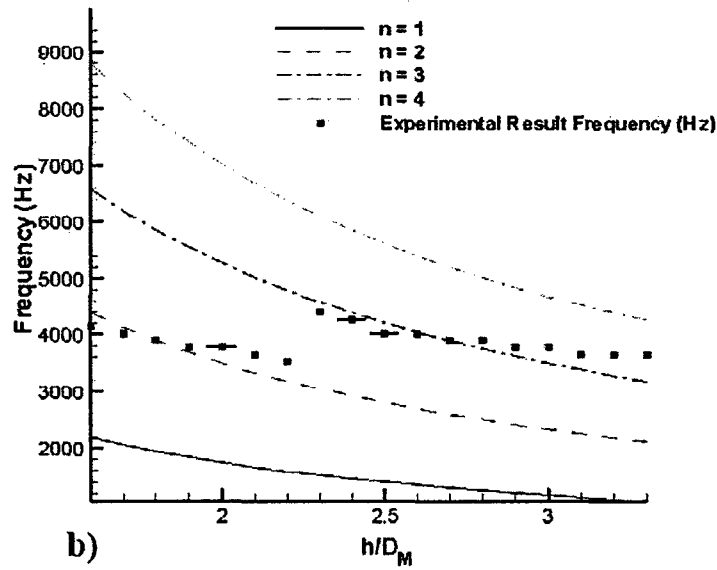
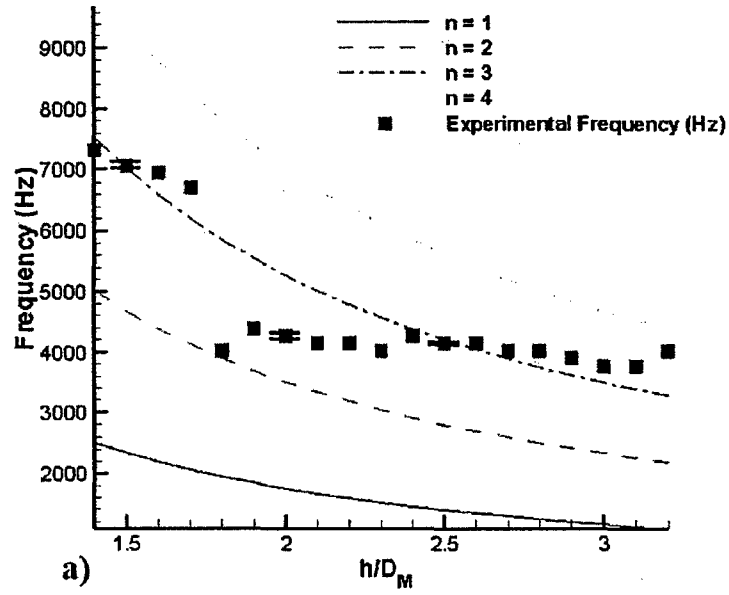


Figure 3.5: Impingement tone frequency staging: comparison of phase lock theory and experimental data a) without lift plate, b) with lift plate ($M_j = 0.86$, $C_1 = 1.66$, $D_M = 1.25''$). Presence of the lift plate improves the fit of the data with the theoretical prediction.

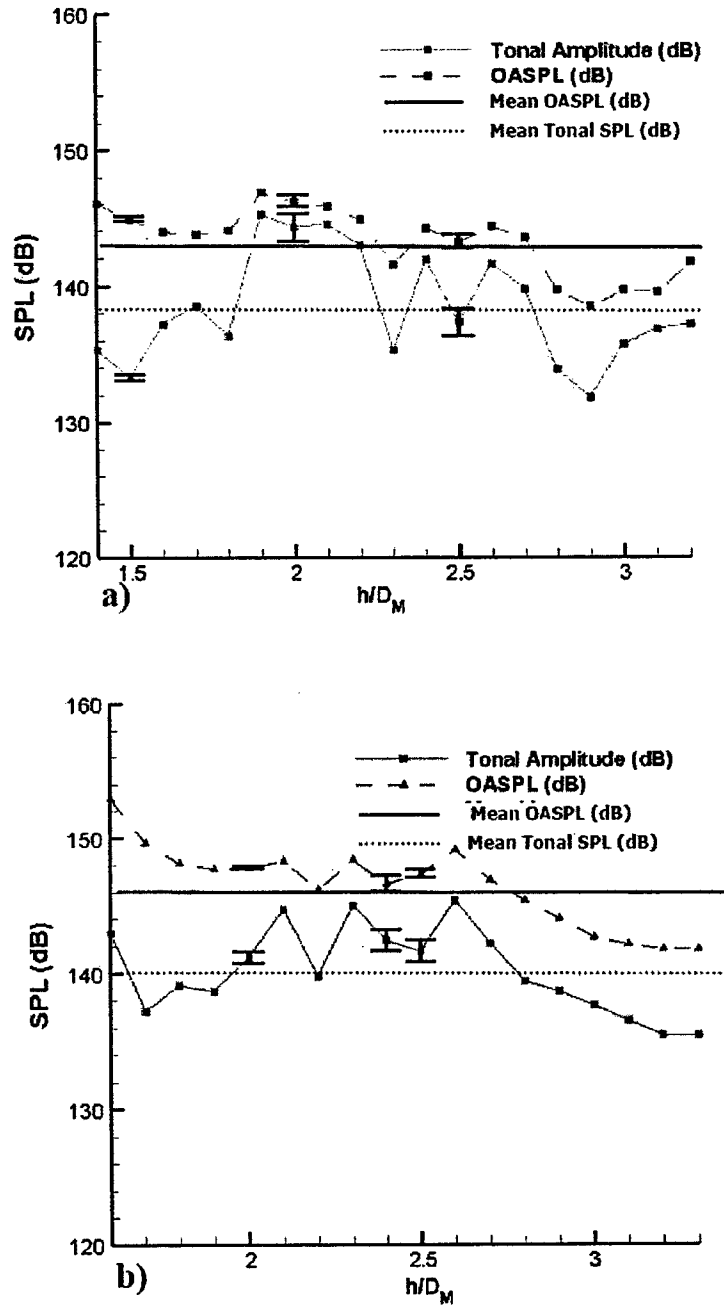


Figure 3.6: Impingement tone amplitude and overall SPL variation a) without lift plate, b) with lift plate ($M_j = 0.86$, $D_M = 1.25''$). Presence of the lift plate increases the mean overall SPL the mean tonal SPL of the impingement tone.

Though not similar in nature, discontinuities in frequency also occur if the main jet Mach number is varied keeping the stand-off distance constant as shown in Figure 3.7. In the case of Figure 3.7(a) the stand-off distance (h/D_M) was set to 2.4, for Figure 3.7(b) it was set to 3.2. For $h/D_M = 2.4$, the jet was run at various Mach numbers from 0.91 to 0.78. Whereas, for $h/D_M = 3.2$, the jet was run in the Mach number range 0.82 to 0.94. During the data acquisition, an attempt was made to narrow the intervals when there a frequency discontinuity occurred. In Figure 3.7(a) one can notice that, as the Mach number is reduced from 0.91, the impingement tone maintains a constant frequency of 3,296 Hz for a period. However, at Mach number around 0.86 the frequency suddenly jumps to 4,272 Hz. This frequency remains unchanged until 0.78 where again the tone jumps to a higher frequency mode. For the stand-off distance 3.2 (Figure 3.7(b)), except for a few data points, the frequency mode of the tone seems to be unaffected by the Mach number.

In both the plots some of the data points are circled. They represent the cases which are to be used as baseline cases for the impingement tone suppression. On the same plots are also shown the "resonant acoustic frequencies". The resonant acoustic frequency is a theoretically calculated full wavelength acoustic frequency based on the standoff distance between lift plate and ground plate. For the stand-off distance (h/D_M) 2.4 and 3.2 this frequency was 4,465 Hz and 3,349 Hz respectively. It will be shown later that it is the proximity of this resonant frequency with the actual impingement tone frequency that is responsible for easier suppression of certain impingement tone frequencies than the others.

Figure 3.8 shows the variation in the impingement tone amplitude and overall SPL for the aforementioned cases. Figure 3.8(a) pertains to the stand-off distance of 2.4, whereas Figure 3.8(b) pertains to that of 3.2. For the stand-off distance of 2.4, both the tonal SPL and overall SPL increase as the Mach number is increased. However, for the stand-off distance of 3.2 the trend is not very clear. There seems to be some optimum Mach number for which both the tonal SPL and overall SPL achieve the highest value.

3.4.2 Impingement Tone Suppression

The last section mentions the cases which were used as baseline impingement tone cases. These impingement tones were suppressed using PRTs. The PRTs were set to produce 10,000 Hz, 12,000 Hz, 14,000 Hz, and 17,500 Hz acoustic signals. The frequency being primarily a function of the PRT depth, this variation in the signal frequency was achieved by appropriate piston settings. So as to keep the variation in the frequency of different PRTs within a limit (less than 500 Hz), the depths of individual PRTs were manually fine tuned. The fine tuning of the PRT depth for 10,000 Hz was done at an NPR of 1.63 (24 psia), 12,000 Hz at an NPR of 2.04 (30 psia), 14,000 Hz at an NPR of 2.72 (40 psia) and 17,500 Hz was done at an NPR of 4.29 (63 psia). It is to be noted that, running the PRTs at pressures other than the ones used for their fine tuning marginally changes their frequency. Thus, the aforementioned frequencies are "nominal frequencies". An experiment was also conducted with the PRT at zero depth. This case did not produce any strong acoustic tones. It was included to examine the effect of pure fluidic excitation to the main jet.

Figure 3.9 shows the variation of the salient features of the acoustic signal produced by the PRT for different nominal frequency settings due to the change in stagnation pressure. Figure 3.9(a) shows variation in the frequency. Since the zero depth PRT did not produce any strong tone which could be tracked for its frequency change, this case was not included in the Figure 3.9(a). It can be seen that, except for the higher end nominal frequencies such as 17,500 Hz and 14,000 Hz, the variation in the frequency due to the change in the stagnation pressure is marginal. Figure 3.9(b) shows the variation in the PRT tonal SPL. As compared to the variation in nominal frequency, the variation in the tonal SPL is very large; of the order of 10 dB. For all the cases, the tonal SPL values steadily increase as the stagnation pressure is increased. However, after a certain level (approximately 135 dB) they seem to be saturated. For zero depth, the SPL values were considerably lower than the

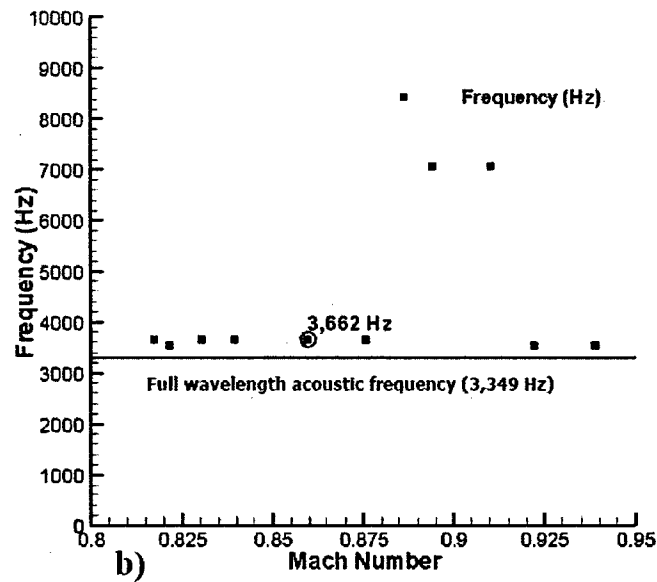
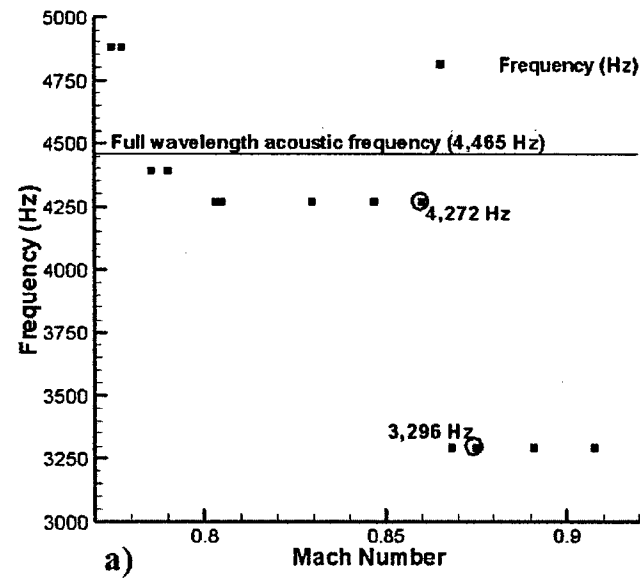


Figure 3.7: Variation in the frequency due to the change in Mach number (a) $h/D_M = 2.4$, (b) $h/D_M = 3.2$. The plots show the location of baseline impingement tone cases which were tested for the suppression and proximity of these tones with the corresponding resonant acoustic frequency (full wavelength acoustic frequency based on the stand-off distance between the lift plate and the ground plate).

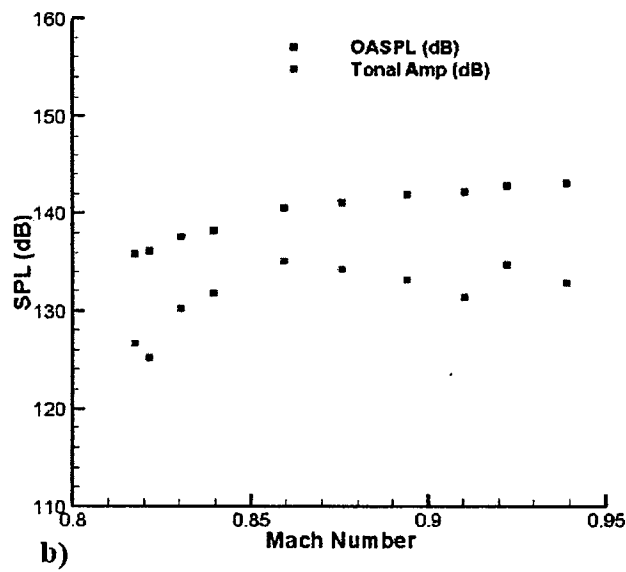
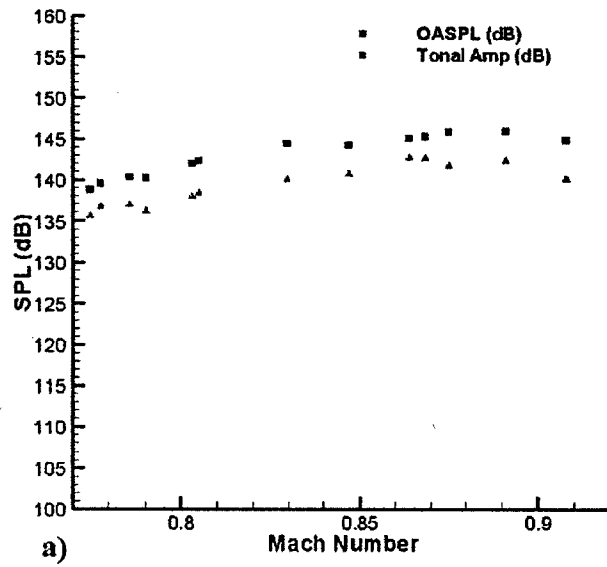


Figure 3.8: Impingement tone amplitude and overall SPL variation due to the change in Mach number. (a) $h/D_M = 2.4$, (b) $h/D_M = 3.2$. For $h/D_M = 3.2$ the impingement tone is weaker as compared to $h/D_M = 2.4$.

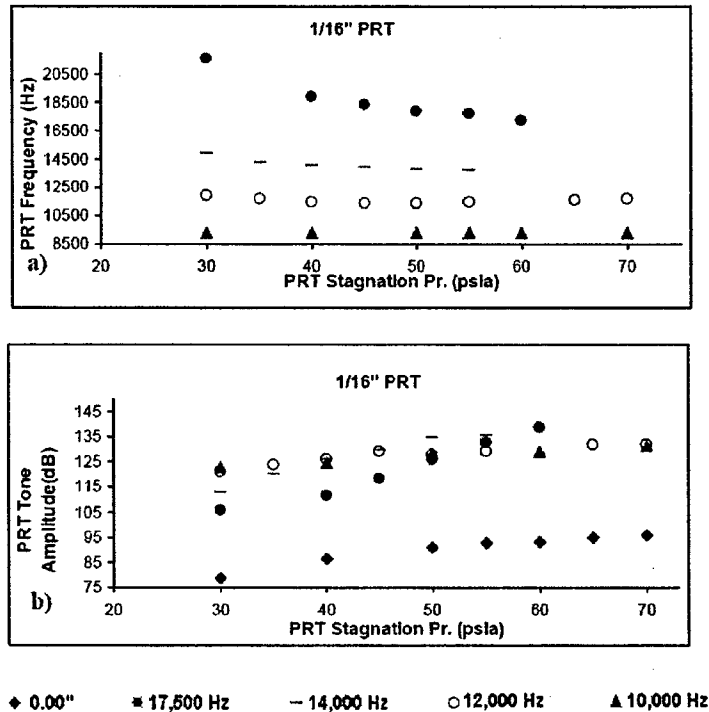


Figure 3.9: Salient features of the PRT for different nominal frequency settings. a) frequency, and b) tonal amplitude. Except for the 17,500 Hz the variation in the nominal frequency of the PRT due to the change in PRT stagnation pressure is marginal. However, variation in the SPL in all the cases is significant of the order of 10 dB.

other cases. Very low SPL values suggest that these values refer to the broadband peak—not a sharp spike characteristic of the acoustic tone.

To examine the effect of the high frequency acoustic excitation on the impingement tone, the main jet was operated in the presence of the activated PRTs. Figure 3.10 shows suppression in the impingement tone spike for different impingement tone and PRT settings. Here the suppression in the impingement tone spike was calculated by subtracting the SPL of the impingement tone when PRTs were activated from the SPL of the impingement tone when PRTs were turned off. Figure 3.10(a) refers to the 4,272 Hz impingement tone, whereas Figure 3.10(b) refers to the 3,296 Hz impingement tone. In both the cases the PRTs could suppress the impingement tone up to 25 dB depending upon the frequency and supply pressure of the PRT. In the case of 3,296 Hz impingement tone, to achieve 20dB suppression, the zero depth PRT had to operate at an NPR of 5.50. However, by introducing an acoustic tone and selecting an appropriate frequency the same suppression can be achieved at an NPR of 2.75. This observation is consistent with 4,272 Hz impingement tone also. The substantial reduction in the NPR and mass flow rate, almost of the order of 50%, confirms the fact that high frequency forcing is an effective element and far superior strategy, as compared to the oscillatory (broadband) mass injection, to suppress the impingement tone.

The suppression experiment involved a number of variables viz. frequency, tonal amplitude, mass

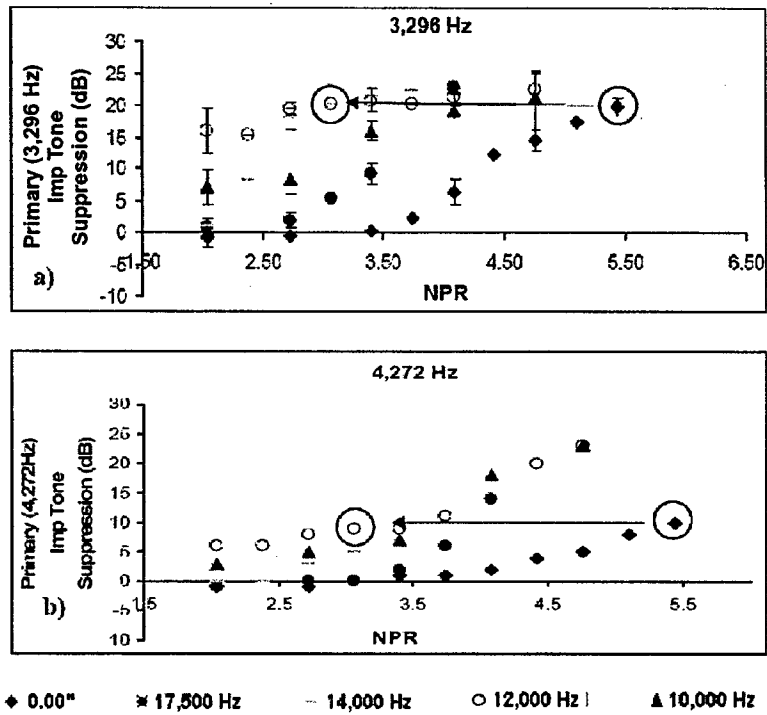


Figure 3.10: Primary impingement tone suppression. (a) 3,296 Hz ($M_j = 0.88$, $h/D_M = 2.4$), and (b) 4,272 Hz ($M_j = 0.86$, h/D_M). For same level of maximum suppression, selecting the acoustic tone of the appropriate frequency reduces the NPR and hence the mass flow rate by 50%. This proves the fact that high frequency forcing is an effective and far superior strategy, as compared to the oscillatory mass injection.

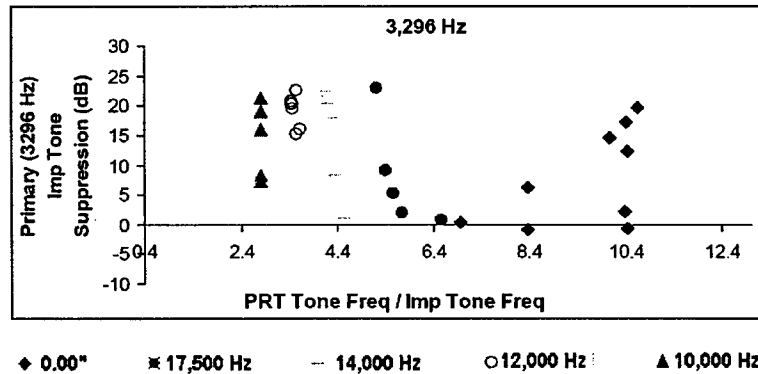


Figure 3.11: Primary impingement tone suppression against the parameter PRT tone frequency/impingement tone frequency ($M_j = 0.88$, $h/D_M = 2.4$). The deterioration in the collapse of the data suggests that frequency might not be the most important variable affecting suppression.

flow rate etc. of the actuation signal and the impingement tone itself. Though the data proved the effectiveness of high frequency forcing, it does not reveal the responsible variable(s) behind the suppression. A search has therefore been conducted for an appropriate scaling parameter which will collapse all the suppression data to a single line.

Some of the parameters considered in this study are: actuation signal frequency, actuation signal amplitude, rate of mass injection, frequency and amplitude of the impingement tone itself, its relation with the natural shedding frequency and feedback acoustic frequency. The PRT actuation signal frequency was the first parameter that was examined. Figure 3.11 shows the distribution of the data for the 3,296 Hz impingement tone case. From the graph it is apparent that this new parameter does not make the data collapse satisfactorily.

For the same pressure, the actuation signal amplitude varied with frequency as shown in Figure 3.9(a). Next, the PRT amplitude in decibels was tried as a new parameter. Figure 3.12 shows impingement tone suppression against the actuation signal amplitude, again for 3,296 Hz impingement tone case. These plots have interesting characteristics. Except for the zero depth setting, data from all the PRT settings collapse onto a single curve. Due to the absence of the acoustic tone, data pertaining to the zero depth setting remained distinct and separate from the other cases. The zero depth PRT achieves its suppression through the splashing of the oscillatory mass flow. This led us to include mass flow rate into the PRT amplitude as a parameter.

Figure 3.13 shows suppression against this newly formulated parameter i.e. "PRT mass flow rate \times PRT tone amplitude". For 3,296 Hz (Figure 3.13(a)), and also for 4,272 Hz (Figure 3.13(b)) impingement tones, this parameter shows the best collapse of the data. Any scatter present throws light on the optimum actuation signal frequency. This scatter is more apparent in the case of 3,296 Hz impingement tone. In this case, one can see that as the frequency of the tone increases from 10,000 Hz the suppression level and hence the effectiveness of the tone increases. In fact 12,000 Hz tone is the most effective. However, further increase in the PRT frequency results in the decrease of suppression level. In fact for 17,500 Hz it is almost same as that of the zero depth case.

The variation in the overall SPL is now discussed. Figure 3.14 shows variation of the overall SPL against the parameter "PRT mass flow rate \times PRT tone amplitude." For the cases run the maximum suppression noted was 12 dB. Turning the PRT on with increasing supply pressure invariably

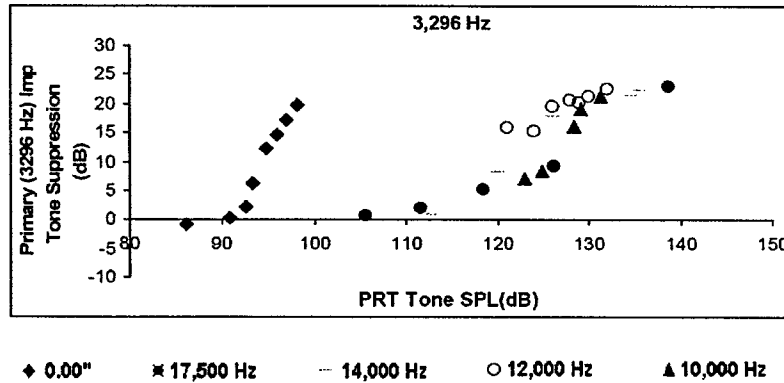


Figure 3.12: Primary impingement tone suppression against the parameter PRT tonal SPL ($M_j = 0.88$, $h/D_M = 2.4$). Tonal SPL proves to be a successful parameter for all the cases except for the no tone case. The zero depth PRT achieves its suppression through the splashing of the oscillatory mass flow. Isolation of the “no tone” PRT hints us mass flow to be one of the crucial variables behind the suppression.

Table 3.1: PNLT analysis for 4272 Hz impingement tone and 17,500 Hz PRT frequency setting

PRT NPR	Primary Tone Suppression (dB)	Overall SPL Suppression (dB)	PRT Amplitude (dB)	PNLT Suppression (dB)
3.74	6	6	132.93	8.01
4.08	14	6	138.77	11.99

increases the impingement tone spike suppression. However, in the process it also adds its own noise. Hence, at higher supply pressure to the PRTs the overall SPL suppression ceases to increase.

The overall SPL is a good measure of the total energy in the acoustic spectrum. However, it does not reflect the human annoyance level to the sound. The scale which measures the annoyance level of the sound, and the one which is widely used in the aircraft industry is Perceived Noise Level Corrected for the Tone (PNLT). As per this scale, the sound energy which falls into the bandwidth of 500 Hz to 5000 Hz is particularly annoying, whereas higher frequencies are less annoying. Turning the PRT on reduces the impingement tone spike SPL but at the cost of the addition of the PRT noise. This may result in the increase in the overall SPL. However, increase in the overall SPL does not necessarily mean increase in the PNL. Since one is cutting down the impingement tone SPL, which lies in the sensitive zone (i.e. 500 Hz to 5,000 Hz), and adding the PRT noise in the less sensitive high frequency range, the PNL value may still decrease. To support this argument, a comparison between the overall SPL suppression and the PNL suppression is made for 4,272 Hz impingement tone and 17,500 Hz PRT frequency setting for two supply pressures. Table 3.1 gives a summary of the analysis. At an NPR of 3.74 (55 psia) the PRTs with 17,500 setting cut down the impingement tone spike by 6 dB. Increasing the PRT supply pressure increases the spike suppression by 8 dB. However, suppression in the overall SPL remain the same i.e. 6 dB. The additional 5.84 dB contributed by the PRT tone should explain this unchanged overall SPL. However, this does not hold true for PNL suppression. For the reasons explained earlier the PNL suppression value increases even though the overall SPL value remains unchanged.

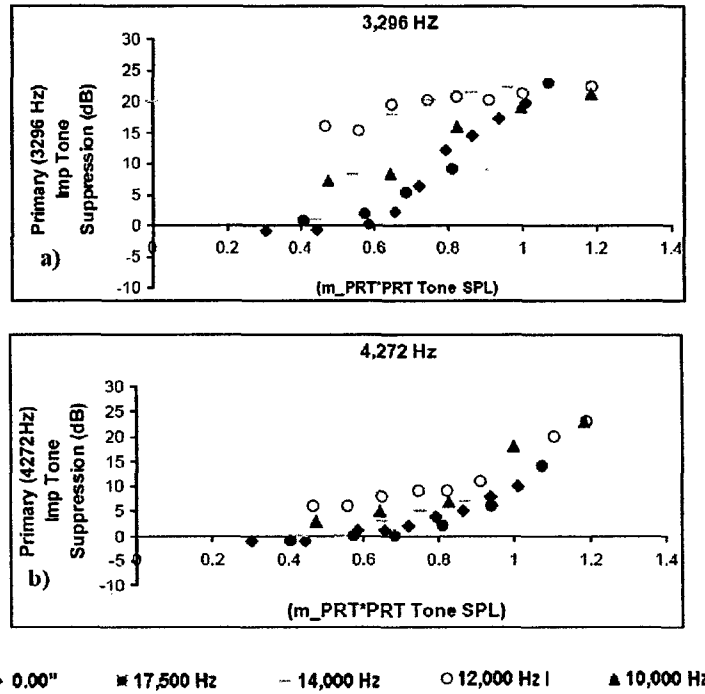


Figure 3.13: Primary impingement tone suppression against the parameter "PRT mass flow rate \times PRT tonal SPL". (a) 3296 Hz ($M_j = 0.88$, $h/D_M = 2.4$), and (b) 4272 Hz ($M_j = 0.86$, $h/D_M = 2.4$). The parameter "PRT mass flow rate \times PRT tonal SPL" proves to be successful for both the impingement tones. Good collapse suggests that, PRT mass flow rate and PRT tonal SPL are the most crucial variables which affect the suppression. The figure (especially (a)) also points out the optimum frequency for the suppression (i.e. 12,000 Hz).

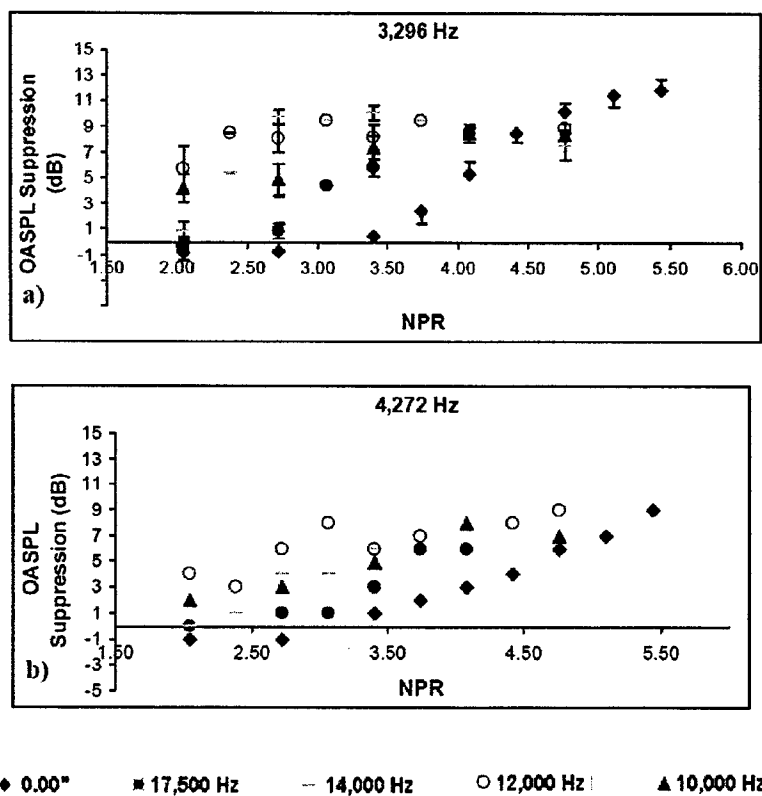


Figure 3.14: overall SPL suppression (a) 3,296 Hz ($M_j = 0.88$, $h/D_M = 2.4$), and (b) 4,272 Hz ($M_j = 0.86$, $h/D_M = 2.4$). As in the case of Figure 3.10, the present figure represents the suppression data in a raw form. As apparent from the figure, PRTs can achieve suppression up to and above 10 dB.

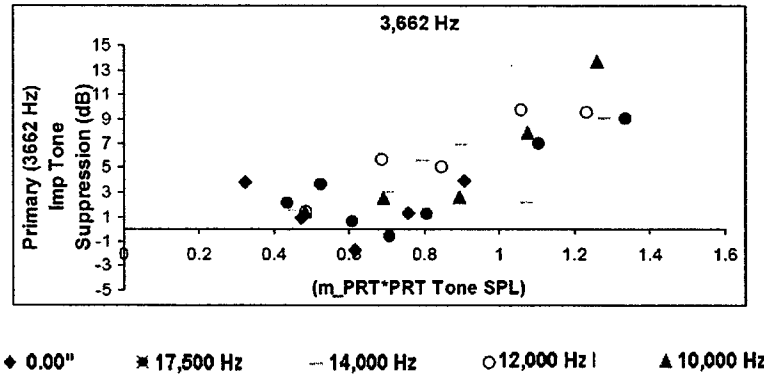


Figure 3.15: Primary impingement tone suppression ($M_j = 0.86$, $h/D_M = 3.2$). Comparison with Figure 3.13(a) and 3.13(b) shows that for 3,662 Hz and 4,272 Hz tones, suppression starts picking up late as compared to 3,296 Hz tone. Hence, 3,662 Hz and 4,272 Hz tones are difficult to suppress. Our conjecture is that the close proximity of these tones with the "resonant acoustic frequency" (Figure 3.7) is responsible their suppression.

3.4.3 Role of Resonant Acoustic Frequency in Impingement Tone Suppression

Referring to Figure 3.13 one can notice that, as compared to the 4,4272 Hz tone, the suppression of the 3,296 Hz impingement tone begins earlier at a "PRT mass flow rate \times PRT tone amplitude" of 0.6. This suggests that, the 3,296 Hz impingement tone is easier to suppress than the 4,272 Hz. Here, the difference between the two impingement tones is not just in the "values" of frequency, but also in the proximity of these values with the resonant acoustic frequency as mentioned in Figure 3.7. For both the impingement tones the resonant acoustic frequency was found to be 4,465 Hz. This suggests that for 4,272 Hz case impingement tone, there was a standing acoustic field between lift plate and ground plate. The conjecture is that the standing wave pattern is difficult to decouple from the shear layer instabilities. Hence, 4,272 Hz case is difficult to suppress.

To support the argument that it is not the increase in the frequency, but the aforementioned conjecture which is responsible for the difficulty in suppression, a new impingement tone frequency (3,662 Hz) at $h/D_M = 3.2$ was tested for the suppression. As mentioned earlier, for this case the resonant acoustic frequency was found to be 3,349 Hz. Close match between the impingement tone and resonant acoustic frequency suggests that 3,662 Hz tone would be difficult to suppress. Figure 3.15 shows suppression for this impingement tone. As expected, the suppression is more difficult as in the case of the 4,272 Hz tone. This fact strengthens the argument that it is not the frequency alone, but the relationship of the impingement tone with the full wavelength standing acoustic frequency which comes into the picture for impingement tone suppression. In this case PRTs can suppress the impingement tone spike by not more than 14 dB.

The moderate (14 dB) maximum suppression noticed for this case can be attributed to the fact that for the 3662 Hz the impingement tone, the spike itself was quite weak.

3.4.4 Augmentation of the Secondary Tone

Figure 3.16 shows the 4272 Hz and the 3,296 Hz impingement tone spectra in the absence and also in the presence of the PRT signal. One can notice that PRTs can suppress not only the impingement tone spike, but also the broadband noise. Comparison of Figure 3.16(a) and 3.16(b) reveals distinct nature of the 4272 Hz and the 3296 Hz impingement tone. The 4272 Hz impingement tone, the one which is very close to the resonant acoustic frequency, is dominated by first few harmonics. Whereas, 3296 Hz spectrum contains only first harmonic and sub-harmonic peaks. Even the PRT suppressed spectra of these two tones show distinctive result. In the case of 3296 Hz spectrum, turning on the PRTs gives rise to an additional spike (referred to as secondary tone) at 4,272 Hz. The degree of the augmentation of this secondary tone depends on the particular PRT setting. As one can see in the Figure 3.17 for certain PRT settings it could grow by 10 dB.

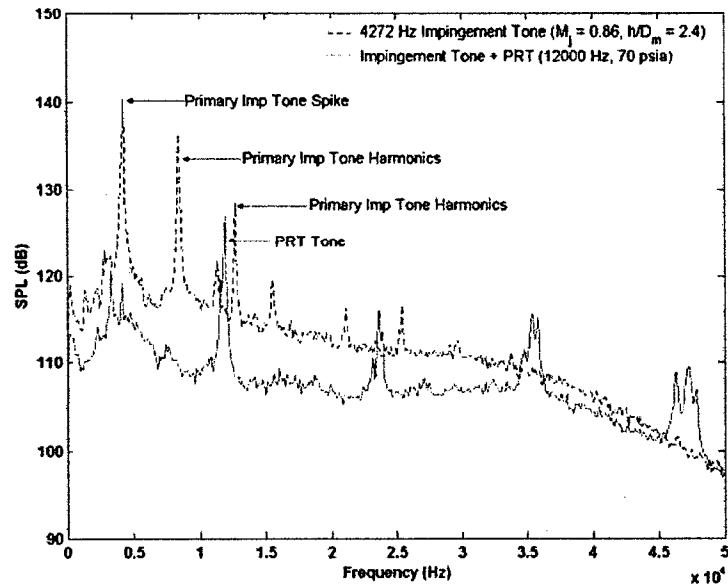
3.5 Conclusions Regarding Suppression of Jet Impingement Tones Using PRTs

In this chapter the suppression of primary jet impingement tones using PRT actuators was explored. The work began by characterizing impingement tone staging behavior for a fixed Mach number and various stand-off distances. Next, PRTs located circumferentially near the main nozzle exit were used to introduce high frequency excitation in the jet's shear layer. The tonal, overall SPL, and PNLTL suppression levels were examined for various actuation conditions (frequency, amplitude, and mass flow rate) at different main jet impingement tone frequencies.

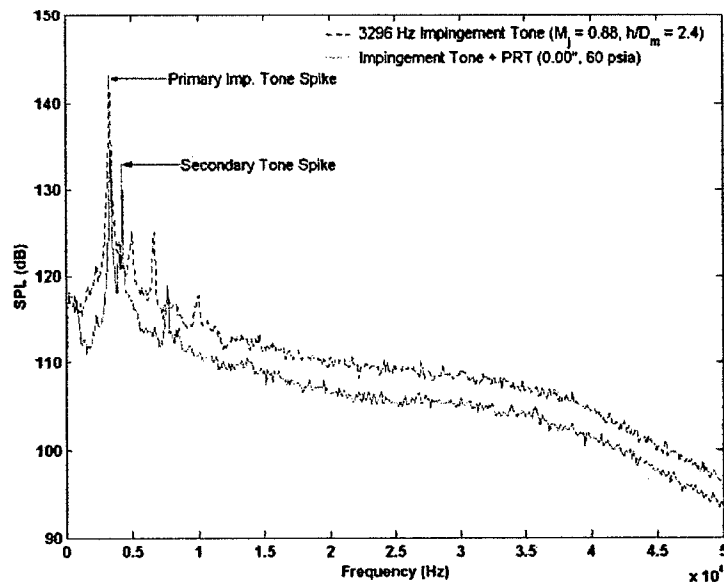
The following important results emerged from this study:

1. The PRT actuator was capable of suppressing tonal, overall SPL and PNLTL levels of the impingement jet from the main nozzle. A combination of parameters that could reconcile the suppression characteristics at various PRT excitation frequencies was deduced.
2. It was observed that the impingement tone could be suppressed either by a strongly resonating PRT or a zero depth PRT (with no dominant tone), both of which were sources of unsteady mass addition. However, the mass flow requirements were substantially lower for the former.
3. It was found that impingement tones that matched the full wavelength acoustic frequency ($h = \lambda$) were more difficult to suppress than the mismatched frequencies

It is hoped that results from this work will stimulate further research leading to further active flow control applications for the aircraft.



a)



b)

Figure 3.16: Primary impingement tone spectrum. (a) 4,272 Hz ($M_j = 0.86$, $h/D_M = 2.4$), and (b) 3,296 Hz ($M_j = 0.88$, $h/D_M = 2.4$). The nature of the suppressed as well as unsuppressed spectra of 4,272 and 3,296 Hz impingement tone is different. When unsuppressed, the 4,272 Hz spectra shows strong harmonic content. The 3,296 Hz spectrum does not contain any strong harmonic, but it shows weak harmonic and sub-harmonic spike. When suppressed, the 3,296 Hz tone shows an additional spike (referred to as a "secondary tone") at 4,272 Hz.

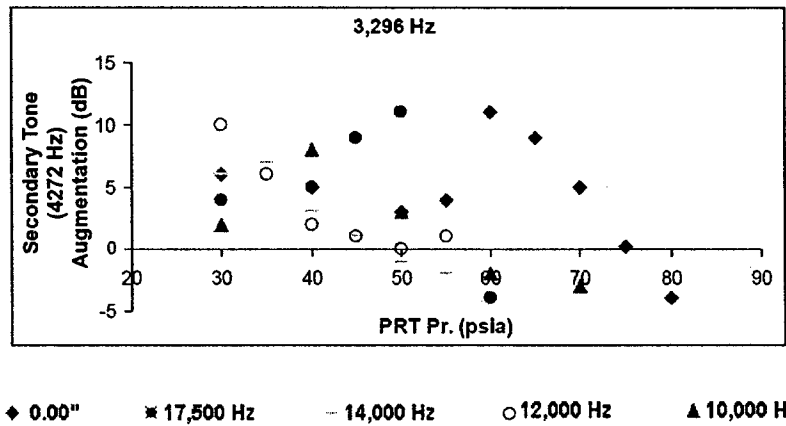


Figure 3.17: Secondary impingement tone augmentation ($M_j = 0.88$, $h/D_M = 2.4$)

Chapter 4

Resonance Characteristics and Actuation Signal Directivity

4.1 Overview

The Powered Resonance Tube (PRT) actuator and its variants are new developments in Active Flow Control (AFC) technology. The PRT is attractive because it has no moving parts and can produce acoustic tones that have amplitude greater than 150 dB over a large frequency bandwidth. The first part of this chapter deals with the resonance characteristics of the PRT as a function of the operating parameters such as jet-to-tube spacing (s), tube depth (l), and Nozzle Pressure Ratio (NPR). It was found that: (i). at low NPR (3.33), the PRT resonates at discrete combinations of spacing and depth. (ii). using theoretical estimates for predicting shock cell lengths, one could observe a correlation between the theoretical prediction for shock cell length and the spacing at which the PRT resonates. (iii). at high NPR (4.29), for a fixed depth, the PRT resonates at virtually all spacings. (iv). the frequency at which the PRT resonates remains approximately constant, regardless of the spacing between the supply jet and the opening of the resonance tube. The second part of the study focused on examining the directivity of the acoustic radiation from the PRT—significant for developing orientation strategies of the PRT with respect to flow control applications. The directivity of the fundamental PRT tone and that of its harmonics were studied for a variety of resonance frequencies, both separately as well as cumulatively. It was found that the fundamental part of the actuation signal radiated predominantly in the downstream direction of the jet for low resonance frequencies. As the resonance frequency was increased from 3 kHz to 12 kHz, the directivity changed from downstream of the jet to vertically upwards, and finally upstream of the jet at the highest frequencies.

4.2 Introduction to the Resonance Tube Characteristics and Directivity Study

The PRT phenomenon was first discovered by J. Hartmann in 1918 during the course of experimental investigations of axial stagnation pressure distribution in a supersonic jet [Hartmann and Troll, 1922] and later, in an effort to improve the resonating characteristics of the actuator, [Savoy, 1950] and [Brocher et al., 1970] experimented with several additional features, commonly known as destabilizing trips viz. stems, and reflective surfaces to name a few. [Cain et al., 2004] made an effort to couple the PRT resonator with the Helmholtz resonator, to reduce the frequency of the PRT tone. The

recent work of [Raman et al., 2004a], [Raman and Cain, 2002], [Kastner and Samimy, 2002], and [Murugappan and Gutmark, 2002] focuses on developing commercially viable high bandwidth actuators for high frequency Active Flow Control (AFC). Several researchers have demonstrated the use of high frequency actuators in practical applications such as jet impingement tone and cavity tone suppression (see [Murugappan and Gutmark, 2003], [Kastner et al., 2004], [Raman and Kibens, 2001], [Raman et al., 2004b], and [Sarpotdar et al., 2005c]).

As mentioned earlier for a PRT to resonate, without any instability trips, one of the prerequisites is that, jet issuing from the nozzle must be in an under-expanded condition. When the jet is under-expanded, the pressure at the exit of the nozzle from which it issues is higher than the ambient pressure. Here, the subsequent expansion of the jet takes place through an alternating train of expansion fans and oblique shock waves. At low pressures, this train is characterized by its diamond shape. However, at NPRs above 3.93, the oblique shock gets truncated and gives rise to an additional disk shock. This shock cell structure is referred to as barrel shock.

The work of [Raman et al., 2004a] studied SPL plots of the PRT with respect to the parameters such as depth, spacing, and pressure. These SPL plots highlighted the fact that the PRT could resonate only at certain discrete spacings. However, in this same work, the nozzle pressure ratio was limited to 3.45 (28.96×10^4 Pa (42 psig) supply line pressure). Hence, it could not capture the response of the PRT when the jet had a barrel shock cell structure.

Though the exact mechanism by which the PRT produces tones is not clear, it can be said that shock cell structure, static pressure gradient [Smith and Powell, 1964], and local Mach number just upstream of the resonator tube inlet [Sarohia and Lloyd, 1979] are some of the governing parameters which determine whether a PRT can resonate at a particular spacing. The motivation behind the study of the PRT resonance characteristics reported in this chapter is to shed some light on the response of the PRT in the context of shock cell structure, and also to see if there is any distinctive change when shock cell structure changes its shape from diamond to barrel.

[Khanafseh, 2002] conducted a preliminary survey of the actuation signal directivity. However, it was inconclusive due to a few shortcomings, viz., the work used a fixed low-pass filter setting (37.5 kHz) which made the signals non-uniform in their harmonic content. It turned out that one could ascribe the directivity change (due to the change in the frequency) in the signal to this non uniform harmonic content. The analysis was restricted to a few actuation signal frequencies (i.e., 3 kHz, 5 kHz, 9 kHz). Moreover, the work also did not give any special treatment to the harmonics of the signal. In the present work an attempt has been made to isolate various harmonics in order to document their individual directivity. It would be interesting to study how the actuation signal changes its directivity behavior when harmonics are included or excluded. e.g., one must consider the possibility that the directivity of the 12 kHz signal will be different from that of the 12 kHz signal which is a second harmonic of 6kHz signal.

4.3 Experimental Methodology

Figure 4.1 (Figure 1.1 repeated for convenience) shows the schematic of a single powered resonance tube. It consists of 6.35 mm (1/4") diameter (D) nozzle with a countersink at its exit. The half angle of the countersink is 41° , whereas the depth is 0.794 mm (1/32"). The countersink is necessary for the production of high amplitude oscillations. The exit of the nozzle faces the open end of the closed-open cylindrical resonance tube (whose diameter, $d = D$). The piston remained fixed while the resonance tube slid over it to change the tube depth. The distance between the jet and the resonator tube is referred to as the "integration slot width" or "spacing" (s). The depth of the resonator tube is referred to as "depth" (l).

For the extended parameter study, the PRT was run at several static pressures ranging from 19.30×10^4 to 39.99×10^4 Pa (28 to 58 psig) in the increments of 1.379×10^4 Pa (2 psig). This corresponds

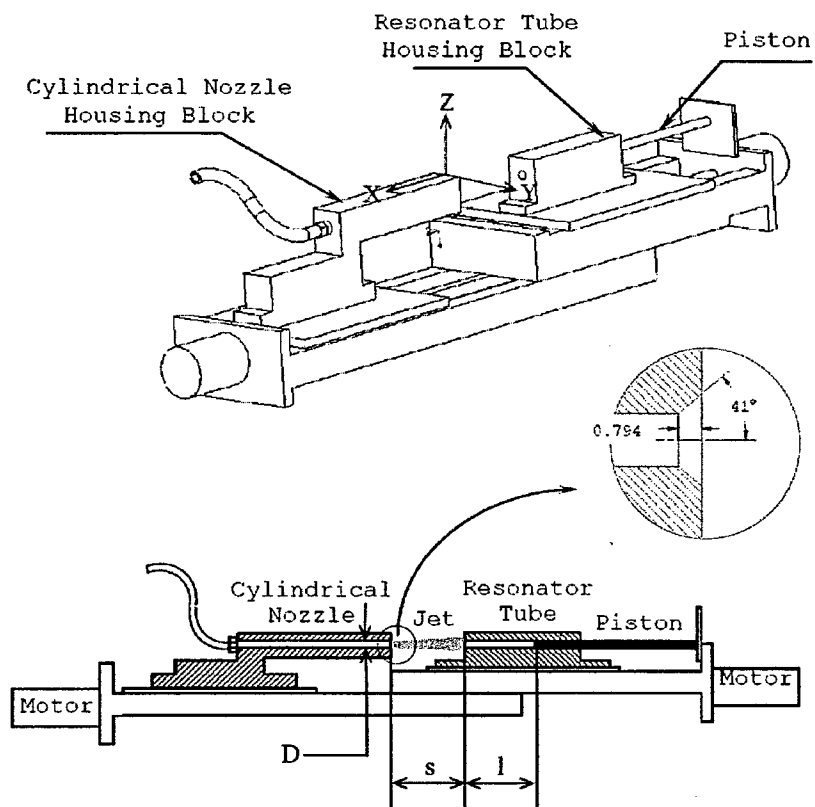


Figure 4.1: Schematic diagram of Powered Resonance Tube (PRT) experimental set-up

to NPR range of 2.62 to 4.41 (see [Khanafseh, 2002] for the relationship between the static pressure and the NPR values; taking into account the pressure losses- this issue was also discussed in Chapter 2). The corresponding mass flow range is 4.93 g/s to 8.30 g/s. At each pressure, the amplitude of the dominant frequency was recorded using a B&K microphone (Model 4939), placed flush with the jet exit, for different combinations of spacing and depth. The spacing was varied from 2.54 mm (0.1") to 37.47 mm (1.475") in the steps of 3.18 mm (0.125") and depth was varied from 0 to 22.86 mm (0" to 0.9") in steps of 2.54 mm (0.1"). This gave us an SPL map of the PRT for the parameters of pressure, depth, and spacing discussed in the next section.

When the PRT is set to produce an actuation signal of a certain frequency, along with the fundamental frequency, f , it also produces harmonics i.e., $2f$, $3f$, $4f$, etc. As the number of the harmonic increases its strength decreases. For practical purposes the third and the subsequent harmonics are found to be weak compared to the fundamental. Hence, in the frequency directivity study is limited to the second harmonic along with the fundamental and first harmonic. To study the directivity of the actuator signal and to distinguish the effect of filtering, phase averaged measurements were performed on signals ranging from 3 to 12 kHz. In each case a reference signal was obtained through a microphone (B&K 4939 microphone with 2670 preamplifier), placed flushed with the PRT exit. It was then passed through an analog Bessel filter (Ithaco 4212) with appropriate filter settings to get a sinusoidal wave. The measurement signal for the phase averaging was acquired using a Kulite pressure transducer at several points on the measurement plane with the help of a traverse mechanism. This signal was also then band-passed through different filter settings to separate a particular harmonic or a set of harmonics for the present study.

A filtering criterion that would keep the harmonic content in the band-passed Kulite signal constant irrespective of the actuation frequency was necessary. Initially, a constant-percent-bandwidth rule, i.e., $0.8 (n \times f)$ to $1.2 (n \times f)$ was attempted. However, it was found to include higher harmonics at higher frequencies, e.g., for $n = 5$, $f = 4$ kHz, the resulting low-pass setting is 24 kHz, which, incidentally is the next higher harmonic corresponding to $n = 6$. To avoid this situation the lower frequency was chosen to be $(n - 0.2)f$, and the higher frequency of the band was $(n + 0.2)f$. This rule is consistent in the harmonic content of the filtered signal.

The spatial grid resolution for the phase averaging measurements is based on 0.15λ (i.e., 6.67 points per acoustic wavelength). The spatial extent of the phase averaging measurement plane was chosen such that it can accommodate approximately four wavelengths in the y -direction and two wavelengths in the z -direction. Here, the origin of the axis is situated at $1/2"$ (12.7 mm) above the center of the nozzle exit. This happens to be the mid-point of the front edge of the PRT nozzle housing block as shown in Figure 4.1. As can be seen in Figure 4.7, for the 4 kHz case the spatial extent was kept constant for all the cases. However the same approach could not be used with 3 kHz case (Figure 4.8) since increasing the resolution to capture the harmonics without reducing spatial extent required excessive computer memory. The filter settings, grid resolution and spatial extent for the current experiments are summarized in Table 4.1.

4.4 Results and Discussion

4.4.1 Resonance Characteristics of the PRT

Figure 4.2 shows SPL maps of the PRT at various NPRs. Also superimposed on these maps are schematics of diamond shock cell and barrel shock cell structure. It is to be noted that internal details of these structures (e.g., position of the conical shock or Mach disk) are not drawn to the scale. The thick vertical lines in the SPL maps indicate shock cell termination distance (x_{shock}). Here the distance between the two lines is equivalent to the shock cell length (L_{shock}) calculated

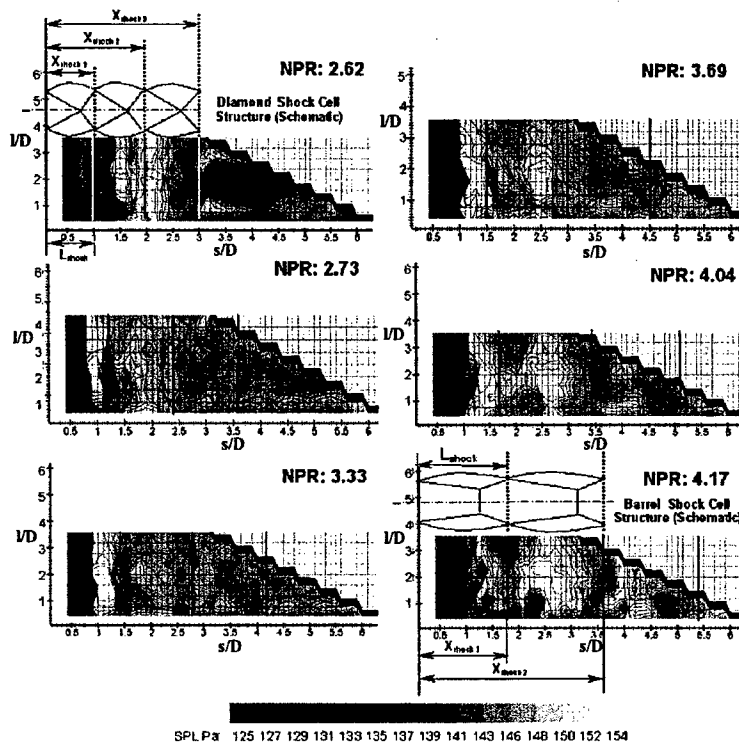


Figure 4.2: SPL map of the PRT at different Nozzle Pressure Ratios (NPRs). The white islands denote the combinations of depth and spacing at which PRT resonates—also referred to as active spacing. The thick lines show shock cell termination distance as per Tam's model [Tam, 1995], thus facilitates a comparison between active spacing and theoretical shock cell length.

Table 4.1: Measurement parameters used in the PRT signal directivity study.

Freq.	Harmonic	High Pass Filter (Hz)		Low Pass Filter (Hz)		Grid Resolution (no. points / λ)		Grid Extent (Spatial Length / λ_n)	
		Actual	Theory	Actual	Theory	X	Z	X	Z
3 kHz	f	2500	2400	3150	3600	6.487	6.487	3.69	1.84
	$2f$	5000	5400	6300	6600	7.568	7.568	3.17	1.58
	$3f$	8000	8400	10,000	9600	7.568	7.568	3.17	1.58
	$f + 2f$	2500	2400	6300	6600	7.568	7.568	6.73	3.83
	$f + 2f + 3f$	2500	2400	10,000	9600	7.568	7.568	10.17	5.54
4 kHz	f	3150	3200	5000	4800	6.812	7.568	3.52	1.58
	$2f$	6300	7200	10,000	8800	5.676	7.568	7.04	2.64
	$3f$	10,000	11,200	12,500	12,800	5.676	6.182	10.57	4.40
	$f + 2f$	3150	3200	10,000	8800	5.676	5.676	7.04	3.52
	$f + 2f + 3f$	3150	3200	12,500	12,800	5.676	5.676	10.57	5.28
6 kHz	f	5000	4800	8000	7200	7.567	7.567	2.17	1.58
8 kHz	f	6300	6400	10,000	9600	5.673	5.673	4.2	2.11
9 kHz	f	8000	7200	10,000	10,800	7.57	7.57	3.17	1.58
12 kHz	f	10,000	9600	12,500	14,400	5.67	5.67	7.40	3.70

using the expression proposed by [Tam, 1995]:

$$L_{shock} = 3.14 \frac{D\sqrt{M^2 - 1}}{2.405} \quad (4.1)$$

One can see that the PRT has amplitude peaks (indicated by white islands) only at certain combinations of spacing and depth. These discrete spacings at which the PRT resonates to produce the tone will henceforth be referred to as “active spacings.” As mentioned earlier, the functioning of the PRT is closely associated with the shock cell structure. In Figure 4.2 one can see that location of the active spacing and the shock cell termination distance increases as the NPR increases.

Figure 4.3 shows a comparison of the active spacing and the shock cell termination distance for the first, second, and third shock cells. It can be seen that increase in the NPR increases both the active spacing and also the shock cell termination distance. It is interesting to note that for the first shock the active spacing lies very close to the shock cell termination distance x_{shock1} . However, for the subsequent shock cells (i.e., second and third) the difference between the active spacing and the shock cell termination distance seems to increase; although the trend is preserved. The reason might be due to the inaccuracies involved in the shock cell model that has been used for the calculation; which assumes a semi-infinite array of shock cells, all of equal strength and length. In reality the shock cells farther away from the nozzle are weaker and of shorter length than the ones nearer to the nozzle exit.

When PRT resonates, it resonates at its fundamental mode. Here the nominal frequency of the tone corresponds to the quarter wavelength of the resonator tube.¹ However, when it is not resonating the sound emanating from it is dominated by higher harmonics. Figure 4.4 shows variation in the PRT tone frequency with spacing, for a fixed depth ($l/D = 0.2$) at a low (3.33 NPR) and high (4.29 NPR) NPR. Here to determine whether the PRT resonates at a particular spacing (s/D),

¹It is to be noted that the actual tonal frequency might be off from the quarter wavelength prediction; especially at shallow depths and high NPR, i.e. NPR above 4. At shallow depths, it is the acoustic coupling between the mass of the fluid within the resonance tube and the integration slot [Kerschen, 2001]; whereas at high NPR, it is the screeching and non-linear effects which are responsible for this deviation [Kerschen et al., 2004].

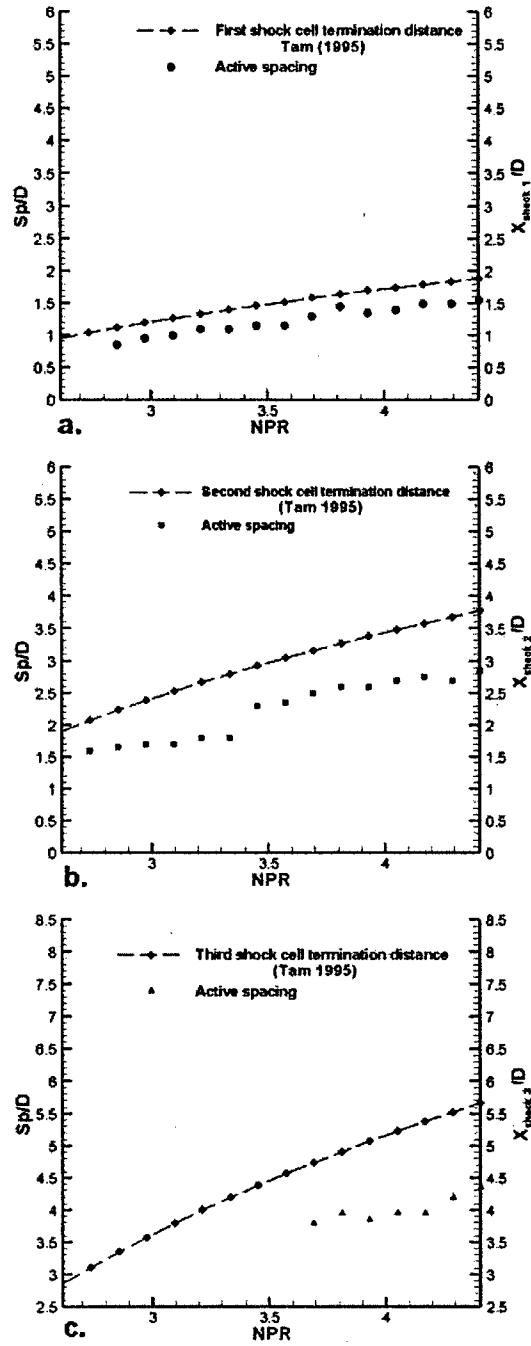


Figure 4.3: Comparison of the PRT Active spacing (s/D)—the spacing at which the PRT resonates—and the shock cell termination distance (x_{shock}/D) (PRT resonator tube depth (l/D) = 0.2). (a) first shock cell (b) second shock cell (c) third shock cell .

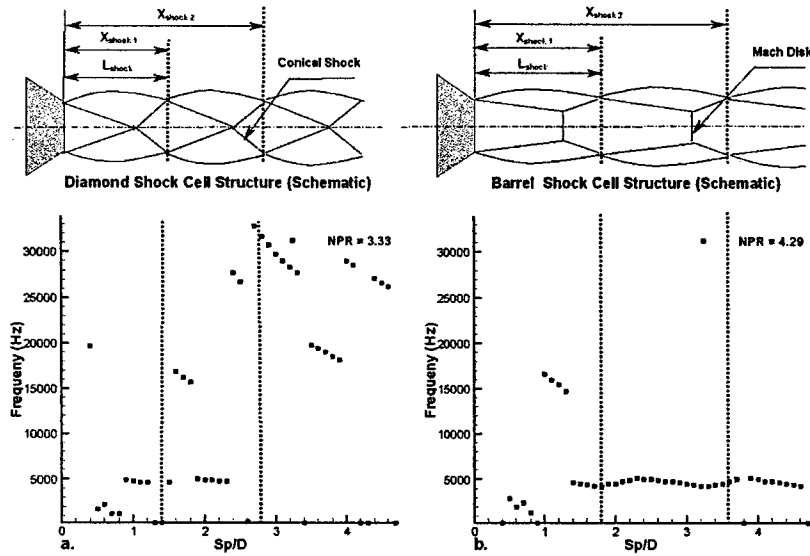


Figure 4.4: Influence of the Nozzle Pressure Ratio (NPR) on the active spacing (s/D)—the spacing at which the PRT resonates—at depth (l/D) = 0.2. (a) NPR = 3.33, i.e., NPR below 4, when the jet shows diamond shock cell structure (b) NPR = 4.29, i.e., NPR above 4, when the jet shows barrel shock cell structure.

one needs to check its tonal frequency. If the frequency matches the fundamental mode frequency (nominal value of 5000 Hz) of the PRT, that spacing can be considered as active spacing. With that in mind Figure 4.4(a) suggests that, at lower NPR (below 4, when the jet shows diamond shock cell structure), the PRT resonates only at certain discrete spacings. However, at higher NPRs (Figure 4.4(b)) the fundamental frequency tone can be seen to persist, once the PRT starts resonating. This suggests that, at higher NPR (above 4, when the jet shows barrel shock cell structure) there does not exist any preferred active spacing. For high NPRs, once the tube starts resonating, its tendency is to produce a tone that persists almost till the end of the second shock cell.

The next set of graphs is constructed to see whether the relation of the frequency with respect to the depth changes as one takes the PRT to its next active spacing. Figure 4.5 shows the plots of the PRT resonance frequency with respect to the depth for different active spacings and at different NPRs. It can be seen that irrespective of the active spacing, the relation between frequency and depth remains the same, i.e., it more or less follows the quarter wavelength theory. One can also see that, especially at higher NPRs, for the same depth and NPR the subsequent spacings give slightly higher values of frequency, e.g., for the second active spacing there is approximately a 2.5% to 10% increase in the frequency.

4.4.2 Actuation signal Directivity

The present work also studies propagation of 3 kHz, 4 kHz, 6 kHz, 8 kHz, 12 kHz actuator signal. In all the cases the measurement signal was filtered using appropriate band-pass limits so that one could see how the individual harmonic and/or combination of harmonics propagate. Figure 4.6 shows snap-shots of the 4 kHz actuator signal bandpassed to include its fundamental along with its first and second harmonic, i.e., 4 kHz ($f + 2f + 3f$). Here, each sub-figure is a phase averaged

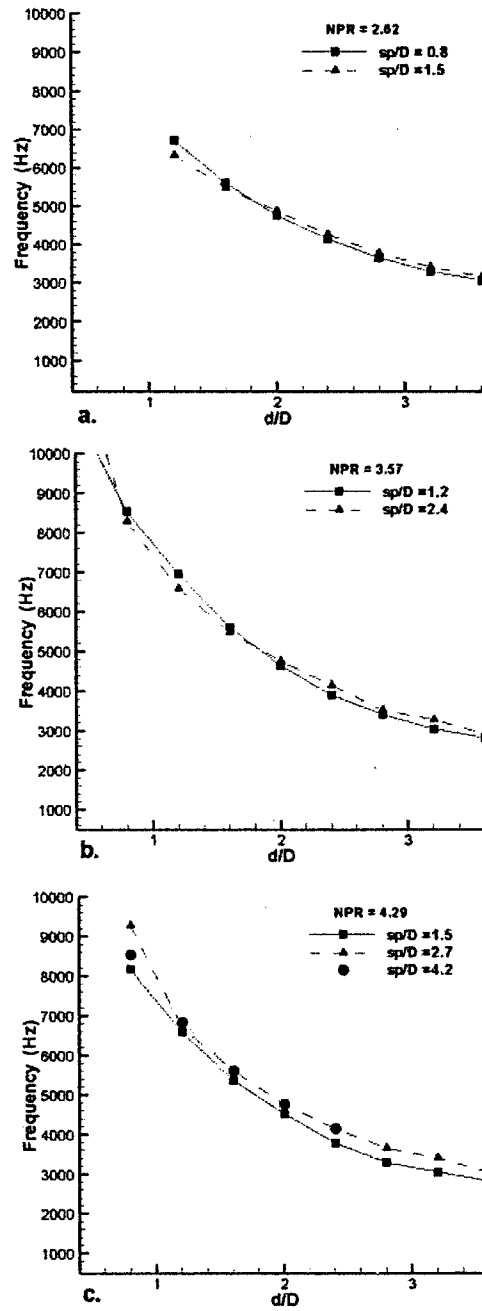


Figure 4.5: Influence of the PRT spacing (s/D) on the its resonance frequency. a. NPR = 2.62 b. NPR = 3.57 c. NPR = 4.29. For a particular depth (l/D), resonant frequency remains unaltered due to the change in spacing (s/D).

snapshot of the acoustic field at a phase interval of 30° . The set of 12 sub-figures represent one acoustic cycle. With the help of grey scale color code one can identify the acoustic pressure at a particular phase angle of the acoustic time cycle. To find out the propagation direction of the signal, these snapshots were run in a continuous animation. After repeatedly watching these animations, strong acoustic lobes (the dark black or white regions enclosed by dotted rectangles) emanating from the space between the PRT nozzle and resonator tube (integration slot) were identified. Then these lobes, were tracked through the subsequent frames to identify their propagation direction. For instance for 4 kHz ($f + 2f + 3f$) signal, the acoustic field was dominated by two lobes, viz., a lobe traveling in positive x -direction and a lobe traveling in a diagonal direction. The propagation of these lobes is also apparent if one studies the changing pattern of the acoustic field in Figure 4.6. Based on this qualitative observation, signal directivity vector is defined to indicate the propagation direction of an individual lobe.

Figure 4.7 summarizes propagation of an individual and/or combination of harmonics for 4 kHz actuator signal. Each figure corresponds to a specific combination of harmonics considered for the analysis. For example, Figure 4.7(a) represents phase-averaged map of 4 kHz fundamental frequency actuation signal. The first harmonic of 4 kHz is shown in the Fig. 4.7(b). Each figure is accompanied by vectors showing the propagation direction of the prominent lobes; enclosed by dotted rectangles.

In Figure 4.7 one can notice that, the fundamental component (f) of the actuation signal is propagating downstream in the form of two lobes. One of them is propagating parallel to the positive x direction, while the other is traveling diagonally in an upstream direction. The directivity of the first ($2f$) as well as second harmonic ($3f$) is also predominantly downstream. Actuation signal ($f + 2f$) and ($f + 2f + 3f$) also showed predominant downstream directivity. For ($f + 2f$) and ($f + 2f + 3f$) cases one can see predominantly downstream directivity accompanied by a vertical traveling lobe as in the case of fundamental.

In Figure 4.8, the directivity of the fundamental part of the actuator signals at different frequencies is compared. One can clearly notice that actuator signal directivity changes as the frequency is changed. For 3 kHz the directivity is predominantly downstream (parallel to the x -axis). The directivity is also predominantly downstream for 4 kHz, accompanied by a lobe traveling in an upstream diagonal direction. For 6 and 8 kHz the predominant directivity is still downstream but it is at an angle with the x -axis. For the 9 kHz case the directivity is vertical. On the other hand for 12 kHz there exists a lobe which also travels in upstream direction. Thus it can be said that, for low frequency signals, the directivity is downstream. As the frequency increases the directivity tends toward the vertical. Finally, at very high frequencies, the actuation signal propagates upstream.

According to the inverse square law one would expect the RMS value of the signal to drop monotonically as the actuation signal propagates. However, in certain cases, instead of a continuous drop, one can see that there is a drop followed by rise in the RMS pressure level. Figure 4.9 shows a set of such p_{rms} plots for the 4 kHz actuator signal. Each plot represents a specific set of band-passed harmonics as explained in the caption. One can easily verify that maximum p_{rms} regions overlap with the directivity vectors in the corresponding phase averaged snapshots. Thus, these plots further strengthen the findings regarding signal directivity.

Figure 4.10 shows a plot of p_{rms} values at different locations for 3 kHz fundamental frequency. The data was taken at the height $z/D = 2.8$. The fluctuating nature of the p_{rms} value validates the previous observation of fluctuating lobes. The graph also shows error bars. One can see the errors in the SPL is less than 1% at all the locations except $y/D = 5.6$, where it is almost 50%. This location is probably in the way of jet exit flow spilling over the nozzle block. Hence one might suspect hydrodynamic fluctuations caused by the jet exit flow to be responsible for such a large error at this location.

Next two signals are compared such that the frequency of the band-passed harmonic of one of the signals is equal to frequency of the band-passed fundamental of the other, e.g., Figure 4.11 shows

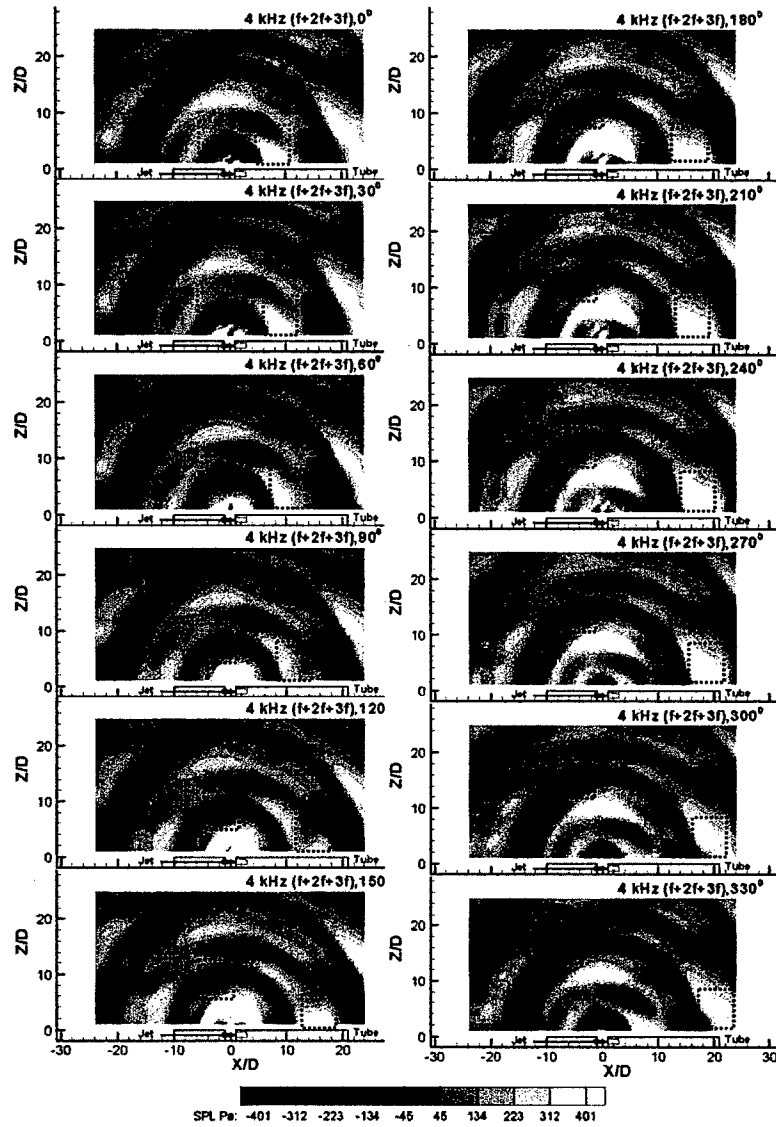


Figure 4.6: Phase averaged snapshots of 4 kHz ($f + 2f + 3f$) PRT signal (NPR = 3.33, PRT jet is flowing from left to right). Each sub-figure is a phase averaged snapshot of the acoustic field at 300 phase interval. The black or white regions, enclosed by dotted rectangles, represent lobes with concentrated acoustic energy.

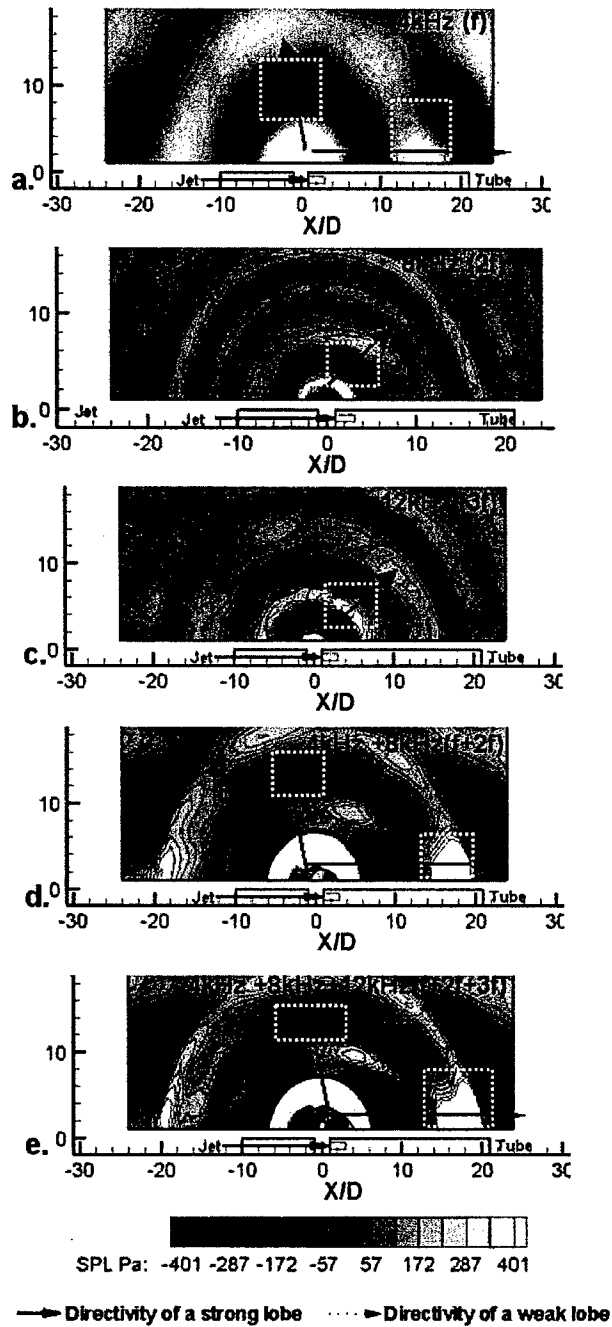


Figure 4.7: Propagation directivity of 4 kHz PRT signal with different harmonic content: (a) fundamental frequency, f (b) first harmonic, $2f$ (c) second harmonic $3f$ (d) $f + 2f$ (e) $f + 2f + 3f$. (NPR = 3.33, the PRT jet is flowing from left to right, dotted rectangles denote the prominent lobes for which directivity vectors are plotted).

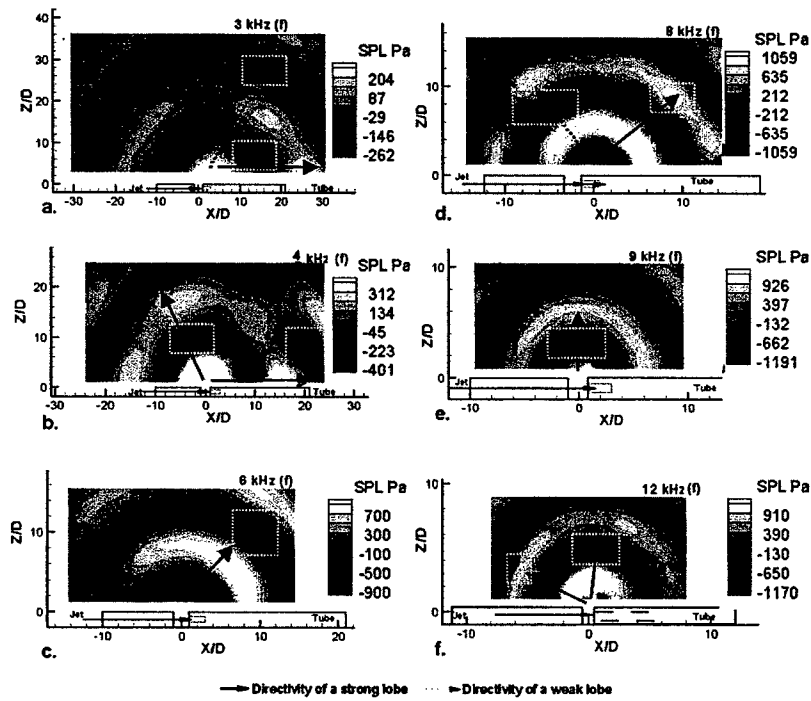


Figure 4.8: Change in the PRT signal directivity due to the change in the frequency. a. 3 kHz (f) b. 4 kHz (f) c. 6 kHz (f) d. 8 kHz (f) e. 9 kHz (f) f. 12 kHz (f) (dotted rectangles denote the prominent lobes for which directivity vectors are plotted).

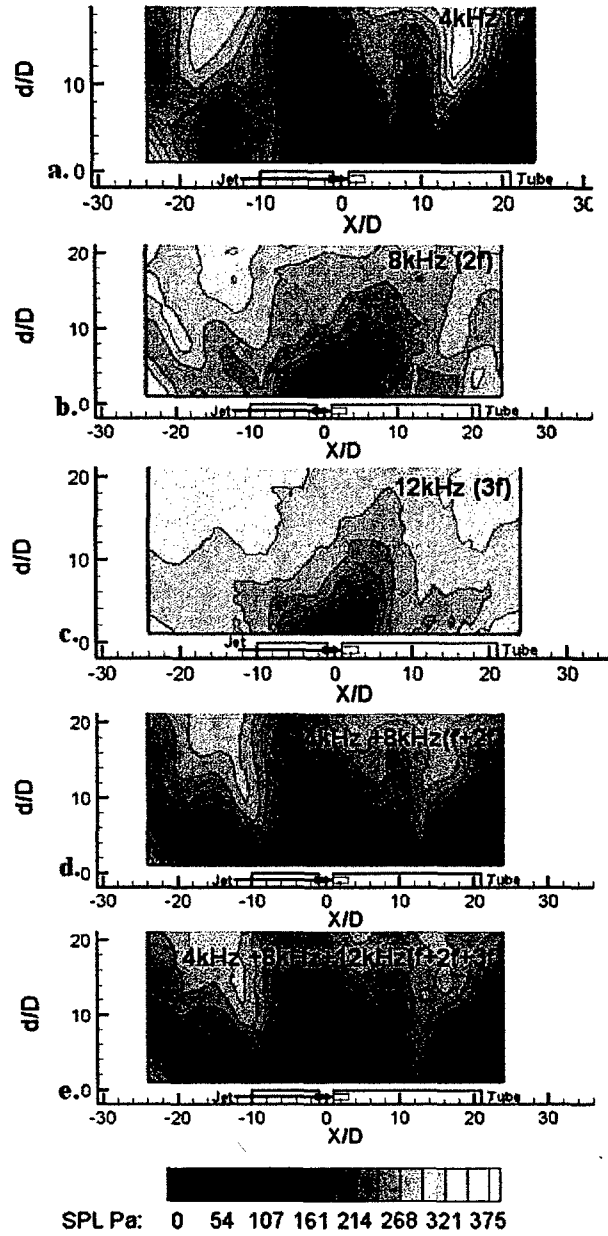


Figure 4.9: p_{rms} map of 4 kHz PRT signal with different harmonic content: (a) fundamental (f) (b) first harmonic ($2f$) (c) second harmonic ($3f$) (d) ($f + 2f$) (e) ($f + 2f + 3f$). (NPR = 3.33, PRT jet is flowing from left to right).

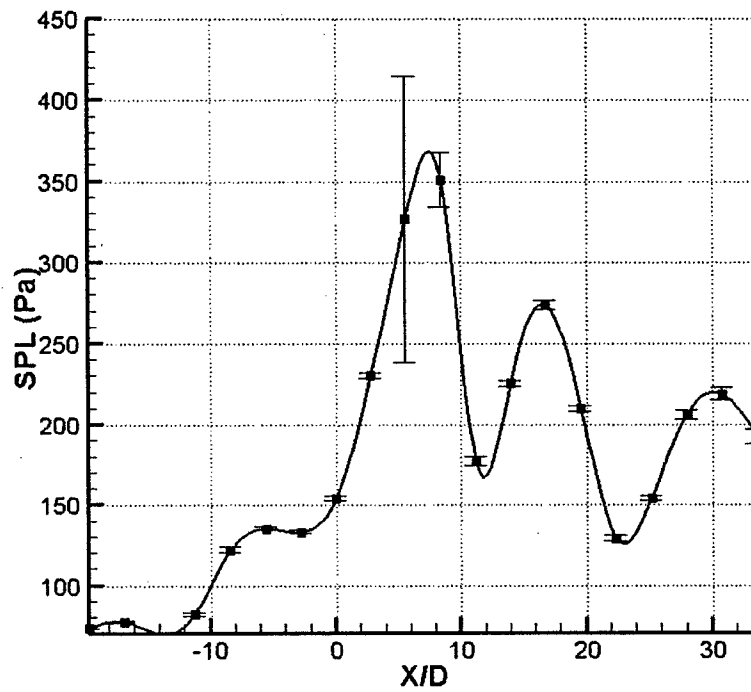


Figure 4.10: Experimental repeatability for pressure variation along the line $z/D = 2.8$ for the PRT signal of 3 kHz (f). (PRT jet is flowing from left to right) The large error bars just downstream of the resonator tube exit ($x/D = 5.6$) are the result of the hydrodynamic fluctuations caused by the jet flow spilling over the nozzle block.

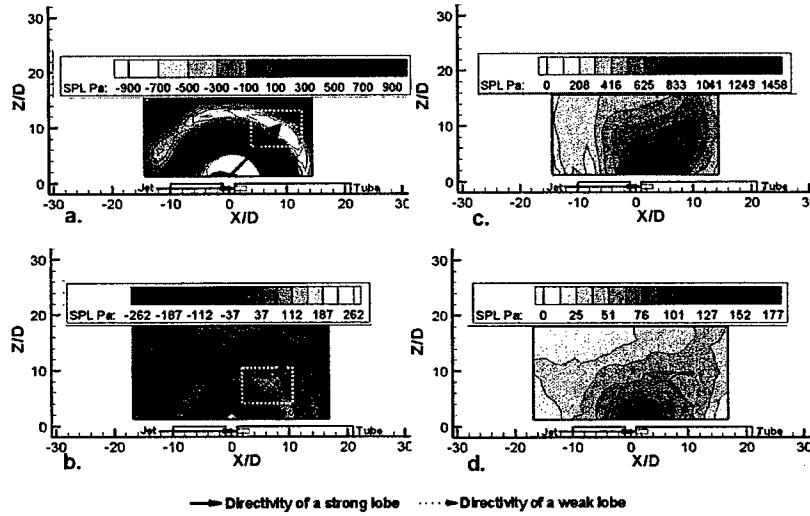


Figure 4.11: Comparison of 6 kHz fundamental and 3 kHz first harmonic PRT signal. (a) 6 kHz (f): phase averaged snapshot (b) 3 kHz ($2f$): phase averaged snapshot (c) 6 kHz (f): p_{rms} plot (d) 3 kHz ($2f$): p_{rms} plot (PRT jet is flowing from left to right, dotted rectangles denote the prominent lobes for which directivity vectors are plotted).

a comparison of the 6 kHz fundamental frequency to that of the 6 kHz which is a part of the 3 kHz first harmonic by means of phase averaged plots and p_{rms} plots. Here part (a) and (b) are phase averaged snapshots, whereas part (c) and (d) are p_{rms} plots. Here one can see that both the signals have downstream directivity. However, the 3 kHz first harmonic fades out earlier than 6 kHz fundamental signal. A similar trend was observed for the 8 kHz fundamental frequency signal and the 8 kHz as a part of the 4 kHz first harmonic. Even for these two cases, the general directivity was found to be downstream.

Figure 4.12 shows that the 12 kHz fundamental travels in an upstream direction. In contrast, the 4 kHz second harmonic travels in the downstream direction. A similar trend was observed when the fundamental part of 9 kHz was compared with the 3 kHz second harmonic. The directivity of the 9 kHz fundamental signal was in a vertical direction. On the other hand the 3 kHz second harmonic was found to travel in the downstream direction.

It is to be noted that NPR for all these cases was kept the same (i.e., 3.33); except for the 12 kHz. For 12 kHz the NPR was increased to 4.04 since the 12 kHz signal was difficult to obtain at low pressures.

4.5 Conclusions from the Experimental Study of Resonance Tube Characteristics and Directivity

A comparison between the PRT response and the theoretical shock cell model makes it clear that there is a correlation between the active spacing (the spacing at which the PRT resonates) and the shock cell termination distance. An increase in the Nozzle Pressure Ratio (NPR) increases the shock cell length. This increase in the shock cell length is found to increase the active spacing. Resonance at discrete spacings is a well documented feature of the PRT, however, at high NPRs where diamond

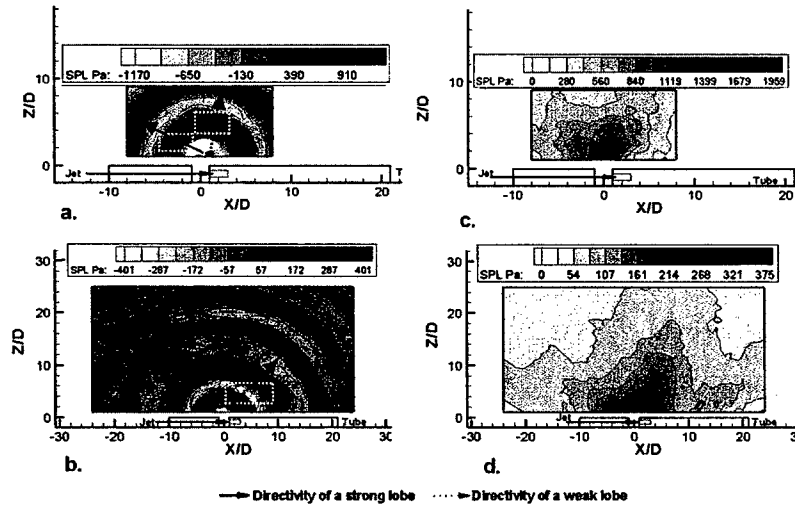


Figure 4.12: Comparison of 12 kHz fundamental and 4 kHz second harmonic PRT signal. (a) 12 kHz (f): phase averaged snapshot (b) 4 kHz ($3f$): phase averaged snapshot (c) 12 kHz (f): p_{rms} plot (d) 4 kHz ($3f$): p_{rms} plot (PRT jet is flowing from left to right, dotted rectangles denote the prominent lobes for which directivity vectors are plotted).

shaped shock cells truncate to become barrel shaped, the PRT was found to resonate regardless of the spacing. A similar result was also reported by [Smith and Powell, 1964]; though the exact reason behind is not clear. It was also confirmed that changing the spacing between the supply jet and the opening of the resonance tube does not alter the frequency to any significant extent; as long as PRT depth is kept constant.

From the actuation signal directivity study one can conclude that by varying the actuation signal frequency, its directivity may change. For lower frequencies the actuation signal propagates predominantly in the downstream direction of the jet. On the other hand, for higher frequencies the signal travels toward the upstream direction of the jet. For intermediate frequencies the directivity is predominantly vertical. One can also observe that, the directivity of the harmonic part of the signal is different from its fundamental part. The signal directivity study could be important during the installation and integration of the PRT into a flow control application. The p_{rms} plots indicate the lobes fluctuate in the strength as they move ahead. Hence, if the target area is placed where the signal loses its strength, the efficiency of the actuator may decrease. Thus along with the orientation, the distance between the actuator and the region where the signal is focused is also important.

Finally note that this chapter is limited to the "identification" of the key issues in the PRT design and its integration to guide end applications. To investigate the size effect and to formulate any scaling laws, further experimentation on PRTs of different sizes is necessary. As far as applicability of these laws for actual integration is concerned, one must also need to address the effect of mean flow from the device around which PRTs are situated. The issue becomes more complicated when arrays of such devices function together, as one would expect in an actual application.

Chapter 5

Simulation of the PRT

5.1 Overview

Simulations have been performed on PRTs for both straight resonance tubes as well as tubes with an expansion to generate lower frequencies for a given actuator length.

5.2 Simulation Methodology

5.2.1 Axisymmetric Geometry Idealization

The geometry fabricated in the laboratory has a number of complexities that would require an unreasonably large grid and enormous computational resources to simulate. In order to do meaningful simulations with reasonable computational resource requirements, simplifying approximations are required. The first such approximation is to assume an axisymmetric geometry and flowfield.

5.2.2 Pressure (Reynolds Number) Scaling

The first simulations are focused on approximating the experiments described in [Raman et al., 2002]. The supply tube typically contains choked flow that vents through the integration slot to atmospheric conditions. To reduce the computational requirements, the freestream pressure in the simulations is reduced to 0.03 psia for what will be referred to as “low” Reynolds number simulations, and to 0.3 psia for what will be referred to as “high” Reynolds number simulations. The ratio of the supply pressure to the freestream pressure is the same as in the laboratory study. The net effect of this scaling of the pressure is to reduce the effective Reynolds number by a factor of 490 for the low Reynolds number case, and by a factor of 49 for the high Reynolds number case. There were also calculations run at an intermediate Reynolds number, and those will be discussed later in the chapter.

The reduced Reynolds number permits a direct numerical simulation with a more modest grid. With this scaling, complete numerical solution and post processing of a single case can be completed in about one week using 2 processors on a 1.6GHz (per processor) AMD system. Simulations at the laboratory conditions would require a grid with up to 490 times as many points in each of two dimensions and the simulation times would increase by a factor of as much as 10^9 .

5.2.3 Flow Solver

Simulations of the several PRT configurations were performed using the Wind-US flow solver (see [Bush et al., 1998][Nelson and Power, 2001][Lankford and Nelson, 2002][Nelson et al., 2004]). Wind-US is a general purpose Euler and Navier-Stokes solver that is developed and distributed by the NPARC Alliance (a collaborative effort headed by NASA Glenn Research Center and the Air Force Arnold Engineering Development Center). Explicit third order Runge-Kutta time integration was used for the present time-accurate calculations. Based on the work of [Cain and Bower, 1995], the fifth order scheme was selected as the best available in Wind (the predecessor code to Wind-US) for acoustic propagation problems. [Cain et al., 1998] successfully applied the Wind code to the receptivity problem with a good match when compared to linear theory. However, because abutting, rather than overlapping, grids were employed for the current work, the importance of numerically transparent zone boundaries dictated use of the third order scheme instead of the otherwise more accurate fifth order scheme.

Buffer zones were added at all farfield boundaries to minimize any reflections due to imperfections in the boundary conditions. Viscous wall boundary conditions were employed for all the solid boundaries in the region of interest except when otherwise stated.

5.3 Simulations of Straight Tube PRT Actuators

Simulations were carried out at three values of the Reynolds number, as discussed previously. Despite the fact that the Reynolds numbers for these cases differ by as much as a factor of 10, the dominant resonance frequencies for the cases were nearly identical. Even more surprising was the fact that the amplitude was also nearly the same. Results are first presented for the resonance frequency as a function of resonance tube depth l . The simulation results are then compared to theoretical predictions and experimental results. Following this, differences in the detailed behavior of the simulation results for the low and high Reynolds number cases are discussed.

The basic geometry for the computation consists of a supply tube feeding an axisymmetric integration slot and resonance tube. The external geometry and acoustic radiation are also axisymmetric. The supply tube begins with a 1/2" diameter at the reservoir end and tapers conically to a 1/4" diameter constant section. The supply tube has a brief flare at the exit into the integration slot. The conical section and the constant diameter section are both 1/2" long. The resonance tube has a 1/4" diameter and variable depth. The diameter and width of the integration slot are 5/8" and 1/4", respectively. See [Cain et al., 2002a] and [Cain et al., 2002b] for additional details.

The resonance frequency obtained in the simulations is plotted as a function of resonance tube depth l in Figure 5.1. The geometry utilized in the simulations is axisymmetric, with an integration slot diameter $s = 5d$ and an integration slot width equal to the resonance tube diameter ($W = d = 1/4$ "). The resonance frequency is seen to increase as the tube depth l decreases. The simulations show little effect of supply pressure on the resonance frequency over the range of 35-40 psig, though [Cain et al., 2002b] showed that larger variations in supply pressure will affect the resonance frequency for short resonance tubes.

The resonance frequency predicted by the new refined theory of Kerschen for an open-closed tube is also plotted in Figure 5.1. The match of the results with the new theory due to Kerschen is very good. In contrast, while the original QWL theory was adequate for large tube length to diameter ratios, it breaks down as the resonance tube gets shorter.

In order to develop a better understanding of the behavior at smaller tube depths, a refined theory was developed [Kerschen, 2001] that considers the acoustic coupling between a resonance tube of diameter d and depth l , and an axisymmetric integration slot of diameter s and width W . The no-penetration boundary condition is applied to the closed end of the resonance tube, while the

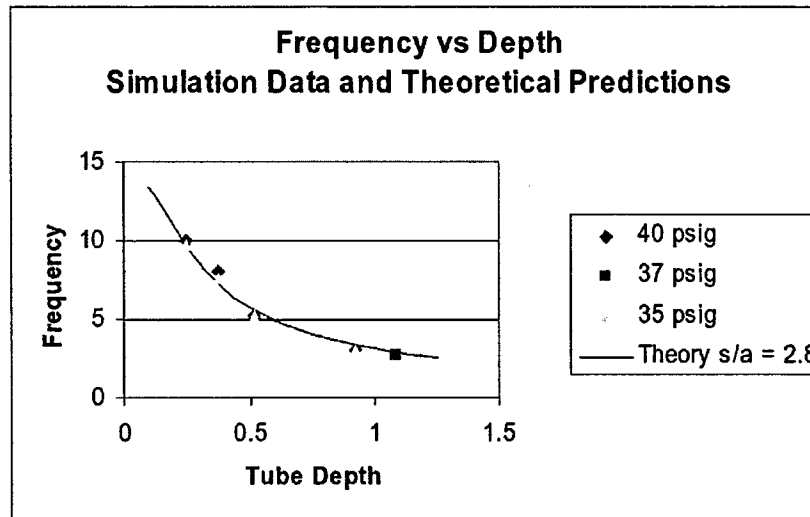


Figure 5.1: A comparison of the results of nonlinear computation and a refined linear theory (including inertia of the fluid in the integration slot) for predicting the effects of resonance tube depth on the resonance frequency.

pressure release boundary condition is applied at the outer edge of the integration slot ($r = s/2$). The pressure and axial velocity are matched across the interface between the tube and slot. The theory ignores the presence of the mean flow, but accounts for the inertia and compressibility of the fluid in the integration slot.

The refined theory was initially developed for comparisons with the experimental data obtained by Raman at the Illinois Institute of Technology (IIT). In these experiments, the geometry of the integration slot is rectangular rather than axisymmetric, and the resonance tube is located off center. Hence, a precise comparison with these experiments cannot be made. In order to estimate an effective integration slot diameter, note that the distance from the axis of the resonance tube to the four edges of the integration slot ranges from 0.25" to 0.5", corresponding to s/d ratios of 2 to 4. Theoretical predictions were obtained for values of s/d in this range and comparisons were made with the IIT data. Good agreement between the predictions of the refined theory and the IIT data were obtained for $s/d = 2.8$ (see Figure 5.2). This value of s/d may be considered an effective value of s/d for the IIT early prototype experiments. Essentially, as the tube depth decreases, the inertia of the fluid in the integration slot becomes more important, lowering the resonance frequency.

In Figure 5.1, the theoretical prediction of the refined theory for $s/d = 2.8$ is compared to the resonance frequencies obtained in the simulations. The refined theory is seen to be in much better agreement with the simulation results than the basic QWL theory. Note that the simulations have been carried out for the case $s/d = 5$, compared to $s/d = 2.8$ for the refined theory. However, additional theoretical results that have been obtained show that the resonant frequency is not very sensitive to the value of s/d for the integration slot geometry and resonance tube depths considered in the simulations. The sensitivity to s/d increases significantly for smaller values of the integration slot width, as well as for very small tube depths beyond the range explored in the simulations. Also note that, at very small tube depths, the resonance frequency would likely be influenced more by the mean flow in the integration slot, which has been neglected in the theory.

Data from the PRT actuator experiments at IIT is presented in Figure 5.2. The quantity plotted is the actuator resonance frequency, as a function of resonance tube depth l , for a supply pressure of

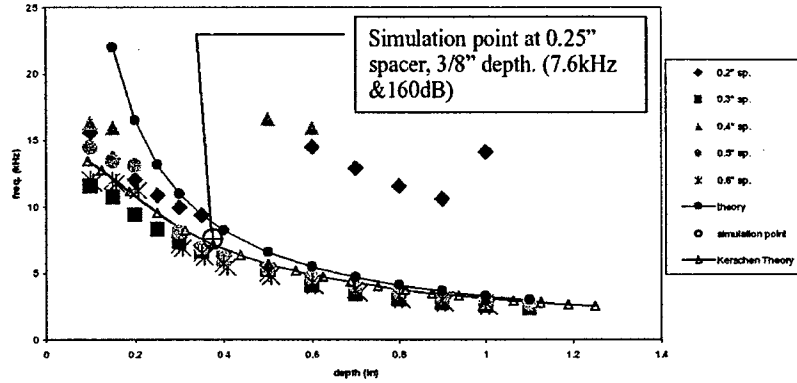


Figure 5.2: Experimental data base of actuator frequency versus actuator depth. Also shown are curves for the basic theory and the refined theory with $s/d = 2.8$, and one simulation data point.

35 psig and a resonance tube diameter $d = 1/4$ " in. Results are shown for several integration slot widths. The primary quantity that determines the resonance frequency is seen to be the resonance tube depth. The width of the integration slot has little influence on the resonance frequency for large tube depths, but becomes more important as the tube depth decreases.

Figure 5.2 also shows two theoretical predictions for the resonance frequency: the basic QWL theory, and the refined theory for $s/d = 2.8$. For long tube depths, the two theoretical predictions are nearly identical and in good agreement with the experimental data. For smaller tube depths, the QWL theory diverges from the experimental data. In contrast, the refined theory remains in good agreement with the experimental data even at small values of the tube depth. Essentially, for small tube depths, the inertia of the fluid in the integration slot becomes important, significantly reducing the resonance frequency relative to the prediction of the QWL theory.

In order to avoid excessive cluttering of Figure 5.2, all the resonance frequency data obtained in the simulations has not been plotted in this figure. Instead, a single simulation point with $l = 0.375$ " has been included in Figure 5.2. This simulation point can be seen to be in good agreement with the experimental results and the refined theory for $s/d = 2.8$. The agreement between the simulations and experiments for other values of tube depth can be established indirectly, by comparing the agreement between simulations and the refined theory for $s/d = 2.8$ in Figure 5.1, and the agreement between the experimental results and the refined theory in Figure 5.2.

In addition, note that the simulations determine the amplitude as well as the frequency of the resonance. Accounting for the pressure scaling discussed earlier, the simulation result shown in Figure 5.2 corresponds to an amplitude of 160 dB, in fairly good agreement with the laboratory value of 157 dB.

The next topic to be considered is the influence of Reynolds number on detailed features of the simulation results. Note that the simulations consider an axisymmetric flow field that is essentially an unsteady laminar flow. Strong three-dimensionality would be present in a turbulent flow field. This feature is not included in the present simulations.

Figures 5.3 and 5.4 show the time history of the pressure at the closed end of the resonance tube for the low and high Reynolds number cases, respectively. The time dependence of the pressure is very regular for the low Reynolds number case. While the high Reynolds number case retains a strong periodic component, it also exhibits a significant amount of higher frequency noise. General intuition

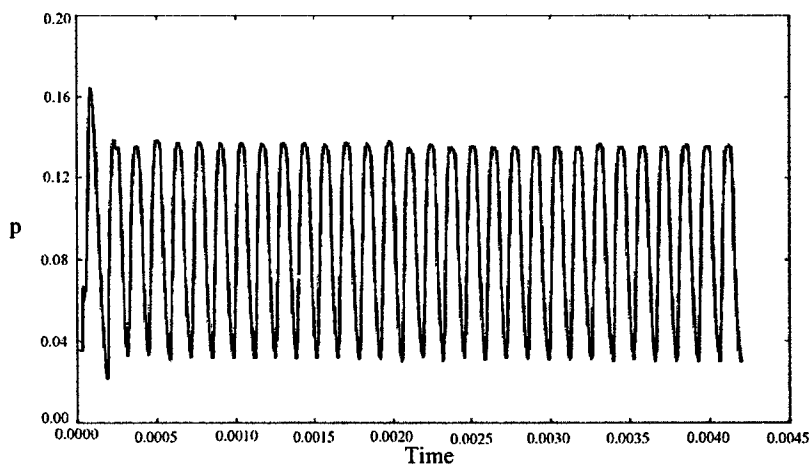


Figure 5.3: Low Reynolds number pressure history of the resonance tube over the first 60,000 time steps.

would support this result but the magnitude of the difference is striking. A plot of a sample of the pressure time history from one of the IIT experiments is shown in Figure 5.5. Note that the character of the pressure time trace is qualitatively very similar to that observed for the high Reynolds number simulation. The frequency spectrum for the low Reynolds number case has sharp, strongly dominant peaks at the fundamental and harmonic frequencies, while the high Reynolds number case shows broader peaks and “hay stacking” around these peaks. A very interesting aspect of this comparison is that the dominant response frequencies for the low and high Reynolds number cases are virtually identical. Even more surprising is the fact that the pressure scaled amplitude (SPL) is also quite similar for the two cases.

Figures 5.6 and 5.7 compare the instantaneous pressure fields of the low and high Reynolds numbers cases after 60,000 time steps. Once again, the low Reynolds number case is more regular than the high Reynolds number case. While the sound radiation external to the integration slot shows some variation with respect to angle, overall the directivity pattern is nearly uniform. Additional discussion of the directivity patterns, including some interesting details, is in Chapter 4 and in [Sarpotdar et al., 2005a].

The instantaneous Mach contours after 60,000 time steps are presented in Figures 5.8 and 5.9. There are several interesting differences between the low and high Reynolds number cases. First, even though the frequencies are nearly the same, after 60,000 time steps the two cases have drifted to a significantly different “phase.” This can be seen by looking at the Mach contours inside the resonance tube in the lower right of each figure. Compression waves propagate along the length of the resonance tube during each cycle. The compression wave is near the entrance to the tube in Figure 5.8, while it has nearly reached the closed end of the tube in Figure 5.9. Next, in the low Reynolds number case the jet along the right-hand side of the integration slot (the small vertical tube) exhibits no sign of hydrodynamic instability, while in the high Reynolds number case the jet appears to have undergone a shear-flow instability. Finally, the high Reynolds number case is seen to have significantly more “bulk” flow impact external to the integration slot than does the low Reynolds number case.

The final two figures present a comparison of the vorticity fields for the low and high Reynolds number cases. In the low Reynolds number case (Figure 5.10), the vorticity contours show a quasi-

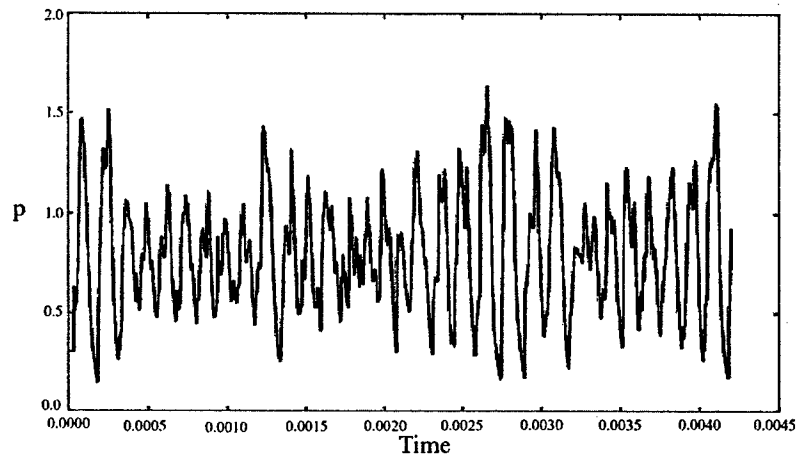


Figure 5.4: High Reynolds number pressure history of the resonance tube over the first 60,000 time steps.

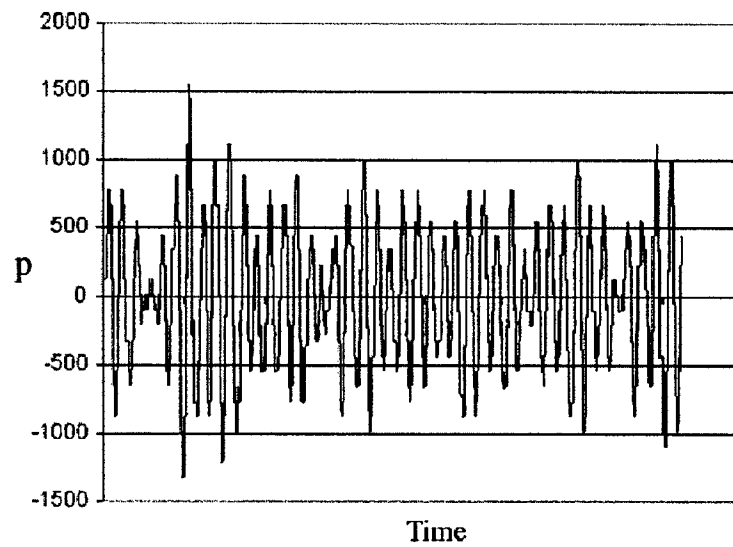


Figure 5.5: Experimental pressure history.

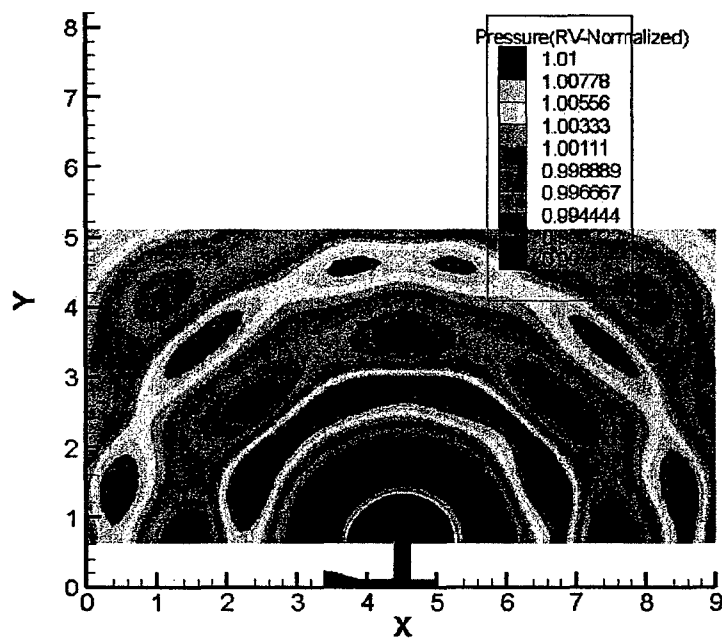


Figure 5.6: Pressure contours for the low Reynolds number case after 60,000 time steps.

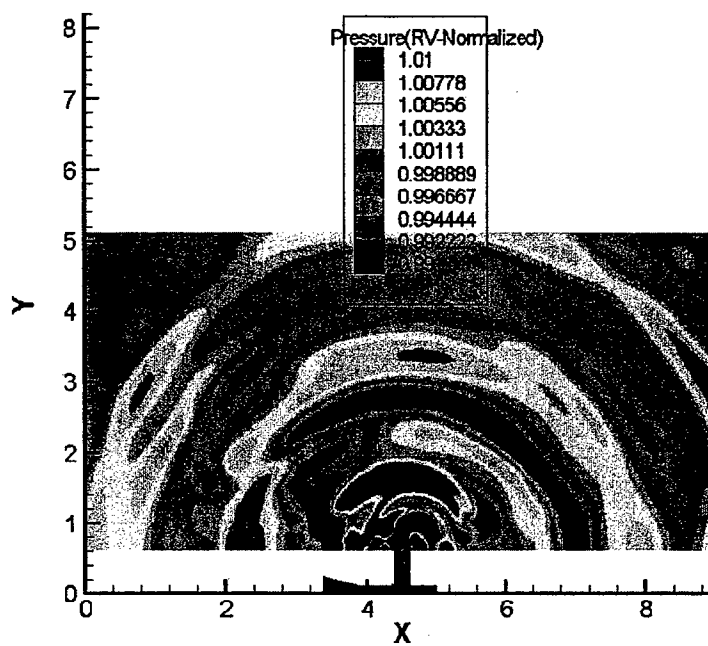


Figure 5.7: Pressure contours for the high Reynolds number case after 60,000 time steps.

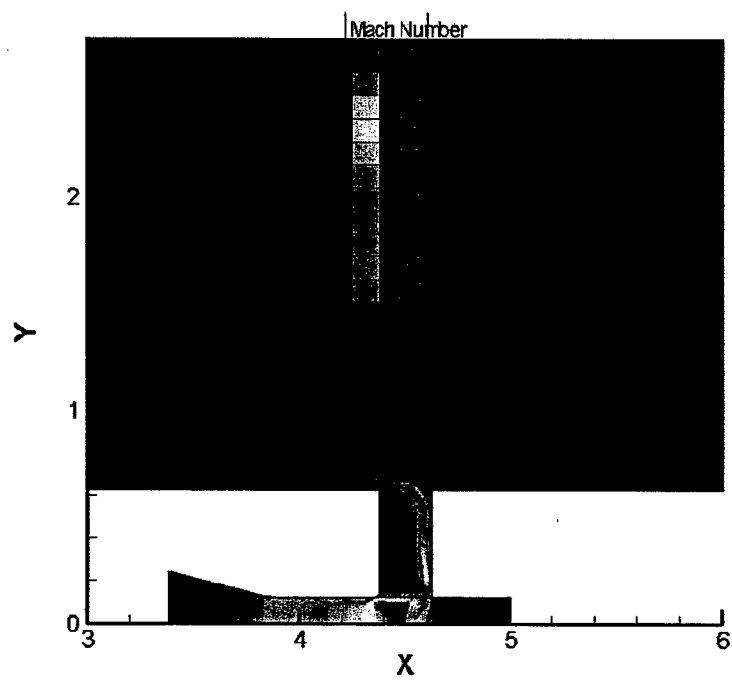


Figure 5.8: Mach contours for the low Reynolds number case after 60,000 time steps.

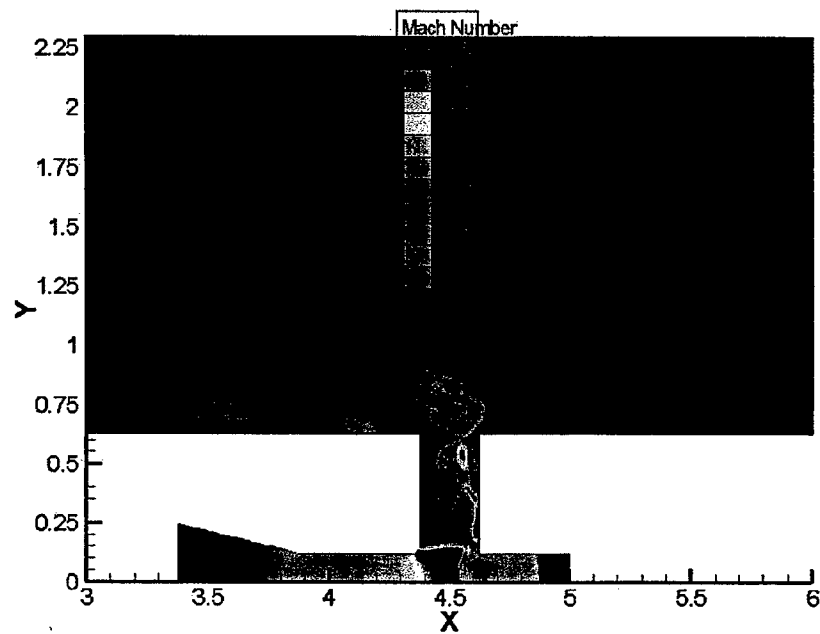


Figure 5.9: Mach contours for the high Reynolds number case after 60,000 time steps.

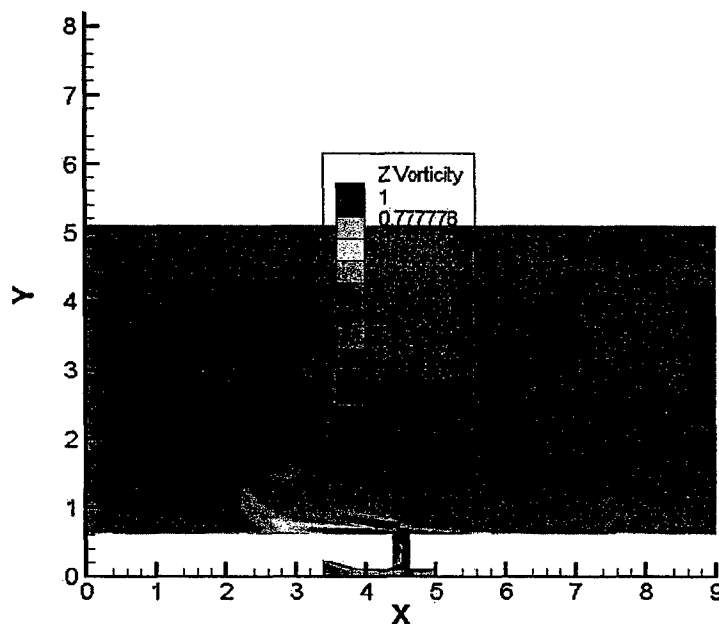


Figure 5.10: Vorticity contours for the low Reynolds number case after 60,000 time steps.

steady jet-like structure exiting the integration slot, while in the high Reynolds number case (Figure 5.11) counter-rotating vortex pairs that resemble a “blooming jet” are seen. It must be remembered that these simulations are axisymmetric, so that these vortices correspond to axisymmetric rings. If a three-dimensional simulation were performed, the instabilities of these vortex rings would cause a breakdown to turbulence, resulting in a substantially more diffuse vorticity field.

5.3.1 Effect of Primary Flow

When a primary flow Mach 0.5 stream and external boundary layer are included in the model, a 3/8" wall perpendicular to the surface is inserted near the upstream boundary of the computational domain. The purpose of the wall is to thicken the boundary layer and increase the Reynolds number. The flow reattaches before reaching the integration slot. With the present grid the boundary layer flow is still stable according to linear theory ($Re_{\delta^*} \approx 320$ at the resonance tube). Higher Reynolds numbers cannot be run with the present grid without degrading the resolution of the unsteady shock motion. Grid refinement and algorithm studies suggest the present results are invariant to grid and algorithm for modest changes.

The presence of a Mach 0.5 freestream flow and boundary layer external to the PRT reduces the resonance frequency by 12% and increases the SPL by 3dB, relative to the no primary flow case. These changes are caused by the modified acoustic impedance of the integration slot exit in the presence of the external stream, and possibly also by changes to the mean flow within the slot. The pressure history for this case at the same spatial point as the no freestream case is given in Figure 5.12. The freestream pressure and supply pressure were both doubled for the case displayed in Figure 5.12; the pressures were increased to raise the Reynolds number. Unfortunately the

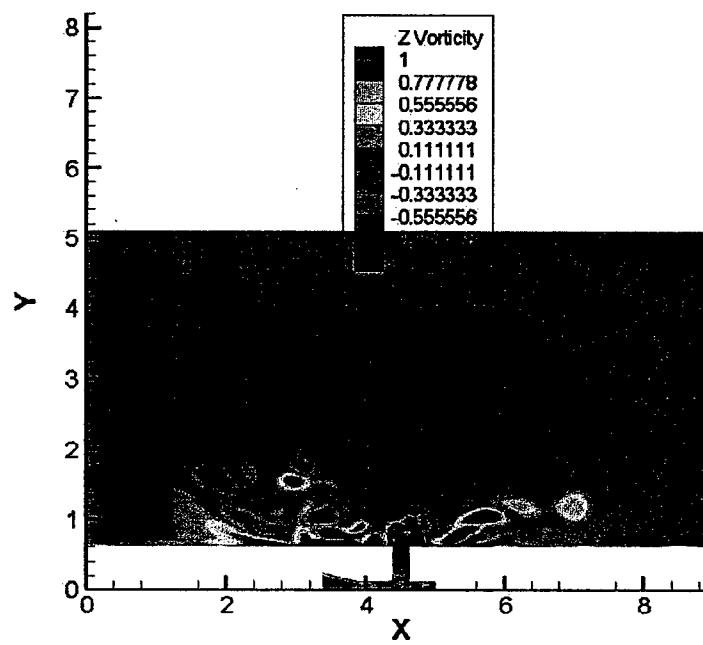


Figure 5.11: Vorticity contours for the low Reynolds number case after 60,000 time steps.

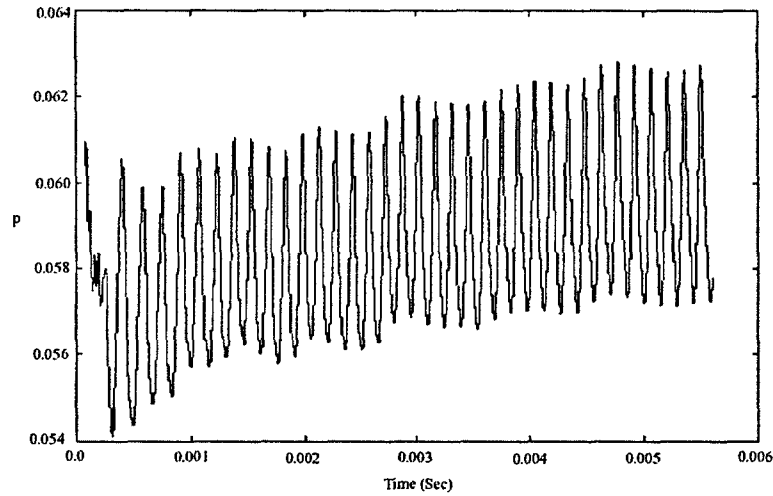


Figure 5.12: Pressure oscillations on the wall in a Mach 0.5 freestream and boundary layer driven from below by a powered resonance tube.

Table 5.1: Frequency as a function of the nozzle pressure ratio. "NR" denotes no resonance.

NPR	Frequency (Hz)
2	NR
2.5	NR
3	6491
3.5	7620
4	7938
4.5	NR
5	NR

Reynolds number of the boundary layer flow is still too low for amplified instability waves to exist in the external boundary layer.

5.3.2 Effect of Nozzle Pressure Ratio

Finally we discuss the effects of nozzle pressure ratio (NPR) on the behavior for a "short" resonance tube which has a "length to diameter ratio" of 1.5. At an NPR of 2.0 the flow exits the supply jet at nearly sonic velocity and no resonance develops. Increasing the NPR to 2.5 produces a supersonic exit flow but still no resonance develops. At NPRs of 3.0, 3.5, and 4.0, strong resonances develop. At higher NPRs the flow again becomes steady after the transient dies out. These behaviors are illustrated in Table 5.1 and Figure 5.13. The experimental studies of [Khanafseh et al., 2002] reveal that in some cases a change in NPR can produce mode shifts with higher harmonics becoming dominant, though usually with reduced amplitude. The computational resolution may be insufficient to capture the shift to the experimentally observed third harmonic.

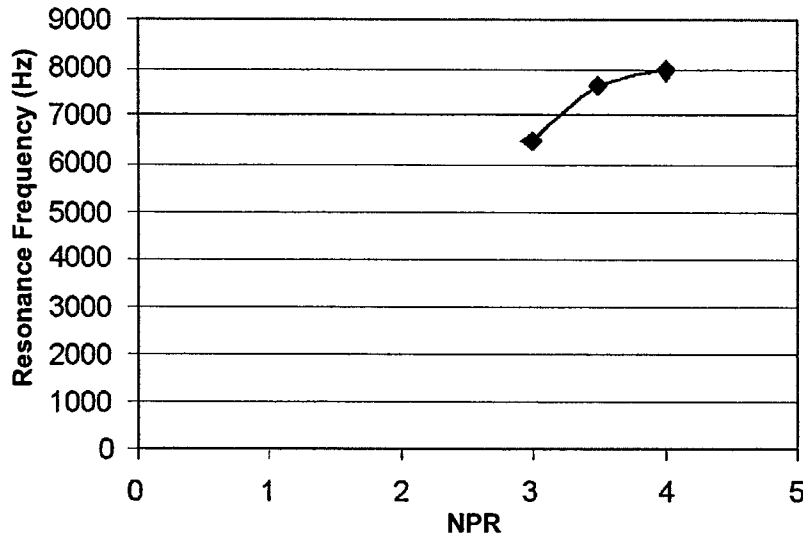


Figure 5.13: Resonance frequency as a function of nozzle pressure ratio (NPR) for a “shallow” resonance tube.

5.3.3 The Effect of Including a Turbulence Model

A simulation was made with the SST turbulence model and compared with the same case run as a laminar flow. The turbulence model had little effect on the dominant resonance frequency and the amplitude was only slightly affected. Since the impact of the SST turbulence model was negligible in the case examined, no further study was done regarding the use of turbulence models.

5.4 Simulation of Helmholtz Based PRT Actuators

5.4.1 Geometry of the Helmholtz PRTs

In evaluating the significance of the Helmholtz concept applied to the PRT, four different geometric configurations have been examined. One had a straight resonator tube (i.e. no Helmholtz resonator), and the other three had Helmholtz resonators of various depths. A schematic is shown in Figure 5.14. While the topology of the detail drawing is correct, the actual dimensions are not those used for the simulations. For this work, the neck length was 0.375”, and the radius was 0.06275”. The expansion transition was 0.0875” in length, widening to the full radius of the Helmholtz resonator of 0.125”.

The straight tube geometry consists of the same “base configuration” without the expansion and resonator sections (i.e. only the neck portion is present). The chamber length (l_c —including expansion region), effective length (l , as per the Kerschen theory), and the ratio of neck length to total length (α_n , from equation 6.17) are summarized in Table 5.2 for all four configurations.

Table 5.2: PRT Geometries

Configuration	Type	$l_c(\text{in})$	$l_{eff}(\text{in})$	α_n
1	Straight	0.0	0.427	1.00
2	Helmholtz	0.1875	0.665	0.718
3	Helmholtz	0.375	0.853	0.560
4	Helmholtz	0.75	1.228	0.389

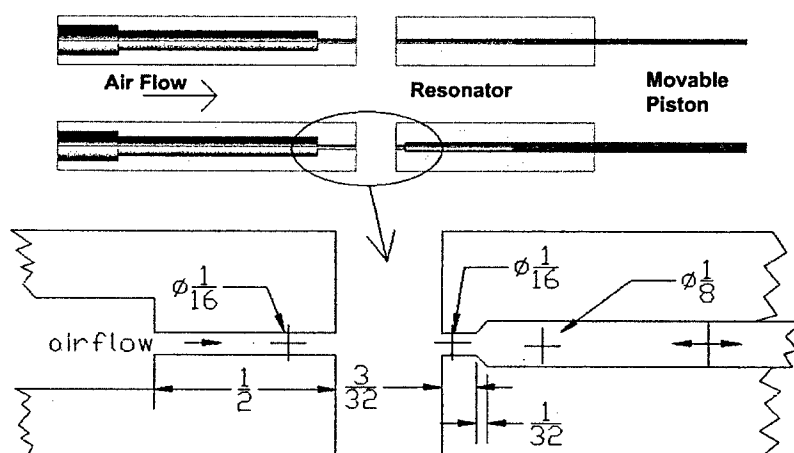


Figure 5.14: Two resonators and detail drawing of a Helmholtz resonator (dimensions in inches)

Table 5.3: Summary of Results

Case	Config.	NPR	Peak f (Hz)	p'_{rms} (psi)	OASPL (dB)	Peak SPL (dB)	Ω (eqn. 6.16)
1	1	3	7143	3.61×10^{-1}	161.9	159.6	1.43
2	2	3	3214	9.46×10^{-2}	150.3	146.1	1.00
3	3	3	2095	5.98×10^{-2}	146.3	139.3	0.84
4	4	3	1500	3.27×10^{-2}	141.0	136.4	0.86
5	1	2.38	7429	2.67×10^{-1}	159.3	159.1	1.48
6	2	2.38	3571	5.36×10^{-2}	145.3	141.8	1.11
7	3	2.38	2280	3.69×10^{-2}	142.1	140.4	0.91
8	4	2.38	1597	2.22×10^{-2}	137.7	134.0	0.92

5.4.2 Operating Conditions Studied

Unless otherwise identified, viscous wall boundary conditions were employed for all the solid boundaries in the region of interest. Two nozzle pressure ratios (the air supply pressure versus freestream pressure) were used for these cases: 3.0 and 2.38. Consistent with previous simulations for this project, these cases were run on axi-symmetric grids with reflection boundary conditions applied at the axis of rotation. To minimize grid-related errors when comparing the results, the grids employed for these cases were all identical except for the Helmholtz resonator chamber grid (if any). No turbulence model was used for these cases.

5.4.3 Results

Numerical simulations allow an exploration of the detailed flow physics and facilitate a better understanding of the dominant mechanisms involved in the phenomena of interest. The results provide details of the unsteady flow inside the actuator, as well as features of the external acoustic radiation field. The results for the first eight Helmholtz PRT cases are summarized in Table 5.3. It is readily apparent that the Helmholtz-based PRT designs are indeed able to produce lower frequency tones in a more compact space than the straight tube alone. Comparing Case 4 to Case 1, one finds that a resonator only three times longer than the straight tube was able to produce dominant tones at one fifth of the frequency. Unfortunately, this increased bandwidth comes at the cost of decreased amplitude, as a steady drop in the peak SPL is observed from almost 160 dB for Case 1 to less than 137 dB for Case 4. Indeed, the RMS of fluctuating pressure for Case 4 is an order of magnitude less than that of the straight tube case. In addition to the overall noise decreasing, as the expansion length of the Helmholtz resonator is increased, a larger portion of the energy goes into the broadband, resulting in a larger difference between the OASPL and the peak SPL values.

The values of the Helmholtz number in the simulations are plotted against the predictions from the Kerschen theory in Figure 5.15. The plot shows that the simulations and theory have very good qualitative agreement. Quantitatively, however, the simulations are predicting an Ω slightly lower than the theoretical values for all but one of the cases simulated here. It is not yet clear why this is the case. It is possible that the limitations of the axi-symmetric and laminar assumptions are hampering the simulations. Alternatively, it may be that neglecting the mean flow in the theory is causing some error. Also, the end corrections for the neck are based on semi-infinite range for the flared neck. Since the flare only extends a short distance, this assumption might need to be modified.

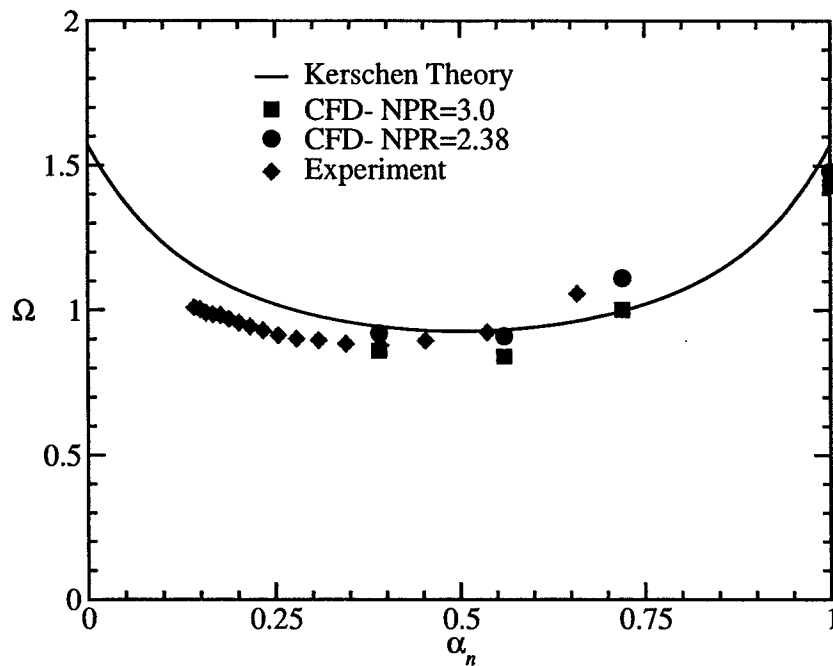
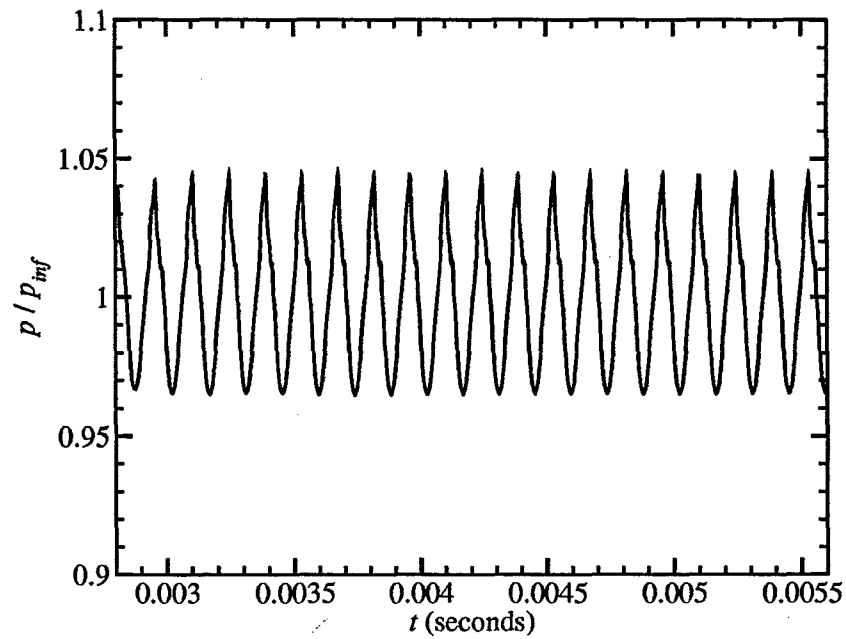


Figure 5.15: Comparison of the simulation results to the Kerschen theory predictions

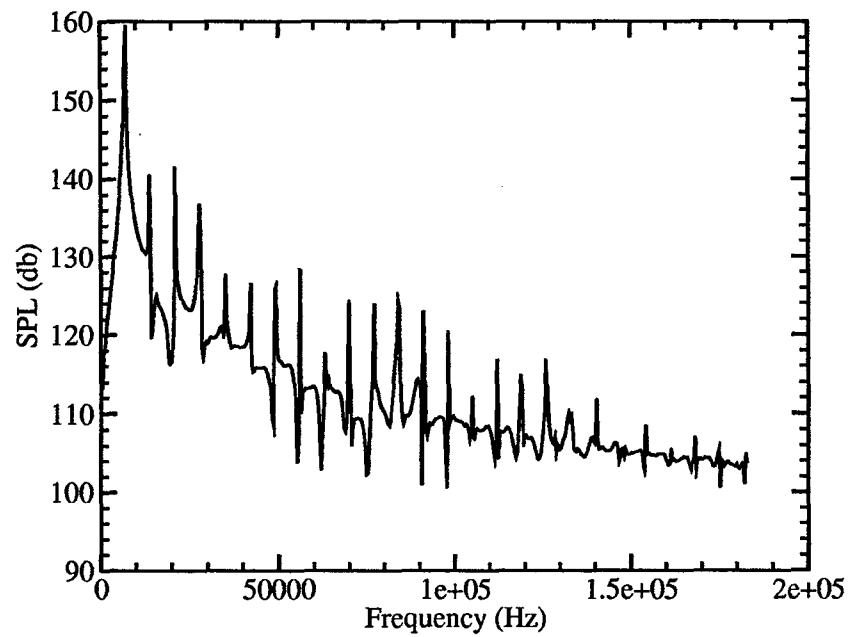
Pressure traces and spectra

Time histories of the pressure were obtained at a point on the outside of the PRT, just downstream of the integration slot. This data has been processed to obtain information about the spectral content of the radiated acoustic field. The results are plotted in Figures 5.16 through 5.19 for cases 1 to 4. Comparing the four figures, one can easily see that the SPL levels drop considerably as the PRTs become larger. Also, note that the pressure traces appear more "noisy" for the Helmholtz based PRTs, as opposed to the straight tube, which has a more regular signal.

Because of the differences in frequency and magnitude in Figures 5.16 through 5.19, it can be difficult to compare the different cases to ascertain whether or not the fundamental spectral behavior is changing. One means of overcoming this is to rescale the curves to enable plotting in a completely non-dimensional space. Hence, Figure 5.20 shows normalized PSD as a function of mode number the four cases with NPR of 3. This plot clearly shows that the straight tube is concentrating more of its energy in the vicinity of the primary tone; higher modes have relatively lower peak values for this case than for the Helmholtz based PRT designs. Also apparent is that there is no clear trend in terms of intermodal "noise" or higher modal peak amplitude among Cases 2, 3, and 4. Case 3 appears to be "noisier" than either Case 2 or 4, in the sense that the curves between the modal peaks show more oscillations. In terms of peak amplitudes, the three cases appear to be very similar to each other when normalized by the total energy in the spectrum. This would suggest that the same physical phenomena are governing the behavior of all three Cases. This in turn suggests that a single theory should be able to predict this behavior.

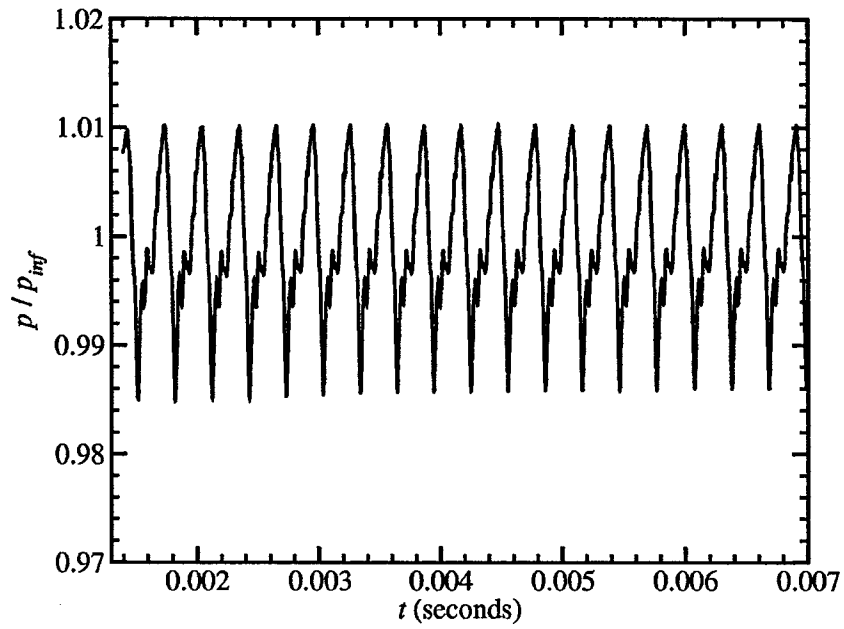


(a) Time history

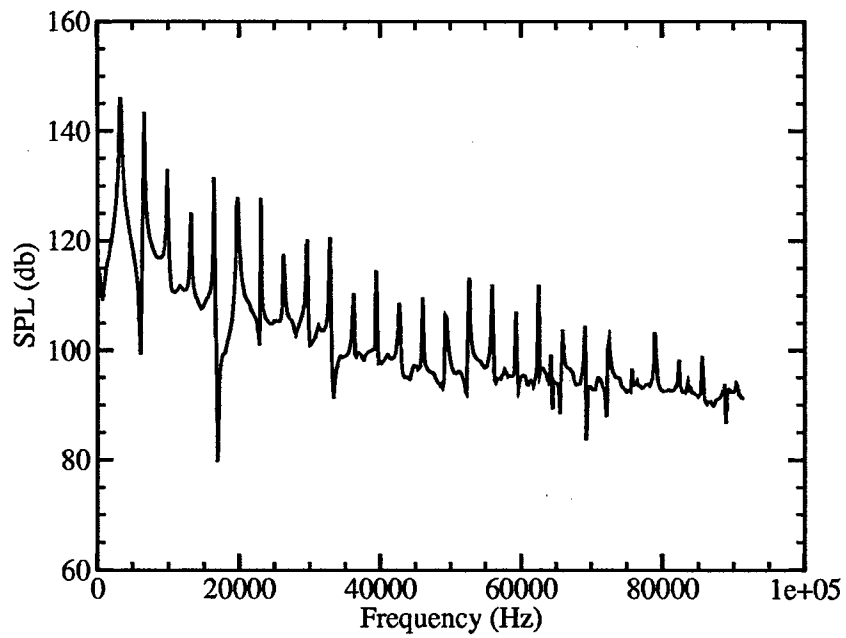


(b) Narrowband SPL

Figure 5.16: Pressure trace and narrowband SPL near the integration slot exit for Case 1

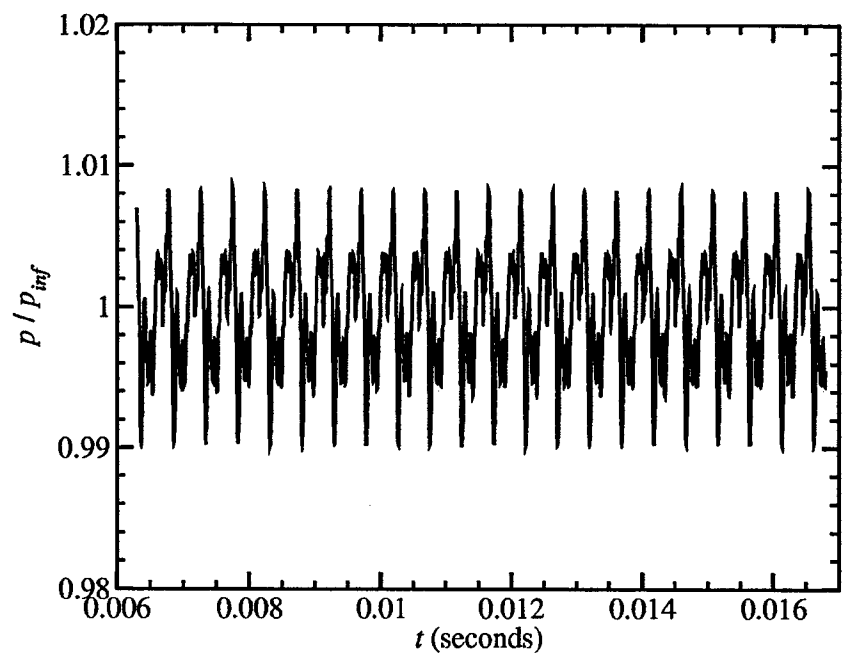


(a) Time history

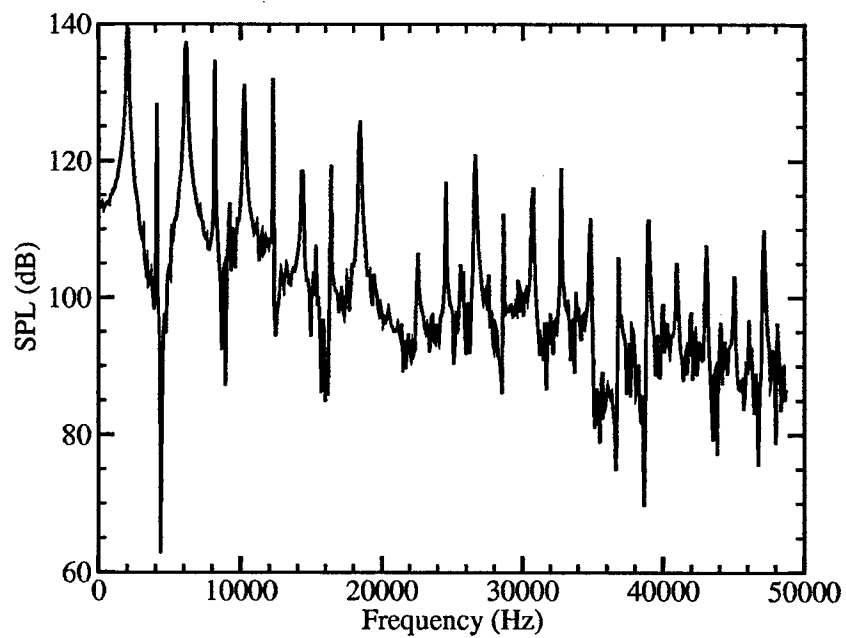


(b) Narrowband SPL

Figure 5.17: Pressure trace and narrowband SPL near the integration slot exit for Case 2

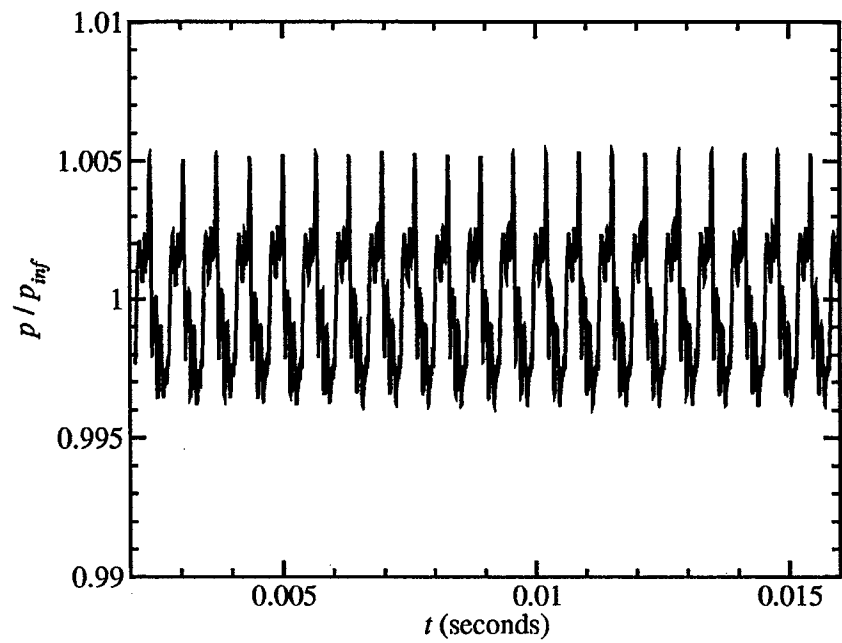


(a) Time history

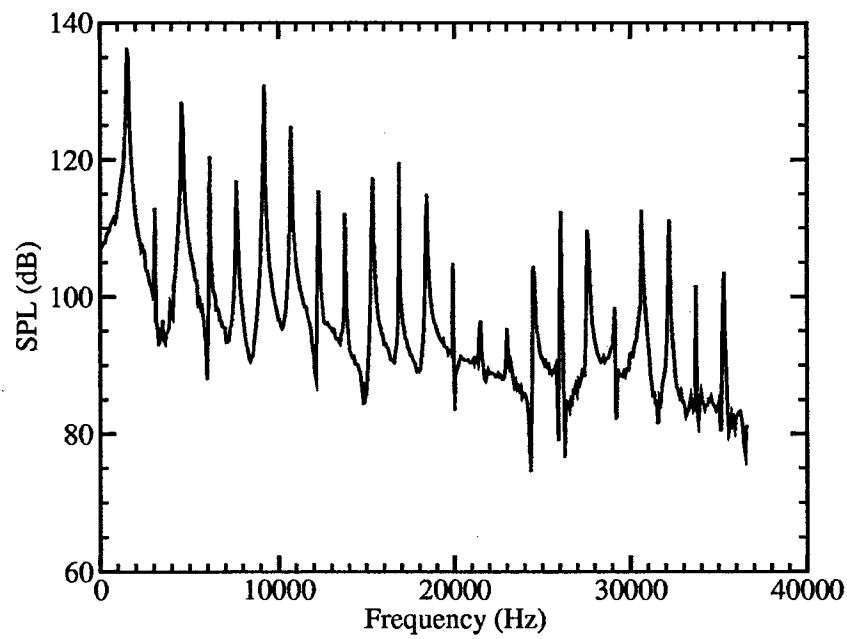


(b) Narrowband SPL

Figure 5.18: Pressure trace and narrowband SPL near the integration slot exit for Case 3



(a) Time history



(b) Narrowband SPL

Figure 5.19: Pressure trace and narrowband SPL near the integration slot exit for Case 4

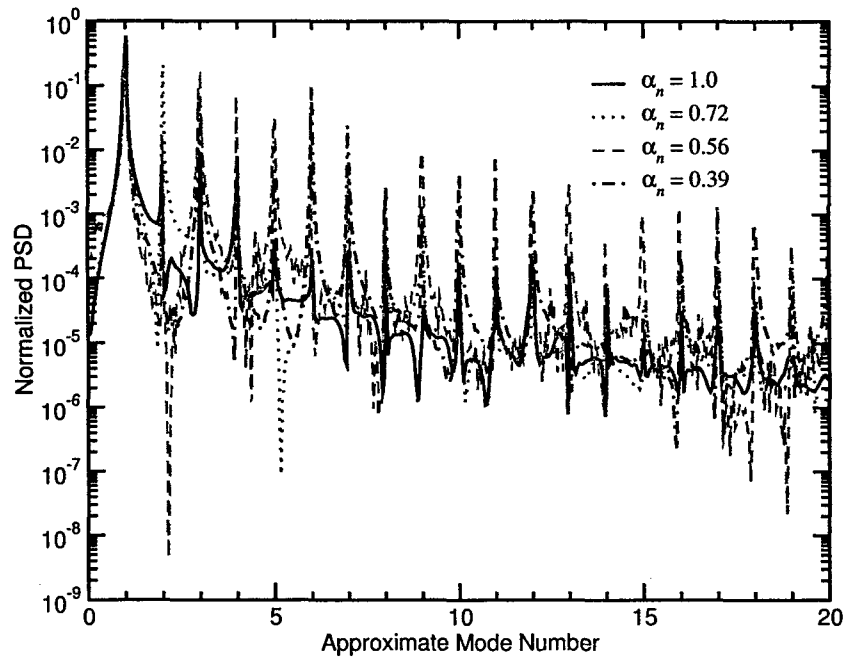


Figure 5.20: Spectral power distribution comparison of four PRT geometries.

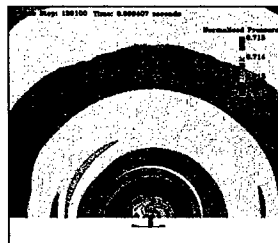
Cyclic behavior

Detailed time histories of the flow were gathered for both Case 1 and Case 3. Snapshots of the flow at various points in a cycle are shown for Case 3. The first series of plots shows the pressure in the nearfield region outside the PRT (Figure 5.21). The six snapshots show the progress of the sound waves as they travel for one full cycle of the radiated signal. Note that the “starting” and “ending” points are just arbitrary points in the cycle, chosen for convenience rather than any physical significance. In addition to the obvious spherical waves emitting from the slot, there appear to be at least two different, more directed signals. The more obvious of the two signals travels downstream in an arc between the x -axis and about 45° up from it (measured from the slot exit). These waves are especially visible in Figure 5.21(d), but are also noticeable in 5.21(b) and 5.21(c). In Figure 5.21(a) and 5.21(f), a similar, but perhaps less obvious, set of waves heads upstream, also in an arc between the x -axis and roughly 45° up from it.

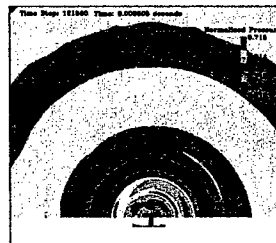
Figure 5.22 shows similar snapshots of pressure, but this time, the scale has been expanded to focus on the activity in the integration slot. The most obvious feature of this sequence of snapshots is the presence of the trapped vortex sitting at the mouth of the integration slot. In Figure 5.22(c), 5.22(d), and 5.22(e), one can see a new vortex emerging from the resonator, moving up the slot, strengthening, and finally displacing the original vortex.

Adjusting the contour levels yet again, Figure 5.23 focuses on the pressure in the air supply nozzle and the resonator. While the air supply appears to experience very little pressure variation throughout the cycle, the resonator shows a strong pumping action. In Figure 5.23(a), the chamber has just emptied, leaving a low pressure region which then begins sucking in new fluid in 5.23(b). The chamber gradually fills in 5.23(c) until, by 5.23(d), it begins to exhaust into the slot. The blowing continues in 5.23(e), until the cycle begins again in 5.23(f).

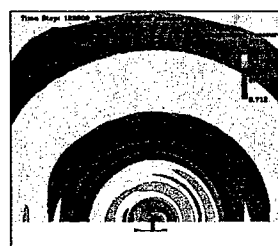
A different perspective on the dynamics of the resonator/slot interactions is seen in the snapshots



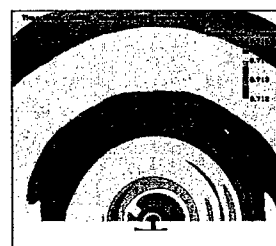
(a) "Initial" state, $t = t_0$



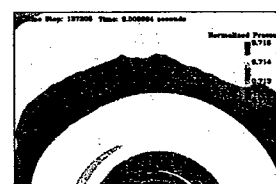
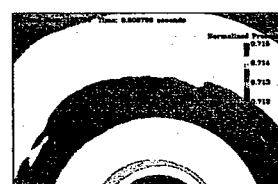
(b) $t = t_0 + T / 5$

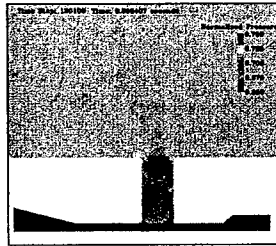


(c) $t = t_0 + 2T / 5$

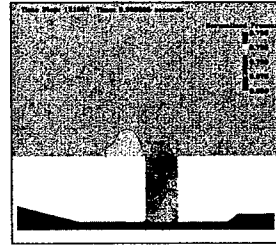


(d) $t = t_0 + 3T / 5$

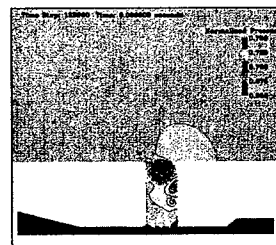




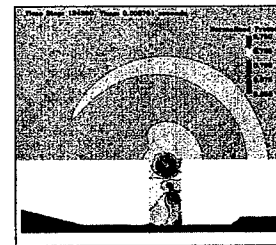
(a) "Initial" state, $t = t_0$



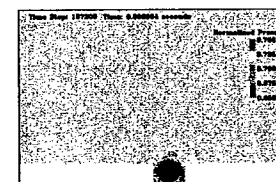
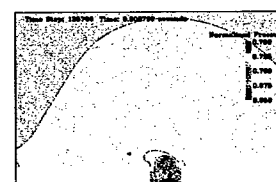
(b) $t = t_0 + T/5$

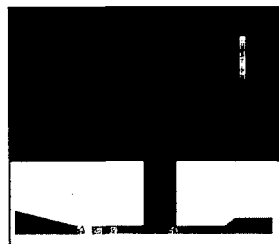


(c) $t = t_0 + 2T/5$

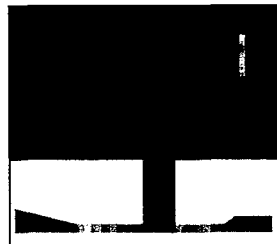


(d) $t = t_0 + 3T/5$

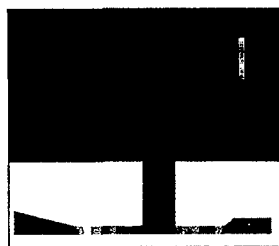




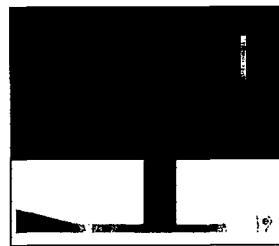
(a) "Initial" state, $t = t_0$



(b) $t = t_0 + T / 5$



(c) $t = t_0 + 2T / 5$



(d) $t = t_0 + 3T / 5$



Table 5.4: Comparison of simulation versus theory for two geometries

Case # / Type of Data	Helmholtz Frequency	Screech Frequency
9 / Simulation	2,264 Hz-decaying	Not observed
9 / Theory	2,210 Hz	N/A
10 / Simulation	2,500Hz-decayed	15,454Hz dominant
10 / Theory	1,753 Hz	15,720 Hz

in Figure 5.24, which shows the vorticity contours throughout the cycle. In the first snapshot, the outflow from the resonator is just changing to inflow as the chamber starts to refill. The trapped vortex sitting at the slot exit is being fed by a shear layer which emerges from the air supply line, crosses to the far side of the slot, and then bends upward and heads for the slot exit. In 5.24(b) and 5.24(c), the chamber is pulling in fluid, which then separates as it passes the expansion section and enters the Helmholtz resonator. The shear layer which feeds the vortex at the slot exit has been disrupted, causing it to weaken. In 5.24(d), the chamber has begun pushing out the fluid it ingested. Interestingly, however, the “replacement” vortex that is forming to take the place of the original vortex at the slot exit is not created by fluid emerging from the cavity (at least not directly). Instead, the vortex appears to be forming due to instabilities that form in the weakened shear layer which was feeding the trapped vortex. In 5.24(d), the new vortex is traveling up the slot until, in 5.24(e), it can be seen displacing the original vortex, which, greatly diminished is shown being pushed out in 5.24(f) (as well as 5.24(a)).

5.4.4 Nonlinear Effects

A big picture comparison between the simulations and the theory for two different geometries is presented in Table 5.4. This data corresponds to a geometry with $s/D = 1$ (integration slot width to supply jet diameter) and a Nozzle Pressure Ratio (NPR) = 3.52. The simulation Reynolds numbers were “low” for these cases (freestream pressure was 0.03 psia). The supply jet and Helmholtz neck diameter were both 1/4” with a Helmholtz backing cavity diameter of 1/2”. The main points to be made from the data in Table 5.4 are that in case 9, the Helmholtz response for the simulation corresponds very closely with the theory (no screech present), while in case 10 screech is present and the agreement between theory and simulation is not nearly as close.

We get more of an idea of the behavior of the Helmholtz system from the data contained in Table 5.5. The tabulated data corresponds to $s/D = 2$. The simulation Reynolds numbers were “medium” for these cases (0.12 psia. freestream pressure). The supply jet and Helmholtz neck diameter were both 1/8” for these cases with a Helmholtz backing cavity diameter of 1/4”. The main themes that can be observed from the data in Table 5.5 include the Helmholtz response predicted by theory is in reasonable agreement with experiment and computation when screech is not present. Also, increasing NPR above 3 decreases the likelihood of a Helmholtz response and increases the likelihood of screech. And finally, the presence of screech seems to shift the Helmholtz response if it is present.

Figures 5.25 and 5.26 show the pressure time histories for simulation cases 9 and 10. The pressure is monitored outside the integration slot about 1/4” from the edge of the slot. Figure 5.25 shows the development of a very periodic signal with weak damping, but as Table 5.4 showed, the Helmholtz frequency matches theory very well. At higher Reynolds numbers this unsteady response would likely not be damped. In Figure 5.26 the signal starts to give a Helmholtz response, but this gives way to a screech response of much higher frequency. As Table 5.4 showed, the screech frequency matches the predicted frequency of a screeching free jet. However, this may be a coincidence since the presence of the resonance tube can be expected to alter the jet shock structure and therefore the screech frequency.

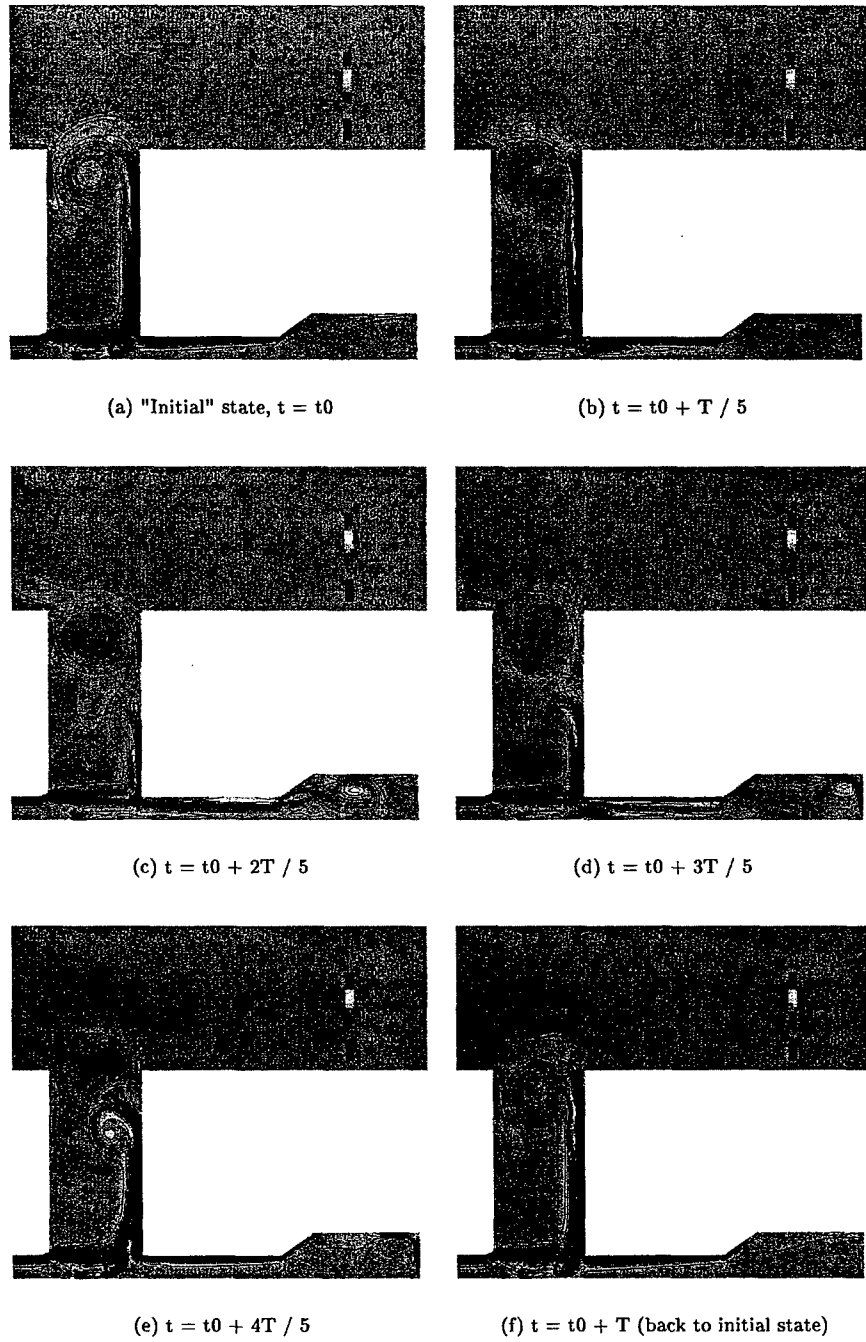


Figure 5.24: Snapshots of vorticity in the nozzle, slot, and resonator from one operational cycle of the PRT

Table 5.5: Comparison of Simulation, Theory, and Experiment

Case # /type	NPR	Helmholtz freq	Screech freq	Peak SPL
11 / Experiment	3	2,500 Hz	Not observed	137 dB
11 / Simulation	3	1,964 Hz	Not observed	142 dB
11 / Theory	N/A	2,290 Hz	Not calculated	Not predicted
12 / Experiment	4.67	~ 4,000 Hz	~18,000 Hz	137 dB
12 / Simulation	4.67	~2,700	~17,500 Hz	Not measured
12 / Theory	N/A	2,290 Hz	Not calculated	Not predicted
13 / Experiment	6	None observed	~14,000 Hz	139 dB
13 / Simulation	6	None observed	~18,000 Hz	Not measured
13 / Theory	N/A	2,290 Hz	Not calculated	Not predicted

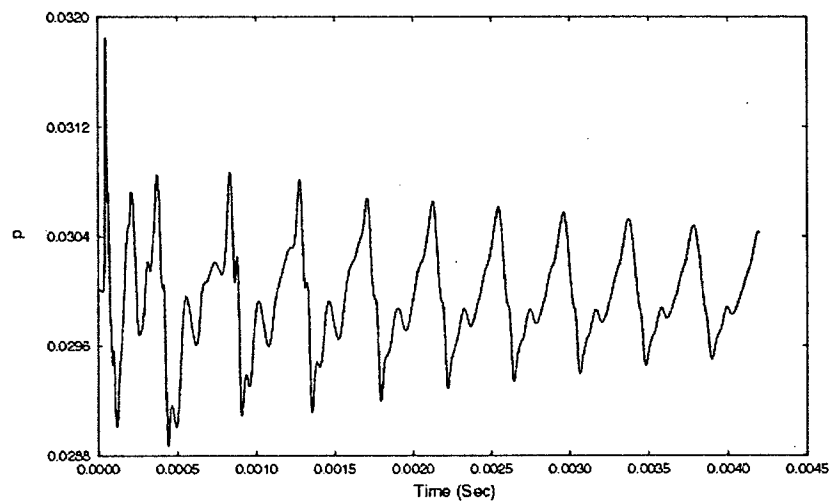


Figure 5.25: Pressure time history for simulation case 9 measured about 1/4" downstream of the integration slot, 60,000 timesteps.

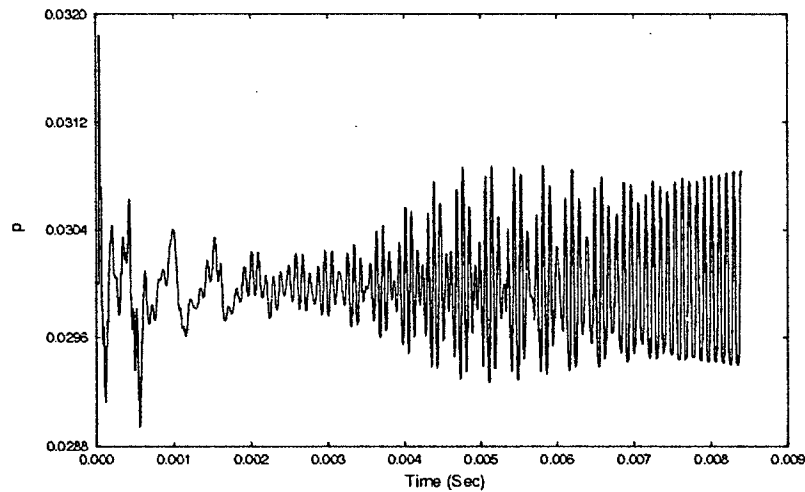


Figure 5.26: Pressure time history for simulation case 10 measured about 1/4" downstream of the integration slot, 120,000 timesteps.

Figure 5.27 presents the pressure time history of simulation case 11. A strongly periodic behavior is apparent in the pressure time history. The signal is a superposition of a primary Helmholtz response and a higher frequency at roughly three times the Helmholtz frequency. The frequency content of Figure 5.27 can be examined by taking the Fourier transform in time, leading to the frequency domain plot shown in Figure 5.28. There are two features in Figure 5.28 that deserve comment. The first feature of significance is the width of the peaks. The relatively broad peaks are due to the relatively short period in which data was collected and the fact that during this short time there was some variation in the structure of the primary waveform, though Figure 5.27 shows a very repeatable pattern.

Figure 5.29 shows instantaneous pressure contours for simulation case 11. The pressure is normalized such that the freestream value is the inverse of the ratio of specific heats. The freestream pressure is 0.12 psia. This value of pressure, and therefore the Reynolds number, is intermediate between the high and low Reynolds number cases shown earlier. Thus, the contours look very consistent with what we should expect for an intermediate Reynolds number case.

5.5 Conclusions regarding PRT Simulations

The simulations of straight tube actuators show that the dominant frequencies, amplitude and directivity of the PRT actuator output field are largely unaffected by the factor of 10 increase in Reynolds number considered here. However, the increase in Reynolds number is shown to substantially affect the width of the resonance peaks, and the vorticity distributions and flow details more generally. The effort to integrate simulations, theory, and experiment has been fruitful. There is general agreement between these three methods in terms of the frequency, amplitude, and directivity of the actuator output field, to the extent that they have been examined.

The present study shows that a Helmholtz based PRT offers a method of substantially improving applicability when there are space constraints. Simulation results for such designs were compared

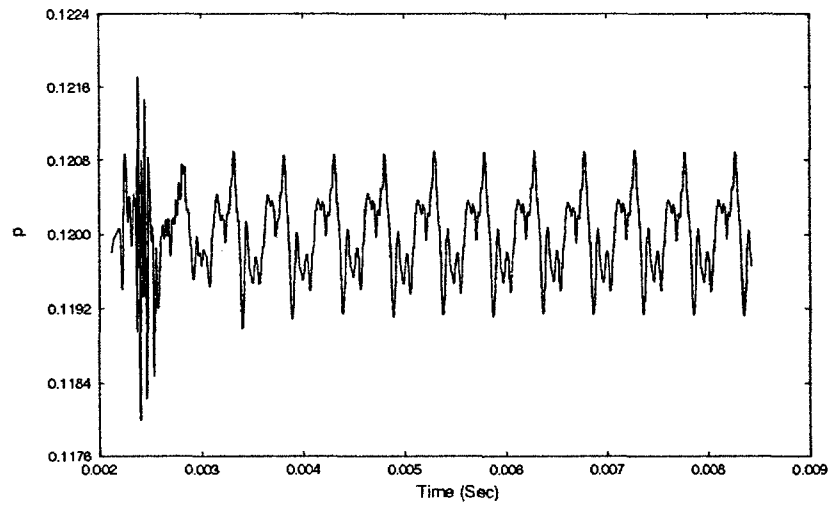


Figure 5.27: Pressure time history for simulation case 11, 90,000 timesteps.

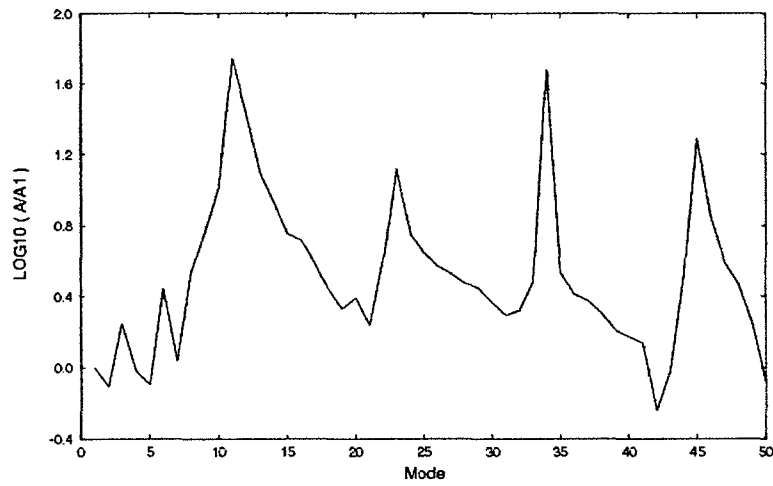


Figure 5.28: The Fourier transform of the pressure time history for simulation case 11.

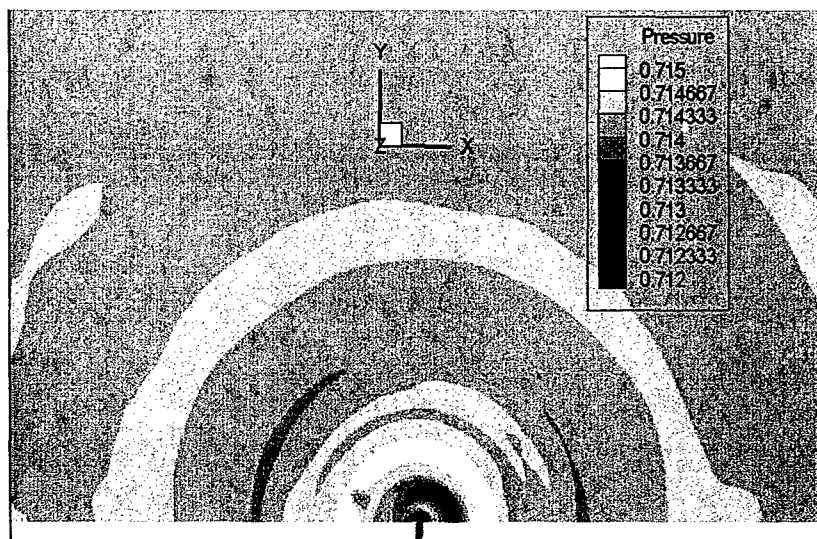


Figure 5.29: Instantaneous pressure contours for case 11 after 120,000 time steps.

to theory and experiment. At low NPR values a Helmholtz response in simulations and experiments shows good correspondence with theory. At higher values of NPR the computational and experimental comparisons to theory suggest that non-linear effects must be considered and that screech in particular can suppress or shift the Helmholtz response. A useful synergy has been demonstrated between simulation, theory, and experiment.

Simulations were conducted of Helmholtz PRT geometries to ascertain the utility of using a Helmholtz resonator in place of a straight tube in order to lower the resonant frequency without increasing the size excessively. In addition, the simulations were compared to the theory of Kerschen to further assess the capabilities of that theory and, conversely, to assist in verifying the simulations. As predicted by the theory, it was found that the Helmholtz resonator based PRTs did lower the frequency of the primary mode, but the peak sound pressure level was also substantially decreased. The Kerschen theory and the simulations, while qualitatively in agreement, showed somewhat more error than in previous work. Other areas which could prove important include the resolution in the resonance cavity and integration slot. Finally, the axi-symmetric assumption could be limiting the accuracy of the solution.

Chapter 6

Helmholtz PRT Theory

6.1 Introduction

Active flow control (AFC) offers the promise of performance improvements for a number of aerospace applications. AFC has been shown to improve mixing in shear flows [Wiltse and Glezer, 1998], reduce or eliminate flow separation [Greenblatt and Wygnanski, 2000], and suppress resonance tones in cavities [Stanek et al., 2001]. AFC applications require actuators that are capable of producing high-amplitude unsteady fields. One candidate actuator technology is the powered resonance tube (PRT) actuator.

The PRT actuator consists of an open-closed quarter-wavelength tube resonator, excited by a high-speed jet that impinges normally on the open end of the tube. An integration slot lies between the exit plane of the driving jet and the open end of the resonance tube. The unsteady flow produced by the PRT actuator exits from the open edge of the integration slot. Under proper geometric and flow conditions, the PRT actuator produces a high-amplitude unsteady field. Additional information concerning PRT actuators may be found in [Kastner and Samimy, 2002], [Raman and Cain, 2004] and [Raman et al., 2004a].

In some applications that require relatively low actuator frequencies, geometrical constraints may be incompatible with the use of a quarter-wavelength resonance tube. Note that the resonance tube length is inversely proportional to the resonant frequency, and is therefore quite long for the case of low resonant frequencies. For example, if one considers a resonant frequency $f = 200$ Hz in air at standard temperature, the quarter-wavelength is $\lambda_{ac}/4 = c/4f = 1.4$ ft.

A Helmholtz resonator can achieve low frequencies without such large linear dimensions, by combining a narrow neck with a backing cavity of much larger cross section. Recall that the resonant frequency of a simple spring-mass system is given by $\omega = (k/m)^{1/2}$, where k is the spring constant and m is the mass. For the Helmholtz resonator, the fluid in the narrow neck provides the mass, while the compressibility of the fluid in the backing cavity provides the spring constant. The frequency can be lowered by increasing the mass in the neck, or by increasing the capacitance of the backing cavity.

The above discussion suggests that the concept of a Helmholtz PRT, in which the quarter-wavelength resonance tube is replaced by a Helmholtz resonator, merits investigation as an alternative to the standard PRT design for the case of low frequencies. In this chapter, an analytical investigation of Helmholtz resonator properties is presented, in order to provide guidance in the selection of appropriate geometries for a Helmholtz PRT. The influence of resonator geometry on the resonant frequency and the capacity of a Helmholtz resonator is examined.

Two theories for Helmholtz resonator behavior have been developed, the axial-wave theory and the low-frequency theory. In both theories, the cross-sectional dimensions of the resonator neck and cavity are assumed small compared to the acoustic wavelength. This allows transverse wave motion to be ignored in the analysis, leading to significant simplifications.

In the axial-wave theory, the cross-sectional dimensions of the neck and cavity are assumed small compared to λ_{ac} , but the lengths of the neck and cavity are assumed to be of the order of λ_{ac} . Hence, the axial-wave theory also predicts the behavior of a quarter-wavelength resonance tube, in the limit where the cross-sectional areas of the neck and the cavity are equal. Thus, the axial-wave theory can be used to investigate the transition from Helmholtz behavior to quarter-wavelength behavior, as the geometry of the resonator is varied.

In the low-frequency theory, the lengths of the neck and the cavity are also assumed to be small compared to the acoustic wavelength. This may be true in many applications, and leads to the simplest formulas. However, the low-frequency theory has the disadvantage that the transition from Helmholtz behavior to quarter-wavelength behavior, as the resonator geometry is varied, cannot be explored with this theory. A second disadvantage is that the low-frequency theory over-predicts the resonant frequency, although the over-prediction is fairly modest for conditions of interest for PRT actuator applications.

The axial-wave theory is developed in section 6.2, and the low-frequency theory is developed in section 6.3. The influence of Helmholtz resonator geometry on the resonant frequency, mode shape and capacity is examined in section 6.4.

Based on the results presented in this paper, resonator geometries were chosen for numerical simulations and laboratory experiments. A preliminary comparison of theoretical predictions to numerical simulations is presented in subsection 6.4.4. Additional comparisons with numerical and experimental results are presented in [Cain et al., 2004].

6.2 Axial-wave theory for a Helmholtz resonator

For the axial-wave theory, one can assume that the cross-sectional dimensions of the neck and cavity are small compared to the acoustic wavelength, but the lengths of the neck and cavity may be of the order of λ_{ac} . In this case, only 'plane' acoustic waves propagate in the neck and cavity—the higher-order transverse modes are cut-off and decay exponentially with axial distance in the neck or cavity. Thus, three-dimensional effects are important only in the vicinity of the junction between the neck and the cavity, and in the vicinity of the entrance to the neck. The length scale for these local regions is the neck diameter d_n , which is assumed small compared to the acoustic wavelength. Hence, the field in these local regions behaves incompressibly. The influence of these local regions on the system behavior can then be accounted for by adding end corrections to the neck length, as discussed in subsection 6.2.1. In the analysis that follows, the neck length l_n includes the end corrections for the neck entrance and for the junction with the backing cavity.

Assuming that the frequency is high enough that the viscous Stokes layer thickness of $O((\nu/\omega)^{1/2})$ is small compared to the cross-sectional dimensions of the neck, acoustic perturbations of a base state with pressure p_0 , density ρ_0 and speed of sound c can now be considered. The pressure and density perturbations are related by the isentropic equation $p = c^2 \rho$. For one-dimensional wave motion, the continuity and momentum equations for the acoustic perturbations then take the form

$$\partial p / \partial t + \rho_0 c^2 \partial u / \partial x = 0 \quad \text{and} \quad \rho_0 \partial u / \partial t = -\partial p / \partial x, \quad (6.1)$$

where $c^2 = \gamma p_0 / \rho_0 = \gamma R T$. These equations can be combined to obtain the one-dimensional wave equation for the acoustic pressure,

$$c^2 \partial^2 p / \partial x^2 - \partial^2 p / \partial t^2 = 0. \quad (6.2)$$

For time-harmonic motion, the solution to the wave equation can be expressed as a superposition of forward- and backward-propagating plane waves

$$p(x, t) = [C_1 e^{ikx} + C_2 e^{-ikx}] e^{-i\omega t}, \quad (6.3)$$

where $k = \omega/c$ and C_1 and C_2 are arbitrary constants.

For convenience, choose the origin of the coordinate system at the entrance to the neck (including the end correction for the neck entrance). The neck length is l_n (including both end corrections) and the cavity length is l_c . The rear surface of the cavity is assumed to be rigid, so that the one-dimensional acoustic field in the cavity has the standing wave form

$$p(x, t) = B_1 \cos k(x - l_n - l_c) e^{-i\omega t}. \quad (6.4)$$

Note that (6.4) satisfies $\partial p / \partial x = 0$ at the back of the cavity ($x = l_n + l_c$). The constant B_1 is arbitrary at this stage.

The acoustic field in the neck is a superposition of forward- and backward-propagating plane waves,

$$p(x, t) = \frac{1}{2} (B_2 e^{ikx} + B_3 e^{-ikx}) e^{-i\omega t}. \quad (6.5)$$

The matching conditions at the junction between the neck and the cavity are continuity of pressure,

$$\frac{1}{2} (B_2 e^{ikl_n} + B_3 e^{-ikl_n}) = B_1 \cos kl_c, \quad (6.6)$$

and continuity of volume flux,

$$\frac{1}{2} A_n (B_2 e^{ikl_n} - B_3 e^{-ikl_n}) = -i A_c B_1 \sin kl_c, \quad (6.7)$$

where A_n and A_c are the cross-sectional areas of the neck and cavity, respectively. Finally, a pressure boundary condition at the entrance to the neck, say $p = p_e e^{-i\omega t}$ at $x = 0$ is specified. This yields

$$\frac{1}{2} (B_2 + B_3) = p_e. \quad (6.8)$$

The cases of free response ($p_e = 0$) and forced response ($p_e \neq 0$) of a Helmholtz resonator are examined in subsections 6.2.2 and 6.2.3, respectively.

6.2.1 End corrections

As mentioned above, three-dimensional effects occur in the vicinity of the junction between the neck and the cavity, and in the vicinity of the entrance to the neck. These three-dimensional effects are associated with the expansion of the flow in exiting the neck, or the contraction of the flow in entering the neck. The three-dimensional flow adds additional inertia to the system, which can be accounted for by adding an end correction Δl_n to the geometric neck length $l_{n\text{geom}}$ (see [Pierce, 1989], pp. 341–350). The effective neck length is then

$$l_{n\text{eff}} = l_{n\text{geom}} + \Delta l_n. \quad (6.9)$$

The end correction Δl_n can be calculated using incompressible potential flow theory, or estimated using upper and lower bounds arising from kinetic energy principles for incompressible potential flow. Here, results from Pierce are quoted for specific cases of interest.

Consider axisymmetric geometries. For a neck length $l_{n\text{geom}}$ that is short compared to the neck diameter d_n , the local flow is similar to flow through a circular orifice in a plate of zero thickness. Using the analytical solution for the potential flow in this case, the end correction is given by

$$\Delta l_n = \frac{1}{4} \pi d_n \doteq 0.785 d_n. \quad (6.10)$$

This expression accounts for the additional inertia due to the three-dimensional flow at both ends of the neck. Next consider neck lengths that are large compared to the neck diameter. If the geometry of the neck end has an infinite flange, the end correction (for one end) is

$$\Delta l_n = 0.41 d_n. \quad (6.11)$$

At the other extreme, if the geometry of the neck end is that of a thin-walled tube protruding into open space, the end correction (for one end) is

$$\Delta l_n = 0.305 d_n. \quad (6.12)$$

The end correction for the thin-walled tube protruding into open space is smaller than that for the flanged tube, because the flow outside the tube has a greater area to expand into and the velocity decays more rapidly. Hence, the flow field outside the tube end has less total inertia in this case.

The geometry currently being considered for the Helmholtz PRT actuator has a flange at both ends of the neck. If the neck length is long compared to the neck diameter, the effective neck length is then

$$l_{n\text{eff}} = l_{n\text{geom}} + 0.82 d_n. \quad (6.13)$$

In order to simplify the notation in the remainder of this report, the symbol l_n is used to denote the effective neck length (including end corrections), rather than the geometric neck length.

6.2.2 Axial-wave theory: free response of a Helmholtz resonator

The natural frequency for the Helmholtz resonator is obtained by setting the pressure p_e at the neck entrance to zero. One then has $B_3 = -B_2$, and the pressure and volume flux matching conditions at the junction between the neck and the cavity provide a homogeneous set of linear equations for B_1 and B_2 ,

$$\begin{bmatrix} \cos kl_c & -i \sin kl_n \\ i \sin kl_c & \frac{A_n}{A_c} \cos kl_n \end{bmatrix} \begin{bmatrix} B_1 \\ B_2 \end{bmatrix} = 0. \quad (6.14)$$

Setting the determinant of the matrix in (6.14) to zero, one obtains a transcendental equation for the natural frequencies of the Helmholtz resonator

$$\frac{A_n}{A_c} \cos kl_n \cos kl_c - \sin kl_n \sin kl_c = 0. \quad (6.15)$$

This equation has an infinite number of roots $k_j = \omega_j/c$, $j = 1, 2, 3, \dots$. The main interest is in the first root, corresponding to the lowest natural frequency of the Helmholtz resonator.

For convenience in interpreting the results, one can recast the transcendental equation in terms of a Helmholtz number

$$\Omega = \omega l/c, \quad (6.16)$$

where $l = l_n + l_c$ is the total effective length of the Helmholtz resonator, including the end corrections at both ends of the neck. Setting

$$\alpha_n = l_n/l, \quad \alpha_c = l_c/l \quad (6.17)$$

and utilizing trigonometric identities, we obtain

$$F(\Omega) = 0, \quad (6.18)$$

where

$$F(\Omega) = \left[1 + \frac{A_n}{A_c} \right] \cos \Omega - \left[1 - \frac{A_n}{A_c} \right] \cos(2\alpha_n - 1)\Omega \quad (6.19)$$

and the relationship $\alpha_n + \alpha_c = 1$ has been used to eliminate α_c .

Considering the Helmholtz resonator eigenvalue relationship (6.18) as an equation for Ω as a function of α_n , implicit differentiation can be used to show that the minimum value of Ω is obtained for $\alpha_n = 1/2$. Hence, for a Helmholtz resonator of fixed length, the minimum frequency is obtained for the case $l_n = l_c$ (where l_n contains the neck end corrections). Setting $\alpha_n = 1/2$, one can solve (6.18) to obtain the following expression for the minimum resonant frequency as a function of the area ratio,

$$\Omega = \cos^{-1} \left[\frac{1 - A_n/A_c}{1 + A_n/A_c} \right] \quad \text{for} \quad \alpha_n = 1/2. \quad (6.20)$$

Note that, for $A_n/A_c < 1$, the resonant frequency of a Helmholtz resonator is lower than that of a quarter-wavelength tube of the same length. Substantial reductions in the resonant frequency can be obtained when A_n/A_c is sufficiently small.

Note that (6.19) is unchanged by the substitution $\alpha_n \rightarrow 1 - \alpha_n$. Thus, the function $\Omega(\alpha_n)$ is symmetric about $\alpha_n = 1/2$. If one recalls that $\alpha_c = 1 - \alpha_n$, it can be seen that the resonant frequency of the Helmholtz resonator is unchanged when the lengths of the neck and cavity are interchanged. While this interchange does not affect the resonant frequency, it does affect the capacity as will be seen in the following subsection.

Finally, the eigenvalue relationship for a quarter-wavelength resonance tube is obtained from (6.18) by setting $A_n = A_c$. The dependence on α_n disappears in this limit and the eigenvalue relationship reduces to $\cos \Omega = 0$, with roots $\Omega_j = (2j - 1)\pi/2$, $j = 1, 2, 3, \dots$

In section 6.4, numerical results are presented that illustrate the variation of the resonant frequency of a Helmholtz resonator, as a function of the cavity area ratio A_c/A_n and the non-dimensional neck length $\alpha_n = l_n/l$.

6.2.3 Axial-wave theory: forced response of a Helmholtz resonator

The unsteady volume flux produced by a PRT actuator is due primarily to the unsteady volume flux stored by the resonator. Thus, in order to assess the suitability of a Helmholtz resonator as a replacement for the quarter-wavelength tube of a PRT actuator, one must also consider the capacity of a Helmholtz resonator.

The capacity of the resonator is defined as the unsteady volume flux which it stores, for a given external pressure fluctuation $p_e e^{-i\omega t}$. Clearly, the capacity is proportional to the cross-sectional area of the mouth of the resonator (A_n in the case of a Helmholtz resonator), and also to the amplitude p_e of the external pressure field for the case of a linear system. In order to remove these dependencies, the non-dimensional capacity is defined as

$$C = \frac{\rho_0 c}{p_e} u|_{x=0}. \quad (6.21)$$

In deriving an expression for the resonant frequency in subsection 6.2.2, the external pressure p_e was set to zero. Therefore, according to the analysis of subsection 6.2.2, the capacity is infinite at the resonant frequency, $\omega = \omega_1$. Essentially, in the absence of any damping mechanisms, finite velocity fluctuations can be maintained with no forcing from the external field. If damping mechanisms such as fluid viscosity and acoustic radiation to the far field were incorporated in the modeling, the unforced 'resonant response' would be a temporal oscillation that decays exponentially in time, corresponding to a complex value of ω_1 . In this situation, a time-harmonic forcing field $p_e e^{-i\omega t}$ would be required in order to obtain a time-harmonic unsteady field in the resonator, and the amplitude of the response (or the capacity) at the resonant frequency would depend on the damping in the system. Estimates of resonator damping may be considered in future work.

An alternative is to consider the capacity at frequencies near, but not equal to, the resonant frequency ω_1 . The following arguments suggest that this measure of capacity may be relevant to the operation

of a PRT actuator. One viewpoint is to consider the unsteady motion in the resonance tube as a response due to forcing by the unsteady field of the supply jet within the integration slot region. A second viewpoint is to consider the PRT actuator as a coupled system involving two resonant components: the unsteady jet field in the integration slot, and the field in the resonance tube. Such coupled systems typically have resonant frequencies that are close to, but not exactly equal to, the resonant frequency for one of the resonant components. Both these viewpoints suggest that the capacity of the resonator (Helmholtz or quarter-wavelength tube) at frequencies close to, but not equal to, the resonator natural frequency ω_1 is of interest.

In order to determine the capacity of a Helmholtz resonator, one simply repeat the analysis of subsection 6.2.2, assuming that the external pressure p_e is non-zero. Substituting the boundary condition (6.8) at the neck entrance into the matching conditions (6.6, 6.7) at the junction between the neck and the cavity, one obtain the simultaneous set of equations

$$\begin{bmatrix} \cos kl_c & -i \sin kl_n \\ i \sin kl_c & \frac{A_n}{A_c} \cos kl_n \end{bmatrix} \begin{bmatrix} B_1 \\ B_2 \end{bmatrix} = \begin{bmatrix} 1 \\ \frac{A_n}{A_c} \end{bmatrix} p_e e^{-ikl_n}. \quad (6.22)$$

Solving this system of equations, and using (6.8) to determine B_3 , one finds

$$B_1 = 2p_e A_n / A_c F(\Omega) \quad (6.23)$$

$$B_2 = p_e [(1 + A_n/A_c)e^{-i\Omega} - (1 - A_n/A_c)e^{-i(2\alpha_n-1)\Omega}] / F(\Omega) \quad (6.24)$$

$$B_3 = p_e [(1 + A_n/A_c)e^{i\Omega} - (1 - A_n/A_c)e^{i(2\alpha_n-1)\Omega}] / F(\Omega), \quad (6.25)$$

where $F(\Omega)$ is defined by (6.19). Note that B_3 is the complex conjugate of B_2 . The capacity is then given by $C = (B_2 - B_3)/2p_e$, which leads to the expression

$$C = -i \frac{(1 + A_n/A_c) \sin \Omega - (1 - A_n/A_c) \sin(2\alpha_n - 1)\Omega}{(1 + A_n/A_c) \cos \Omega - (1 - A_n/A_c) \cos(2\alpha_n - 1)\Omega} \quad (6.26)$$

where the denominator of (6.26) is $F(\Omega)$. The capacity of the Helmholtz resonator is seen to be purely imaginary, as it must be for a time-harmonic solution in the absence of damping mechanisms. Since the natural frequencies of the Helmholtz resonator are given by $F(\Omega) = 0$, one can see that the capacity is infinite when $\Omega = \Omega_1$, as expected.

The capacity for a quarter-wavelength resonance tube is obtained from (6.26) by setting $A_n/A_c = 1$, leading to

$$C_{qw} = -i \tan \Omega. \quad (6.27)$$

Note that the capacity of a quarter-wavelength tube is a periodic function of frequency. It is infinite at the resonant frequencies, $\Omega_j = (2j - 1)\pi/2$, $j = 1, 2, 3, \dots$, as expected. The capacity is negative imaginary below the first resonant frequency ($\Omega < \pi/2$), while it is positive imaginary above the first resonant frequency in the range $\pi/2 < \Omega < \pi$.

The capacity for a Helmholtz resonator is also negative imaginary for frequencies below the first resonant frequency, and positive imaginary in a frequency range above the first resonant frequency. In section 6.4.3, numerical results are presented for the capacity of Helmholtz resonators as a function of the cavity area ratio A_c/A_n and the non-dimensional neck length $\alpha_n = l_n/l$. These results demonstrate that, with proper choice of geometric parameters, the capacity of a Helmholtz resonator exceeds that for a quarter-wavelength tube with the same resonant frequency.

6.3 Low-frequency theory for a Helmholtz resonator

In this section, a simpler low-frequency theory for the Helmholtz resonator is developed, in order to further illuminate the physical behavior. In the low-frequency theory, one assumes that all linear

dimensions of the Helmholtz resonator are small compared to the acoustic wavelength. In this case, the fluid in the neck can be considered incompressible. Assuming that the frequency is high enough that the viscous Stokes layer thickness of $O((\nu/\omega)^{1/2})$ is small compared to the cross-sectional dimensions of the neck, the fluid in the neck can be approximated by a unidirectional plug flow,

$$u(x, t) = u_n e^{-i\omega t}. \quad (6.28)$$

It is assumed that the pressure at the entrance to the neck is specified, say $p = p_e e^{-i\omega t}$ at $x = 0$. Noting that the pressure gradient for an incompressible unidirectional flow is independent of x , the momentum equation can be integrated to determine the pressure at the interface with the backing cavity,

$$p(l_n, t) = (p_e + i\omega\rho_0 l_n u_n) e^{-i\omega t}. \quad (6.29)$$

Next consider the backing cavity. Since the cross-sectional area of the backing cavity is assumed large compared to that of the neck, the velocities within the backing cavity are negligible. If one also assumes that the linear dimensions of the backing cavity are small compared to the acoustic wavelength, the density ρ_b and pressure p_b in the backing cavity are approximately uniform. The density perturbation is related to the volume inflow/outflow from the neck. Application of the integral continuity equation to the backing cavity produces

$$-i\omega\rho_b V_c - \rho_0 u_n A_n = 0,$$

where V_c is the volume of the backing cavity and A_n is the cross-sectional area of the neck. Assuming that the pressure and density perturbations in the backing cavity satisfy the isentropic equation of state ($p_b = c^2 \rho_b$), one obtains

$$p_b = i \frac{\rho_0 c^2 A_n}{\omega V_c} u_n. \quad (6.30)$$

Finally, the pressure must be continuous at the interface between the neck and backing cavity, so that $p(l_n, t) = p_b e^{-i\omega t}$. Equating (6.29) and (6.30), yields obtain

$$p_b - p_e = i\omega\rho_0 l_n u_n. \quad (6.31)$$

Equations (6.30) and (6.31) control the dynamics of the Helmholtz resonator.

6.3.1 Low-frequency theory: free response of a Helmholtz resonator

The natural frequency for the Helmholtz resonator is obtained by setting the pressure p_e at the neck entrance ($x = 0$) to zero. Equations (6.30) and (6.31) then provide a homogeneous set of linear equations for u_n and p_b ,

$$\begin{bmatrix} \rho_0 c^2 A_n & i\omega V_c \\ -i\omega\rho_0 l_n & 1 \end{bmatrix} \begin{bmatrix} u_n \\ p_b \end{bmatrix} = \mathbf{0}. \quad (6.32)$$

Non-trivial solutions to (6.32) exist only when the determinant of the coefficient matrix is zero. Setting the determinant equal to zero, the natural frequency of the Helmholtz resonator is found to be

$$\omega_1 = c(A_n/l_n V_c)^{1/2}. \quad (6.33)$$

The low-frequency theory provides an approximate expression for the lowest natural frequency of the Helmholtz resonator; therefore the natural frequency has been labeled as ω_1 , for consistency with the notation of section 6.2.2. We see that the resonant frequency of the Helmholtz resonator can be decreased by increasing the length of the neck, or by increasing the volume of the backing cavity.

Consider a backing cavity of cross-sectional area A_c and length l_c . The natural frequency of the Helmholtz resonator then takes the form

$$\omega_1 = c \frac{(A_n/A_c)^{1/2}}{(l_n l_c)^{1/2}}. \quad (6.34)$$

Recasting this expression in terms of the Helmholtz number $\Omega = \omega l/c$, where $l = l_n + l_c$, and introducing other notation from section 6.2.2, one obtains

$$\Omega_1 = \frac{(A_n/A_c)^{1/2}}{[(1 - \alpha_n)\alpha_n]^{1/2}}. \quad (6.35)$$

The low-frequency theory has assumed that the cross-sectional area of the neck is small compared to that of the backing cavity ($A_n/A_c \ll 1$). In the low-frequency limit, the Helmholtz number is seen to be proportional to the square root of the area ratio. For an axisymmetric geometry with neck diameter d_n and cavity diameter d_c , Ω_1 depends linearly on d_n/d_c .

Next consider the dependence of Ω_1 on the neck length parameter $\alpha_n = l_n/l$. It is easy to show that Ω_1 takes on its minimum value at $\alpha_n = 1/2$, corresponding to $l_n = l_c = l/2$. This feature was also seen in the axial-wave theory. Setting $\alpha_n = 1/2$ in (6.35), yields the low-frequency prediction

$$\Omega_1 = \frac{1}{2} (A_n/A_c)^{1/2} \quad \text{for} \quad \alpha_n = 1/2. \quad (6.36)$$

The explicit form of (6.35) allows the influence of changes in the neck length to be examined easily. For example, if one sets $\alpha_n = 0.25$ or 0.75 , the resonant frequency Ω_1 is increased by only 15% relative to the value for $\alpha_n = 0.5$. Thus, the 'minimum' of Ω_1 as a function of α_n is fairly broad, so that values of $\alpha_n \neq 0.5$ produce only a modest increase above the minimum resonant frequency, as long as one stays away from the end points $\alpha_n = 0$ or 1 .

Comparisons of the axial-wave and low-frequency predictions for the natural frequency of a Helmholtz resonator are presented in subsection 6.4.1.

6.3.2 Low-frequency theory: forced response of a Helmholtz resonator

To analyze the forced response of a Helmholtz resonator, one repeats the analysis of subsection 6.3.1, assuming a non-zero value of the external pressure p_e . Combining (6.30) and (6.31), the inhomogeneous system of linear equations is obtained

$$\begin{bmatrix} \rho_0 c^2 A_n & i\omega V_c \\ -i\rho_0 \omega l_n & 1 \end{bmatrix} \begin{bmatrix} u_n \\ p_b \end{bmatrix} = \begin{bmatrix} 0 \\ p_e \end{bmatrix}. \quad (6.37)$$

The solution to this inhomogeneous matrix equation is

$$\begin{bmatrix} u_n \\ p_b \end{bmatrix} = \frac{p_e}{(c^2 A_n - \omega^2 l_n V_c)} \begin{bmatrix} -i\omega V_c \\ c^2 A_n \end{bmatrix}. \quad (6.38)$$

Using this result in (6.21), one obtains the low-frequency prediction for the Helmholtz resonator capacity,

$$C = -i \frac{V_c}{c A_n} \frac{\omega}{[1 - (\omega/\omega_1)^2]}. \quad (6.39)$$

For a backing cavity of cross-sectional area A_c and length l_c , (6.39) takes the form

$$C = -i \left[\frac{(1 - \alpha_n) A_c}{\alpha_n A_n} \right] \frac{\Omega/\Omega_1}{[1 - (\Omega/\Omega_1)^2]}, \quad (6.40)$$

where 6.35 has been utilized.

Several features of the physical behavior are apparent from the low-frequency expression (6.40) for the capacity. The low-frequency theory requires $A_c/A_n \gg 1$; one can see that the capacity is $O((A_c/A_n)^{1/2})$ in this limit. As was seen from the axial-wave theory, the capacity is negative imaginary for $\Omega < \Omega_1$, positive imaginary for $\Omega > \Omega_1$, and infinite at $\Omega = \Omega_1$. From (6.35), it can be seen that the resonant frequency Ω_1 is invariant to an interchange of l_n and l_c (or equivalently, to the substitution $\alpha_n \rightarrow 1 - \alpha_n$). However, the capacity does not have this property. Noting that $(1 - \alpha_n)/\alpha_n = l_c/l_n$, it can be seen that the capacity is increased if the interchange of l_n and l_c decreases the neck length, whereas the capacity is decreased if the interchange increases the neck length.

The low-frequency expression (6.40) for the capacity allows the influence of neck length to be easily examined. In subsection 6.3.1, it was seen that a change in the neck length parameter α_n from 0.5 to 0.25 (or 0.75) increased the resonant frequency by only 15%. However, these changes in the neck length have a major influence on the Helmholtz resonator capacity. A decrease in the neck length parameter α_n from 0.5 to 0.25 increases the capacity by a factor of 1.73, whereas an increase in α_n from 0.5 to 0.75 decreases the capacity by this same factor. While the cases $\alpha_n = 0.25$ and 0.75 have the same resonant frequency, the capacity for $\alpha_n = 0.25$ is three times that for $\alpha_n = 0.75$.

In subsection 6.4.3, the axial-wave and low-frequency predictions for the capacity of a Helmholtz resonator are compared.

6.4 Numerical results and discussion

In this section, numerical results for the free and forced response of a Helmholtz resonator, obtained from the axial-wave theory and the low-frequency theory are presented. The numerical results were obtained using *Mathematica* [Wolfram, 1996] on a personal computer.

6.4.1 Resonance frequencies

The resonant frequencies for the Helmholtz resonator are the roots of (6.18), a transcendental equation which has an infinite number of roots. Since the investigation of Helmholtz resonators is motivated by a desire for low resonant frequencies, the focus is on the lowest root $j = 1$. In Figure 6.1 (Figure 1.4 repeated for convenience), the non-dimensional resonant frequency $\Omega_1 = \omega_1 l/c$ obtained from the axial-wave theory is plotted as a function of normalized neck length $\alpha_n = l_n/l$ (including the neck end corrections), for several values of the area ratio A_c/A_n . For $\alpha_n = 0$ or 1 , the geometry degenerates to a quarter-wavelength tube and the resonant frequency takes on the quarter-wavelength value $\Omega_1 = \pi/2 \doteq 1.571$. For $A_c/A_n = 1$ (not shown in Figure 6.1), the geometry also degenerates to a quarter-wavelength tube and the resonant frequency is $\Omega_1 = \pi/2$ for all values of α_n . Results for four different values of the area ratio, $A_c/A_n = 4, 9, 16$ and 25 , are plotted in Figure 6.1. The results show that, when A_c/A_n is sufficiently large, the resonant frequency of the Helmholtz resonator is much lower than the resonant frequency of a quarter-wavelength tube of the same length.

For a fixed value of A_c/A_n , the resonant frequency takes on its minimum value at $\alpha_n = 1/2$, corresponding to $l_n = l_c$ (where the neck length l_n includes the end corrections). For the special case $\alpha_n = 1/2$, the eigenvalue relationship (6.18) can be solved explicitly to obtain the expression (6.20) for the minimum resonant frequency. The minimum resonant frequency is plotted as a function of the inverse area ratio A_n/A_c in Figure 6.2. As the inverse area ratio A_n/A_c is decreased from one, the minimum resonant frequency drops gradually at first, and then drops rapidly as A_n/A_c approaches zero.

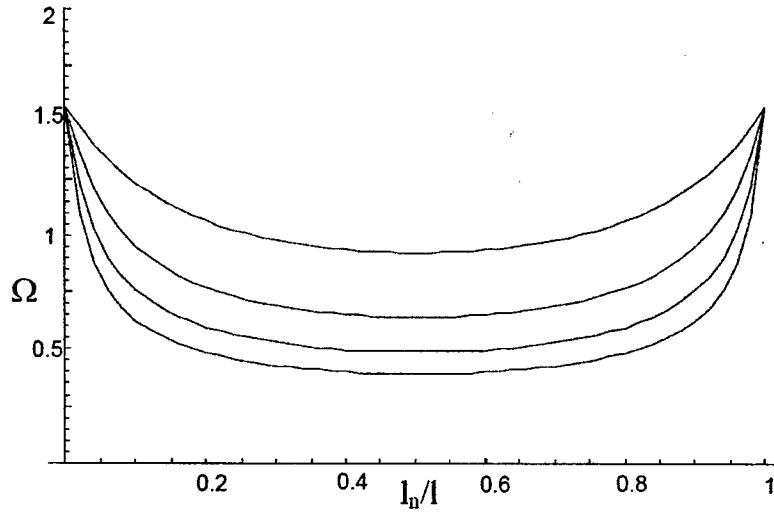


Figure 6.1: Non-dimensional resonant frequency Ω_1 of a Helmholtz resonator, as a function of the nondimensional neck length α_n . $A_c/A_n = 4, 9, 16$, and 25 (top curve to bottom curve).

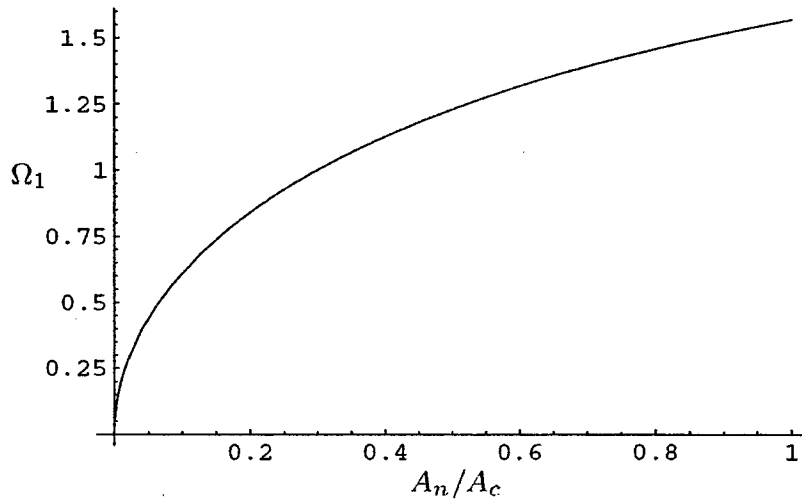


Figure 6.2: Resonant frequency Ω_1 of a Helmholtz resonator as a function of the area ratio A_n/A_c , for the case of optimum geometry ($\alpha_n = 0.5$).

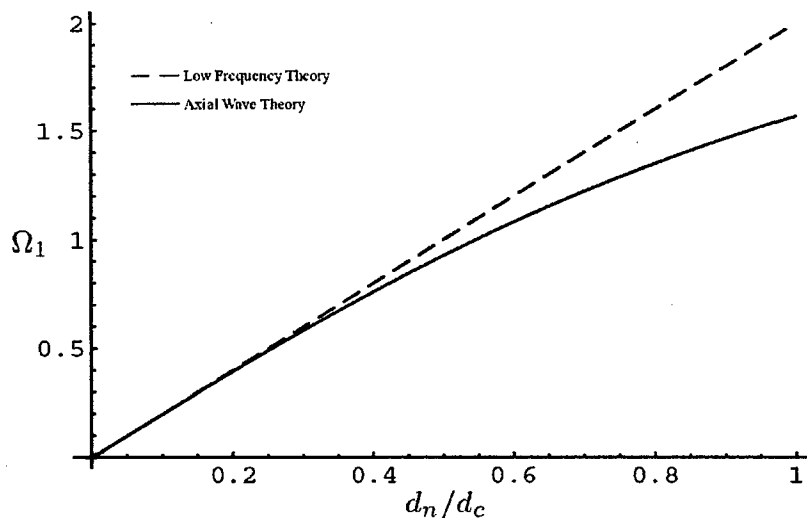


Figure 6.3: Resonant frequency Ω_1 of an axisymmetric Helmholtz resonator as a function of the diameter ratio d_n/d_c , for the case of optimum geometry ($l_n = l_c$).

It is illuminating to re-plot the results in Figure 6.2 as a function of d_n/d_c , for the case of an axisymmetric geometry ($A_n/A_c = (d_n/d_c)^2$). The result is shown in Figure 6.3. From Figure 6.3, it can be seen that the minimum resonant frequency is a linear function of d_n/d_c for small values of this parameter, corresponding to a square root function of the inverse area ratio ($\Omega_1 \propto (A_n/A_c)^{1/2}$). Since the resonant frequency approaches zero as $A_n/A_c \rightarrow 0$, it is natural to seek a connection with the low-frequency theory of section 6.3.1. The low-frequency prediction for the minimum resonant frequency for the case of an axisymmetric geometry, equation (6.36), is plotted as a dashed line in Figure 6.3. One can see that the low-frequency theory corresponds to the tangent line at the origin for the curve from the axial-wave theory. The low-frequency theory provides a remarkably accurate expression for the minimum resonant frequency as a function of d_n/d_c ; the low-frequency prediction differs from that of the axial-wave theory by less than 8% for values of $d_n/d_c < 0.5$. Values of $d_n/d_c > 0.5$ are of less practical interest, since these geometries produce only modest reductions of the resonant frequency.

If the only criterion were to obtain the lowest resonant frequency for a fixed resonator length, the optimum geometry would correspond to $\alpha_n = 1/2$. However, the case $\alpha_n = 1/2$ may be incompatible with other requirements for the geometry. In addition, values of α_n different from $1/2$ are advantageous when considering the Helmholtz resonator capacity. Hence, it is worthwhile to consider the influence on the resonant frequency of deviations from the optimum value $\alpha_n = 1/2$. From Figure 6.1, it can be seen that the curves of Ω_1 versus α_n are relatively flat in the central region surrounding the optimum, but rise rapidly to the quarter-wavelength value $\Omega_1 = \pi/2$ near the end points $\alpha_n = 0$ and 1 . Thus, the resonant frequency is increased only slightly when α_n is moved away from the optimum value of $\alpha_n = 1/2$. For example, for the case $\alpha_n = 0.24$ or 0.76 , the resonant frequency increases by only about 15% relative to the optimum case ($\alpha_n = 1/2$). Hence, deviations from $\alpha_n = 1/2$ have only a modest effect on the resonant frequency, as long as one stays away from the end points $\alpha_n = 0$ and 1 .

It was seen in Figure 6.3 that the low-frequency theory provides a very good prediction for Ω_1 as a function of d_n/d_c , for the case $\alpha_n = 1/2$. Given the relative simplicity of the low-frequency expression (6.35) for Ω_1 , it is of interest to examine the accuracy of this expression for $\alpha_n \neq 1/2$.

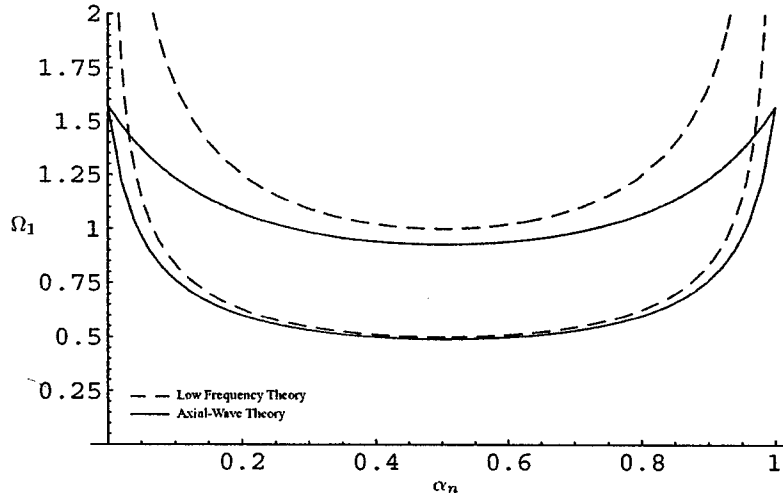


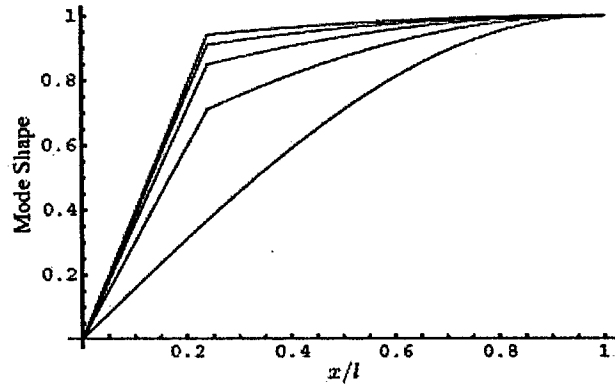
Figure 6.4: Comparison of the low-frequency theory and axial-wave theory predictions for the resonant frequency Ω_1 as a function of α_n . $A_c/A_n = 4$ (top curves) and 16 (bottom curves).

In Figure 6.4, the low-frequency and axial-wave predictions for Ω_1 are plotted as a function of α_n , for two values of A_c/A_n . Two trends can be seen in the results. First, consider the behavior as a function of the area ratio A_c/A_n . The predictions of the low-frequency theory are more accurate for larger values of A_c/A_n . This trend is expected, since the resonant frequency decreases as A_c/A_n is increased; it is only at low frequencies that the simplifying assumptions of the low-frequency theory are valid. Second, consider the behavior as a function of α_n . The low-frequency theory is most accurate at $\alpha_n = 1/2$, and remains useful for a range of α_n surrounding $1/2$. However, the theory fails completely in the vicinity of the end points $\alpha_n = 0$ and 1 . Essentially, as α_n approaches 0 or 1 , the dominant physical behavior is a quarter-wavelength resonance in the cavity or neck, respectively. The assumptions inherent in the low-frequency theory preclude the prediction of a quarter-wavelength resonance. Despite the failure at the end points, the low-frequency theory is quite accurate in the central band of α_n of most practical interest, especially for larger values of A_c/A_n .

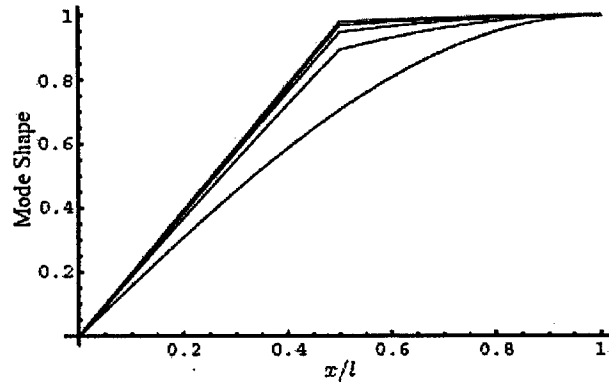
6.4.2 Mode shapes

Results for the pressure field mode shape corresponding to the lowest resonant frequency ($j = 1$), for several values of α_n and A_c/A_n are presented. The results presented in this section were obtained from the axial-wave theory. In Figure 6.5, the pressure amplitude for the $j = 1$ mode is plotted as a function of non-dimensional axial distance x/l . Results are presented for $\alpha_n = 0.24, 0.5$ and 0.76 in parts (a), (b) and (c), respectively. In each plot, results for five values of the area ratio are presented, $A_c/A_n = 1, 4, 9, 16$ and 25 . Note that the case $A_c/A_n = 1$ corresponds to a quarter-wavelength tube.

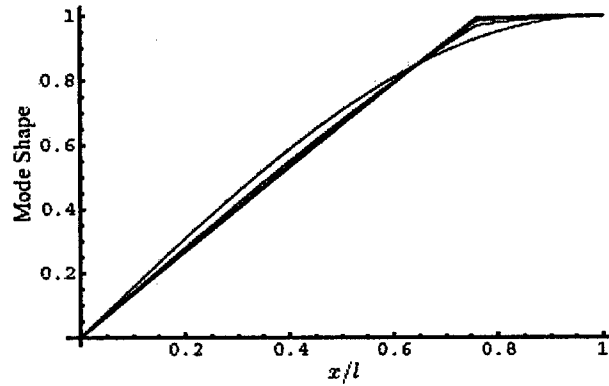
First consider the mode shapes for $\alpha_n = 0.24$ in Figure 6.5(a). For values of $A_c/A_n \neq 1$, the slope of the pressure field is discontinuous at $x/l = 0.24$, the location of the junction between the neck and the cavity. This discontinuity in slope arises from the volume flux matching condition between the neck and cavity, and is an artifact of the approximations that have been introduced in the theory. In a more refined analysis, the discontinuity in slope would be smoothed out by a local solution



(a) $\alpha_n = 0.24$



(b) $\alpha_n = 0.5$



(c) $\alpha_n = 0.76$

Figure 6.5: Pressure mode shapes for free resonance of a Helmholtz resonator, plotted as a function of x/l . $A_c/A_n = 1, 4, 9, 16$ and 25 (bottom curve to top curve for $x/l > \alpha_n$).

in the vicinity of the junction. However, this local solution is not required in order to determine global properties of the acoustic field such as the resonant frequency and global mode shape. As the area ratio A_c/A_n is increased, the resonant frequency decreases (see Figure 6.1) and the mode shape tends to its low-frequency limit, which corresponds to a linear profile of slope $1/\alpha_n$ in the region $0 < x/l < \alpha_n$, connected to a constant amplitude profile $p = 1$ in the region $\alpha_n < x/l < 1$. Note that the slope of the profile in the neck region increases with A_c/A_n . In the low-frequency limit, the slope of the pressure field at the resonator mouth ($x/l = 0$) is approximately twice that for the quarter-wavelength response. The increased slope at $x/l = 0$ relative to that for the quarter-wavelength response indicates that the capacity of the Helmholtz resonator increases with A_c/A_n . The Helmholtz resonator capacity will be examined in the following subsection.

Next consider the mode shapes for $\alpha_n = 0.5$ and 0.76 , presented in Figures 6.5(b) and (c). The general behaviors discussed in the previous paragraph for the case $\alpha_n = 0.24$ also apply here. For $A_c/A_n \neq 1$, the mode shapes have a discontinuous slope at $x/l = \alpha_n$, the location of the junction between the neck and cavity. The mode shapes tend to the low-frequency limit as A_c/A_n increases. Compared to the case $\alpha_n = 0.24$, the slope of the pressure field in the neck in the low-frequency limit is smaller by a factor of two for the case $\alpha_n = 0.5$, and smaller by a factor of three for the case $\alpha_n = 0.76$. For $\alpha_n = 0.76$, it is interesting to note that the slope $\partial p/\partial x$ at the resonator mouth ($x/l = 0$) in the low-frequency limit is slightly smaller than that for the quarter-wavelength response. In contrast, for $\alpha_n = 0.5$ and 0.24 , the slope at the resonator mouth in the low-frequency limit is significantly larger than that for the quarter-wavelength response.

The approach of the mode shape to the low-frequency limit (with increasing A_c/A_n) occurs more rapidly for the case $\alpha_n = 0.5$ than for $\alpha_n = 0.24$. The approach of the mode shape to the low-frequency limit is even more rapid for the case $\alpha_n = 0.76$. The rate at which the mode shape approaches the low-frequency limit appears to be related to the degree of similarity between the mode shapes for the quarter-wavelength response ($A_c/A_n = 1$) and the low-frequency limit ($A_c/A_n \gg 1$). The quarter-wavelength and low-frequency mode shapes are most similar for the case $\alpha_n = 0.76$, and least similar for $\alpha_n = 0.24$.

6.4.3 Capacities

The capacity is a normalized measure of the volume flux that the resonator stores, for a given external pressure fluctuation $p_e e^{-i\omega t}$. The capacity C is defined by (6.21). The capacity is a function of the frequency ω of the external forcing, and becomes unbounded at the resonant frequency $\omega = \omega_1$ (in the absence of damping mechanisms). The capacity is purely imaginary for the inviscid linear theory that was developed, indicating that the velocity at the mouth of the resonator is out of phase with the external pressure field. The capacity is negative imaginary for $\omega < \omega_0$, indicating that the velocity field leads the pressure field by 90° , while the capacity is positive imaginary for $\omega > \omega_0$, indicating that the velocity field lags the pressure field by 90° .

Results for the Helmholtz resonator capacity, calculated from the axial-wave theory expression (6.26), are presented in Figure 6.6. The magnitude of the capacity is plotted as a function of the non-dimensional frequency ratio Ω/Ω_1 , for the cases $\alpha_n = 0.24, 0.5$ and 0.76 in Figures 6.6(a), (b) and (c), respectively. In each plot, results for three area ratios are presented, $A_c/A_n = 1, 4$ and 16 . The lowest curve in each plot is the result for $A_c/A_n = 1$, corresponding to a quarter-wavelength tube. Note that the magnitude of the capacity for a quarter-wavelength tube is symmetric about $\Omega = \Omega_1$, for the frequency range plotted in Figure 6.6. This symmetry is not present for the Helmholtz resonator geometries, where the capacity for frequencies $\Omega > \Omega_1$ is larger than the capacity for $\Omega < \Omega_1$.

The results in Figure 6.6 show that the neck length has a strong influence on the Helmholtz resonator capacity. For the case $\alpha_n = 0.24$, the capacities for $A_c/A_n = 4$ and 16 exceed that for a quarter-wavelength tube by factors of approximately 3 and 6, respectively. For $\alpha_n = 0.5$, the capacities

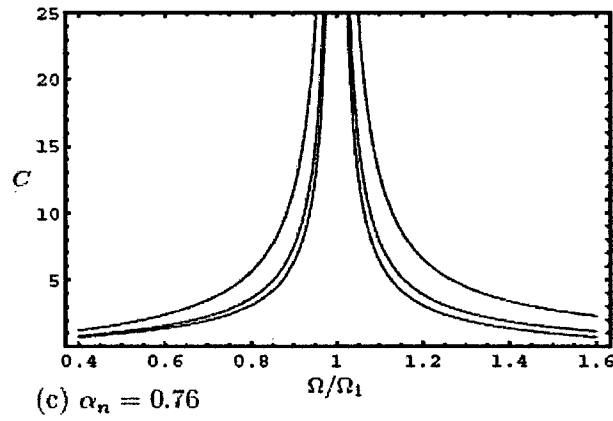
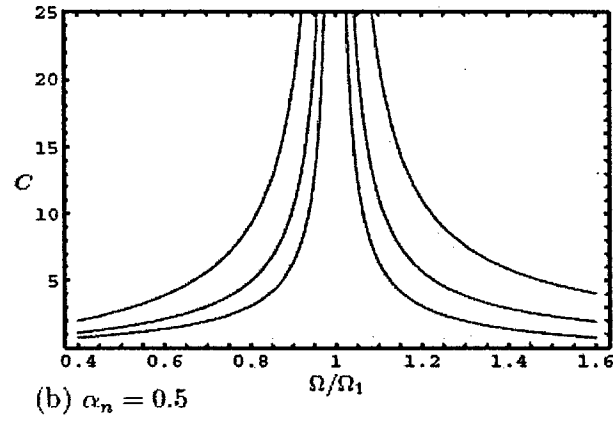
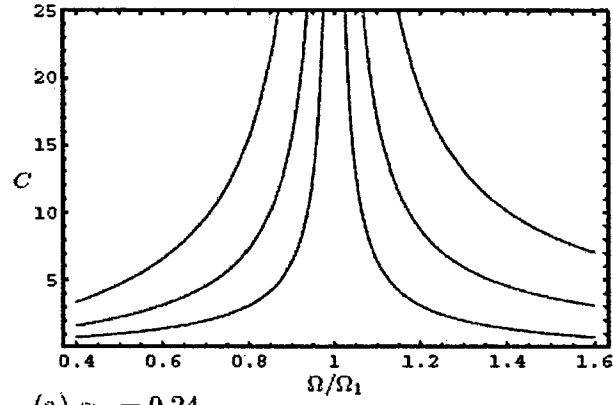


Figure 6.6: The capacity C for forced response of a Helmholtz resonator at frequency Ω , plotted as a function of the frequency ratio Ω/Ω_1 . $A_c/A_n = 1, 4$ and 16 (bottom curve to top curve).

for $A_c/A_n = 4$ and 16 exceed that for a quarter-wavelength tube by factors of nearly 2 and 4, respectively. For $\alpha_n = 0.76$, the capacity for $A_c/A_n = 4$ is only slightly higher than that for the quarter-wavelength tube, while the capacity for $A_c/A_n = 16$ is approximately twice that for the quarter-wavelength tube. Comparing the capacities for the same area ratio but different neck lengths, one finds that the capacity for $\alpha_n = 0.24$ is approximately three times that for $\alpha_n = 0.76$.

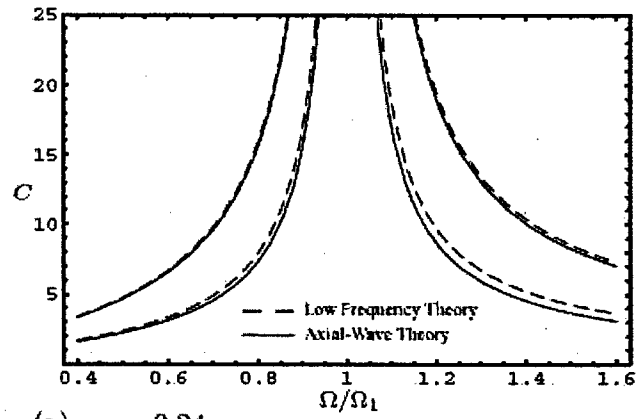
Although the mode shapes in Figure 6.5 are not directly applicable for the case of forced response, they are indicative of the pressure fields for frequencies in the vicinity of $\Omega = \Omega_1$, which are of the most interest for the Helmholtz PRT. Hence the mode shapes can be used to provide some guidance in understanding the influence of neck length on the resonator capacity. Note from (6.21) that the capacity is proportional to u (or $(\partial p/\partial x)/\omega$), evaluated at $x = 0$. The Helmholtz geometries increase capacity by increasing $\partial p/\partial x|_{x=0}$ and by decreasing ω . The difference in capacity between the cases $\alpha_n = 0.24$ and 0.76 is due solely to the difference in $\partial p/\partial x|_{x=0}$, since the resonant frequency Ω_1 is the same for these two cases. From the mode shapes presented in Figure 6.5, it was seen that $\partial p/\partial x|_{x=0}$ is larger for the shorter neck length. Physically, there are two effects that cause the capacity for $\alpha_n = 0.24$ to be much larger than that for $\alpha_n = 0.76$. First, due to the shorter neck, there is a smaller amount of fluid mass in the neck, so that the fluid in the neck is more easily accelerated. Second, due to the longer cavity, more fluid can be absorbed into the cavity for a given pressure rise. Both these effects contribute to the increase in resonator capacity with a decrease in α_n .

The simplifications introduced in the low-frequency theory lead to an expression (6.40) for the capacity that is much simpler than the result (6.26) from the axial-wave theory. In Figure 6.7, predictions for the capacity based on the simpler low-frequency theory are compared to those from the axial-wave theory. The low-frequency prediction is plotted as a dashed line, while the axial-wave result is plotted as a solid line. The conditions are the same as those in Figure 6.6, except that results for $A_c/A_n = 1$ are not presented since the low-frequency theory is not applicable to the quarter-wavelength tube geometry. The results presented in Figure 6.7 demonstrate that the low-frequency theory is more accurate at higher values of A_c/A_n . The reasons for this were discussed in connection with Figure 6.4. For fixed A_c/A_n , the accuracy of the low-frequency theory is highest for $\alpha_n = 0.5$, and decreases somewhat for $\alpha_n = 0.24$ and 0.76. However, the general accuracy of the low-frequency theory is impressive, considering the simplicity of the expressions.

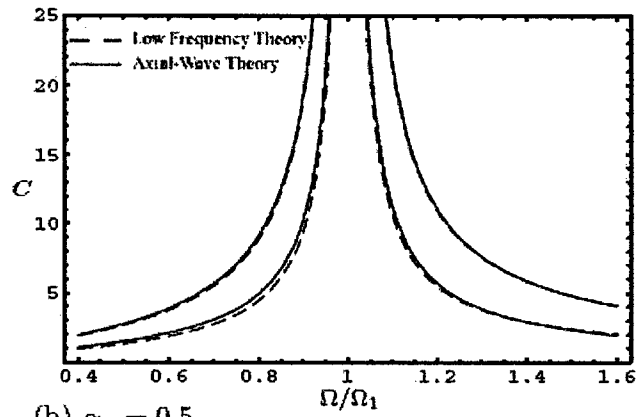
6.4.4 Comparison to numerical simulation

Finally, the current analytical predictions for the resonant frequencies are compared to a result obtained in a companion numerical simulation [Cain et al., 2004] of a Helmholtz resonator based PRT. An axisymmetric geometry is considered, with a neck-to-cavity diameter ratio $d_n/d_c = 0.5$, a neck-to-cavity length ratio $l_{n\text{geom}}/l_c = 0.25$, and a neck length-to-diameter ratio $l_{n\text{geom}}/d_n = 0.64$. The ratios quoted in the previous sentence are based on the geometric length of the neck. Since the neck length is relatively short, the end correction (6.10) applies.

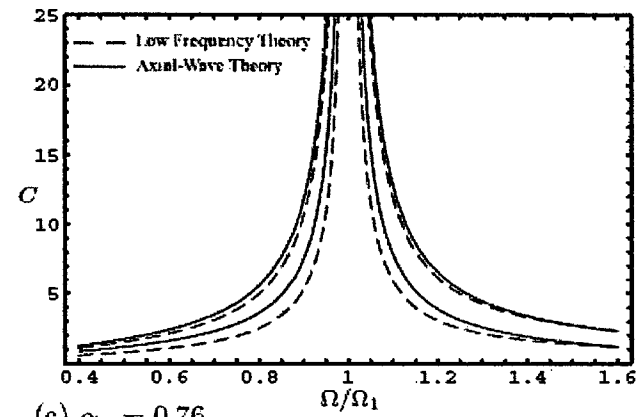
In Figure 6.8 (repeated from Figure 1.5 for convenience), the resonant frequency obtained in the simulations is compared to analytical predictions of varying degrees of sophistication. Dimensional values of the resonant frequency are plotted as a function of total (geometric) length of the actuator, $l_{\text{geom}} = l_{n\text{geom}} + l_c$. The low-frequency theory in the absence of neck end corrections leads to the highest prediction for the resonant frequency. This prediction lies substantially above the simulation point. The geometry considered in the simulations has a very short neck, so that the end corrections substantially increase the effective mass in the neck, lowering the resonant frequency. The low-frequency theory with neck end corrections lies just slightly above the simulation point. Finally, for the parameter values in this case, the more refined axial-wave theory provides a prediction that is slightly lower than the corresponding result from the low-frequency theory. The prediction of the axial wave theory with neck end corrections is in very good agreement with the result obtained from



(a) $\alpha_n = 0.24$



(b) $\alpha_n = 0.5$



(c) $\alpha_n = 0.76$

Figure 6.7: Comparison of the low-frequency theory and axial-wave theory predictions for the capacity C of a Helmholtz resonator, plotted as a function of the frequency ratio Ω/Ω_1 . $A_c/A_n = 4$ (bottom curves) and 16 (top curves).

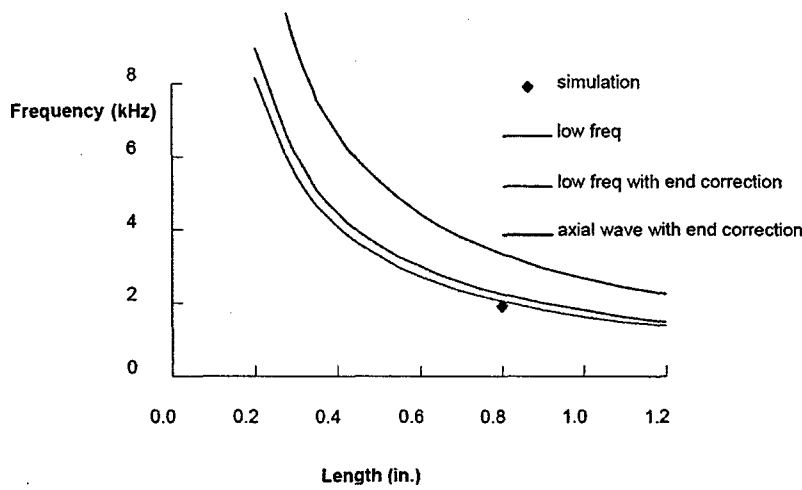


Figure 6.8: Comparison of the frequency obtained in the simulation to that predicted by the various analytical models.

the numerical simulation. Additional comparisons of theoretical results with numerical simulations and also with experiments are presented in [Cain et al., 2004].

6.5 Conclusions Regarding a Helmholtz Based PRT

In summary, analytical models for Helmholtz resonator behavior have been developed which provide guidance for the design of Helmholtz resonator based PRT actuators. The primary benefits of the Helmholtz geometry, relative to a quarter-wavelength resonance tube, are a reduction in the resonator length for a specified resonant frequency, and an increase in the capacity of the resonator. These features provide additional flexibility in the design of PRT actuators for low-frequency applications, particularly in the presence of geometric length constraints.

The analytical models provide predictions for the resonant frequency, acoustic mode shape and capacity of the Helmholtz resonator, as a function of resonator geometry. Two analytical models have been developed, the axial-wave theory and the low-frequency theory. The axial wave theory accounts for acoustic propagation effects along the axis of the resonator, and is capable of describing the transition from quarter-wavelength tube to Helmholtz resonator behavior as the geometry is varied. The low-frequency theory requires $A_c/A_n \gg 1$, which is generally satisfied for Helmholtz resonator geometries, but precludes consideration of geometries that differ only slightly from a constant-area resonance tube.

The low-frequency theory leads to relatively simple expressions whose accuracy has been demonstrated by comparisons with results from the axial-wave theory. For an axisymmetric geometry, in the low-frequency limit the resonant frequency is proportional to $(A_c/A_n)^{1/2}$ and the capacity is proportional to $(l_c A_c/l_n A_n)^{1/2}$, where l_n , A_n and l_c , A_c are the length and cross-sectional area of the neck and backing cavity, respectively. The simplicity of the low-frequency expressions make these very attractive for applications such as preliminary design.

For a Helmholtz resonator based Powered Resonance Tube actuator, a low resonant frequency and high capacity are generally desirable. The lowest value of the resonant frequency for a fixed resonator

length $l = l_n + l_c$ is obtained by setting $l_n = l_c$. However, since the resonant frequency is a relatively flat function of $\alpha_n = l_n/(l_n + l_c)$ in the vicinity of the minimum at $\alpha_n = 0.5$, the resonant frequency remains quite low over a range of α_n , say $0.25 \leq \alpha_n \leq 0.75$. The capacity is proportional to $(l_c/l_n)^{1/2}$. In order to increase the capacity while retaining a low resonant frequency, a neck length shorter than the cavity length should be chosen. As an illustration, relative to the case $\alpha_n = 0.5$, reducing the neck length to $\alpha_n = 0.25$ raises the resonant frequency by only 15%, but increases the capacity by 73%.

Chapter 7

Miniaturized PRT

7.1 Overview

In addition to the development of a high-bandwidth PRT actuator, and a Helmholtz PRT actuator for low frequencies, as discussed in Chapters 1 and 2, a prototype miniaturized high-bandwidth PRT actuator was also constructed. It consists of three cylindrical actuators of identical outside dimensions. Each had a variable depth by way of a movable piston and a constant area nozzle jet of the same diameter as the resonator openings. This chapter will summarize the results of tests with the miniaturized actuators.

7.2 Setup

Three cylindrical actuators of identical outside dimensions were constructed. Each had a variable depth by way of a movable piston and a constant area nozzle jet of the same diameter as the resonator openings. The resonators were a 1/8" straight tube, a 1/16" straight tube, and a 1/16" \times 1/8" Helmholtz resonator. The 1/16" straight tube and Helmholtz resonators are detailed in Figure 1.6 (repeated from Figure 1.6 for convenience).

The resonators were in turn mounted in a traversing assembly which moved the piston and resonator relative to the jet which was fixed. An identical initial test matrix was run for each actuator. The supply pressure was varied from 25 to 60psig in increments of 5psi; The spacing was varied from 0 to 0.25" in increments of 0.01"; the depth was varied from 0.2" to 1" in increments of 0.05". For all points a Breiul & Kjiar microphone was mounted in foam 0.5" downstream and 0.75" above the center of the resonator mouth. At all points the signal from the microphone was run through an FFT program. The frequency in Hz and SPL in dB for the highest peak in the spectrum was extracted and recorded in a table. Since the narrower jet was more sensitive to changes in spacing than the wider tube, a more detailed data set was needed for the actuators using the smaller jet. For the actuators using the 1/16" jet (the 1/16" straight tube and Helmholtz actuators) a jet-tube spacing range was extracted from the first test matrix that yielded resonance for each pressure. A second test matrix was then run for these actuators using the same pressure and depth ranges and increments and the spacing ranges extracted from the first data set with an increment of 0.0025".

Non-resonating cases were then deleted from the data sets. A control program was written which used the data from the test matrix to find a starting position of the actuator based on a target frequency and either the supply pressure or minimum required SPL. The program would output the minimum supply pressure if a minimum SPL was given. Then the spacing and depth were set

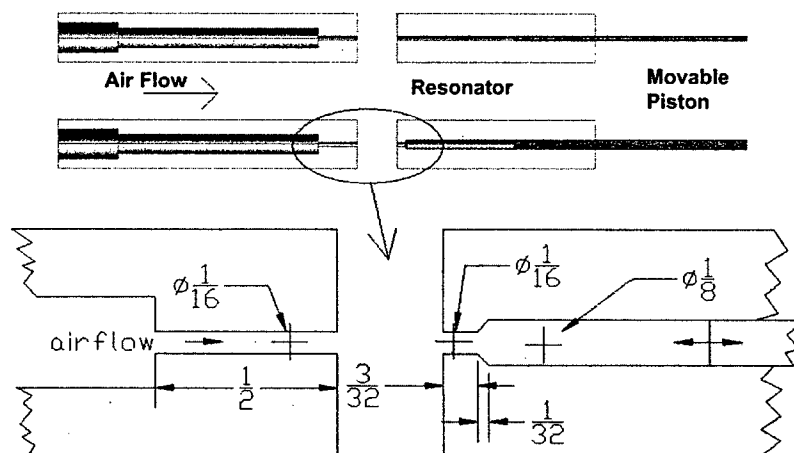


Figure 7.1: The miniaturized quarter wavelength and Helmholtz PRT actuators and a close-up detail of the Helmholtz resonator. (repeat of Figure 1.6).

to the position giving the maximum SPL at that pressure and frequency from the data table. The spacing was varied iteratively to maximize the SPL, then the depth was varied iteratively to tune the frequency to within 5Hz, which was the frequency resolution of the FFT program.

Frequency spectra and time series data were taken for a few frequencies and pressures for the 1/16" straight tube and Helmholtz actuators. Comparison plots for a few of them are shown below in Figures 7.2 through 7.5.

The data from the Helmholtz resonator was further processed to extract only resonating cases operation on the base mode, i.e. the peak SPL is on the first harmonic. The spacing that gave the highest SPL without mode jumps at 35 psig supply pressure was found. The frequency versus depth data was extracted for that spacing and pressure. It was plotted against curves generated by the Graphical User Interface (GUI) described in Chapter 8. The GUI was programmed using the theory developed by Kerschen. The plot is shown in Figure 7.6. A scatter plot of all points taken was also plotted against the theoretical data to show the range of frequencies possible at the different depths. This plot is shown in Figure 7.7.

Both theories with end corrections fell within the range of the measured data. The dependence of frequency on spacing for a fixed depth and pressure is shown in the tables below (Table 7.1 and Table 7.2). The relation was found to be periodic. This would be consistent with a dependence on pressure and temperature at the resonator mouth. The period and amplitude of the variation depended on pressure. The relation however was too inconsistent to create a reliable model from.

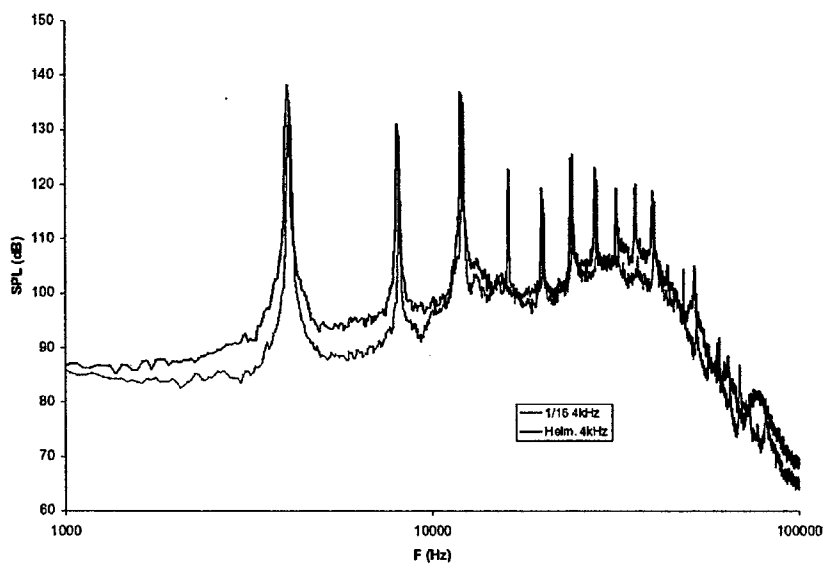


Figure 7.2: Spectra for the 1/16" straight tube and Helmholtz resonator with the apparatus set at 4kHz.

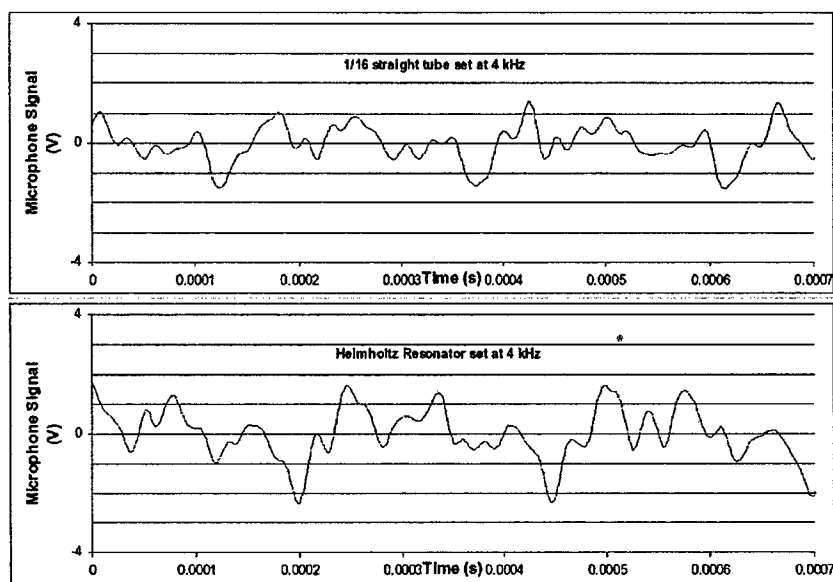


Figure 7.3: Time series for the 1/16" straight tube and Helmholtz resonator with the apparatus set at 4kHz.

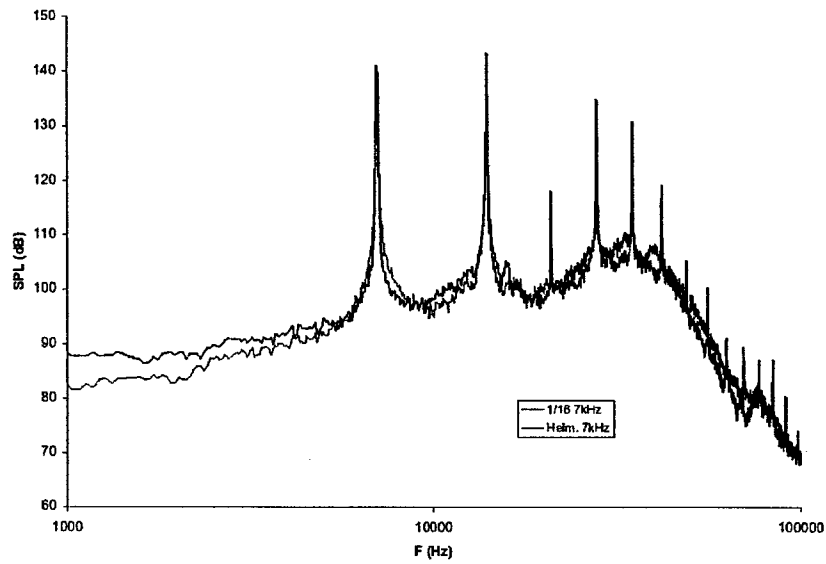


Figure 7.4: Spectra for the 1/16" straight tube and Helmholtz resonator with the apparatus set at 7kHz.

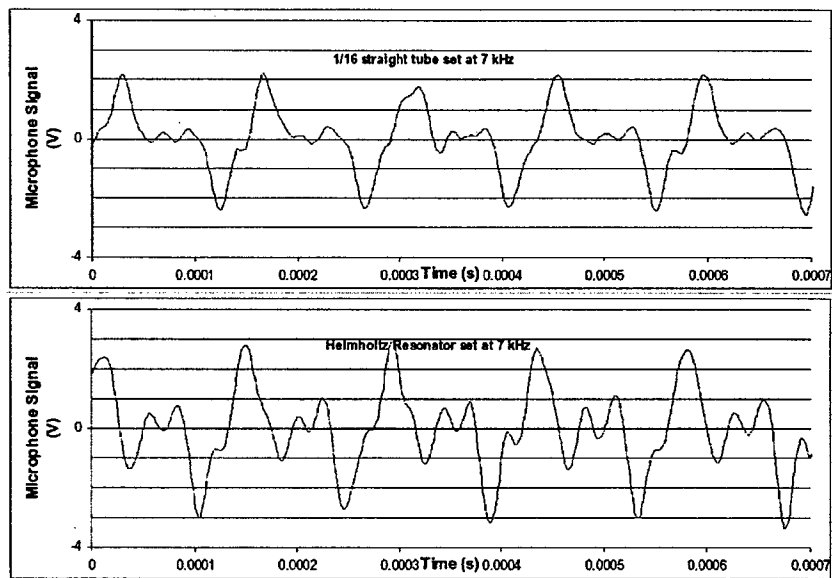


Figure 7.5: Time series for the 1/16" straight tube and Helmholtz resonator with the apparatus set at 7kHz.

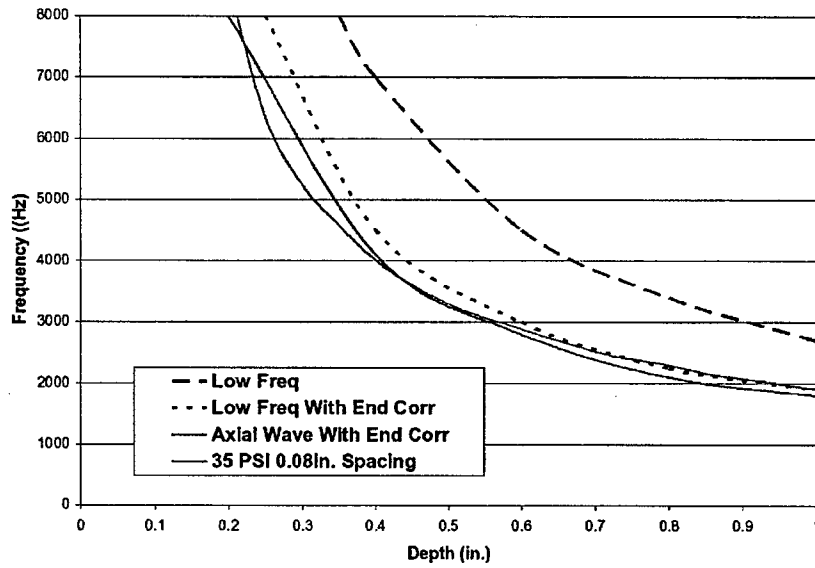


Figure 7.6: Frequency versus depth with theoretical and measured values.

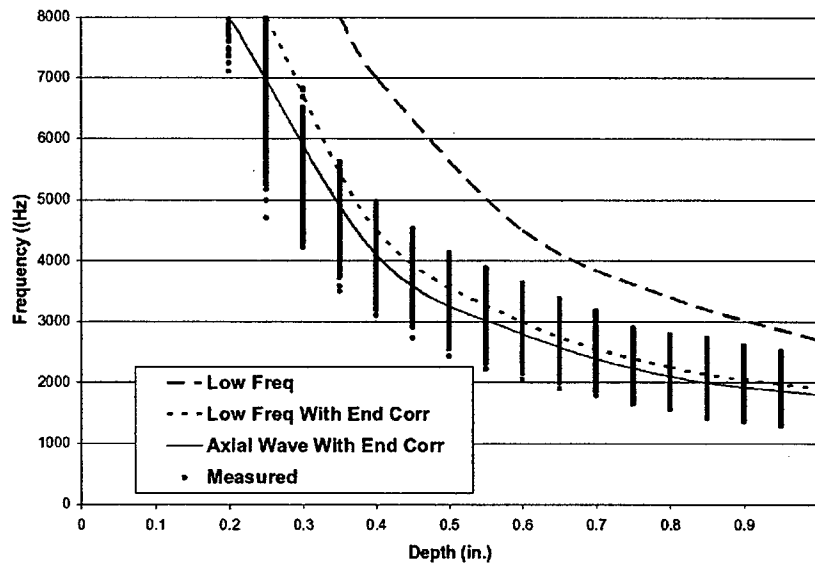


Figure 7.7: Frequency versus depth with theoretical data and all resonating measured values.

Table 7.1: A table of Frequency vs. spacing and pressure for a depth of 1/2" in the Helmholtz resonator.

S(in.) P(Psi)→	0.5 in. Depth Helmholtz							
	25 PSI	30 PSI	35 PSI	40 PSI	45 PSI	50 PSI	55 PSI	60 PSI
0	***	***	***	***	***	***	***	***
0.01	5530	6150	5815	5825	6115	6465	6455	6495
0.02	4185	3915	4045	3900	4055	4005	3905	4320
0.03	4435	4130	4145	13915	4550	13470	5415	14120
0.04	4410	13465	14010	11820	13280	11955	13320	13545
0.05	3905	***	13955	13270	14010	11705	11630	12530
0.06	3765	3760	***	***	11810	14010	11525	12200
0.07	4040	3505	3580	***	***	11950	13010	11600
0.08	4220	3320	3300	3400	4330	11925	11905	12415
0.09	4420	4195	2940	3110	3260	4100	3990	11360
0.1	4435	4425	4095	2645	2930	3215	4180	3975
0.11	3975	11725	4475	3915	2495	8545	6315	4185
0.12	3905	***	11760	12280	3700	7820	11900	8620
0.13	4135	3875	***	11485	3765	2625	8485	7610
0.14	4285	3730	***	11995	12105	7955	8520	11655
0.15	4220	4010	3700	***	***	3755	8550	5735
0.16	4020	4260	3480	***	***	4055	2920	5750
0.17	4035	11800	3810	3500	***	4070	11930	2925
0.18	4410	11445	4260	3215	3540	3915	3465	11945
0.19	11350	11885	4130	3990	3255	3490	3575	11945
0.2	11455	11745	4740	4190	2905	3235	3380	11800
0.21	11635	13015	***	11360	3850	8755	3155	8725
0.22	11755	9390	3840	***	***	2600	8685	8465
0.23	***	10495	3670	***	***	3715	8220	8375
0.24	7350	11980	3550	4150	***	3870	2890	2830
0.25	4295	11490	11275	3720	4050	4170	3680	2870

Table 7.2: A table of Frequency vs. spacing and pressure for a depth of 1/2" in the 1/16" straight tube resonator.

S(in.)\ P(PSI)→	0.5 in. Depth Straight Tube							
	25 PSI	30 PSI	35 PSI	40 PSI	45 PSI	50 PSI	55 PSI	60 PSI
0	***	***	***	***	***	***	***	***
0.01	***	***	***	***	***	***	***	***
0.02	5975	6140	6445	6710	5785	6205	6285	5915
0.03	6315	6630	6305	6270	6405	6670	6370	7170
0.04	6430	6305	12855	13945	13780	13535	13800	13800
0.05	6380	13485	13965	13565	13870	13260	12480	13135
0.06	***	***	13670	13865	12425	12395	13595	12775
0.07	5795	***	***	8455	11790	13165	12405	11780
0.08	6220	5405	5435	***	13005	9610	12175	12895
0.09	6380	6235	5145	5250	8285	6725	11735	9170
0.1	6570	6520	5130	4880	6575	9445	8930	11540
0.11	6450	7115	6275	4495	4655	6345	6280	11525
0.12	6065	12040	12415	5930	4380	4570	6095	6200
0.13	6080	6330	12170	12135	5760	4500	6315	***
0.14	6305	5915	12030	11980	6885	4470	4705	4900
0.15	6710	5750	***	11970	11990	4630	4895	4775
0.16	6395	6200	***	12600	12040	6450	5000	4845
0.17	6295	6345	5510	5820	6395	6310	5045	5020
0.18	6275	11540	6020	5445	6330	6480	5510	5005
0.19	6260	6960	6770	5305	5435	6005	5830	4955
0.2	6740	7800	6690	6395	5130	5420	5570	5065
0.21	6965	5980	11770	6470	5065	5065	5295	5170
0.22	6835	6345	11600	11835	5830	4835	5060	5115
0.23	6970	7150	6560	11680	11540	5565	4980	5040
0.24	9615	11820	5760	11445	11495	5895	4990	5015
0.25	6085	7120	6085	***	10710	6740	5690	5045

Chapter 8

Helmholtz PRT Design Tool

8.1 Overview

The powered resonance tube (PRT) is one type of active flow control (AFC) device that shows promise in producing performance improvements for various aerospace applications. Recently, Kerschen [Kerschen and Cain, 2003] proposed the use of a Helmholtz resonator in place of the quarter-wavelength resonance tube normally found in PRTs.

The PRT Design Tool uses Kerschen's Helmholtz resonator results based on low-frequency theory [Kerschen et al., 2004], in order to calculate:

1. Resonant frequency for a given input geometry
2. Geometry characteristics that result in a given input frequency

The program requires entry of a few basic inputs and maintains a set of default system variables—which can be modified—in order to perform its calculations. The inputs and calculations are discussed in detail below.

8.2 Screen Layout

The PRT Tool screen consists of a graphical depiction of the basic geometry of a Helmholtz resonator PRT actuator, three tabs for entry and calculation of geometry and frequency data, and an “Exit” button in the lower right corner, which closes the PRT Tool window and exits the program. Clicking anywhere on the figure displays a window that describes the geometry and frequency variables.

Three different tabs provide calculation of resonant frequency from geometric inputs, calculation of geometry based on frequency input, and entry of system variables, respectively. Click on the title of each tab (e.g., “Solve for geometry”), just below the figure, to access that tab's functions. Figure 8.1 shows the screen when calculating the resonant frequency based on the input geometry.

8.3 Frequency Calculation

The first tab calculates resonant frequency based on input neck length, cavity depth, and the ratio of the neck radius to the cavity radius. The user fills in any blank boxes, or change any values

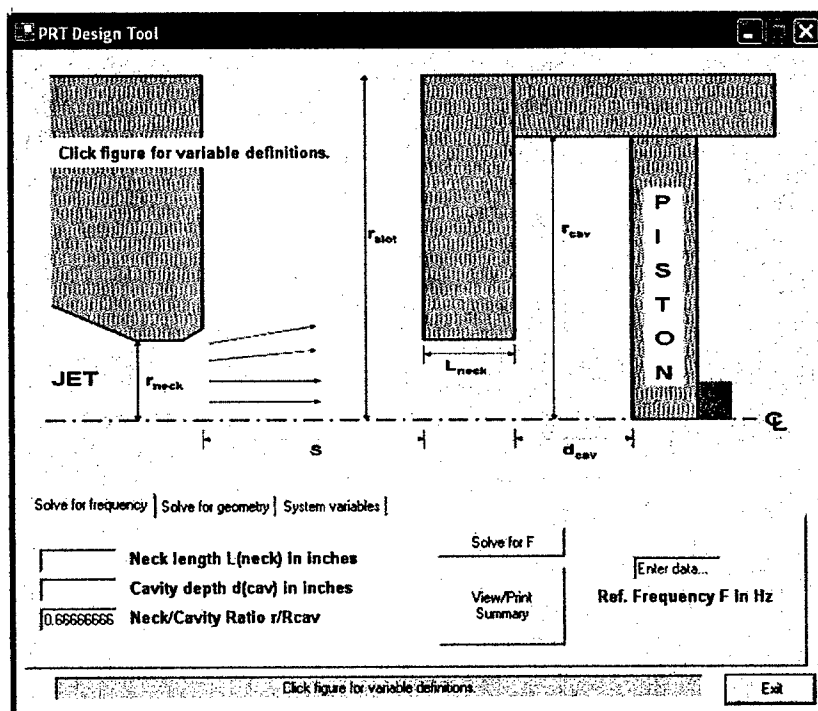


Figure 8.1: Design tool appearance when computing Helmholtz PRT actuator geometry based on a desired frequency

they desire, and clicks the “Solve for F” button. The calculated frequency will appear in the Ref. Frequency box at the right side of the tab.

For the frequency calculation, it is recommended that the geometric neck length be less than three times the neck radius. If it is not, the program will display a message suggesting that the user correct either of these input values before the calculation is made.

Next, an effective neck length is calculated to account for three-dimensional flow effects in this model’s axisymmetric geometry. If the ratio of the neck radius to the cavity radius is less than 2/3, and the cavity depth is greater than 1.5 times the neck radius, a correction is added at both ends of the neck. Otherwise, the correction is added only at one end. For details, see Algorithm 1.

Algorithm 1 Effective neck length calculation

IF ($r_n/r_c < 2/3$) AND ($l_c \geq 1.5r_n$) THEN

$$l_{neff} = l_n + 0.41d_n + 0.41d_n = l_n + 1.64r_n$$

ELSE

$$l_{neff} = l_n + 0.41d_n = l_n + 0.82r_n$$

END IF

The low-frequency approximation is then calculated using equation 6.34. In order to obtain a more accurate solution for the resonant frequency, a Newton-Raphson iteration scheme is utilized to find the roots to equations 6.18 and 6.19 using the low frequency calculation as an initial guess and marching from $\alpha_n = l_n/l = 0.5$ toward a solution at the α_n corresponding to our input geometry. Equation 6.20 gives the solution to equations 6.18 and 6.19 for $\alpha_n = 0.5$. The details of the implementation are given below in Algorithm 2.

Algorithm 2 Algorithm to find the resonant frequency of a Helmholtz PRT actuator

1. Calculate Ω for $\alpha_n = 0.5$.
 2. Step from $\alpha_n = 0.5$ to the next α_n using 10 intervals between $\alpha_n = 0.5$ and the α_n for the current geometry (i.e. $\Delta\alpha = 0.1 * (\alpha_n - 0.5)$).
 3. Use Newton-Raphson iteration to solve for a new Ω in equations 6.18 and 6.19.
 4. Use $\alpha_n = 0.5$, α_n for the desired geometry, Ω from step 1, and Ω from step 3 to compute a linear approximation of the final Ω for our value α_n .
 5. Step to the next α_n .
 6. Use Newton-Raphson iteration to solve for the new Ω .
 7. Use the results from steps 1, 3, 5, and 6 (three data points) to compute a quadratic approximation of the final Ω for the desired α_n .
 8. Using the final value of α_n and the guess for Ω from step 7, use Newton-Raphson iteration to solve for the final value of Ω .
 9. Compute the resonant frequency: $\omega = \Omega c/l$
-

The Newton-Raphson algorithm for marching from a known root of equation 6.18 to other, nearby roots is given in Algorithm 3.

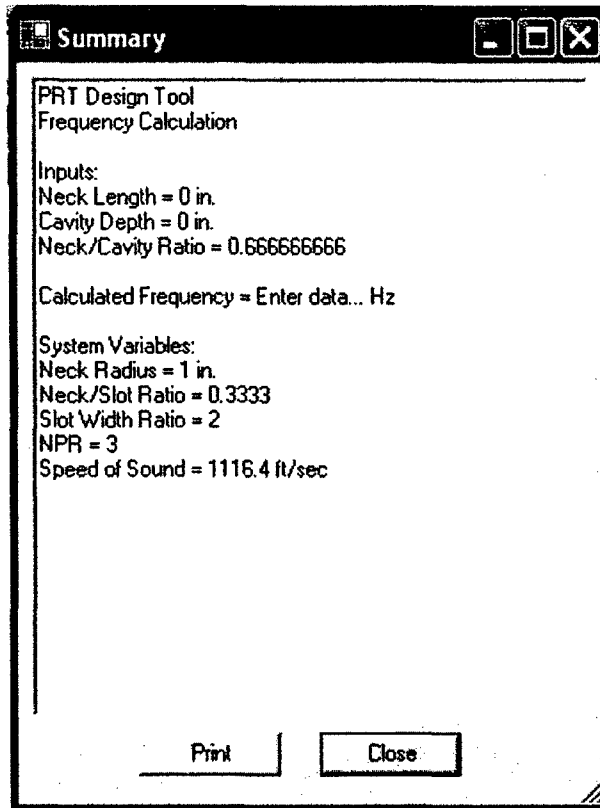


Figure 8.2: Summary window of the Helmholtz PRT actuator design code

Algorithm 3 Newton-Raphson Algorithm

Given an initial guess, Ω_0 , and the functions:

$$F(\Omega) = \left[1 + \frac{A_n}{A_c}\right] \cos \Omega - \left[1 - \frac{A_n}{A_c}\right] \cos(2\alpha_n - 1)\Omega$$

$$F'(\Omega) = \left[1 + \frac{A_n}{A_c}\right] \sin \Omega - \left[1 - \frac{A_n}{A_c}\right] (2\alpha_n - 1) \sin(2\alpha_n - 1)\Omega$$

the iteration scheme is:

$$\Omega_{n+1} = \Omega_n - \frac{F(\Omega_n)}{F'(\Omega_n)}$$

and the iteration proceeds until $\Omega_{n+1} - \Omega_n \leq 1.0 \times 10^{-8}$

One may click the “View/Print Summary” button to view a window (see Figure 8.2) containing a summary of all input, output, and system variables, which can be printed with the Print button in that window. Click the Close button to close the Summary window.

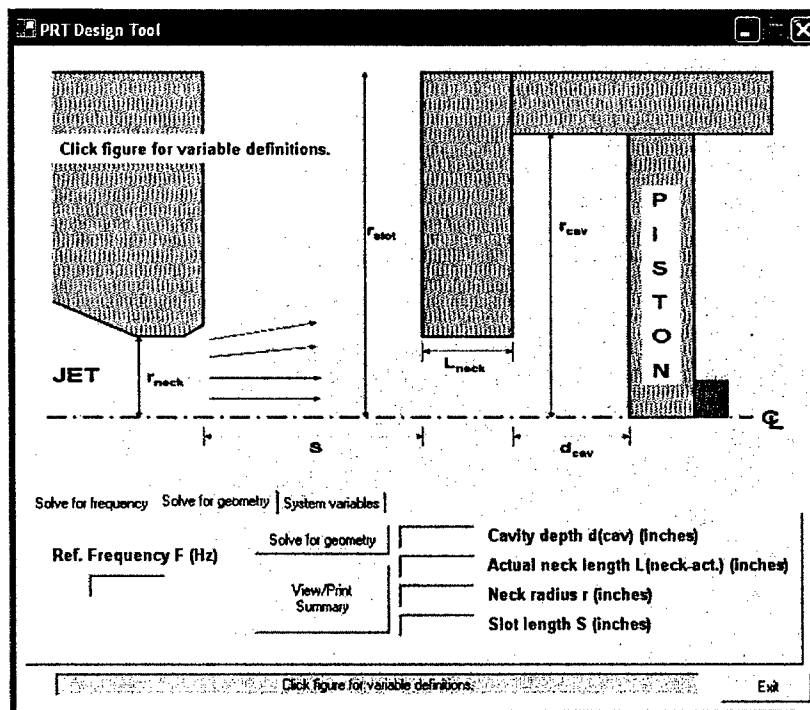


Figure 8.3: Design tool appearance when computing Helmholtz PRT actuator geometry based on a desired frequency

8.4 Geometry Calculation

The second tab calculates a basic geometry from an input resonant frequency. Simply enter a frequency on the left side of the tab, and click the “Solve for geometry” button (see Figure 8.3). Results will appear on the right side of the tab.

The geometry calculation assumes a slot with a flange at both ends, thereby requiring the previously discussed “double correction” to the neck length. Using Kerschen’s results for axial wave theory, the geometry is computed using Algorithm 4. The final results are reduced to the next lowest multiple of $1/32$ ” for practical design use.

Algorithm 4 Computation of Helmholtz PRT actuator geometry given the desired frequency

Given the desired frequency, ω , assuming that the chamber radius is twice the neck radius ($r_c = 2r_n$), one can determine the desired value of Ω :

$$\Omega = \cos^{-1} \left[\frac{1 - (r_n/r_c)^2}{1 + (r_n/r_c)^2} \right] = \cos^{-1} \left(\frac{0.75}{1.25} \right) = 0.9273 \text{ radians}$$

From the definition of Ω and assuming that the effective neck length will be half the total effective length ($l = 2l_n$), one obtains

$$l_n = \frac{c\Omega}{2\omega}$$

From the definition of the end corrections, the geometric neck length is computed as

$$l_{n_{geom}} = l_n - 1.64r_n$$

The geometry is thus entirely determined, as the chamber length, l_c , is set to l_n , and the integration slot width, s , is $2r_n$.

Acknowledgements

A work of this magnitude would be impossible without the assistance of many people. In this section, the authors would like to acknowledge the contributions of several people whose input was especially significant. In particular, the authors would like to acknowledge the contributions of Dr. Steven Walker whose input helped to focus the work early on. Two of Dr. Ganesh Raman's graduate students made important contributions to the work: S. Khanafseh helped develop the feedback control capability and S. Sharpotdar played a major role in the impingement tone suppression work and understanding issues associated with directivity. In addition, we wish to acknowledge the contribution of Jonathan Hovde in developing the miniaturized version of the PRT. Thanks are also due to J. M. Tassy and A. Mills. William W. Romer assisted in developing the Helmholtz PRT design code GUI. Finally, the feedback from Dr. John Schmisser, AFOSR Program Manager during this Phase II effort, was greatly appreciated.

Bibliography

- [Alvi et al., 2003] Alvi, F. S., Shish, C., Elavarasan, R., Garg, G., and Krothapalli, A., 2003. Control of supersonic impinging jet flows using supersonic microjets. *AIAA Journal*, volume 41(7):1347–1362.
- [Aratani et al., 1995] Aratani, S., Narayanswami, N., Ojima, H., and Takayama, K., 1995. Studies of supersonic jets and shock waves generated during glass tempering process. *Transactions of the Japan Society of Mechanical Engineers (B)*, volume 61(590):1277–1282.
- [Brocher et al., 1970] Brocher, E., Maresca, C., and Bournay, M. H., 1970. Fluid dynamics of the resonance tube. *Journal of Fluid Mechanics*, volume 43(2):369–384.
- [Bush et al., 1998] Bush, R. H., Power, G. D., and Towne, C. E., 1998. WIND: The production flow solver of the NPARC alliance. AIAA Paper 98–0935.
- [Cain, 1997] Cain, A. B., 1997. Use of high frequency excitation to suppress flow induced resonance. Private Communication.
- [Cain and Bower, 1995] Cain, A. B. and Bower, W. W., 1995. Comparison of spatial numerical operations for duct-nozzle acoustics. In *Proceedings of the Computational Aeroacoustics Workshop*. NASA Langley.
- [Cain and Kerschen, 2003] Cain, A. B. and Kerschen, E. J., 2003. Simulation of a helmholtz powered resonance tube actuator. In *Division of Fluid Dynamics of the American Physical Society Meeting*. Meadowlands, NJ.
- [Cain et al., 1998] Cain, A. B., Vaporean, C. N., and Parekh, D. E., 1998. Computational characterization of receptivity in jet flow control. FEDSM 98–5310, ASME.
- [Cain et al., 2001] Cain, A. B., Rogers, M. M., Kibens, V., and Raman, G., 2001. Simulations of high-frequency excitation of a plane wake. AIAA Paper 2001–0514.
- [Cain et al., 2002a] Cain, A. B., Kerschen, E. J., and Raman, G., 2002a. Simulation of powered resonance tubes: Effects of pressure ratio and freestream flow. AIAA Paper 2002–2400.
- [Cain et al., 2002b] Cain, A. B., Kerschen, E. J., Raman, G., and Khanafseh, S., 2002b. Simulation of powered resonance tubes: Effects of pressure ratio and freestream flow. AIAA Paper 2002–2821.
- [Cain et al., 2003a] Cain, A. B., Kerschen, E. J., Raman, G., and Sarpotdar, S., 2003a. Simulation of powered resonance tubes: Understanding parameter space. AIAA Paper 2003–3103.
- [Cain et al., 2003b] Cain, A. B., Rogers, M. M., and Kibens, V., 2003b. Characterization of high frequency excitation of a wake by simulation. AIAA Paper 2003–0179.
- [Cain et al., 2004] Cain, A. B., Kerschen, E. J., Tassy, J. M., and Raman, G., 2004. Simulation of powered resonance tubes: Helmholtz resonator geometries. AIAA Paper 2004–2690.

- [Gad-el Hak, 2000] Gad-el Hak, M., 2000. *Flow Control: Passive, Active, and Reactive Flow Management*. Cambridge University Press.
- [Greenblatt and Wygnanski, 2000] Greenblatt, D. and Wygnanski, I. J., 2000. The control of flow separation by periodic excitation. *Progress in Aerospace Sciences*, volume 36(10):487–545.
- [Hartmann, 1931] Hartmann, J., 1931. On the production of acoustic waves by means of an air-jet of a velocity exceeding that of sound. *Philosophical Magazine and Journal of Science*, volume XI:926.
- [Hartmann and Troll, 1922] Hartmann, J. and Troll, B., 1922. On a new method on the generation of the sound waves. *Physics Review*, volume 20:719–727.
- [Iwamoto, 1990] Iwamoto, J., 1990. Experimental study in a rectangular jet-driven tube. *Transactions of the American Society of Mechanical Engineers Journal of Fluids Engineering*, volume 112(1):23–27.
- [Iwamoto and Deckker, 1985] Iwamoto, J. and Deckker, B. E. L., 1985. A study of the Hartmann-Sprenger tube using the hydraulic analogy. *Experiments in Fluids*, volume 3:245–252.
- [Kastner and Samimy, 2002] Kastner, J. and Samimy, M., 2002. Development and characterization of hartmann tube fluidic actuators for high-speed flow control. *AIAA Journal*, volume 40(10):1926–1934.
- [Kastner et al., 2004] Kastner, J., Hileman, J., and Samimy, M., 2004. Exploring high-speed axisymmetric jet noise control using hartmann tube fluidic actuators. AIAA Paper 2004-0186.
- [Kerschen, 2001] Kerschen, E. J., 2001. Analytical modeling of the resonant frequencies of a powered resonance tube. In *Division of Fluid Dynamics of the American Physical Society Meeting*. San Diego, CA.
- [Kerschen and Cain, 2003] Kerschen, E. J. and Cain, A. B., 2003. Analytical modeling of a helmholtz powered resonance tube actuator. In *Division of Fluid Dynamics of the American Physical Society Meeting*. Meadowlands, NJ.
- [Kerschen et al., 2004] Kerschen, E. J., Cain, A. B., and Raman, G., 2004. Analytical modeling of helmholtz resonator based powered resonance tubes. AIAA Paper 2004-2691.
- [Khanafseh et al., 2002] Khanafseh, S., Raman, G., and Cain, A. B., 2002. High bandwidth actuators for flow control applications. AIAA Paper 2002-2820.
- [Khanafseh, 2002] Khanafseh, S. M., 2002. *High Bandwidth Powered Resonance Tube Actuators with Feedback Control*. Master's thesis, Illinois Institute of Technology, Chicago, IL.
- [Kibens, 1980] Kibens, V., 1980. Discrete noise spectrum generated by an acoustically excited jet. *AIAA Journal*, volume 18(4):434–441.
- [Kral, 1999] Kral, L., 1999. Active flow control technology. In *American Society of Mechanical Engineers Tech Brief*.
- [Krothapalli et al., 1999] Krothapalli, A., Rajakuperan, E., Alvi, F. S., and Lourenco, L., 1999. Flow field and noise characteristics of a supersonic impinging jet. *Journal of Fluid Mechanics*, volume 392:155–181.
- [Lankford and Nelson, 2002] Lankford, D. W. and Nelson, C. C., 2002. Application of the Wind flow solver to chemically reacting flows. *AIAA-2002-0673*.

- [Masuda and Nakamura, 1992] Masuda, W. and Nakamura, T., 1992. A feasibility study on aerodynamic characteristics of underexpanded annular impinging jets for assisting laser cutting. In *Proceedings of LAMP '92*, pp. 613–654.
- [Murugappan and Gutmark, 2002] Murugappan, S. and Gutmark, E., 2002. Parametric study of Hartmann-Sprenger tube. AIAA Paper 2002–1012.
- [Murugappan and Gutmark, 2003] Murugappan, S. and Gutmark, E., 2003. Experimental and computational study of high frequency actuation of supersonic jets. AIAA Paper 2003–0370.
- [Nelson and Power, 2001] Nelson, C. C. and Power, G. D., 2001. CHSSI project CFD-7: The NPARC alliance flow simulation system. AIAA Paper 2001–0594.
- [Nelson et al., 2004] Nelson, C. C., Lankford, D. W., and Nichols, R. H., 2004. Recent improvements to the Wind(-US) code at AEDC. AIAA Paper 2004–0527.
- [Nelson et al., 2006] Nelson, C. C., Cain, A. B., Kerschen, E. J., and Raman, G., 2006. Simulations of helmholtz resonator powered resonance tubes at moderate pressure ratios. AIAA Paper 2006–0800.
- [Pierce, 1989] Pierce, A. D., 1989. *Acoustics: An Introduction to its Physical Principles and Applications*, pp. 341–350. Acoustical Society of America.
- [Powell, 1953] Powell, A., 1953. On edgetones and associated phenomena. *Acoustica* 3, pp. 233–243.
- [Power and Underwood, 1999] Power, G. D. and Underwood, M. L., 1999. Wind 2.0- progress on an applications-oriented CFD code. AIAA Paper 99–3212.
- [Raman and Cain, 2002] Raman, G. and Cain, A. B., 2002. Innovative actuators for flow and noise control. *Proceedings of the Institution of Mechanical Engineers, Part G: Journal of Aerospace Engineering*, volume 216:303–324.
- [Raman and Cain, 2004] Raman, G. and Cain, A. B., 2004. A perspective on high bandwidth powered resonance tube actuators. AIAA Paper 2004–2856.
- [Raman and Kibens, 2001] Raman, G. and Kibens, V., 2001. Active flow control using integrated powered resonance tube actuators. AIAA Paper 2001–3024.
- [Raman et al., 1999] Raman, G., Envia, E., and Bencic, T. J., 1999. Tone noise and nearfield pressure produced by jet cavity interaction. AIAA Paper 99–0604.
- [Raman et al., 2000] Raman, G., Kibens, V., Cain, A. B., and Lepicovsky, J., 2000. Advanced actuator concepts for active aeroacoustic control. AIAA Paper 2000–1930.
- [Raman et al., 2001] Raman, G., Mills, A., Othman, S., and Kibens, V., 2001. Development of powered resonance tube actuators for active flow control. FEDSM 2001–18273.
- [Raman et al., 2002] Raman, G., Khanafseh, S., and Cain, A., 2002. Development of high bandwidth actuators for aeroacoustic control. AIAA Paper 2002–0664.
- [Raman et al., 2004a] Raman, G., Khanafseh, S., Cain, A. B., and Kerschen, E., 2004a. Development of high bandwidth powered resonance tube actuators with feedback control. *Journal of Sound and Vibration*, volume 269:1031–1062.
- [Raman et al., 2004b] Raman, G., Mills, A., and Kibens, V., 2004b. Development of powered resonance-tube actuators for aircraft flow control applications. *Journal of Aircraft*, volume 41:1306–1314.

- [Sarohia and Lloyd, 1979] Sarohia, V. and Lloyd, H. B., 1979. Experimental investigation of flow and heating in a resonance tube. *Journal of Fluid Mechanics*, volume 94:649–672.
- [Sarpotdar et al., 2005a] Sarpotdar, S., Raman, G., and Cain, A. B., 2005a. Powered resonance tubes: Resonance characteristics and actuation signal directivity. *Experiments in Fluids*.
- [Sarpotdar et al., 2005b] Sarpotdar, S., Raman, G., Sharma, S. D., and Cain, A. B., 2005b. Impingement tone suppression using powered resonance tubes. submitted for publication in the AIAA Journal.
- [Sarpotdar et al., 2005c] Sarpotdar, S., Raman, G., Sharma, S. D., and Cain, A. B., 2005c. Impingement tone suppression using powered resonance tubes. AIAA Paper 2005–0797.
- [Savoy, 1950] Savoy, L. E., 1950. Experiments with the hartmann acoustic generator. *Engineering*, volume 170(99-100):136–138.
- [Sheplak and Spina, 1994] Sheplak, M. and Spina, E. F., 1994. Control of high speed impinging jet resonance. *AIAA Journal*, volume 32(8):1583–1588.
- [Smith and Powell, 1964] Smith, T. J. B. and Powell, A., 1964. Experiments concerning the hartmann whistle. UCLA Report 64–41.
- [Stanek, 2005] Stanek, M. J., 2005. *A Numerical Study of the Effect of Frequency of Pulsed Flow Control Applied to a Rectangular Cavity in Supersonic Crossflow*. Ph.D. thesis, University of Cincinnati, Cincinnati, OH.
- [Stanek et al., 2000] Stanek, M. J., Raman, G., Kibens, V., Ross, J., Peto, J., and Odedra, J., 2000. Cavity tone suppression using high frequency excitation. AIAA Paper 2000–1905.
- [Stanek et al., 2001] Stanek, M. J., Raman, G., Kibens, V., Ross, J., Peto, J., and Odedra, J., 2001. Suppression of cavity resonance using high frequency forcing - the characteristic signature of effective devices. AIAA Paper 2001–2128.
- [Tam, 1995] Tam, C. K. W., 1995. *Aeroacoustics of Flight Vehicles, Theory and Practice*, volume I, chapter Jet Noise Generated by Large-Scale Coherent Motion. Acoustical Society of America.
- [Tam and Ahuja, 1990] Tam, C. K. W. and Ahuja, K. K., 1990. Theoretical model of discrete tone generation by impinging jets. *Journal of Fluid Mechanics*, volume 214:67–87.
- [Thompson et al., 1992] Thompson, M. C., Hourigan, K., Welsh, M. C., and Brocher, E., 1992. Acoustic sources in a tripped flow past a resonator tube. *AIAA Journal*, volume 30(6):1484–1491.
- [Wilson, 1958] Wilson, J., 1958. *An Investigation of Resonance*. Master's thesis, Cornell University Graduate School of Aeronautical Engineering, Ithaca, NY.
- [Wilson and Resler, 1959] Wilson, J. and Resler, J., E. L., 1959. A mechanism of resonance tubes. *Aerospace Sciences Readers Forum Journal*, volume 26(7).
- [Wiltse and Glezer, 1993] Wiltse, J. M. and Glezer, A., 1993. Manipulation of free shear flows using piezoelectric actuators. *Journal of Fluid Mechanics*, volume 249:261–285.
- [Wiltse and Glezer, 1998] Wiltse, J. M. and Glezer, A., 1998. Direct excitation of small-scale motions in free shear flows. *Physics of Fluids*, volume 10(8):2026–2036.
- [Wolfram, 1996] Wolfram, S., 1996. *The Mathematica Book*. Cambridge University Press.

Appendix A

Helmholtz PRT Actuator Design Code Source

The core *Visual Basic* routines of the Helmholtz PRT actuator design code are listed here.

```
Imports System.Math
Imports System.IO
Imports System.Drawing.Printing
Public Class frmMain
    Inherits System.Windows.Forms.Form

    Dim Pi As Double
    Dim NeckRadius As Double
    Dim NeckCavityRatio As Double
    Dim NeckLength As Double
    Dim NeckLengthEff As Double
    Dim CavLength As Double
    Dim DDepthTotEff As Double
    Dim SoundSpeed As Double
    Dim FreqRef As Double
    Dim FreqRefG As Double
    Dim AlphaNeck As Double
    Dim DCav As Double
    Dim NeckFactor As Double
    Dim SlotLength As Double
    Dim DDepthEff As Double

    Private Sub Button1_Click(ByVal sender As System.Object, ByVal e As System.EventArgs) Handles _
        btnExit.Click
        End
    End Sub

    Private Sub frmMain_Load(ByVal sender As System.Object, ByVal e As System.EventArgs) Handles _
        MyBase.Load
        Pi = 3.1415927
        NeckCavityRatio = 0.666666666
        SoundSpeed = 1116.4
        NeckFactor = 0.82
        NeckRadius = 1
        DCav = 0.0
        NeckLength = 0.0
        FreqRefG = 0.0
        tbxfNeckCavityRatio.Text = NeckCavityRatio
        tbxSoundSpeed.Text = SoundSpeed
    End Sub
End Class
```

```

        tbxNeckRadius.Text = NeckRadius
        tbxFFreq.Text = "Enter data..."
    End Sub

Private Sub frmMain_SizeChanged(ByVal sender As Object, ByVal e As System.EventArgs) Handles _
    MyBase.SizeChanged
    pbxGeom.SetBounds(10, 10, Me.Size.Width - 30, Me.Size.Height - 230)
    btnExit.SetBounds(Me.Size.Width - 90, Me.Size.Height - 65, btnExit.Width, btnExit.Height)
    btnPrintIllustration.SetBounds(Me.Size.Width - 200, Me.Size.Height - 65, _
        btnPrintIllustration.Width, _
        btnPrintIllustration.Height)
    tbxStatus.SetBounds(32, Me.Size.Height - 65, Me.Size.Width - 64 - btnExit.Width - _
        btnPrintIllustration.Width, tbxStatus.Height)
    tabVariables.SetBounds(8, pbxGeom.Location.Y + pbxGeom.Height + 5, Me.Size.Width - 30, _
        tabVariables.Height)
End Sub

Private Sub pbxGeom_Click(ByVal sender As System.Object, ByVal e As System.EventArgs) Handles _
    pbxGeom.Click
    Dim frmVarDefs As New PRTVariables
    frmVarDefs.ShowDialog()
End Sub

Private Sub pbxGeom_MouseHover(ByVal sender As Object, ByVal e As System.EventArgs) Handles _
    pbxGeom.MouseHover
    tbxStatus.Text = "Click figure for variable definitions."
End Sub

Private Sub btnFSolve_Click(ByVal sender As System.Object, ByVal e As System.EventArgs) _
    Handles btnFSolve.Click
    UpdateFrequency()
End Sub

Private Sub tbxfLNeck_TextChanged(ByVal sender As System.Object, ByVal e As System.EventArgs) _
    Handles tbxfLNeck.TextChanged
    If Not IsNumeric(tbxFLNeck.Text) Then
        If tbxfLNeck.Text <> "." Then
            tbxfLNeck.Text = ""
        End If
    Else
        NeckLength = tbxfLNeck.Text
    End If
    tbxNeckRadius.Text = NeckRadius
End Sub

Private Sub tbxfDCav_TextChanged(ByVal sender As System.Object, ByVal e As System.EventArgs) _
    Handles tbxfDCav.TextChanged
    If Not IsNumeric(tbxDCav.Text) Then
        If tbxfDCav.Text <> "." Then
            tbxfDCav.Text = ""
        End If
    Else
        DCav = tbxfDCav.Text
    End If
End Sub

Private Sub tbxfNeckCavityRatio_TextChanged(ByVal sender As System.Object, ByVal e As _
    System.EventArgs) Handles _
    tbxfNeckCavityRatio.TextChanged
    If Not IsNumeric(tbxNeckCavityRatio.Text) Then
        If tbxfNeckCavityRatio.Text <> "." Then
            tbxfNeckCavityRatio.Text = ""
        End If
    Else

```

```

        NeckCavityRatio = tboxfNeckCavityRatio.Text
    End If
End Sub

Private Sub UpdateFrequency()
    Dim Omega, Omega2, Omega3, OmegaFinal, AlphaNeck2, AlphaNeck3, A, B, C As Double
    Dim iErr As Boolean
    NeckLength = tboxfLNeck.Text
    DCav = tboxfDCav.Text
    NeckCavityRatio = tboxfNeckCavityRatio.Text
    If NeckLength < (3 * NeckRadius) Then
        MsgBox("It is recommended that the neck length be at least 3 times the neck radius.")
    End If

    If (DCav > 0.0) And (NeckLength > 0.0) Then
        If NeckCavityRatio <= 0.6666666 And DCav >= (1.5 * NeckRadius) Then
            NeckLengthEff = NeckLength + (2.0 * NeckFactor * NeckRadius)
        Else
            NeckLengthEff = NeckLength + (NeckFactor * NeckRadius)
        End If
        FreqRef = 12.0 * SoundSpeed * NeckCavityRatio / Sqrt(DCav * NeckLengthEff) / 2.0 / Pi
        ' Find final frequency using combination Newton-Raphson iteration and linear/quadratic
        ' approximations
        ' 1. Calculate Omega when AlphaN = 0.5
        ' 2. Step to next AlphaN (use 10 intervals between 0.5 and our value)
        ' 3. Iterate to find new Omega
        ' 4. Use these two points to make linear approximation of new Omega at next AlphaN
        ' 5. Step to next AlphaN
        ' 6. Use guess from #4 and iterate to find new Omega
        ' 7. Use these three points to calculate quadratic approximation of next Omega at
        '    final AlphaN
        ' 8. Step to final AlphaN
        ' 9. Use guess from #7 and iterate to find final Omega
        ' 10. Calculate frequency from Omega
        DDepthTotEff = NeckLengthEff + DCav
        Omega = Acos((1.0 - NeckCavityRatio ^ 2) / (1.0 + NeckCavityRatio ^ 2))
        AlphaNeck = NeckLengthEff / DDepthTotEff
        AlphaNeck2 = 0.5 + (0.1 * (AlphaNeck - 0.5))
        iErr = False
        Omega2 = Omega
        OmegaSolve(NeckCavityRatio ^ 2, AlphaNeck2, Omega2, iErr)
        If iErr Then
            MsgBox("Unable to compute Omega.", MsgBoxStyle.OKCancel)
            Exit Sub
        End If
        AlphaNeck3 = AlphaNeck2 + (0.1 * (AlphaNeck - 0.5))
        Omega3 = Omega + (AlphaNeck3 - 0.5) * (Omega2 - Omega) / (AlphaNeck2 - 0.5)
        iErr = False
        OmegaSolve(NeckCavityRatio ^ 2, AlphaNeck3, Omega3, iErr)
        If iErr Then
            MsgBox("Unable to compute Omega.", MsgBoxStyle.OKCancel)
            Exit Sub
        End If
        A = (Omega3 - Omega2) / ((AlphaNeck3 - AlphaNeck2) * (AlphaNeck3 - 0.5)) - _
            ((Omega - Omega2) / ((0.5 - AlphaNeck2) * (AlphaNeck3 - 0.5)))
        B = (Omega - Omega2 + (A * (AlphaNeck2 ^ 2 - 0.5 ^ 2))) / (0.5 - AlphaNeck2)
        C = Omega - (A * 0.5 ^ 2) - (B * 0.5)
        OmegaFinal = (A * AlphaNeck ^ 2) + (B * AlphaNeck) + C
        iErr = False
        OmegaSolve(NeckCavityRatio ^ 2, AlphaNeck, OmegaFinal, iErr)
        If iErr Then
            MsgBox("Unable to compute Omega.", MsgBoxStyle.OKCancel)
            Exit Sub
        End If
    End If
End Sub

```

```

        FreqRef = 12.0 * SoundSpeed * OmegaFinal / DDepthTotEff / 2.0 / Pi
        tbxFFreq.Text = Math.Round(FreqRef, 4)
    Else
        tbxFFreq.Text = "Enter data..."
    End If
End Sub

Private Sub tbxNeckRadius_TextChanged(ByVal sender As System.Object, _
    ByVal e As System.EventArgs) Handles _
    tbxNeckRadius.TextChanged
    If Not IsNumeric(tbxNeckRadius.Text) Then
        If tbxNeckRadius.Text <> "." Then
            tbxNeckRadius.Text = ""
        End If
    Else
        NeckRadius = tbxNeckRadius.Text
    End If
End Sub

Private Sub btnGSolve_Click(ByVal sender As System.Object, ByVal e As System.EventArgs) _
    Handles btnGSolve.Click
    Dim i, loopCount As Integer
    Dim j As Integer
    Dim NeckRadiusFinal, N1, N2, Nnew, deltaNeck, F1, F2, Fg, Fgnew, Fp As Double
    Dim OmegaG, BigOmega As Double
    Dim convg As Boolean
    If FreqRefG = 0.0 Then
        MsgBox("Please enter a desired frequency that is different from the frequency" & _
            "calculated earlier.")
        Exit Sub
    End If

    ' Assume  $r(n) / r(c) = 0.5$ , therefore  $A(n)/A(c) = (r(n)/r(c))^2 = 0.25$ 

    OmegaG = 2.0 * Pi * FreqRefG
    BigOmega = Acos(0.75 / 1.25)
    NeckLengthEff = 12.0 * SoundSpeed * BigOmega / (2.0 * OmegaG)
    NeckLength = NeckLengthEff - (2.0 * NeckFactor * NeckRadius)
    DCav = NeckLengthEff

    i = 0
    Do While i <= Int(NeckLength)
        i = i + 1
    Loop
    i = i - 1
    j = 0
    Do While NeckLength >= (i + (j / 32.0))
        j = j + 1
    Loop
    j = j - 1
    NeckLength = i + (j / 32.0)

    i = 0
    Do While i <= Int(DCav)
        i = i + 1
    Loop
    i = i - 1
    j = 0
    Do While DCav >= (i + (j / 32.0))
        j = j + 1
    Loop
    j = j - 1
    DCav = i + (j / 32.0)

```



```

tbxGNeckLength.Text = NeckLength
tbxGNeckRadius.Text = NeckRadius
tbxGSlotLength.Text = 2.0 * tbxGNeckRadius.Text
tbxGDCav.Text = DCav
End Sub

Private Sub btnFSummary_Click(ByVal sender As System.Object, ByVal e As System.EventArgs) _
    Handles btnFSummary.Click
    Dim frmSummary As New Summary
    Dim sText As String
    sText = "PRT Design Tool" & vbCrLf & "Frequency Calculation" & vbCrLf & vbCrLf
    sText = sText & "Inputs:" & vbCrLf
    sText = sText & "Neck Length = " & NeckLength & " in." & vbCrLf
    sText = sText & "Cavity Depth = " & DCav & " in." & vbCrLf
    sText = sText & "Neck/Cavity Ratio = " & NeckCavityRatio & vbCrLf & vbCrLf
    sText = sText & "Calculated Frequency = " & tbxFFreq.Text & " Hz" & vbCrLf & vbCrLf
    sText = sText & "System Variables:" & vbCrLf
    sText = sText & "Neck Radius = " & Math.Round(NeckRadius, 4) & " in." & vbCrLf
    sText = sText & "Speed of Sound = " & SoundSpeed & " ft/sec"
    frmSummary.tbxFSummary.Text = sText
    frmSummary.ShowDialog()
End Sub

Private Sub btnGSummary_Click(ByVal sender As System.Object, ByVal e As System.EventArgs) _
    Handles btnGSummary.Click
    Dim frmSummary As New Summary
    Dim sText As String
    sText = "PRT Design Tool" & vbCrLf & "Geometry Calculation" & vbCrLf & vbCrLf
    sText = sText & "Inputs:" & vbCrLf
    sText = sText & "Reference Frequency = " & FreqRefG & " Hz" & vbCrLf & vbCrLf
    sText = sText & "Calculated Cavity Depth = " & tbxGDCav.Text & " in." & vbCrLf
    sText = sText & "Calculated Actual Neck Length = " & tbxGNeckLength.Text & " in." & vbCrLf
    sText = sText & "Calculated Neck Radius = " & tbxGNeckRadius.Text & " in." & vbCrLf
    sText = sText & "Calculated Slot Width = " & tbxGSlotLength.Text & " in." & vbCrLf & vbCrLf
    sText = sText & "System Variables:" & vbCrLf
    sText = sText & "Speed of Sound = " & SoundSpeed & " ft/sec"
    frmSummary.tbxGSummary.Text = sText
    frmSummary.ShowDialog()
End Sub

Private Sub btnPrintIllustration_Click(ByVal sender As System.Object, ByVal e As _
    System.EventArgs) Handles btnPrintIllustration.Click
    Try
        AddHandler PrintDocument1.PrintPage, AddressOf Me.PrintGraphic
        PrintDocument1.Print()
    Catch ex As Exception
        MessageBox.Show("Sorry--there is a problem printing", _
            ex.ToString())
    End Try
End Sub

Private Sub PrintGraphic(ByVal sender As Object, _
    ByVal ev As PrintPageEventArgs)
    ev.Graphics.DrawImage(pbxGeom.Image, ev.Graphics.VisibleClipBounds)
    ev.HasMorePages = False
End Sub

Private Function FOmega(ByVal NeckCavityRatio As Double, ByVal Alphan As Double, _
    ByVal Omega As Double)

    FOmega = (1.0 + NeckCavityRatio) * Cos(Omega) - _
        (1.0 - NeckCavityRatio) * Cos((2.0 * Alphan - 1.0) * Omega)

```

```

End Function

Private Function FpOmega(ByVal NeckCavityRatio As Double, ByVal Alphan As Double, _
    ByVal Omega As Double)

    FpOmega = -(1.0 + NeckCavityRatio) * Sin(Omega) + (1.0 - NeckCavityRatio) * _
        (2.0 * Alphan - 1.0) * Sin(Omega * (2.0 * Alphan - 1.0))

End Function

Private Sub OmegaSolve(ByVal NeckCavityRatio As Double, ByVal Alphan As Double, _
    ByRef Omega As Double, ByRef iErr As Boolean)

    Dim DeltaConv, DeltaOmega, OmegaTmp, OmegaTmpNew As Double
    Dim iCount As Integer

    DeltaConv = 0.00000001
    DeltaOmega = 999.0
    iCount = 0
    iErr = False
    OmegaTmp = Omega

    Do While ((DeltaOmega > DeltaConv) And (Not iErr))
        OmegaTmpNew = OmegaTmp - (FOmega(NeckCavityRatio, Alphan, OmegaTmp) / _
            FpOmega(NeckCavityRatio, Alphan, Omega))

        iCount = iCount + 1
        If iCount > 20 Then
            iErr = True
        Else
            DeltaOmega = Abs(OmegaTmpNew - OmegaTmp) / OmegaTmp
            OmegaTmp = OmegaTmpNew
        End If
    Loop

    If Not iErr Then
        Omega = OmegaTmpNew
    Else
        End If
    End If

End Sub

Private Sub tbxGFreqRef_TextChanged(ByVal sender As System.Object, _
    ByVal e As System.EventArgs) Handles _
    tbxGFreqRef.TextChanged

    If Not IsNumeric(tbxGFreqRef.Text) Then
        If tbxGFreqRef.Text <> "." Then
            tbxGFreqRef.Text = ""
        End If
    Else
        FreqRefG = tbxGFreqRef.Text
    End If
End Sub

End Class

```